

# **Biophysical Studies of Lipid Membranes by Solid State NMR and Molecular Dynamics Simulations**

Dissertation zur Erlangung des Doktorgrades der Naturwissenschaften

vorgelegt dem Fachbereich Biochemie, Chemie, Pharmazie

Institut für Biophysikalische Chemie

der Johann Wolfgang Goethe Universität Frankfurt am Main

von

**Bercem Dutagaci**

Aus

Eskisehir – Türkei

Frankfurt am Main - 2013

vom Fachbereich 14 der  
Goethe Universität als Dissertation angenommen.

Dekan: Prof. Dr. Prisner

Gutachter : Prof. Dr. Glaubitz

Prof. Dr. Güntert

Datum der Disputation:

*to my parents*

Zusammenfassung.....	1
Summary .....	6
1 Introduction.....	9
1.1 Lipids Membranes .....	9
1.1.1 Structures and Physical Properties.....	9
1.1.2 Functional Importance of Physical Properties of Lipid Bilayers .....	16
1.2 Solid State NMR.....	17
1.2.1 Theory .....	17
1.2.1.1 Magic Angle Spinning (MAS).....	18
1.2.2 Solid-State NMR on Lipid Membranes .....	19
1.2.3 Probing Lipid Phases via $^{31}\text{P}$ -NMR/Chemical Shift Anisotropy Measurements (CSA) ...	20
1.2.4 Characterizing Lipids by Quadrupolar NMR: $^2\text{H}$ and $^{14}\text{N}$ .....	23
1.2.5 $^{13}\text{C}$ - $^1\text{H}$ Dipolar Order Parameters .....	24
1.2.6 MAS – $^{13}\text{C}$ and $^1\text{H}$ Chemical Shifts.....	25
1.2.7 $^1\text{H}$ -MAS NOESY.....	26
1.3 Molecular Dynamics.....	28
1.3.1 Theory .....	28
1.3.2 Molecular dynamics on membranes .....	29
1.3.3 Limitations .....	30
1.3.3.1 Classical Mechanics .....	30
1.3.3.2 Time-scales .....	31
1.3.3.3 Force-fields .....	31
1.3.3.4 Boundary effects .....	31
1.3.3.5 Ensembles.....	32
1.4 Aim of This Study .....	33
2 Material and Methods.....	35
2.1 Solid-State NMR .....	35
2.1.1 Materials.....	35
2.1.2 Sample Preparation .....	35
2.1.3 SS-NMR Instrumentation.....	37
2.1.4 SS-NMR Experiments .....	37
2.1.4.1 $^1\text{H}$ - $^1\text{H}$ -MAS NOESY.....	37
2.1.4.2 $^1\text{H}$ - $^1\text{H}$ -MAS RFDR .....	38
2.1.4.3 $^2\text{H}$ Quadrupolar Coupling Measurements .....	39
2.1.4.4 $^{13}\text{C}$ - $^1\text{H}$ Separated Local Field Experiments .....	41
2.1.4.5 Laboratory Frame Spin-Lattice Relaxation Time ( $T_1$ ).....	44
2.1.4.6 Rotating Frame Spin-Lattice Relaxation Time ( $T_{1\rho}$ ).....	46
2.1.4.7 Static and MAS $^{31}\text{P}$ NMR.....	47
2.1.4.8 $^{14}\text{N}$ MAS Measurements .....	48



2.1.4.9	<sup>31</sup> P- Static and MAS Exchange Experiments .....	49
2.2	Molecular Dynamics.....	52
2.2.1	Simulation Details .....	52
2.2.2	Energy Minimization .....	52
2.2.3	Time Steps.....	52
2.2.4	Output Options .....	53
2.2.5	Neighbor Searching .....	53
2.2.6	Electrostatics and Van der Waals Interactions .....	53
2.2.7	Temperature Coupling.....	54
2.2.8	Pressure Coupling .....	54
2.2.9	Constraint on Bonds.....	54
2.2.10	Position Restraints .....	55
3	Probing Lipid Interactions of Pirinixic Acid Derivatives .....	56
3.1	Introduction .....	56
3.1.1	Objectives.....	59
3.2	Materials and Methods.....	59
3.2.1	Sample Preparation .....	59
3.2.2	Solid State NMR.....	60
3.2.3	Partition Coefficients .....	61
3.2.4	MD Simulations.....	61
3.2.4.1	Methods .....	61
3.2.4.2	Starting Structures.....	61
3.2.4.3	Force-fields .....	62
3.2.4.4	Simulation Parameters.....	62
3.2.4.5	Restraints .....	63
3.2.4.6	Analysis .....	63
3.3	Results and Discussion .....	63
3.3.1	Solid State NMR.....	63
3.3.1.1	<sup>1</sup> H Chemical Shift Differences .....	63
3.3.1.2	<sup>1</sup> H-MAS NOESY .....	66
3.3.1.3	<sup>1</sup> H-MAS RFDR.....	75
3.4	Molecular Dynamics.....	80
3.5	Conclusion .....	90
4	Characterization of Drug – Lipid Complexes by Solid-State NMR .....	92
4.1	Introduction .....	92
4.1.1	Objectives.....	94
4.2	Materials and Methods.....	95
4.2.1	Sample Preparation .....	95
4.2.2	Solid State NMR.....	95

4.3	Results and Discussion .....	96
4.3.1	1D $^1\text{H}$ MAS NMR .....	96
4.3.2	$^1\text{H}$ - $^1\text{H}$ -MAS NOESY NMR.....	98
4.3.3	Static $^{31}\text{P}$ -NMR Spectroscopy.....	104
4.3.4	Conclusion.....	106
5	Ceramide – Lipid Bilayer Studies .....	107
5.1	Introduction .....	107
5.1.1	Objective .....	109
5.2	Materials and Methods.....	110
5.2.1	MD Simulation .....	110
5.2.1.1	Method .....	110
5.2.1.2	Starting Structures.....	111
5.2.1.3	Force-fields .....	111
5.2.1.4	Parameters used for the Simulations .....	112
5.2.1.5	Analysis .....	112
5.2.2	Sample Preparation .....	117
5.2.3	Solid State NMR.....	117
5.3	Results and Discussion .....	120
5.3.1	MD Simulations.....	121
5.3.1.1	Area per Lipid .....	122
5.3.1.2	Density Profiles.....	124
5.3.1.3	Chain Order Parameters .....	125
5.3.1.4	Hydrogen bonding.....	127
5.3.1.5	Radial Distribution Function .....	130
5.3.1.6	Electrostatic Potential.....	132
5.3.1.7	P-N Vector Orientation.....	132
5.3.2	Solid State NMR.....	135
5.3.2.1	Static $^{31}\text{P}$ -NMR.....	135
5.3.2.2	Temperature dependent $^1\text{H}$ -MAS NMR and $^1\text{H}$ -MAS NOESY .....	136
5.3.2.3	$^{14}\text{N}$ -MAS NMR.....	153
5.3.2.4	Dipolar Order Parameters.....	157
5.3.2.5	$^{31}\text{P}$ -CODEX Measurements.....	162
5.3.2.6	$^{31}\text{P}$ Static Exchange Measurements.....	165
5.4	Conclusion .....	169
6	Investigation of Hydrophobic Polarizing Agents for DNP.....	171
6.1	Introduction .....	171
6.1.1	Objectives.....	172
6.2	Materials and Methods.....	173
6.2.1	Sample Preparation .....	173
6.2.2	Solid-State NMR .....	173
6.2.3	Molecular Dynamics.....	173

6.2.3.1	Starting Structures.....	173
6.2.3.2	Force-fields.....	174
6.2.3.3	Simulation Parameters.....	174
6.2.3.4	Analysis.....	174
6.3	Results and Discussion.....	175
6.4	Conclusion.....	180
7	Conclusion and Outlook.....	182
8	Appendix.....	185
8.1	Solid State NMR Studies on POPC – Ceramide Systems.....	185
8.1.1	Dipolar Order Parameters.....	185
8.1.2	Quadrupolar Order Parameters.....	187
8.1.3	<sup>31</sup> P-NMR.....	189
8.1.4	Spin-Lattice Relaxation Times at Laboratory Frame.....	190
8.1.5	Spin-Lattice Relaxation Times at Rotating Frame.....	192
8.2	MD Studies on POPC – Ceramide Systems.....	195
8.2.1	Area per Lipid.....	195
8.2.2	Density Profile.....	197
8.2.3	Chain Order Parameters.....	199
8.2.4	Hydrogen-bonding.....	205
8.2.5	Radial Distribution Function.....	207
	References.....	208
	List of Abbreviations.....	221
	List of Figures.....	223
	List of Tables.....	231
	Curriculum Vitae.....	232
	Acknowledgement.....	235

## Zusammenfassung

Biologische Membranen stellen eine Permeabilitätsbarriere zwischen dem Inneren und dem Äußeren von Zellen dar, die im Wesentlichen über die eingebetteten Membranproteine gesteuert wird. Für die mit der Membran assoziierten funktionalen Prozesse spielen aber auch Lipidbestandteile eine wichtige Rolle, was deren genaue Charakterisierung erforderlich macht. Beispiele hierfür sind u.a. laterale Phasentrennung/Rafts, Auflösung von Doppelschichtphasen bei der Zellfusion, die Rolle bestimmter Lipidbestandteile als sekundäre Botenstoffe, Modulierung der Aktivität von Membranproteinen über spezifische Lipidinteraktionen oder veränderte physikalische Membranparameter oder auch die Interaktion lipophiler Pharmaka mit Lipiden. Festkörper-NMR bietet einen idealen Zugang zu diesen Fragestellungen, da diese Technik direkte Experimente an verschiedensten Lipidphasen zulässt sowie über eine sehr große dynamische Bandbreite verfügt, über die mit geeigneten Experimenten viele dynamische Prozesse in der Membran detektiert werden können. Komplementär zu Festkörper-NMR können MD-Simulationen an vollständigen Lipiddoppelschichten zum Einsatz gebracht werden, um entweder Vorhersagen machen zu können, die mittels NMR überprüft werden können, oder um im Falle von unvollständigen NMR Datensätzen zu einem vollständigeren molekularen Bild des betrachteten Systems zu gelangen. Ziel dieser Dissertation war es daher, einen kombinierten FK-NMR/MD-Simulationsansatz für die Untersuchung kleiner Moleküle in der Lipidmembran zu etablieren und an mehreren Beispielen zu demonstrieren.

Alle verwendeten Methoden, insbesondere Details zu den verwendeten MD-Simulationstechniken und zur Festkörper-NMR sind im **Kapitel 2** dargestellt.

Ziel von **Kapitel 3** war es den Einbau von Wirkstoffen in die Membran in einem kombinierten Festkörper-NMR / MD-Simulationsansatz am Beispiel von zwei Pirinixinsäurederivaten, die freundlicherweise von der Gruppe von Prof. M. Schubert-Zsilavicz zur Verfügung gestellt wurden, zu demonstrieren. Diese Substanzen sind von Interesse als Leistrukturen für mögliche Aktivatoren der Peroxisomen Proliferator-aktivierten Rezeptoren (PPARs) sowie für mögliche Inhibitoren von zwei

Schlüsselenzymen der Arachidonsäurekaskade, nämlich der 5-Lipoxygenase (5-LO) und der mikrosomalen Prostaglandin E2-Synthase-1 (mPGES-1). Insbesondere im Falle der 5-Lipoxygenase spielen Fragen einer membranassoziierten Aktivierung oder Inhibierung eine Rolle, wofür ein genaues Verständnis der Lipidinteraktion der entsprechenden Wirkstoffe von Interesse ist.

Bei den untersuchten Derivaten handelt es sich um 2-(4-Chloro-6-(Quinolin-6-Ylamino)Pyrimidin-2-Ylthio)Octansäure und 2-(4-Chloro-6-(Quinolin-6-Ylamino)Pyrimidin-2-Ylthio)Octansäurester. Beide Substanzen wurden in Lipiddoppelschichten aus POPC eingebaut. Eine Analyse der  $^1\text{H}$  chemischen Verschiebungen von POPC, die aus  $^1\text{H}$ -MAS NMR Spektren erhalten wurden, zeigt größere Effekte des Ester- verglichen zum Säurederivat. Im den Membraneinbau genauer studieren zu können wurden Serien von  $^1\text{H}$ -MAS NOESY Spektren bei unterschiedlichen Mischzeiten aufgenommen und die Aufbauraten der Lipid-Derivat Kreuzpeaks bestimmt. Hieraus ließen sich Aufenthaltsverteilungen der Protonen der Substrate bezogen auf die Lipide ableiten. Um ein genaueres Bild zu erhalten wurden diese Daten als Randbedingungen für MD-Simulationen benutzt, in denen die Derivate explizit in einer POPC Lipiddoppelschicht simuliert wurden. Die Daten zeigen eine klare Lipidassoziation beider Substanzen aber deutliche Unterschiede im Einbau. Das Säurederivat ist eher mit den Lipidkopfgruppen assoziiert, während die Esterform sich in die Kettenregion einlagert. Diese Daten zeigen, dass die Kombination aus FK-NMR und MD-Simulationen sehr genaue Einblicke ermöglicht, die anders nicht zu erhalten wären. Der hier verfolgte Ansatz beruht auf der Analyse intermolekularer Kontakte unter Ausnutzung des NOE. Dieser Effekt ist im Festkörper normalerweise nicht beobachtbar und funktioniert hier nur wegen der hohen anisotropen Beweglichkeit der Lipide. Eine generelle Alternative stellen dipolare Rückkopplungsexperimente dar. Der Vorteil wäre, dass wegen der  $1/r^3$  Abhängigkeit schnellere Aufbauraten zu erwarten sind. Daher wurden an beiden Proben auch  $^1\text{H}$ - $^1\text{H}$  RFDR Datensätze aufgenommen und Aufbauraten bestimmt. Allerdings zeigen sich deutliche Unterschiede in der Analyse der intermolekularen verglichen zu den intramolekularen Kreuzpeaks. Ein Grund hierfür ist, dass im Falle von Lipiden im RFDR Experiment intramolekulare Kontakte stärker gewichtet, das NOESY Experiment jedoch von intermolekularen Kontakten dominiert ist. Daher stellt das direkte dipolare RFDR Experiment keine effiziente Alternative zum NOESY-MAS Experiment für die Analyse von Lipid-Substrat Interaktionen dar.

Die Verabreichung bestimmter Pharmaka in Form von Lipidkomplexen erfreut sich zunehmender Popularität. Zum einen werden Phospholipide benutzt, um die Löslichkeit und Aufnahme lipophiler Phytopharmaka zu erhöhen. Zum anderen konnte gezeigt werden, dass die gastrointestinale Toxizität

nichtsteroidaler Antirheumatika auf diese Weise reduziert werden kann. Da aber verschiedene Wirkstoffe sich in ihrer Membrangängigkeit unterscheiden stellt sich die Frage, ob sich in allen Fällen tatsächlich Phospholipidkomplexe ausbilden, bzw. wie diese beschaffen sind. In **Kapitel 4** wurde daher mittels Festkörper-NMR die Interaktion von Diclofenac, Ibuprofen und Piroxicam mit dem Phospholipid DPPC untersucht.  $^1\text{H}$ -NOESY MAS NMR Experimente zeigen direkte Interaktionen zwischen Diclofenac und Ibuprofen mit DPPC. Im Gegensatz dazu konnte für Piroxicam keine Wechselwirkung mit den Lipiden beobachtet werden. Statische  $^{31}\text{P}$ -NMR Experimente, aus denen sich direkt Polymorphismus und Phasenverhalten von Phospholipidproben ableiten lässt, zeigen insbesondere für Ibuprofen eine starke Störung der Linienform, was auf Phasentrennung oder Störung der Doppelschicht hinweist. Allerdings weist die Linienform sowohl für Ibuprofen als auch für Diclofenac insgesamt auf die Ausbildung von liposomalen Strukturen hin, was die beobachteten positiven pharmakologischen Effekte der Phospholipid-Wirkstoffkomplexe zumindest für diese beiden Substanzen erklärt. Diese Experimente waren eine Kooperation im Rahmen einer umfassende Studie zu Phospholipidkomplexen mit dem Labor von Dr. M. Tawab.

Neben Lipid-Substratinteraktionen lassen sich auch Lipid-Lipidwechselwirkungen durch eine Kombination aus FK-NMR und MD-Simulationen sehr gut beschreiben. Dies ist von besonderem Interesse wenn man berücksichtigt, dass Membranbestandteile wie bspw. Cholesterin oder Sphingolipide eine indirekte und direkte funktionale Bedeutung haben. In **Kapitel 5** sollte daher die Interaktion von Ceramiden mit Phospholipiden umfassend beschreiben werden. Ceramide sind bioaktive Sphingolipide die als sekundäre Botenstoffe in der Zellmembran eine wichtige Rolle spielen. Sie modulieren die Aktivität bestimmter Enzyme und tragen damit zur Induktion von Prozessen wie Apoptose, Zelldifferenzierung oder Zellalterung bei. Weiterhin gibt es Hinweise darauf, dass Ceramide Lipidplattformen wie Rafts stabilisieren bzw. das Phasenverhalten und die allgemeinen physikalischen Eigenschaften von Phospholipidmembranen modulieren können.

Um einen genauen Einblick auf atomarer Ebene zu gewinnen wurden daher DMPC Doppelschichten als Modell gewählt, in welches Ceramid-16 eingebaut wurde. Es wurden umfangreiche MD Simulationen durchgeführt, um mögliche DMPC-Ceramid Interaktionen vorhersagen zu können, welche dann mittels Festkörper-NMR überprüft werden sollten. Diese Simulationen sagten voraus, dass die Zugabe von Ceramid die Kettenordnung der Lipide deutlich erhöht. Gleichzeitig ist die Kettenordnung der Ceramide höher, als die der Lipide. Dies weist entweder auf *Clustering* oder Ceramid-Lipid Komplexe hin. Letzteres wird gestützt durch die Vorhersage von Wasserstoffbrücken

zwischen Ceramid und DMPC. Um diese Vorhersagen überprüfen zu können, wurden umfangreiche Festkörper-NMR Experimente mit verschiedenen Kernen ( $^1\text{H}$ ,  $^{31}\text{P}$ ,  $^{13}\text{C}$ ,  $^2\text{H}$ ,  $^{14}\text{N}$ ) durchgeführt. Die Erhöhung der Kettenordnung wurde mittels dipolarer PISEMA-MAS Experimente überprüft. Bei diesem 2D Experiment werden dipolare C-H Kopplungen im Lipid als auch im Ceramid bestimmt um daraus einen Ordnungsparameter bestimmen zu können. Diese Experimente zeigen in der Tat, dass die aus der Simulation abgeleiteten Vorhersagen korrekt sind. Um Lipid-Ceramid Kontakte direkt nachweisen zu können wurden  $^1\text{H}$ -NOESY-MAS Experimente an Proben durchgeführt, in denen DMPC partiell deuteriert war. Trotz Signalüberlappung konnten spezifische Kontakte zwischen Glycerol- und Sphingosinprotonen detektiert werden. Hinweise auf die Ausbildung einer Wasserstoffbrücke ergaben sich aus der Detektion einer zusätzlichen Resonanz im  $^1\text{H}$  als auch im  $^{14}\text{N}$ -MAS NMR Spektrum.

Die hier präsentierte Kombination aus MD-Simulation und FK-NMR Daten zeigt sehr deutlich, dass Ceramide einen starken Einfluss auf Phospholipidmembranen haben und dass sich sehr wahrscheinlich Lipid-Ceramid Komplexe in der Membran bilden.

**Kapitel 6** widmet sich der Lipidinteraktion von stabilen Radikalen, welche für *Dynamic Nuclear Polarisation (DNP)* benötigt werden. DNP ermöglicht es die Empfindlichkeit von Festkörper-NMR um mehrere Größenordnungen zu steigern, indem Magnetisierung von in der Probe vorhandenen ungepaarten Elektronen über den *Cross Effect* auf Kerne übertragen werden. Hierfür ist es jedoch nötig die Probe mittels stabiler Radikale zu „dopen“. Als besonders wirksam haben sich Biradikale auf der Basis von Nitroxiden wie bspw. TOTAPOL oder bTbK erwiesen. Insbesondere letztere Substanz ermöglicht sehr große Signalverstärkungen, da die g-Tensoren der beiden paramagnetischen Zentren senkrecht zueinander fixiert sind. Allerdings erwies sich bTbK als nicht löslich, was seine Einsatzmöglichkeiten stark einschränkt. Da Studien an Membranproteinen ein Hauptanwendungsgebiet von DNP-Festkörper-NMR darstellen, stellte sich die Frage, ob bTbK nicht doch als möglicherweise membrangängiges Polarisationszentrum genutzt werden könnte. Mit denen in dieser Dissertation etablierten Methoden sollte daher die Membraninteraktion von bTbK am Beispiel von DMPC charakterisiert werden. Da der Einbau eines paramagnetischen Zentrums in die Lipiddoppelschicht zu einer Verbreiterung der Resonanzlinien der unmittelbar benachbarten Lipidmoleküle führt, ist der MAS-NOESY Ansatz ungeeignet. Stattdessen wurden  $^1\text{H}$ - $T_1$  Relaxationszeiten über  $^{13}\text{C}$  detektierte Experimente bestimmt. In einem zweiten Schritt wurden MD-Simulationen an bTbK in DMPC ausgeführt. Beide Ansätze zeigen, dass bTbK sich tatsächlich in die Membran einbaut und tendenziell

eher in der hydrophoben Kettenregion zu finden ist. Weitere Studien in der Arbeitsgruppe haben gezeigt, dass in dieser Situation bTbK tatsächlich genutzt werden kann, um Membranproteine mittels DNP aus der Membran heraus zu polarisieren.



## Summary

Biological membranes separate the cell interior from the outside and have diverse functions from signal transduction, apoptosis to transportations of ions and small molecules in and out of the cell. Most of these functions are fulfilled by proteins incorporated in the membrane. However, lipids as the main component of membrane not only serve as structural element for bilayer formation but they are also directly involved e.g. signalling processes and bilayer properties are important to mediate protein interactions. To fully understand the role of lipids, it is necessary to develop a molecular understanding of how certain membrane components modify bulk bilayer structure and dynamics.

Membranes are known to have many different motions in different conditions and time scales. Temperature, pH, water content and many other conditions change membrane dynamics in a high degree. In addition to this, time scales of motions in membranes vary from ns to ms range corresponding to fast motion and slow motion, respectively. Therefore, membranes are needed to be studied systematically by varying the conditions and using methods to investigate motions in various time scales separately.

The aim of this study was therefore perform a combined solid-state NMR / molecular dynamics study on model membranes. Different substrates, such as potential drugs, polarizing agents and signaling lipids were incorporated into bilayers and their location within the membrane and their effect onto the membrane was probed.

NSAIDs (non-steroidal anti-inflammatory drugs), pirinixic acid derivatives, ceramides and polarizing agents were the substrates for membranes in this study. There were several experimental methods that were applied in order to investigate effects of these substrates on membrane dynamics. Different kind of phospholipids including POPC, DMPC and DPPC were used. In addition to experimental work, with the information gathered from solid state NMR experiments molecular dynamics simulations were performed to obtain more information about the membranes at the molecular level. As a result, combination of solid-state NMR with molecular dynamics simulations provides very systematic way of investigating membrane dynamics in a large range of time scales.

Pirinixic acid derivatives were special interest of this study because of their activity on peroxisome proliferator-activated receptor (PPAR) as an agonist as well as on enzymes of microsomal

prostaglandin E2 synthase-1 (PGE2s) -1 and 5-lipoxygenase (5-LO) as dual inhibitor. Two potent piroxic acid derivatives, 2-(4-chloro-6-(quinolin-6-ylamino)pyrimidin-2-ylthio)octanoic acid (compound **2**) and 2-(4-chloro-6-(quinolin-6-ylamino)pyrimidin-2-ylthio)octanoate (compound **3**), have been worked and their insertion depths were investigated by combining of solid state NMR and molecular dynamics simulations. Both experimental and theoretical results pointed out that compound **3** was inserted the phospholipid bilayer more deeply than **2**.

NSAIDs – lipid mixtures have been also studied here. It is known that consumption of NSAIDs as in mixture with lipids results much fewer side effects than consumption of the drugs alone. Thus, it is crucial to understand interactions of NSAIDs with lipids and investigate the possible complex formation of drugs with lipids. In this study, interactions of three widely used NSAIDs, ibuprofen, diclofenac and piroxicam, with DPPC were investigated by solid-state NMR.  $^1\text{H}$  and  $^{31}\text{P}$  NMR results depicted that ibuprofen and diclofenac had interactions with lipids, which is an indication of drug-lipid complex formation whereas piroxicam didn't show any interactions with lipids suggesting that no complex formation occurred in the case of piroxicam.

Ceramides are known to play key roles in many cell processes and many studies showed that the functions of ceramides are related with the ceramide effects on biological membranes. Therefore, in this study, influences of ceramides on biophysics of lipid bilayers were investigated by using various solid state NMR techniques and molecular dynamics simulations. Results from molecular dynamics simulations clearly showed that ceramide and lipids have strong interactions. More evidences about ceramide-lipid interactions were provided from  $^1\text{H}$  and  $^{14}\text{N}$  NMR results. In addition, it was indicated by both simulation and experimental methods that ceramide increased the rigidity of DMPC by increasing chain order parameters.

BTbk is a biradical, which is used as polarizing agent for dynamic nuclear polarization (DNP) experiments and found to be more efficient than other widely used polarizing agents such as TOTAPOL. Since it is a hydrophobic compound, which prefers to stay inside lipid bilayer it is important to investigate the location and orientation of bTbk along the bilayer in order to understand its enhancement profile in DNP measurements. In this study, both NMR relaxation time measurements and molecular dynamics simulations revealed that bTbk tends to stay more close to hydrophobic chain of lipids than the interfacial part of lipids at bilayer surface.

In the first part of this work, a brief introduction on lipid membranes as well as a theoretical summary on both methods of solid-state NMR and molecular dynamics simulations is given. Then, in the second part methodology is introduced for both solid-state NMR spectrometer and theoretical calculations. Afterwards, results of different membrane systems are discussed in the following parts for both solid state NMR and MD. Finally, in the last part, a summary and the conclusion of the overall results together with some future plans are explained.

# 1 Introduction

## 1.1 *Lipids Membranes*

### 1.1.1 Structures and Physical Properties

Biological membranes are two dimensional liquids and are composed of lipids and proteins (Singer and Nicolson 1972). Membrane proteins embedded inside lipid bilayers are functioning as channels, pumps, receptors and enzymes. In most cases, their function and specific activity is directly linked to the lipids in the bilayer either through specific lipid-protein interactions or through general properties by the lipid bilayer (e.g. phase, charges, curvature, lateral pressure, electrostatic potential and hydrophobic profile across membrane) (Epanand 1998; Marsh 2008). It is therefore necessary to fully understand chemical and physical properties of lipid membranes and to link them with functional data of membrane proteins.

Lipids are diverse biological compounds. They are diverse in terms of chemical structure as well as in terms of their functions. Fats and oils are known as storage lipids whereas phospholipids, glycolipids and sterols are functioning as structural lipids, which form biological membranes. The most relevant membrane structure is the lipid bilayer, which creates a hydrophobic barrier against polar and charged molecules. Membrane lipids are amphiphatic molecules, which contain hydrophobic tails and hydrophilic head groups linked via a backbone. Lipids are classified with respect to their head groups, chain lengths, backbone and degree of unsaturation. For example, glycerophospholipids contain fatty acids and phosphorus head group, which are linked by glycerol unit as backbone. Sphingolipids are similar to phospholipids except the presence of sphingosine, which serves as backbone unit instead of glycerol. Finally, sterols are very different from the rest of lipid types in terms of structure, which have a sterol backbone unit that connects polar head group and hydrocarbon tail (Nelson and Cox 2005).

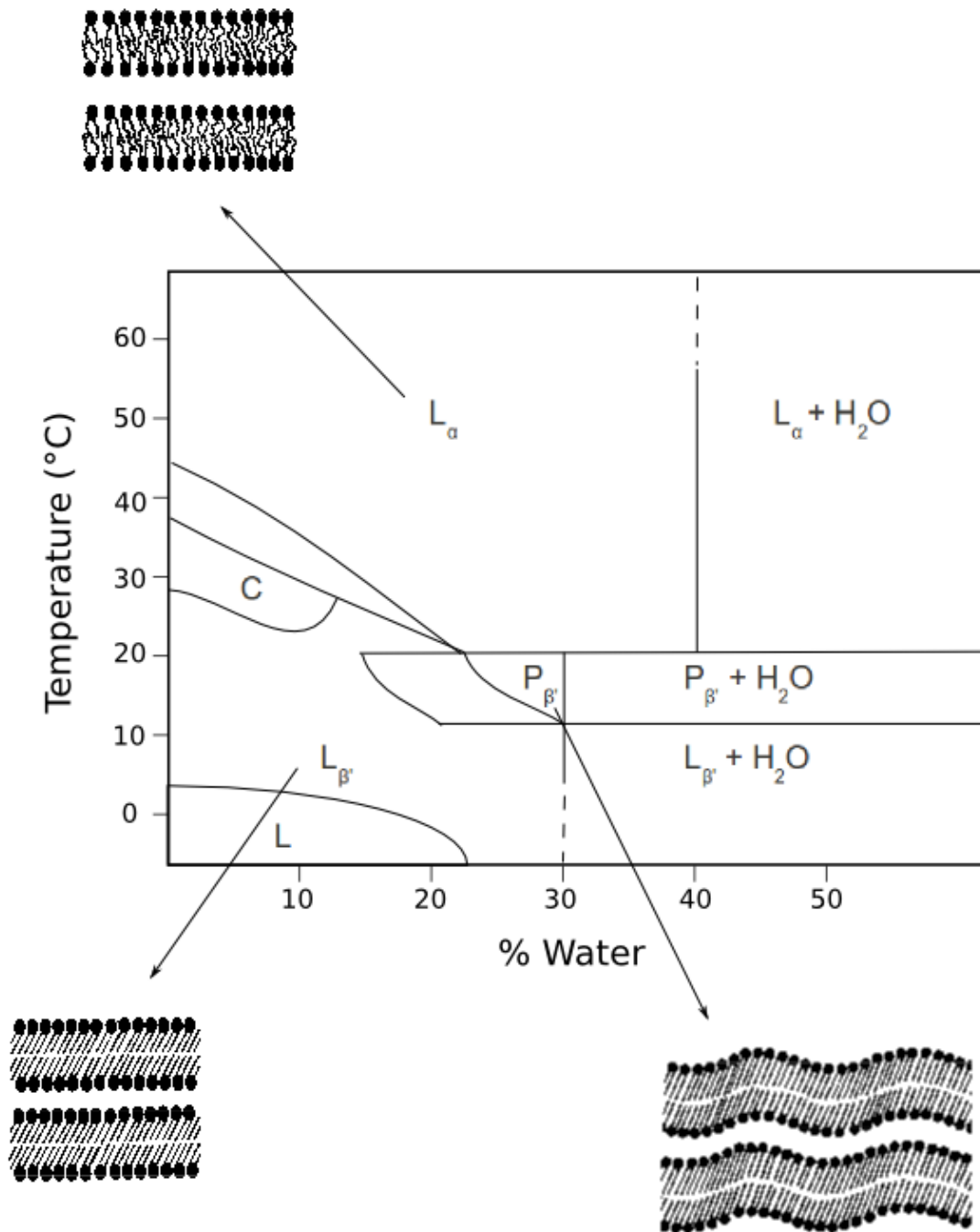


Figure 1-1: Phase transition diagram of a binary DMPC-Water system: L, lamellar phase; L<sub>β'</sub>, gel phase; L<sub>α</sub>, liquid crystalline phase; P<sub>β'</sub>, rippled gel phase; C, hydrated crystalline phase; (Janiak, Small et al. 1979).

Lipids self-assemble into various supra-molecular structures in aqueous environment. This is an entropy-driven process (hydrophobic effect) in which the hydrophilic head-group interacts with water

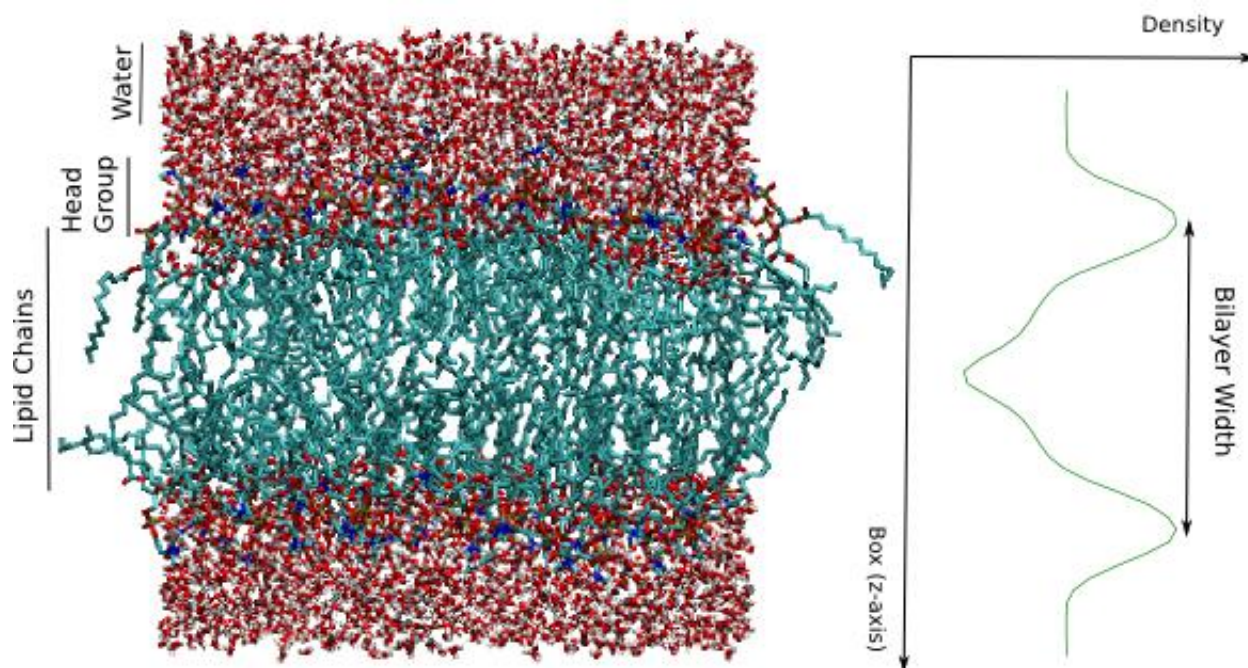
while the hydrophobic chains cluster together pointing away from bulk water. Depending on type of headgroup and chains, temperature, water contents and other physical parameters, lipids can assemble into a multitude of structures including e.g. the biologically most relevant lamellar liquid crystalline (fluid) phase, lamellar gel phase, inverted hexagonal phase and cubic phases. Temperature of environment and hydration level of membranes is the driving forces for the transition from one phase to other phase of membranes.

Figure 1-1 showed a typical phase transition diagram for a DMPC (dipalmitoylphosphatidylcholine) /water system (Janiak, Small et al. 1979). At low temperatures and low water content, DMPC forms a gel phase ( $L_{\beta}'$ ). As temperature increases, a phase transition from the gel to the liquid crystalline (fluid) phase ( $L_{\alpha}$ ) takes place. At certain hydration levels and temperatures, DMPC forms a so-called rippled gel phase. Mixture of different phases can coexist at the boundaries of phases. The main focus of this study is on fluid and gel phases. Therefore, the most important phase transition temperature discussed in the following is the one between both phases.

Figure 1-2 shows a snapshot of a MD simulation of a DMPC bilayer in the liquid crystalline phase including a mass density profile. The bilayer thickness is defined in different ways. One widely used definition uses the distance between the headgroup phosphate atoms across the bilayer as obtained from electron or mass density profiles. Head to head bilayer thickness varies from 3 to 4 nm (Kucerka, Liu et al. 2005; Kucerka, Tristram-Nagle et al. 2005) for phospholipids according to their chain lengths and saturation levels. DMPC bilayer width was recorded as 3.53 nm by X-ray scattering (Kucerka, Liu et al. 2005). Bilayer thickness is related with area per lipid. Area per lipid is inversely proportional with bilayer thickness and can be calculated from measured bilayer volume and bilayer thickness (McIntosh and Simon 1986; Nagle and Tristram-Nagle 2000). Area per lipid in fluid phase is around 50-60  $\text{\AA}^2$  for phospholipids (Kucerka, Liu et al. 2005; Kucerka, Tristram-Nagle et al. 2005). An area per lipid of 60.6  $\text{\AA}^2$  was recorded for DMPC (Kucerka, Liu et al. 2005).

Bilayer thickness and area per lipid are strongly dependent on lipid chain dynamics. Lipid bilayers in the gel phase have a higher bilayer thickness and smaller area per lipid than in the fluid phase. The main reason is the restricted motion of lipids in gel phase. Lipid chain order parameters are high (Tardieu, Luzzati et al. 1973; Davis 1979) in the gel phase. In addition to this, hydrocarbon chain of lipids is considered to be all-trans conformations in gel phase (Lippert and Peticola. Wl 1971; Rothman 1973; Yellin and Levin 1977). As the transition from gel to fluid phase occurs, chain order parameters

started to decrease and trans-gauche isomerization takes place (Yellin and Levin 1977). Therefore, smaller bilayer thickness and consequently larger area per lipid is observed in liquid crystalline phase.



*Figure 1-2: Structure of a DMPC lipid bilayer as illustrated by a united-atom MD simulation. The bilayer width, i.e head-to-head distance of 3.2 nm is illustrated on the right as a mass-density profile plotted across the bilayer.*

Solid-state NMR is very powerful technique to monitor dynamics of lipid bilayers. As can be seen in Figure 1-3, different solid-state NMR techniques can probe movement and dynamics of head group and hydrophobic chains. Static  $^2\text{H}$  quadrupolar coupling experiments can be used to investigate lipid chain dynamics. By this method, lipid chain order parameters ( $S_{\text{CD}}$ ) can be calculated.  $S_{\text{CD}}$  provides smoothed order parameter profiles, which are assumed to decrease from the beginning to the end of the tail. Another method for probing chain dynamics is measuring  $^{13}\text{C}$ - $^1\text{H}$  dipolar coupling constants under fast MAS spinning. This method provides real order parameters ( $S_{\text{CH}}$ ) of the hydrocarbon tails, which are easier to interpret.  $^{31}\text{P}$  NMR and  $^{14}\text{N}$  NMR static and MAS experiments are important to observe head group orientation of the lipids. In addition,  $^{31}\text{P}$  NMR is very important method to probe phase state of lipid bilayers and monitor phase transition of lipids from gel phase to liquid crystalline phase.

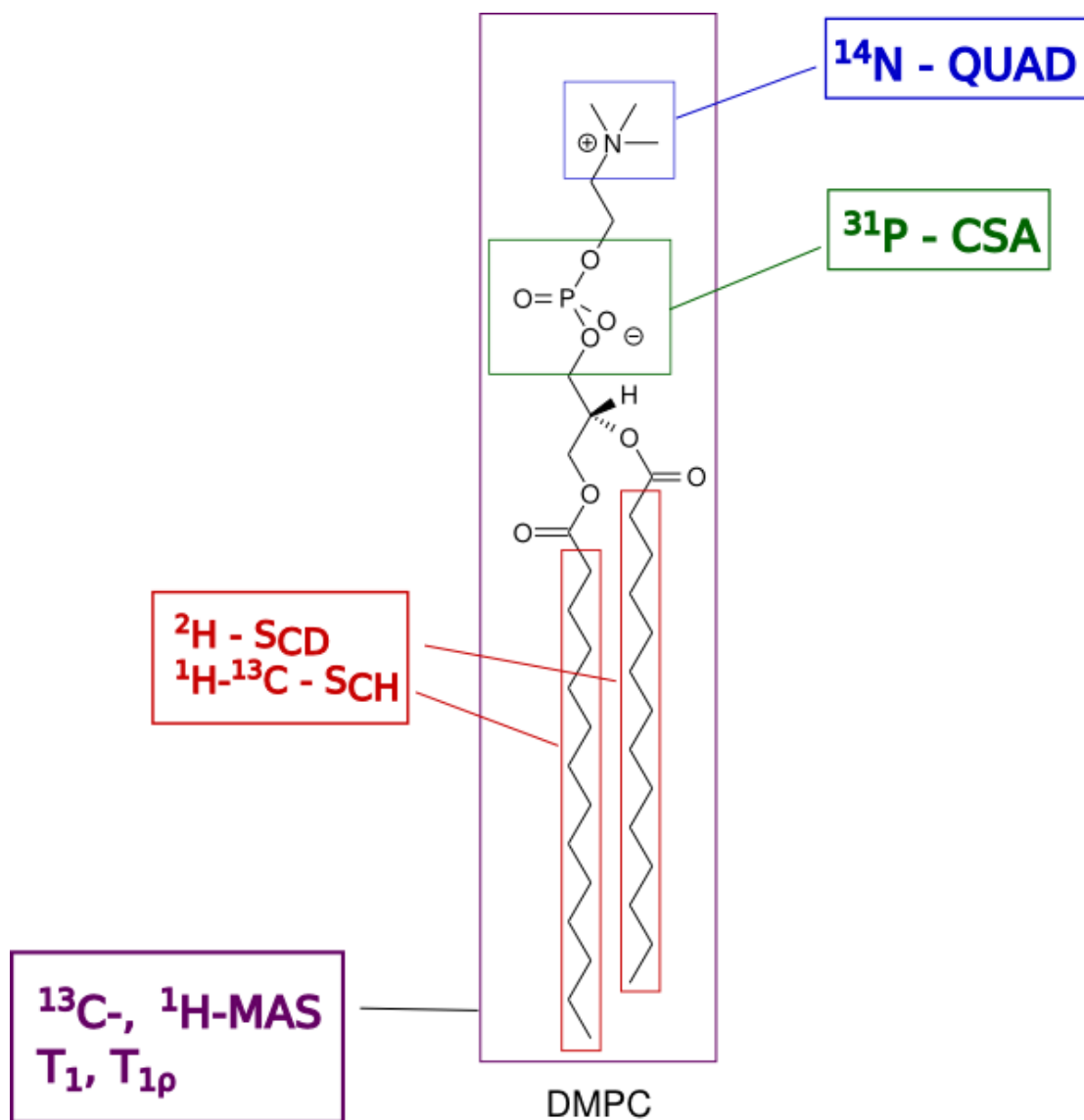


*Figure 1-3: Schematic representation of NMR parameters, which can be extracted from phospholipids and which report on bilayer structure and dynamics: information on lipid chain order and dynamics can be obtained in form of order parameters from C-H dipole couplings or C-D deuterium quadrupole couplings.  $T_1$  is the spin-lattice relaxation time in laboratory frame and  $T_{1\rho}$  is spin-lattice relaxation time in rotating frame along the acyl chains. The  $^{31}\text{P}$  CSA and  $^{14}\text{N}$  quadrupole coupling are sensitive parameters for the lipid phase and for charge effects at the membrane surface. In addition  $^1\text{H}$  chemical shifts of all sites in the lipids offer insight into lipid-lipid interactions via 2D NOESY-MAS NMR correlation spectroscopy.*



Another important aspect about membrane dynamics is the time scale of a particular type of motion. In different time scales different kind of dynamic processes can occur. Intramolecular, intermolecular and collective lipid motions can be investigated by probing the right time scales. There are different experimental methods that provide informations on fast and slow motions of membranes (Brown 1996; Brown, Thurmond et al. 2001). Fast motions like trans-gauche isomerization and chemical bond rotation occur at picosecond time scale. Around nanosecond timescale, lipids undergo rotation around molecular axis. At microsecond time region, lipid molecules started to move laterally in one monolayer and at millisecond, lipid movements across the bilayer takes place. At longer time scales, up to seconds, collective undulatory movements of lipid bilayer can be observed. Therefore, it is important to use proper method for each time scale to investigate different kind of lipid motions. In this study, solid-state NMR and molecular dynamics are used to investigate lipid bilayer dynamics. Figure 1-4 shows time scales covered by these methods and different motions in lipid bilayers, which can be investigated.

As can be seen from the Figure 1-4, different solid-state NMR parameters are sensitive to a wide range of time scales covering all motions occurring in membranes. For the nanosecond time scale, spin lattice relaxation time ( $T_1$ ) measurements are useful. In order to investigate microsecond-millisecond time scale motions, rotating frame  $T_1$  ( $T_{1\rho}$ ) measurements as well as line shape analysis included  $^2\text{H}$  quadrupolar coupling,  $^{13}\text{C}$ - $^1\text{H}$  dipolar coupling and  $^{31}\text{P}$  CSA measurement can be used. For longer time scales up to seconds, static and MAS exchange experiments as well as spin-spin relaxation time measurements ( $T_2$ ) can be performed. Therefore, motions in lipid bilayers from picosecond to second can be monitored by different kind of experiments, which solid-state NMR spectroscopy offers.

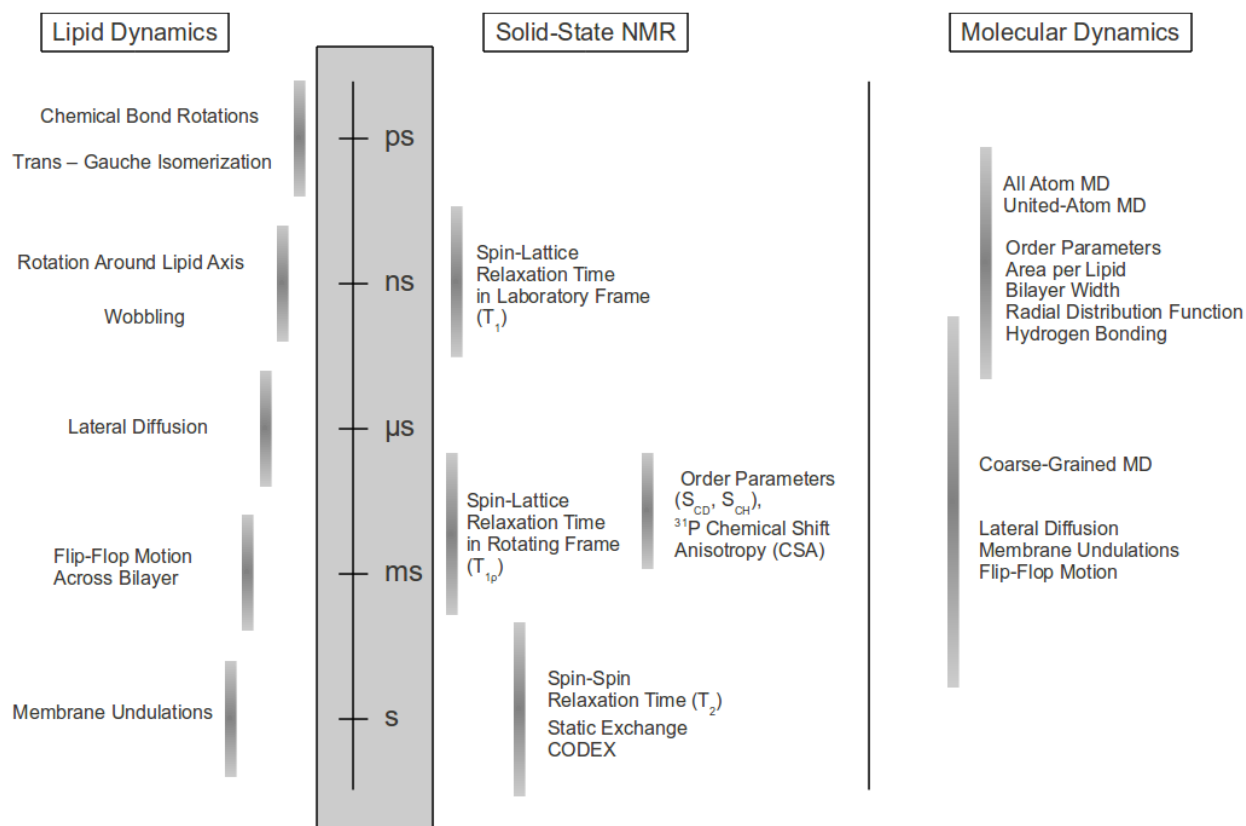


Figure 1-4: Accessibility of motions occurring in lipid membranes by solid-state NMR experiments and by MD simulations.

In addition to NMR measurements, all-atom and united atom molecular dynamics simulations provide information on lipid motions at nanosecond scale. Thus, they can be linked with experimental results. However, due to high computational cost, united atom simulations cannot be performed for longer time scales than nanoseconds. In order to overcome time-scale problem, coarse-grained simulations can be used (Smit, Hilbers et al. 1990; Marrink, Risselada et al. 2007). In coarse-grained method, lipid and water molecules can be defined with less detailed structures and by this way simulations can be performed up to milliseconds. Therefore, longer time-scale motions such as lateral diffusion, flip-flop motions and membrane undulations, can also be covered by molecular dynamics simulations.

### 1.1.2 Functional Importance of Physical Properties of Lipid Bilayers

As outlined above, biological membranes are not only important as structural element to create closed cells but also for many other physiological processes, which are vital for living organisms. Membranes are protecting cells from outside environment as well as supplying communication with outside environments and with neighboring cells. They have crucial roles transporting or pumping substances in and out of the cells by proteins that are embedded into their structures. They also actively transport small molecules by direct diffusion through their hydrophobic environment. Recent studies also showed that lipid membranes composition and their lateral organization are crucial in signal transduction (Grassme, Jekle et al. 2001; Gulbins and Kolesnick 2003).

There is increasing evidence that also direct physical properties of lipid bilayers have a direct functional importance. Examples include the phenomenon of lipid rafts, processes involving lipids as signalling molecules such as ceramides or designing new drugs, which have to cross the membrane or which target proteins.

Cell membranes contain high amounts of phospholipids, sphingolipids and cholesterol. It was investigated by several studies that these lipids are not distributed homogeneously in cell membranes (Simons and Ikonen 1997; Brown and London 1998). These studies indicated that sphingolipids together with cholesterol forms distinct membrane domains named rafts. Raft formation results in lateral organization in cell membrane. Since main component of rafts are sphingolipids, lipid rafts may play a key role in sphingolipid signaling (Kolesnick, Goni et al. 2000). Several studies suggested that lipid rafts could be transformed into larger membrane platforms, which initiate signal transduction via clustering of receptors (Grassme, Jekle et al. 2001; Gulbins and Kolesnick 2003). Ceramides are known to play a key role in formation of larger membrane platforms by fusing into the pre-formed lipid rafts (tenGrotenhuis, Demel et al. 1996; Holopainen, Subramanian et al. 1998; Huang, Goldberg et al. 1999; Veiga, Arrondo et al. 1999).

Hydrophobicity is also a very important aspect in drug design. Drugs should be hydrophobic to be able to partition inside membrane. Uptake of drugs as lipid-drug complex may provide a solution to partition problem of polar or charged molecules inside membranes. Because of this, several studies were done in the literature about formation and investigation of drug – lipid complexes (Bombardelli,

Curri et al. 1989; Mouritsen and Jorgensen 1998; Jain, Gupta et al. 2010; Semalty, Semalty et al. 2010).

There are many effects of drugs on lipid membranes (Joachim K. Seydel 2002). Firstly, they modify the fluidity of membranes. Changes in membrane fluidity may have many different consequences. For example, increase in fluidity makes membrane more permeable and as a result drug diffusion through membrane increases. Fluidity of membranes also affects enzyme and receptor activities. Secondly, drugs may change curvature of membranes that cause disturbance in lamellar structures. It is known that, non-lamellar structure of membranes form during membrane fusion (Kinnunen 1996) and formation of non-lamellar phases may affect actions of some membrane proteins (Lundbaek, Maer et al. 1997). In addition, drugs may cause phase separation and domain formation in membranes (Zhou, Hancock et al. 2010; Wesolowska, Michalak et al. 2011). Domain formation of membranes is known to be important for the action of many enzymes (Gulbins, Dreschers et al. 2004).

## **1.2 Solid State NMR**

### **1.2.1 Theory**

In the following part, a short introduction to solid-state NMR spectroscopy with focus on the method used here will be given.

Frequencies of NMR spectra are related with external magnetic field as well as the chemical environment and coupling with neighboring spins. The Hamiltonian of internal interactions contains the sum of all this interactions as follow:

$$1-1 \quad H_{int} = H_{CS} + H_J + H_D + H_Q$$

Where  $H_{CS}$  is chemical shift,  $H_J$  is J-coupling,  $H_D$  is dipolar coupling and  $H_Q$  is the quadrupolar coupling Hamiltonian. In solution state NMR, due to fast motions most of the anisotropic interactions are averaged that results in well-resolved spectra. However in solid-state NMR, no motion-induced averaging takes place. As a result, most of the anisotropic interactions are fully present. Therefore, very broad and complicated spectra are obtained in the solid-state. Special methods such as MAS-NMR

have to be employed to simplify spectra.

### 1.2.1.1 Magic Angle Spinning (MAS)

In solid-state NMR, molecular tumbling of samples is so slow that the orientation of sample becomes important. In order to suppress orientation dependent interactions magic angle spinning (MAS) technique was developed (Andrew, Bradbury et al. 1959). Fast sample rotation around an axis tilted at the magic angle ( $54.7^\circ$ ) with respect to  $B_0$  averages all anisotropic interactions from chemical shift, dipolar and quadrupolar Hamiltonians (Figure 1-5). At spin rate smaller than the dominating anisotropic interaction spinning sidebands occur (Figure 1-5).

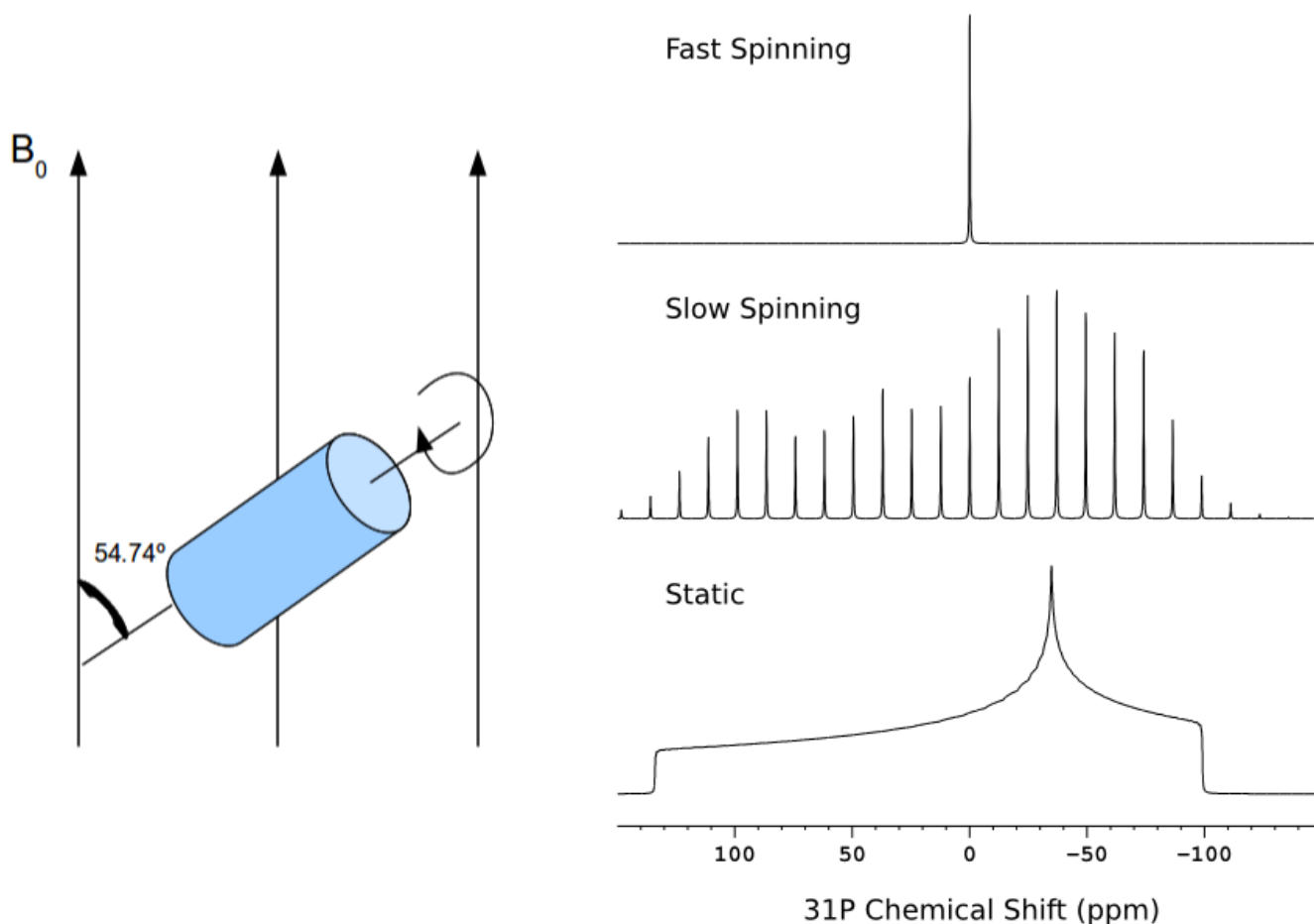


Figure 1-5: The basic-principle of magic angle spinning NMR: Rotating samples about the magic angle with respect to external magnetic field (left), averages anisotropic NMR interactions if the sample rotation rate exceeds the size of the anisotropy as illustrated here for the case of chemical shift

*anisotropy (right). Without sample rotations, the full CSA tensor is observed, if the spinning speed smaller than the CSA; spinning sidebands occur and if the spinning speed exceeds the size of the CSA, only the isotropic chemical shift remains. Simulations shown here correspond to  $^{31}\text{P}$ -spectra of DPPC static, slow spinning (2 kHz) and fast spinning (10 kHz) (Schiller, Muller et al. 2007).*

## 1.2.2 Solid-State NMR on Lipid Membranes

Solid-state NMR is known to be a useful method to study membranes and membrane embedded molecules. Membranes are two-dimensional liquids in which the lipids undergo fast but anisotropic motions. Dynamic properties as well as structural changes within the membrane environment can be investigated by solid-state NMR.

$^{31}\text{P}$  NMR is a powerful method to probe structure of lipid membranes. Phases and morphology of lipid membranes can be investigated using solid-state static  $^{31}\text{P}$  NMR spectroscopy. Since  $^{31}\text{P}$ -NMR spectral shapes are sensitive to head group orientation of lipids, they provide strong indications of phase states of lipid membranes.

Lipid membranes are relatively flexible compared with real solids. Therefore, it is possible to obtain chain order parameters of lipids by using the information from dipolar coupling and quadrupolar coupling measurements. Chain order parameters are defined with the orientation of C-H (D) bonds with respect to bilayer normal. Thus, order parameters provide information on flexibility of lipid chains and orientation of bonds. The power of solid-state NMR over other techniques is that solid-state NMR gives order parameters of individual segments, which provide higher resolution on chain dynamics, whereas other techniques provide an average order on lipid bilayers cross-section (Seelig 1977).

To investigate location and distribution of small molecules along the bilayer has great importance on drug research. Solid-state NMR provides very powerful tools in order to investigate distribution probabilities of drugs in the bilayers.  $^1\text{H}$ -NOESY NMR spectroscopy under MAS is applied to lipid membranes to obtain cross relaxation rates, which allow investigating direct lipid-substrate contacts. Thus solid-state  $^1\text{H}$ -MAS NOESY is extremely helpful method to understand drug-lipid interactions and obtain insight on drugs insertion within the bilayer.

### 1.2.3 Probing Lipid Phases via $^{31}\text{P}$ -NMR/Chemical Shift Anisotropy Measurements (CSA)

$^{31}\text{P}$  occurs at naturally abundance of 100 percent. It has very high gyromagnetic ratio ( $10.84 \times 10^7 \text{ rad s}^{-1} \text{ T}^{-1}$ ) and has spin number  $\frac{1}{2}$ . Especially, to investigate the physical and dynamic properties of lipid membranes,  $^{31}\text{P}$ -NMR appears as a very appropriate technique since phosphorus is one of the main components of phospholipids. The unique chemical shifts can be detected under MAS. In addition, static anisotropic spectrum can be recorded to investigate chemical shift anisotropy (CSA). CSA provides information on head group orientation, which will be further used to understand self assembled lipid phases.

It is necessary to introduce the Hamiltonians of the chemical shifts to understand the basics of isotropic and anisotropic chemical shifts for  $^{31}\text{P}$ -NMR. Hamiltonian for the chemical shift is defined as:

$$1-2 \quad H_{CS} = \gamma(I_x\sigma_{xz} + I_y\sigma_{yx} + I_z\sigma_{zz})B_0$$

Where  $I_i$  is the spin angular momentum and  $\sigma_{ij}$  is chemical shift tensor in the laboratory frame. Only  $I_z$  is contributing to the chemical shift. Therefore Hamiltonian can be taken just as:

$$1-3 \quad H_{CS} = \gamma(I_z\sigma_{zz})B_0$$

In order to explain anisotropy, it should be switched to the principal axis frame where the angular chemical shift frequency is defined as:

$$1-4 \quad \omega_{CS} = \gamma\sigma_{zz}B_0 = -\sigma_{zz}\omega_0$$

where  $\omega_0$  is the larmor frequency of  $^{31}\text{P}$  nucleus. In order to convert  $\sigma_{zz}$  from laboratory frame to the principal axis frame several mathematical conversions are done and the polar coordinates  $(\theta, \phi)$  are implemented to the chemical shift angular dependent frequency that is found as follows:

$$1-5 \quad \omega_{CS} = \omega_0(\sigma_{xx}(\cos\phi\sin\theta)^2 + \sigma_{yy}(\sin\phi\sin\theta)^2 + \sigma_{zz}(\cos\theta)^2)$$

It is possible to separate isotropic and anisotropic part of angular chemical shift frequency by extracting isotropic dependency from the whole formula as  $\sigma_i = \sigma_{ii} - \sigma_{iso}$ , where  $\sigma_{iso}$  is defined as  $\sigma_{iso} = 1/3(\sigma_{xx} + \sigma_{yy} + \sigma_{zz})$  at the principal axis frame. Then, the anisotropic chemical shift frequency is found as below:

$$1-6 \quad \omega(\theta, \phi)_{CS} = -\sigma_{iso}\omega_0 + \frac{\delta}{2}(3\cos^2\theta - 1 - \eta\sin^2\theta \cos(2\phi))$$

In this formula,  $\eta$  is the asymmetry parameter and  $\delta$  is the anisotropy parameter. More detailed theoretical calculations can be found in the review of Schiller et al. (Schiller, Muller et al. 2007). The important property about the asymmetry parameter and the anisotropy parameter is that they provide information about the spectral lineshape. In case of  $^{31}\text{P}$ , this lineshape is a sensitive measure of membrane phases. Membranes can be self assembled in several different forms according to their hydration level, head group properties and temperature. If lipids are in the form of dry powder it becomes possible to observe all the principal axis contributions in the spectrum (Figure 1-6-a). However, if the membrane is in liquid state, fast axial motions cause an averaging in the principal axis (Figure 1-6-b). Therefore, it becomes as  $\sigma_{xx} = \sigma_{yy} = \sigma_{\perp}$  and  $\sigma_{zz} = \sigma_{\parallel}$ , where asymmetry parameters become zero. Depending on temperature, some phospholipids, such as phosphatidylethanolamines, can form inverted hexagonal phases. In this phase, lipid molecules forms cylinders in which water molecules locate inside cylinder and lipid head groups face interior part of cylinders where water molecules locate. Therefore, rotation around the cylinder axis causes a further averaging in anisotropy (Figure 1-6-c). If axial motion is fast enough, it is also possible to average out all the anisotropic motion and observe only the isotropic chemical shift (Figure 1-6-d). This is possible for the lipids that are solved in organic solvent or form micelles in detergent. Another way to achieve fast motion is to record  $^{31}\text{P}$  spectrum under MAS, so all the anisotropic tensors can be canceled out.



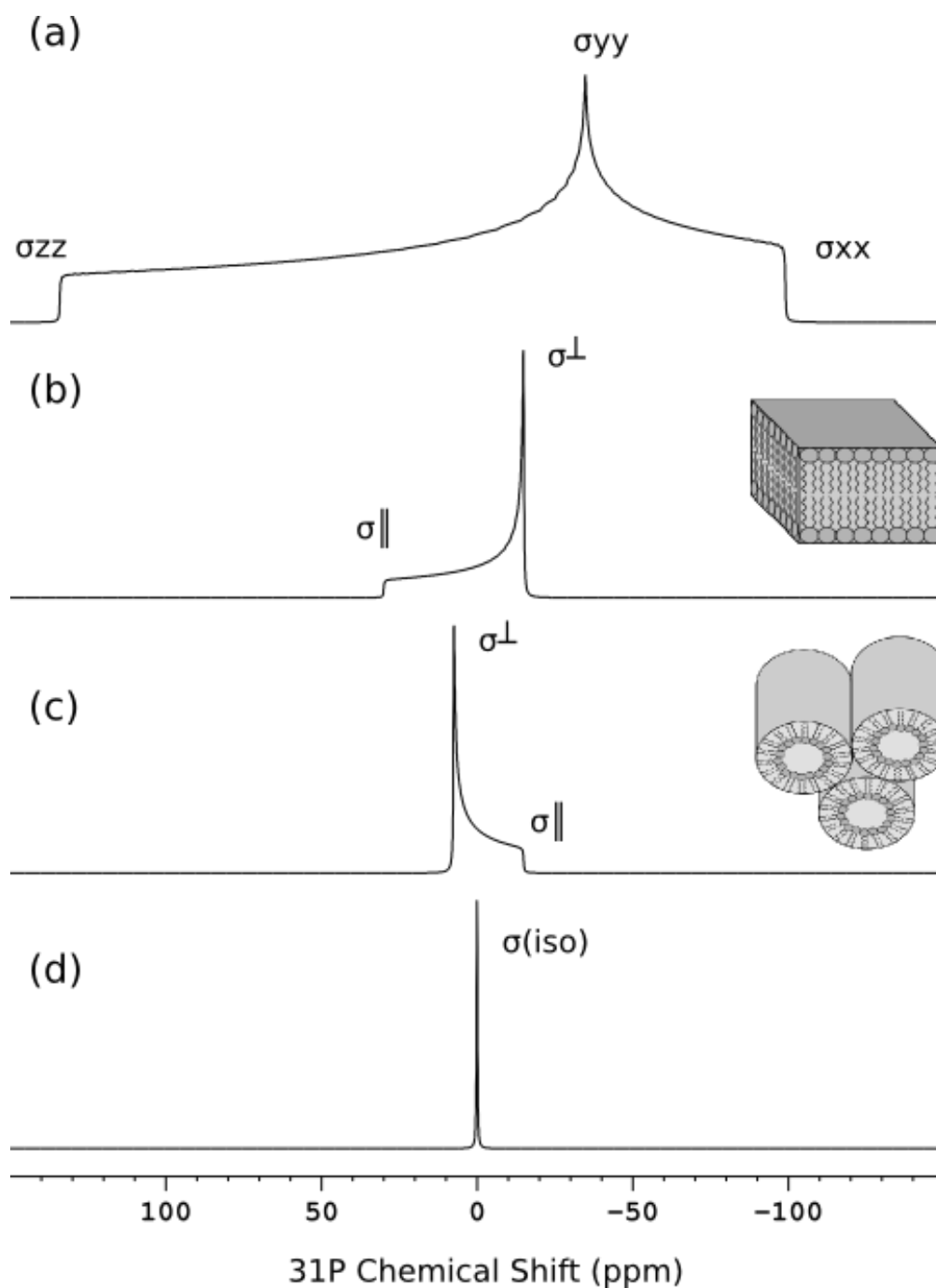


Figure 1-6: Lipid polymorphism and typical  $^{31}\text{P}$ -lineshapes. Simulations of static  $^{31}\text{P}$  NMR line shapes are shown for a dry powder sample (a), liquid crystalline phase (b), inverted hexagonal phase (c) and liquid crystalline phase under MAS (d); The spectra were simulated based on principle CSA tensor values taken from Schiller et al. (Schiller, Muller et al. 2007)

$^{31}\text{P}$  NMR serve very powerful tool for the investigation of lipid bilayer phases. Especially for drug-lipid

studies, the change in lipid phases can be monitored. Moreover,  $^{31}\text{P}$  NMR can be also used to observe domain formation by the effect of drug molecules. In addition, phase transition of lipids can be also probed by  $^{31}\text{P}$  NMR. Due to restriction in motion, at gel phase, CSA was larger than at fluid phase. Therefore, phase transition profiles of lipids and lipid-drugs systems can be also studied by solid-state  $^{31}\text{P}$  NMR.

#### 1.2.4 Characterizing Lipids by Quadrupolar NMR: $^2\text{H}$ and $^{14}\text{N}$

$^2\text{H}$  NMR is a common method to investigate dynamics of lipid chains. Deuterium has spin number 1 and therefore it has a quadrupolar moment. The use of  $^2\text{H}$  quadrupole couplings to obtain order parameters ( $S_{CD}$ ) for C-D bonds in lipids is well established (Davis, Jeffrey et al. 1976; Seelig 1977; Seelig and Waesperarcevic 1978). Quadrupolar splittings ( $\Delta\nu$ ) that are extracted from  $^2\text{H}$  Pake spectra are used to calculate ( $S_{CD}$ ) of deuterium:

$$1-7 \quad \Delta\nu = \frac{3}{4} \left( \frac{eQV_{ZZ}}{h} \right) S_{CD}$$

$(eQV_{ZZ}/h)$  is the quadrupolar coupling constant,  $e$  is the elementary charge,  $Q$  is the nuclear quadrupolar moment,  $V_{ZZ}$  is the principle component of electric field gradient and  $h$  is the Planck constant.  $S_{CD}$  is related with orientation angle  $\theta$  of C-D bond as follows:

$$1-8 \quad S_{CD} = \left\langle \frac{1}{2} (3\cos^2\theta - 1) \right\rangle$$

Order parameters of C-D bonds along the acyl chain extracted from fully labeled lipids result in a smoothed order parameter profile (Lafleur, Fine et al. 1989). As splitting cannot be assigned to individual chain segments, the order parameters are assumed to be decreased along the acyl chain. Therefore, by this experiment information about the dynamics of lipid chains can be obtained by reading out order parameters from  $^2\text{H}$  static spectra.

Similar to  $^2\text{H}$  nucleus,  $^{14}\text{N}$  nucleus has also spin number 1 and as a result has a quadrupolar moment.  $^{14}\text{N}$  nucleus has one advantage over  $^2\text{H}$  that it is naturally abundant nucleus. Since  $^{14}\text{N}$  measurements do not require labeling of the sample it would be very useful method. However, different from  $^2\text{H}$ ,

standard quadrupolar couplings are very large that it is not possible to measure splittings and observe resonances for many systems. Fortunately, phospholipid bilayers are exceptions because of their mobility due to the fast axial tumbling of lipids and the tetrahedral symmetry of the choline group. Therefore, it is possible to measure quadrupolar splittings of static spectrum of membranes in liquid-crystalline phase. In addition, quadrupolar splittings can be quantitatively analyzed from side bands of the MAS spectra.

$^{14}\text{N}$  NMR measurements provide two important informations namely isotropic chemical shift and quadrupolar splittings. In the case of biological membranes, both results are related with the electrostatic potential of the membrane surface at the side of choline unit. Isotropic chemical shift is sensitive to the size of the electrostatic potential whereas quadrupolar splittings senses the effect of the surface potential in the orientation of choline headgroup (Lindstrom, Williamson et al. 2005).

In addition,  $^{14}\text{N}$  measurements can be applied in combination with  $^{31}\text{P}$  NMR experiments to probe electrostatic potential at the surface of membranes and the orientation change of the headgroup as a reaction of surface potential differences (Lindstrom, Williamson et al. 2005). In the work of Lindstrom et al, positively charged  $^{14}\text{N}$  and negatively charged  $^{31}\text{P}$  were used together as a voltmeter for measuring the surface potential. They measured the quadrupolar splittings for  $^{14}\text{N}$  and chemical shift anisotropy for  $^{31}\text{P}$  to find out the orientation of  $\text{P}^- - \text{N}^+$  vector. Using this method, they investigated the bilayer surface potential map of DMPC bilayer by systematic addition of different amounts of positively and negatively charged lipids to the DMPC membrane. Furthermore, they suggested using this method to reveal binding affinities of peptides to the membrane mixtures, which have different membrane surface potential.

### 1.2.5 $^{13}\text{C}$ - $^1\text{H}$ Dipolar Order Parameters

Besides  $^2\text{H}$  quadrupolar coupling, another way to obtain information on lipid chain order is to measure  $^{13}\text{C}$ - $^1\text{H}$  dipolar coupling between carbon and adjacent protons. In solid-state NMR, MAS provides sensitivity and well resolved spectra. However it suppresses  $^{13}\text{C}$ - $^1\text{H}$  dipolar coupling that contains information about dynamics of the systems. In order to retrieve informative dipolar couplings, recoupling experiments were developed. One common experiment to obtain dipolar coupling is called polarization inversion spin exchange at magic angle (PISEMA) experiment (Wu, Ramamoorthy et al.

1994; Dvinskikh, Castro et al. 2005; Dvinskikh, Zimmermann et al. 2005). This experiment correlates  $^{13}\text{C}$  chemical shifts with  $^{13}\text{C}$ - $^1\text{H}$  dipole couplings. PISEMA experiment allows investigating C-H order parameters of unoriented lipid bilayers. The resulting order parameters calculated from  $^{13}\text{C}$ - $^1\text{H}$  dipolar couplings are comparable with  $^2\text{H}$  quadrupolar order parameters. One advantage of dipolar coupling measurements is that, it does not require usage of deuterated lipids as in the case of  $^2\text{H}$  measurements. In addition, in dipolar coupling experiments, 2-dimensional spectra are obtained in which direct dimension gives  $^{13}\text{C}$  frequencies and the indirect dimension gives dipolar splittings. Therefore, dipolar couplings can be calculated for each respective  $^{13}\text{C}$  nuclei, which results in the true order parameter profile in contrast to a smoothed profile obtained from  $^2\text{H}$  quadrupolar experiments.

### 1.2.6 MAS – $^{13}\text{C}$ and $^1\text{H}$ Chemical Shifts

Chemical shift values are related with chemical and electronic environment of nuclei and are therefore very useful parameters to probe structure and interactions of lipids within the membrane.

In solution state NMR, motions in molecules are so fast that anisotropic motions are averaged out. Therefore, very sharp and resolved peaks can be obtained. However, for solid state NMR, molecules are moving slower than NMR time scale, as a result, anisotropic interactions are also observed. Thus solid-state NMR provides broader spectra than solution state. Fortunately, spinning samples at the magic angle averages out most of the anisotropic interaction resulting in well-resolved spectra.

In addition to this, lipid bilayers are more flexible comparing to powder solids. The fast anisotropic tumbling motions in lipids cause less broadening in the peaks. Therefore,  $^1\text{H}$  and  $^{13}\text{C}$  chemical shifts can be assigned for lipid samples under MAS. Chemical shift measurements are useful in many aspects. First of all, phase transition of lipid bilayers can be monitored by probing chemical shifts of  $^1\text{H}$  and  $^{13}\text{C}$  nuclei. Lipids are very flexible in fluid phase and as a result,  $^1\text{H}$  and  $^{13}\text{C}$  NMR spectra of lipids provide well resolved resonances. As temperature decreased, linewidths are increasing and broader spectra are observed. In the gel phase, motions of lipids are very restricted. As a result, very broad  $^1\text{H}$  and  $^{13}\text{C}$  spectra are obtained. Therefore, phase transition profile of lipids can be probed by  $^1\text{H}$  and  $^{13}\text{C}$  solid-state NMR measurements.

Chemical shift measurements are also useful to investigate drug-lipid interactions (Scheidt, Pampel et

al. 2004). It is known that chemical shifts change with chemical environment. Therefore, interactions between drugs and lipid molecules cause chemical shift changes in lipid resonances. Hence, distribution probabilities of drugs along the bilayer can be investigated by observing chemical shift differences of lipid atoms.

### 1.2.7 $^1\text{H}$ -MAS NOESY

$^1\text{H}$ -MAS NOESY experiments on lipid membranes provide highly resolved NMR spectra (Holte and Gawrisch 1997). The classical  $^1\text{H}$ -NOESY experiment would not work in solids, because anisotropic interactions of solids are not averaged out efficiently as in liquids. Thus very broad spectra are obtained for solids. Application of MAS in solid-state NMR results in averaging of anisotropic interactions. In addition, anisotropic interactions in lipid bilayers have an axial symmetry along the bilayer and lipids rotate around their own axis in the liquid crystalline phase (Davis, Auger et al. 1995), which result a further averaging in chemical shift anisotropy under MAS. This allows the acquisition of well-resolved  $^1\text{H}$ -MAS NOESY spectrum of lipid membranes in the liquid crystalline phase.

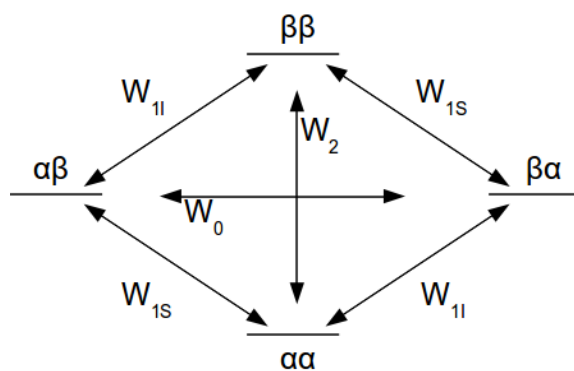


Figure 1-7: Schematic representation of NOE transitions between energy levels of two spins.  $W_0$ ,  $W_1$  and  $W_2$  denote zero quantum, single quantum and double quantum transitions, respectively.

NOE (nuclear Overhauser effect) (Overhauser 1953) can be described as the effect of a perturbation on one nuclear spin to the other spins via dipolar interactions. NOE in between two spins, I and S, depends on cross-relaxation rate ( $\sigma_{IS}$ ), which is proportional with  $r^{-6}$  where  $r$  is the distance between two spins. For two-spin systems there are 4 different energy levels as depicted in Figure 1-7. Three different kinds of transition are possible for such a system, which are single ( $W_{1I}$ ,  $W_{1S}$ ), double ( $W_2$ ) and zero ( $W_0$ ) quantum transitions. NOE is a result of zero and double quantum transitions, which are not allowed in

normal spectroscopy. The magnetization of one spin change the magnetization of the other with the transitions of  $W_0$  and  $W_2$  and this process is called as cross relaxation. Quantum transitions between two spins, cross relaxation and NOE can be explained more clearly by using Solomon equations (Solomon 1955) that are well summarized in the book of J. Keeler (Keeler 2005).

Cross relaxation rates can be calculated in three different methods: single mixing time approximation, two-spin approximation and full matrix approach (Huster, Arnold et al. 1999; Scheidt and Huster 2008). The first two methods are simplified approximations, whereas the full matrix approach is a more detailed and reliable calculation method. In this method, all the cross- and diagonal-peaks at a mixing time are used together in a matrix  $A(t_m)$  that is related with relaxation matrix,  $R$ , as follows:

$$1-9 \quad A(t_m) = \exp(-Rt_m) A(0)$$

Where  $A(t_m)$  is peak volume matrix at mixing time  $t_m$ ,  $R$  is relaxation matrix and  $A(0)$  is peak volume matrix at mixing time zero. Relaxation matrix ( $R$ ) contains all the relaxation rates where  $\sigma_{ij}$  stands for cross-,  $\rho_{ij}$  stands for diagonal-relaxation rates and  $ij$  describes magnetization transfer from spin  $i$  to spin  $j$  as shown below:

$$1-10 \quad R = \begin{bmatrix} \rho_{11} & \sigma_{12} & \sigma_{13} & \dots & \sigma_{1N} \\ \sigma_{21} & \rho_{22} & \sigma_{23} & \dots & \sigma_{2N} \\ \sigma_{31} & \sigma_{32} & \rho_{33} & \dots & \sigma_{3N} \\ \vdots & \vdots & \vdots & \ddots & \vdots \\ \sigma_{N1} & \sigma_{N2} & \sigma_{N3} & \dots & \rho_{NN} \end{bmatrix}$$

The relaxation rate matrix is not symmetrical. However for each proton transfer rate, there is symmetry in which cross relaxation rates can be expressed by:

$$1-11 \quad n_j \sigma_{ij} = n_i \sigma_{ji}$$

Where  $n_i$  and  $n_j$  are number of spins for  $i$  and  $j$  resonances, respectively. Therefore, relaxation rate matrix at a fixed mixing time can be calculated by rewriting the equation 1.12 as follows:

$$1-12 \quad R = -\frac{X(\ln D)X^{-1}}{t_m}$$

X and D are calculated from normalized peak volume matrix,  $a(t_m)$ , where, X is the matrix of eigenvectors and D is the diagonal matrix of eigenvalues of  $a(t_m)$ :

$$1-13 \quad a(t_m) = A(t_m)(A(0)^{-1})$$

<sup>1</sup>H-MAS NOESY is known to be a powerful technique to characterize the distribution probabilities of drugs within the lipid bilayers (Holte and Gawrisch 1997; Huster, Arnold et al. 1999). It was found by Gawrisch and co-workers that NOE crosspeaks are mainly caused by inter-molecular interactions rather than intra-molecular interactions (Feller, Huster et al. 1999; Yau and Gawrisch 2000). Therefore, lipid bilayer-drug interactions can be monitored by using the NOESY-MAS technique. Crosspeak intensities can provide drug distribution along the membrane. Several studies, which were done on investigation of small molecules distribution in lipid bilayers by using NOESY-MAS method (Holte and Gawrisch 1997; Scheidt, Pampel et al. 2004; Siarheyeva, Lopez et al. 2006) showed that <sup>1</sup>H-MAS NOESY is a very useful tool to examine location of small molecules inside lipid bilayers.

## 1.3 Molecular Dynamics

### 1.3.1 Theory

Molecular dynamics is a method to simulate time-dependent behaviors of macromolecules. In this method, positions and velocities of atoms in a system are calculated by using Newton's second law for the specified time intervals.

$$1-14 \quad F = ma$$

$$1-15 \quad F_i = m_i \frac{\partial^2 x_i}{\partial t^2}, \quad i = 1, 2, \dots, N$$

The Second Law is applied to N number of atoms to calculate new coordinates of the system. Output of the calculations is written as a function of time in a trajectory file. The system can be further analyzed by averaging the trajectories to obtain conformational and dynamic properties (Vangunsteren and Berendsen 1990; Leach 2001; Schlick 2002).

### 1.3.2 Molecular dynamics on membranes

Molecular dynamics is a very useful method to investigate membrane dynamics and structures in atomic level. There has been always an interest to simulate lipid systems but due to the computational limitations, first simulations were carried out in the 1980s (Vanderploeg and Berendsen 1982; Vanderploeg and Berendsen 1983; Egberts and Berendsen 1988). Nowadays, bilayer systems that contain around 100-200 lipids can be simulated up to hundreds of nanoseconds. The longest atomistic bilayer simulations, which were performed so far were around 800 ns (Wohlert and Edholm 2006) – 1 $\mu$ s (Bjelkmar, Niemela et al. 2009). In nanosecond time-scale, certain lipid movements can be examined such as rotations of chemical bonds, order of the lipid chains and trans-gauche isomerizations. However, lipid dynamics on slow time ranges cannot be understood by molecular dynamics simulations in nanosecond scale. Coarse-grained methods can be a solution to time limit problems (Smit, Hilbers et al. 1990; Marrink, Risselada et al. 2007). In this method, systems are defined with reduced degrees of freedom and with less interaction details that make it possible to obtain information up to microsecond range for large macromolecules. However, with this method, the interactions are more approximate than all-atom and united-atom methods. Thus, it gives less precise results about membrane dynamics.

There are several structural and dynamics features of lipid bilayers that have been obtained from molecular dynamics for many lipid bilayers (Tieleman, Marrink et al. 1997; Nagle and Tristram-Nagle 2000; Vermeer, de Groot et al. 2007). Most common ones are surface area and area per lipid, order parameters of lipid chains, bilayer width from electron and mass density profiles and radial distribution functions. This information has been validated by several different experimental methods including solid-state NMR, X-ray and neutron diffraction studies (Davis, Jeffrey et al. 1976; Seelig 1977; Wiener



and White 1992; Nagle, Zhang et al. 1996; Koenig, Strey et al. 1997; Dvinskikh, Castro et al. 2005; Kucerka, Liu et al. 2005; Kucerka, Tristram-Nagle et al. 2005).

In addition, it is shown by many studies that solid-state NMR and molecular dynamics calculations can be linked very strongly in terms of thermodynamic properties of lipid bilayers (Marcelja 1974; Schindler and Seelig 1975; Nagle 1980; Salmon, Dodd et al. 1987). Segmental order parameters, which are obtained from NMR measurements, provide the length of lipid chains, which further used to calculate bilayer width and area per lipid. Studies showed that order parameters, bilayer length and area per lipid values from both NMR experiments and MD simulations are comparable with each other (Tieleman, Marrink et al. 1997; Nagle and Tristram-Nagle 2000; Vermeer, de Groot et al. 2007). Besides thermodynamic properties, solid-state NMR and MD calculations can be compared in terms of lipid bilayer-drug interactions. Distribution profile of drugs can be investigated by the combining method of NOESY-MAS experiment with refined MD simulations.

Therefore, molecular dynamics is a very powerful method together with experimental techniques to give detailed picture of dynamics and structure of bilayers. Experimental data can be use to validate results of molecular dynamics calculation as well as to improve calculation techniques by application of several refinement methods. Although molecular dynamics is an extremely useful method to investigate structure and dynamics of biomolecules; it suffers from several limitations as outlined below.

### **1.3.3 Limitations**

#### **1.3.3.1 Classical Mechanics**

Molecular dynamics simulations are performed by using classical mechanics. Although it is a useful method in general, there are some cases in which classical mechanics are not valid. Behavior of hydrogen atoms, bond vibrations and chemical reactions are some of the examples of these cases where quantum mechanical calculations are needed instead of classical mechanics. Harmonic oscillator in classical mechanics can not be applied to the motions that have frequencies ( $\nu$ ) equal or greater than  $k_B T/h$ , where  $k_B$  is the Boltzmann's constant, T is the temperature and h is Planck's constant. Therefore,

molecular dynamics simulations are not much convenient for the processes, which occur at high frequencies such as bond vibrations, bond angle bending and stretching as well as electronic motions.

### **1.3.3.2 Time-scales**

Another limitation is the range of time-scales in which simulations are feasible to be applied. For macromolecules, molecular dynamics simulations need large computational time and space. It is already becoming computationally expensive to simulate a large system more than nanosecond time range. There are many approaches to overcome these limitations. For example, instead of using all-atom method united atom method can be applied. In this method, all the non-polar hydrogen atoms are excluded during the calculations and this helps to save computational time. Coarse-grain method is another way to deal with time limitations of molecular dynamics simulations especially for the processes, which are occurred on longer time scales, such as membrane fusion.

### **1.3.3.3 Force-fields**

Force fields are consisting of bonding and non-bonding parameters of atoms. In force fields, all the forces for covalent interactions and as well as non-covalent interactions are defined for a number of different types of atoms. For each simulation, all the atoms in the system are described by using the atom types in the existing force fields. Therefore, parameters in force fields should be simple and applicable to the each molecule. However, this makes them become approximate and may cause uncertainties in different systems. In addition, force fields define non-bonding interactions of atoms in a pairwise manner. This cannot supply information about non-pair interactions. For long-range electrostatic interactions a cutoff radius can be applied. However, application of cutoff may create problems especially if the system contains charged particles.

### **1.3.3.4 Boundary effects**

In molecular dynamics simulations the size of systems are limited because of the high computational costs. Normally, number of atoms does not exceed tens of thousands. Therefore the boundaries of the systems with vacuum create unnatural effects on the systems. There are couples of methods to

overcome boundary effects. One common method is to apply periodic boundary conditions in which the system is supposed to be surrounded by its infinite number of copies. By this method a more realistic environment can be created at the boundaries of the system.

### 1.3.3.5 Ensembles

Molecular dynamics is a method that works with the rules of statistical mechanics, which means that the system of interest is defined as Boltzmann's distribution of structures instead of one particular structure. Ensemble average of the system is calculated to understand the structure and the thermodynamic properties. Microcanonical ensemble (N,V,E) where the energy and volume of each configuration are constant, is appropriate for molecular dynamics calculations. However, it is not applicable for each molecular system. For most biomolecular systems, constant pressure and temperature (NPT) or constant volume and temperature (NVT) ensembles may be more appropriate than microcanonical ensemble. It is possible to control the temperature and pressure by using one of the coupling methods, which are described in the literature. For temperature coupling, Berendsen (Berendsen, Postma et al. 1984) thermostat can be applied by correcting the temperature with a time constant  $\tau$ :

$$1-16 \quad \frac{dT}{dt} = \frac{T_0 - T}{\tau_T}$$

However, Berendsen method is a weak coupling scheme that may not be applicable for every system. In some cases, it may be necessary to use an extended coupling method. Nose-Hoover (Nose 1984; Hoover 1985) method is another temperature coupling method that is extended by adding a thermal reservoir to the system and a thermal frictional term ( $\zeta$ ) to the equation of motion:

$$1-17 \quad \frac{d^2 r_i}{dt^2} = \frac{f_i}{m_i} + \zeta \frac{dr_i}{dt}$$

In Berendsen coupling method the reference temperature is achieved by an exponential decay of the temperature to the reference value. In Nose-Hoover method, constant temperature is obtained by

oscillations in kinetic energy between the system and the thermal reservoir. By this way a canonical distribution of the system with corrected temperature can be achieved.

Berendsen algorithm can be also applied to obtain constant pressure ensemble. In Berendsen barostat, the pressure of the system is corrected with small time intervals ( $\tau$ ) by scaling the velocities from each directions in which coupling is performed. Scaling is calculated by using a matrix ( $\mu$ ) and a given compressibility factor ( $\beta$ ).

$$1-18 \quad \frac{dP}{dt} = \frac{P_0 - P}{\tau_P}$$

$$1-19 \quad \mu_{ij} = \delta_{ij} - \frac{\Delta t}{3\tau_P} \beta_{ij} (P_{0ij} - P_{ij}(t))$$

Parrinello-Rahman barostat (Parrinello and Rahman 1981; Nose and Klein 1983) is another pressure coupling method that is similar to Nose-Hoover thermostat. In this method, there is a barostatic friction term, which is incorporated into the equation of motion.

## 1.4 Aim of This Study

The aim of this work was to describe lipid bilayer properties in dependence of various lipophilic compounds by a combined use of solid-state NMR and MD simulations.

In the first part of the thesis, drugs lipids interactions are investigated. A class of potential drugs namely pirinixic acid derivatives were studied to understand their interactions with phospholipids bilayers. They are known to be dual inhibitor for mPGES-1 and 5-LO and consequently decrease inflammations. Here, their incorporation and location within the lipid bilayer are probed by combining method of solid-state NMR experiments and MD simulations.

The second part deals with commercially available drugs against inflammatory processes. Non-

steroidal anti-inflammatory drugs (NSAIDs) are well known drugs that they inhibit action of key enzymes in inflammatory processes. However, these drugs have many side effects especially in the case of long term usage. There is an ongoing research on these drugs to decrease their side effects by consumption of them as drug-lipid complexes instead of consumption as drug alone. Here, 3 common NSAIDs, namely ibuprofen, diclofenac and piroxicam, were studied as in lipid-drug complex by 1D-<sup>1</sup>H, 2D-<sup>1</sup>H-MAS NOESY and <sup>31</sup>P NMR experiments to investigate their interactions with lipids.

In the third part, organization of ceramides within lipid bilayer and their effect onto lipids were probed. Ceramides are similar to phospholipids in terms of structure that they also have hydrophobic tails and relatively polar head groups. However, head groups are different resulting in different biophysical properties. What make ceramide interesting are their functions in many key biological processes ranging from apoptosis to cell signaling. It is not well known how ceramide act in certain cell processes yet. However, there are strong findings that the function of ceramide is related with its effects on lipid membrane dynamics. Therefore, it is very important to investigate effects of ceramides on membrane biophysical properties. Here, several solid state NMR techniques were applied on ceramide-phospholipids bilayer mixtures to observe the possible effects of ceramides on the dynamics of phospholipids bilayers. In addition to solid-state NMR, MD simulations were carried out for lipid bilayers, which contain ceramide molecules in different concentrations, in order to have more detailed insight of ceramide-lipid interactions at atomic level.

## 2 Material and Methods

### 2.1 Solid-State NMR

#### 2.1.1 Materials

The lipids used in this study were DMPC (1,2-dimyristoyl-sn-glycerol-3-phosphocholine), DPPC (1,2-palmitoyl-sn-glycerol-3-phosphocholine), POPC (1-palmitoyl-2-oleoyl-sn-glycerol-3-phosphocholine), DMPC-d67 (1,2-dimyristoyl(d54)-sn-glycero-3-phosphocholine-1,1,2,2-d4-N,N,N-trimethyl-d9) and POPC-d31 (1-palmitoyl(d31)-2-oleoyl-sn-glycero-3-phosphocholine) (Figure 2-1). They were purchased from AVANTI LIPID. The ceramides, C4-ceramide (N-butyroyl-D-erythro-sphingosine), C12-ceramide (N-lauroyl-D-erythro-sphingosine), and C16-ceramide (N-palmitoyl-D-erythro-sphingosine), as well as the deuterated ceramide, C16-ceramide-d31 (N-palmitoyl(d31)-D-erythro-sphingosine) were purchased also from the same company. For  $^2\text{H}$  NMR measurements depleted water was purchased from Sigma-ISOTECH. Deuterated water was purchased from Sigma-Aldrich. Other materials for each project were explained in each material section in details.

#### 2.1.2 Sample Preparation

Multilamellar vesicles were prepared using standard methods (Szoka and Papahadjopoulos 1980). Lipids (usually 20 mg) and respective membrane components under investigation were codissolved in chloroform (5 mL) and shaken until a clear solution is obtained. Bulk solvents were evaporated under stream of nitrogen gas followed by drying in a rotary evaporator under high vacuum overnight resulting in a lipid-substrate film. Samples were rehydrated (usually with 1mL water) slowly inside the round bottom flask under slow rotation until lipid bilayers in form of a multilamellar dispersion has formed. Hydrated samples were transferred to an eppendorf tube and pelleted by centrifugation (1 hour with 16060 g-force). Bulk water was removed and samples were lyophilized to be dehydrated. After this step, samples were rehydrated again with a small amount of water (10 $\mu\text{L}$  natural abundant, deuterated or depleted water according to the type of experiments). Experiences showed that this additional step, which sufficiently hydrates the bilayer but avoids bulk water, is required to obtain best-resolved MAS-NMR spectra of lipid vesicles. Finally, 3 - 4 freeze-thaw cycles were performed at the temperatures that

were below and above transition temperatures of the lipids to obtain more homogeneous liposomes.

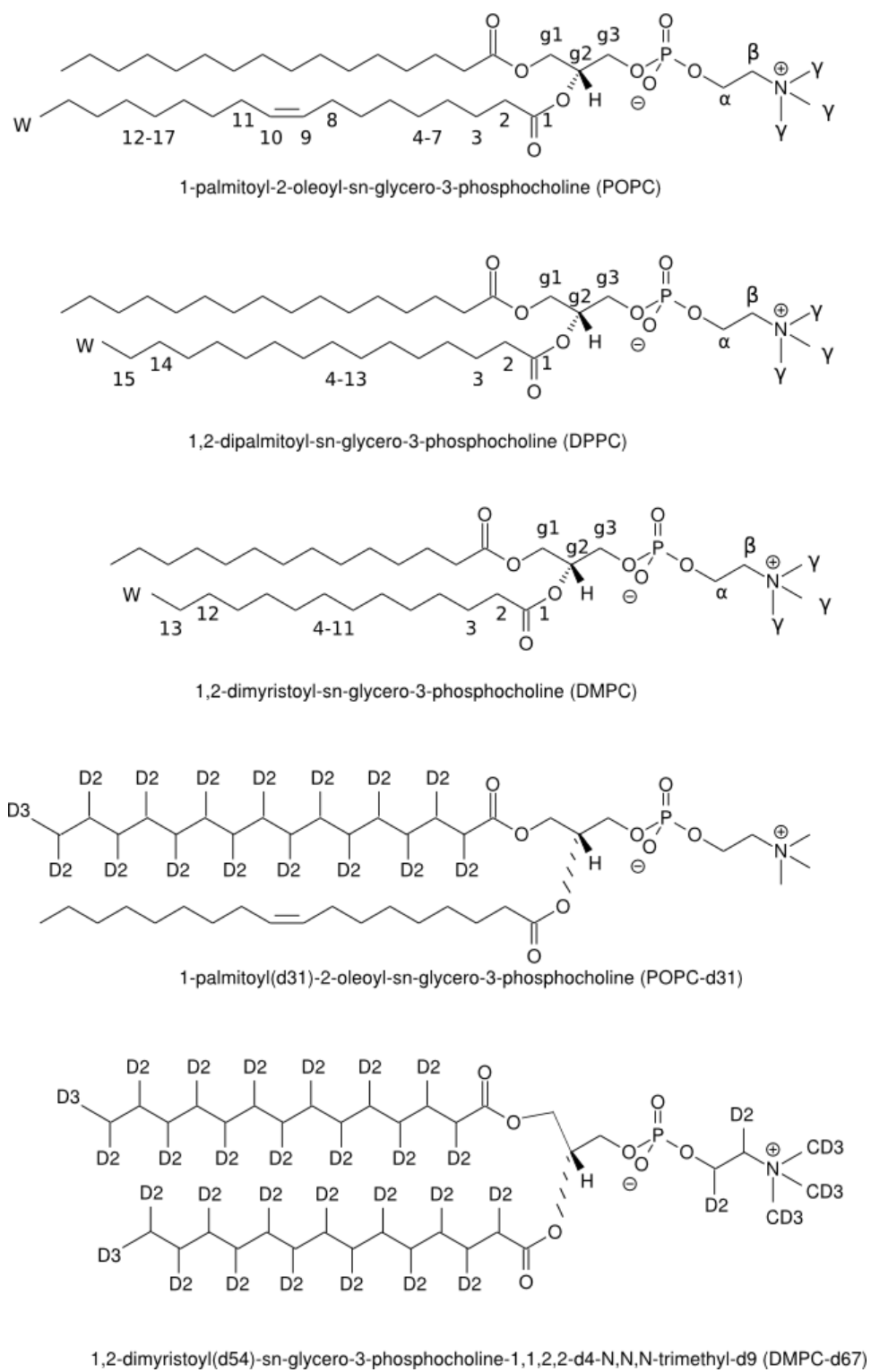


Figure 2-1: Structures of lipid: POPC, DPPC, DMPC, POPC-d31 and DMPC-d67.

### 2.1.3 SS-NMR Instrumentation

All experiments were carried out on either Bruker 850WB Avance II, Bruker 600WB Avance II or Bruker 400WB Avance II solid-state NMR spectrometers using 3.2 or 4 mm DVT MAS probeheads. 3.2 and 4 mm zirconium rotors, caps and inserts were obtained from RototecSpintec. Topspin version 2.1 was used for data acquisition and analysis. Topspin Plot Editor 2.1 was used for creating figures from NMR experiments. All other details for each experiment will be given in each section.

### 2.1.4 SS-NMR Experiments

#### 2.1.4.1 $^1\text{H}$ - $^1\text{H}$ -MAS NOESY

NOESY spectroscopy is the standard approach in liquid-state NMR to observe through-space spin-spin correlations. It is based on dipolar cross relaxation and forms the foundation for NMR based structure determination (Jeener, Meier et al. 1979; Macura, Huang et al. 1981). The pulse sequence for a 2D NOESY is displayed in Figure 2-2. It starts with a  $90^\circ$  pulse to obtain transverse magnetization and it evolves during  $t_1$ . After  $t_1$  another  $90^\circ$  pulse is applied to align the magnetization to z-direction in order to provide transitions between spins during mixing time. After mixing, the last  $90^\circ$  pulse flip the magnetization on the x-y plane and it evolves during acquisition time ( $t_2$ ). At the end of the experiment, a two dimensional spectrum is obtained, which contains diagonal and crosspeaks. Crosspeaks are resulting from the cross relaxation of two spins that are relatively close to each other. Crosspeak intensities depend on the spin-spin distance by  $r^{-6}$ . To interpret distances between atoms more quantitatively, it is necessary to calculate cross relaxation rates from crosspeak intensities.



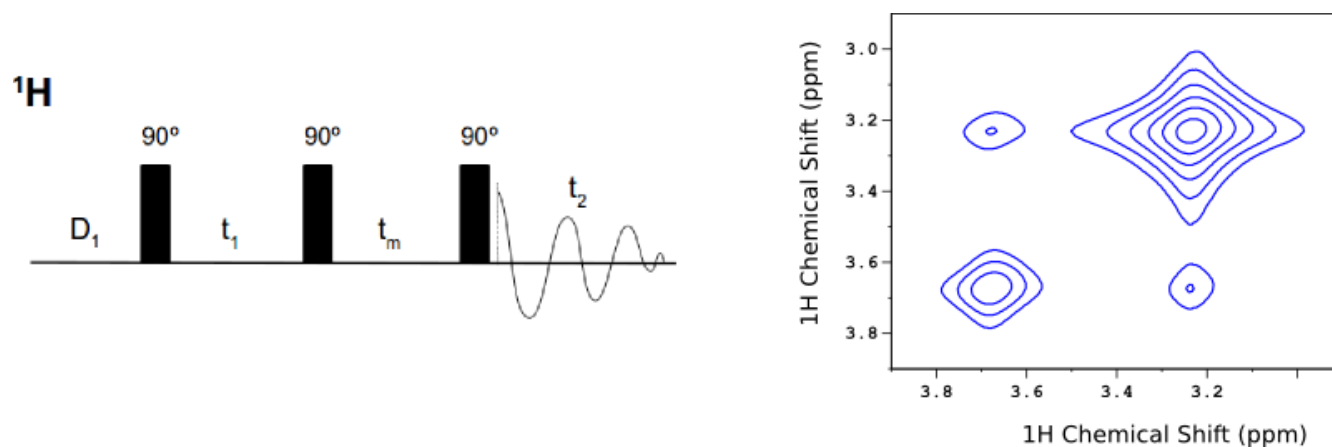


Figure 2-2: Pulse sequence (left) and spectral shape (right) of NOESY experiment. Magnetization transfer between nuclei takes place during mixing time ( $t_m$ ).

Usually, a NOE could not be observed in a solid as the necessary molecular dynamics is missing. However, lipid bilayers show a high degree of anisotropic mobility and it has been shown that NOESY spectroscopy in combination with MAS can be used to obtain distances constraints within membranes (Feller, Huster et al. 1999; Yau and Gawrisch 2000). Thus, locations and orientations of substrates inside the membrane can be easily predicted by using this powerful NMR technique.

#### 2.1.4.2 $^1\text{H}$ - $^1\text{H}$ -MAS RFDR

In solid-state NMR through-space correlations are usually established via dipolar recoupling experiments. One of the most widely used homonuclear variants is radiofrequency driven dipolar recoupling (RFDR), which provides dipolar recoupling by introducing rotor synchronized  $\pi$  pulse during the mixing time selectively disrupting the MAS averaging process. It has been shown that implementation of  $\pi$  pulses results in longitudinal magnetization transfers between different atoms via dipolar couplings (Sodickson, Levitt et al. 1993). Because of this, RFDR has been applied to many biological systems, including membranes, in order to investigate inter- and intra- molecular interactions (Kühne, Geahigan et al. 1999; Raya, Bianco et al. 2002; Aucoin, Camenares et al. 2009).

The pulse sequence for  $^1\text{H}$ -MAS RFDR (Figure 2-3) is very similar to  $^1\text{H}$ -MAS NOESY except implementation of  $\pi$  pulses during mixing time to obtain broadband dipolar recoupling. In both experiments magnetization transfer occurs during mixing time. However the main difference between

two experiments is that, for RFDR magnetization transfer occurs via dipolar coupling whereas for NOESY it occurs via nuclear Overhauser effect. Dipolar couplings are related with  $1/r^3$  that results in much faster exchange than nuclear Overhauser effect, which is related with  $1/r^6$  where  $r$  is the distance between two spins. Therefore, RFDR, as NOESY, can be used to obtain spatial distances for large systems.

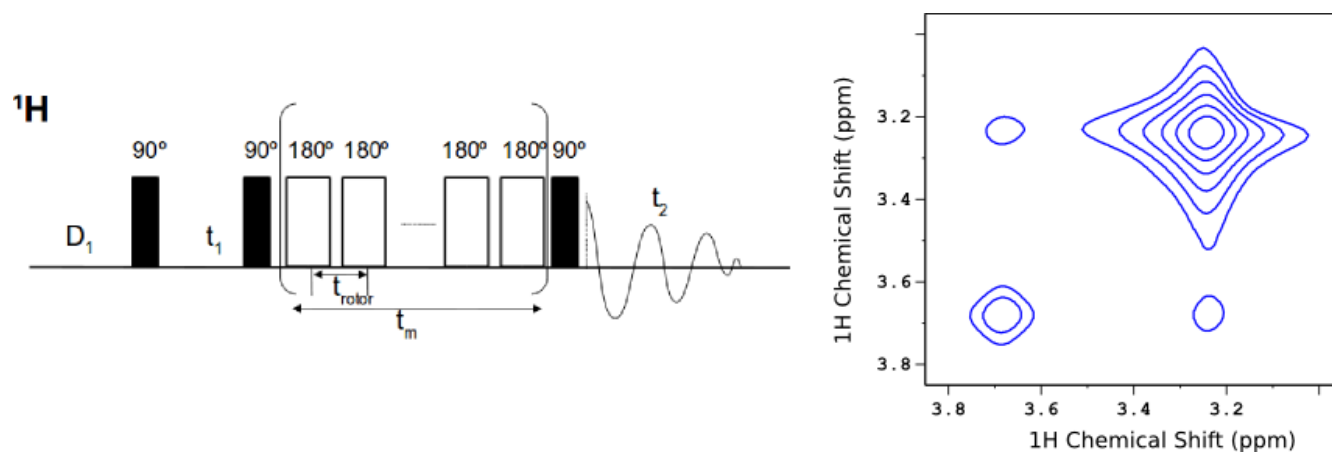


Figure 2-3: Pulse sequence (left) and spectral shape (right) of RFDR experiment. Magnetization transfer between nuclei takes place by application of recoupling pulses at rotor period ( $t_{rotor}$ ) during mixing time ( $t_m$ ).

NOESY is an already very convenient method to investigate locations of small molecules inside membranes. However in some cases, it is not possible to use high concentration of substrates because of the aggregation tendency of molecules inside bilayers. On the other hand, if concentrations of substrates are low, crosspeaks between lipids and substrates appear too weak to be observed. In such cases, RFDR can be used to investigate lipid-substrate interactions. RFDR results in faster magnetization transfer for the same mixing time as NOESY and stronger crosspeaks may be observed as indicated in the literature (Aucoin, Camenares et al. 2009)

### 2.1.4.3 $^2\text{H}$ Quadrupolar Coupling Measurements

For measuring static  $^2\text{H}$  NMR spectra, the quadrupolar echo pulse sequence (Figure 2-4) was

introduced by Davis et al (Davis, Jeffrey et al. 1976). The reason to use an echo is to regain information that was lost at the beginning of the FID because of the spectrometer dead time. In the pulse sequence, transverse magnetization is obtained with the first  $90^\circ$  pulse. After a time  $\tau$ , a second  $90^\circ$  pulse is applied refocussing magnetization at the time  $2\tau$  after the first pulse. In contrast to the classical spin echo experiment, refocusing is achieved by a second  $90^\circ$  pulse as a  $180^\circ$  pulse has no effect on spin evolution under dipolar and quadrupolar Hamiltonians.

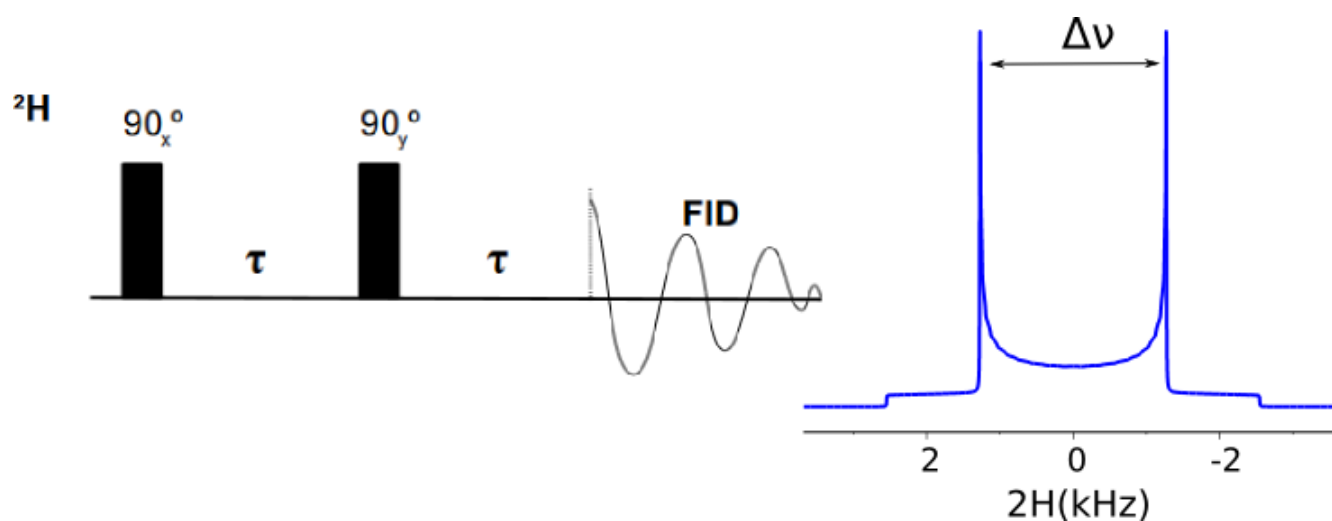


Figure 2-4:  $^2\text{H}$ -NMR quadrupolar echo pulse sequence (left) and a static quadrupolar spectrum (right),  $\tau$  is the delay to refocus the signal.  $\Delta\nu$  is the quadrupolar splitting.

As can be seen in the Figure 2-4, static  $^2\text{H}$  NMR measurements leads to typical PAKE spectra.  $\Delta\nu$  is used to calculate quadrupolar couplings for the specific nucleus. In case of fully deuterated lipid acyl chains, many overlapping Pake-pattern will be observed. The size of the observed quadrupolar coupling varies depending on the mobility of each  $\text{CD}_2$  segments. This enables to obtain a smoothed order parameter profile. An explicit profile can usually not be obtained since an assignment is not possible (Lafleur, Fine et al. 1989).

### 2.1.4.4 $^{13}\text{C}$ - $^1\text{H}$ Separated Local Field Experiments

To obtain dipolar  $^{13}\text{C}$ - $^1\text{H}$  lipid acyl chain order parameters, the PISEMA pulse sequence was used. In this experiment, spin exchange and frequency-switched Lee-Goldburg (FSLG) decoupling (Lee and Goldberg 1965; Wu, Ramamoorthy et al. 1994) are combined to correlate isotropic chemical shifts with heteronuclear dipolar couplings. The pulse sequence (Figure 2-7) starts with usual CP magnetization transfer from  $^1\text{H}$  to  $^{13}\text{C}$ . Then magnetization is aligned at the magic angle by an appropriate pulse ( $35.3^\circ$ ) followed by a  $^1\text{H}$  off-resonance field satisfying the Lee-Goldburg condition, which matches at the same time the Hartmann-Hahn condition with  $^{13}\text{C}$ . For the length of the incremented contact time  $t_1$ ,  $^1\text{H}$ - $^{13}\text{C}$  dipole couplings evolve which are correlated with  $^{13}\text{C}$  chemical shifts recorded during  $t_2$ .

To achieve homonuclear decoupling, the following Lee-Goldburg condition (Figure 2-5) (Lee and Goldberg 1965) has to be fulfilled:

$$2-1 \quad \Delta v_{LG} = \frac{v_1}{\sqrt{2}}$$

$$2-2 \quad v_{eff} = \sqrt{v_1^2 + \Delta v_{LG}^2}$$

$$2-3 \quad \theta_m = \arctan(\sqrt{2}) = \arctan\left(\frac{|v_1|}{\Delta v_{LG}}\right)$$

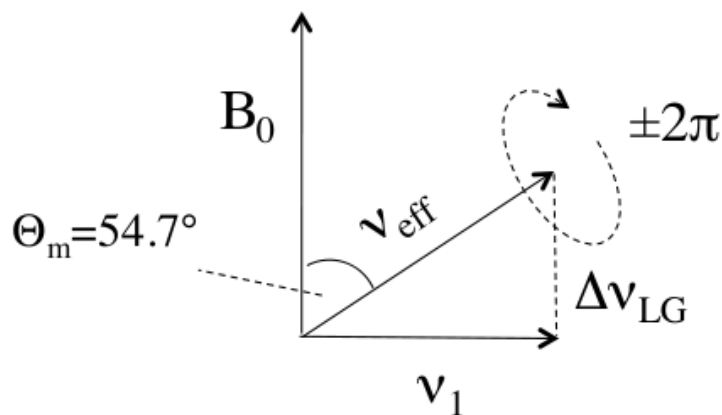


Figure 2-5: Representation of effective magnetic field at the rotating frame at Lee-Goldburg condition.

Further improvements are achieved with frequency switched decoupling (see Figure 2-6) during which offset frequency jumps between  $\pm \Delta\nu_{LG}$  for the lengths of a  $360^\circ$  pulse (van Rossum, de Groot et al. 2000).

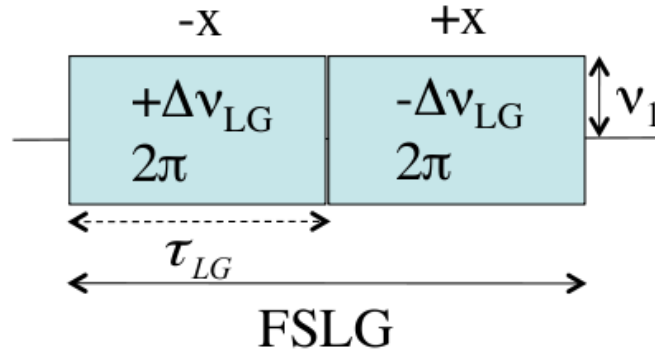


Figure 2-6: Schematic representation of FSLG -  $^1H$  pulses

The pulse lengths have to fulfill this condition:

$$2-4 \quad \tau_{LG} = \frac{2\pi}{\omega_{eff}} = \frac{1}{\nu_{eff}} = \sqrt{\frac{2}{3\nu_1^2}}$$

For cross polarization under LG conditions, the Hartmann-Hahn condition has to be fulfilled at  $\pm 1$  spinning side bands (Stejskal, Schaefer et al. 1977):

$$2-5 \quad \omega_{eff,H} - \omega_{1,C} = m\omega_r$$

Where the efficient  $^1H$  magnetization is:

$$2-6 \quad \omega_{eff,H} = \sqrt{3/2} \gamma_H B_{1,H}$$

It was shown that heteronuclear recoupling in FSLG-CP can be achieved most efficiently by alternating the  $^{13}C$  rf pulses ( $\omega_{1,C}^+$  and  $\omega_{1,C}^-$ ) at +1 and -1 sidebands with simultaneously changing the phases as displayed in the pulse sequence scheme in Figure 2-7 (Dvinskikh, Zimmermann et al. 2003; Dvinskikh,

Castro et al. 2005; Dvinskikh, Zimmermann et al. 2005).

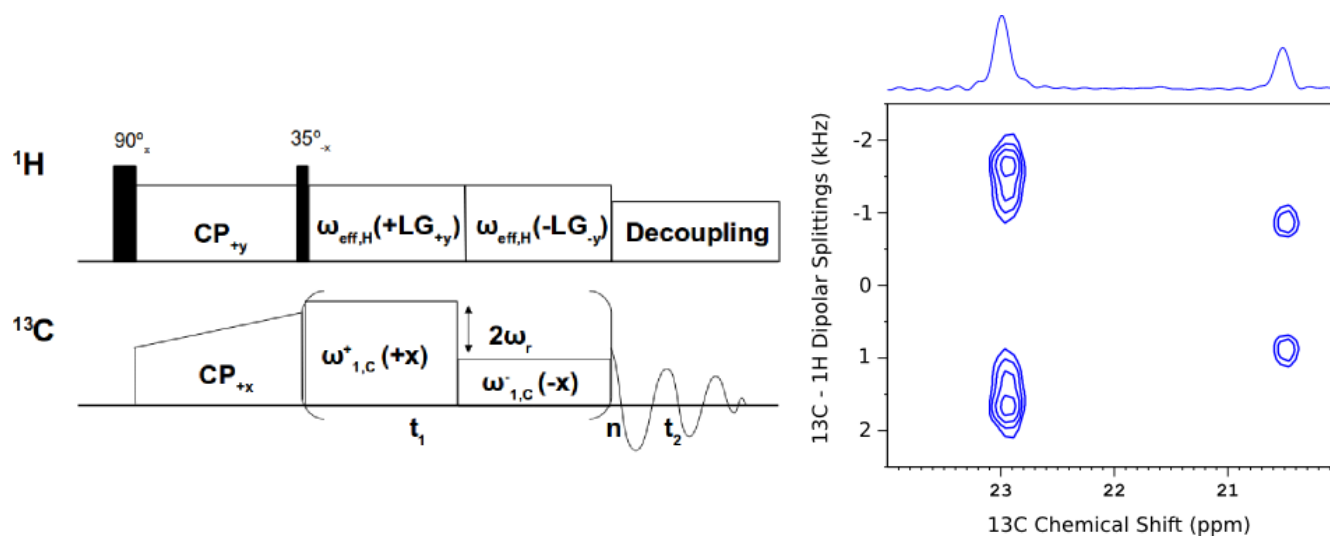


Figure 2-7: FSLG-CP pulse sequence (left) and spectral shape (right).

The splittings obtain from the 2D spectra give the dipolar couplings that are scaled differently for CH, CH<sub>2</sub> and CH<sub>3</sub> groups. For CH groups, splittings,  $\Delta\nu_{\text{CH}}$ , is scaled by the cosine of magic angle that results in 0.577 dipolar scaling factor. However, for CH<sub>2</sub> groups, it is more complicated that each proton is contributing separately to the dipolar coupling. In order to make it easier, it can be assumed that dipolar interactions for two protons are equal. Therefore the dipolar scaling can be calculated as 0.816 as follows (Davis, Auger et al. 1995; Dvinskikh, Castro et al. 2005):

$$2-7 \quad \Delta\nu_{\text{CH}_2} = \sqrt{2} \cos(\theta_m) d_{\text{CH}_2} \approx 0.816$$

For CH<sub>3</sub> groups it is even more complicated that calculations results in three different dipolar scaling factors, which are 0.577, 1 and 1.155 (Gan 2000).

Solid-state NMR provides two powerful techniques to obtain order parameters of lipid chains. Quadrupolar couplings of <sup>2</sup>H nuclei can give smoothed order parameters whereas dipolar coupling measurements supply assigned order parameters for each CH and CH<sub>2</sub> groups along the lipid chains as well as for the head group.

### 2.1.4.5 Laboratory Frame Spin-Lattice Relaxation Time ( $T_1$ )

$T_1$  spin lattice relaxation time describes the time needed by a spin system to return to Boltzmann equilibrium. It can be described by the following equation:

$$2-8 \quad M_z(t) = M_z^0(1 - \exp(-t/T_1))$$

where  $M_z(t)$  is the z-magnetization at time  $t$ ,  $M_z^0$  is the equilibrium z-magnetization and  $T_1$  is a time constant that is called longitudinal or spin-lattice relaxation time.

$T_1$  is sensitive to motions on the Larmor frequency time scale, which corresponds to nanoseconds as depicted Figure 1-4.

$^1\text{H}$ - $T_1$  experiment measures either directly if resolution is good enough using the standard inversion recovery or in case of protons indirectly via  $^{13}\text{C}$  or  $^{15}\text{N}$  CP-MAS experiments based on saturation recovery.  $^{13}\text{C}$ - $T_1$  is usually measured after CP using inversion recovery by following the decay of CP polarization to Boltzmann equilibrium.

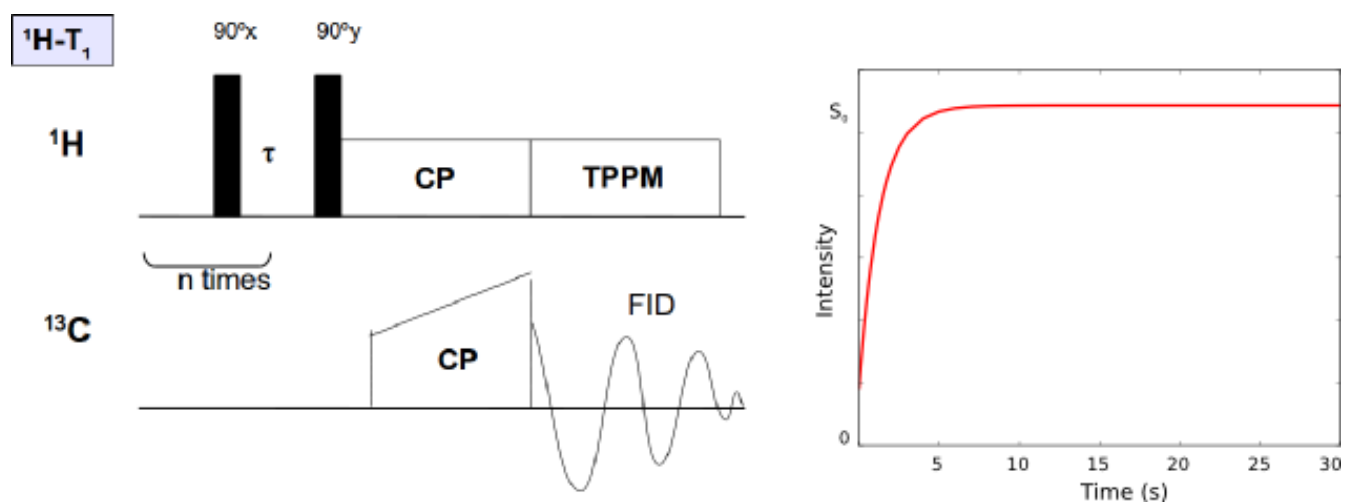


Figure 2-8: Pulse sequences to measure  $T_1$  relaxation times of  $^1\text{H}$  (left) and saturation recovery curve (right);  $S_0$  is the maximum intensity,  $n$  times  $90^\circ$  pulses are repeated to saturate magnetization, delay time  $\tau$  is varied to observe recovery.

There are several techniques to measure  $T_1$ . Saturation recovery and magnetization decay experiments are some common experiments (Figure 2-8 and Figure 2-9, respectively).  $^1\text{H}$ - $T_1$  can be found indirectly from  $^{13}\text{C}$  resonances by using saturation recovery experiments. Since  $^{13}\text{C}$  peaks are much well resolved than  $^1\text{H}$  peaks, indirect  $T_1$  measurements allow to obtain data for the protons, which can not be assigned with  $^1\text{H}$  NMR. In saturation recovery experiments, first a series of  $90^\circ$  pulses are applied to saturate the magnetization and after a time  $\tau$  another  $90^\circ$  pulse is applied and FID is recorded. If the time  $\tau$  is very short, close to zero, all the magnetization is flipped back to its initial value. Therefore no magnetization will be observed. By varying the time  $\tau$  magnetization recovery can be described by exponential function. Relaxation time of  $^1\text{H}$  nuclei can be calculated from saturation recovery curves by using equation 2.8. For  $^{13}\text{C}$   $T_1$  measurements, magnetization decay experiment can be used. In this experiment, magnetization is flipped to the z-direction just after CP transfer. Then, after a time delay  $\tau$ , a final  $90^\circ$  pulse is applied and the signals are received for detection. Variation of time interval  $\tau$  from short time to longer times cause an exponential decay in the signal that give relaxation time of the  $^{13}\text{C}$  nuclei.

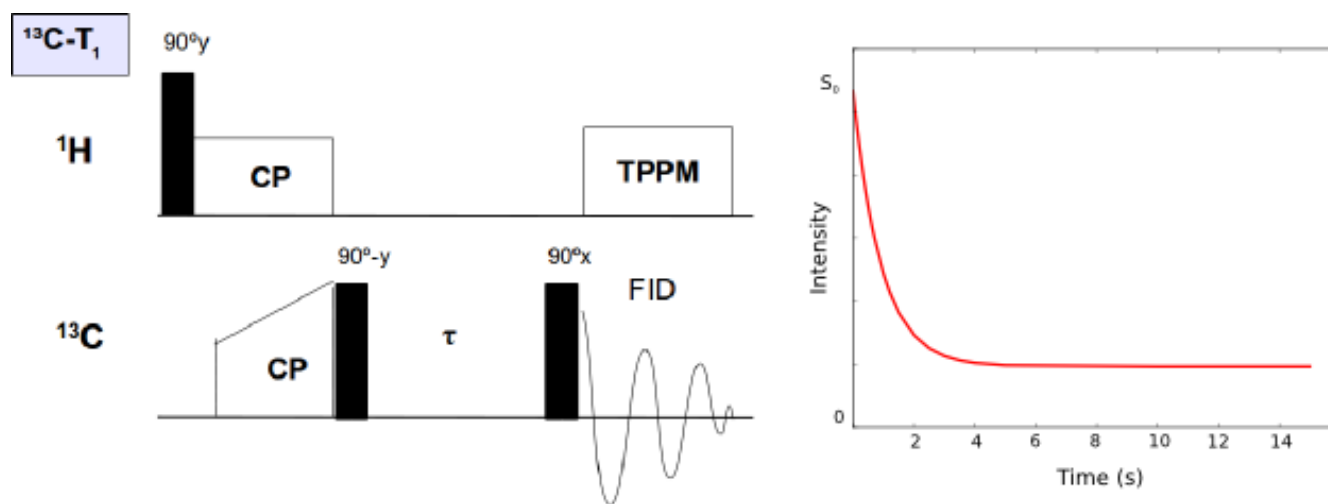


Figure 2-9: Pulse sequences to measure  $T_1$  relaxation times of  $^{13}\text{C}$  (left) and decay curve (right);  $S_0$  is the maximum intensity, delay time  $\tau$  is varied to observe magnetization delay.

Spin-lattice relaxation time is sensitive to motions on the Larmor frequency time scale. This means that  $T_1$  is sensitive to motions on the nanosecond time scale. The dependency between  $T_1$  and  $\tau_c$  is rather



complicated. In solution,  $T_1$  has its lowest value, when correlation time equals to  $1/\omega_0$ , where  $\omega_0$  is larmor frequency. At shorter correlation times, the motion is described as fast motion regime and at larger correlation times it is called slow motion regime. In the slow motion regime,  $T_1$  is positively correlated with  $\tau_c$  whereas in the fast motion regime, it is negatively correlated with  $\tau_c$ . Small molecules and large molecules stay at the two extreme side of the  $T_1$ -  $\tau_c$  dependency curve, so both have quite long relaxation times. For lipid molecules, it is not easy to guess from which side of the curve the relaxation time is. Therefore, the relation between relaxation time and motion is not always easy to resolve. Temperature dependent experiments may help to understand the correlation between motions and relaxation times. Another way may be to assume that the chain mobility increased towards the end of the chain. Therefore  $T_1$  values along the chain may be compared to understand how mobility affects the relaxation times.

#### **2.1.4.6 Rotating Frame Spin-Lattice Relaxation Time ( $T_{1\rho}$ )**

$T_1$  is the spin-lattice relaxation time in laboratory frame whereas  $T_{1\rho}$  is defined as the spin-lattice relaxation time in the rotating frame.  $T_{1\rho}$  describes  $T_1$  relaxation along  $B_1$  as the main quantization axis in the rotating frame (Jones 1966). Because of this,  $T_{1\rho}$  is sensitive to the motions on the microsecond time scale. Therefore  $T_{1\rho}$  measurements are very useful to obtain information on motions of membranes at longer time scales than  $T_1$  relaxation time measurements.

In order to measure  $^{13}\text{C}$ - $T_{1\rho}$ , the pulse sequence in the Figure 2-10 can be used. Firstly, transverse magnetization is created by CP. After CP the  $^{13}\text{C}$  spin lock remains for a variable delay  $\tau$  and signal is detected as a function of  $\tau$ .

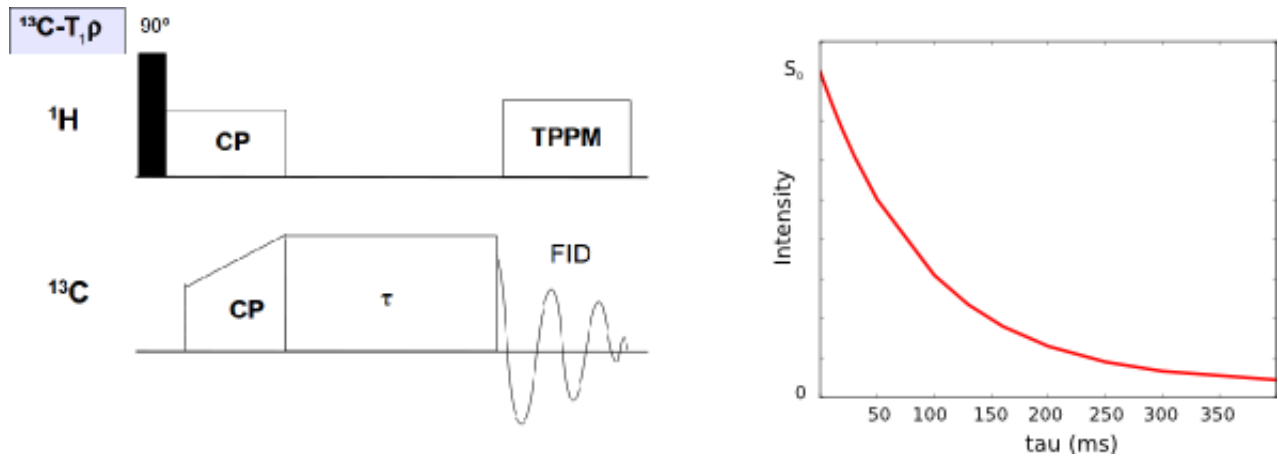


Figure 2-10: Pulse sequence to measure  $T_1$  relaxation time in rotating frame for  $^{13}\text{C}$  nucleus (left) and decay curve (right);  $S_0$  is the maximum intensity. Pulse length  $\tau$  is varied to observe relaxation process.

Applications of relaxation time experiments allow obtaining information about motions, which occurs in time scales from ns to  $\mu\text{s}$  for  $T_1$  and  $T_{1\rho}$ , respectively. Therefore relaxation time measurements can be very useful to monitor changes in motions of membranes in different time scales.

#### 2.1.4.7 Static and MAS $^{31}\text{P}$ NMR

In case of lipid samples,  $^{31}\text{P}$  NMR spectra can be obtained with good S/N by direct polarization due to their 100% abundance. Static spectra are recorded using a standard spin echo experiment (Figure 2-11) to avoid lineshape distortions due to spectrometer dead time. A  $180^\circ$  pulse is applied at time  $\tau$  after the first  $90^\circ$  pulse to refocus the signal at time  $2\tau$ .

As explained above,  $^{31}\text{P}$  NMR is a very useful and common method to observe membrane dynamics. Phase behavior of membranes as well as the self assembly structures of phospholipids can be analyzed by solid state  $^{31}\text{P}$  NMR measurements. In the case of different membrane-substrate systems, it is also a powerful tool to monitor phase separations, changes in the phase transition temperatures and changes in self-associated structure of membranes with the effect of substrate addition.

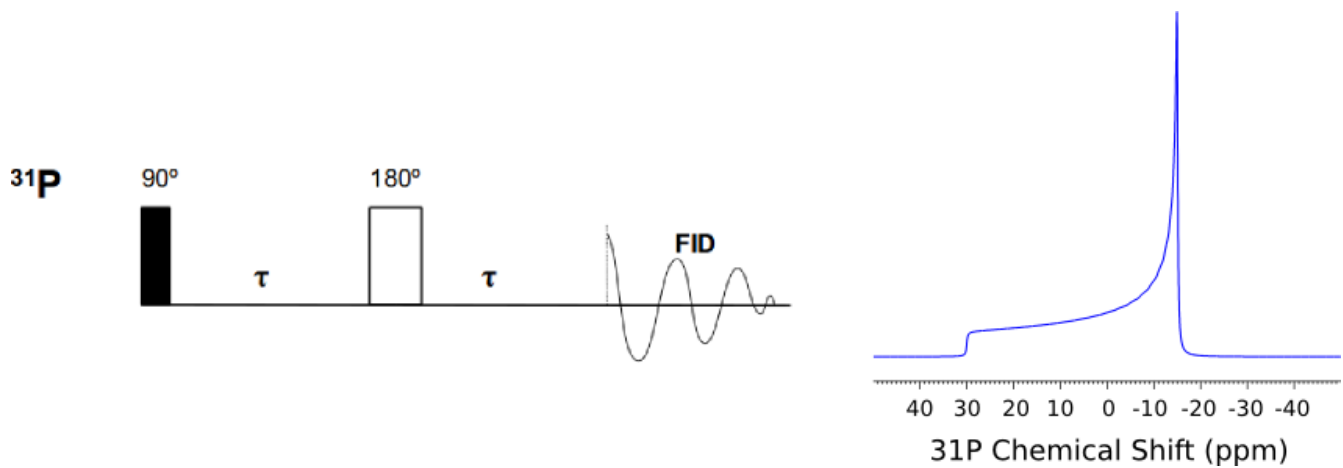


Figure 2-11:  $^{31}\text{P}$  NMR Hahn echo pulse sequence (left) and static spectral shape (right),  $\tau$  is the delay to refocus the signal.

#### 2.1.4.8 $^{14}\text{N}$ MAS Measurements

$^{14}\text{N}$  is a spin 1 nucleus and has therefore a quadrupolar moment as  $^2\text{H}$ . Therefore, the same pulse sequence (quadrupolar echo), which was depicted in Figure 2-4, can be used to observe  $^{14}\text{N}$  resonances. However,  $^{14}\text{N}$  quadrupolar couplings are much larger than  $^2\text{H}$  quadrupolar couplings. In many cases, quadrupolar couplings are in the range of MHz, which makes it difficult to detect full spectra. Fortunately, phospholipids are an exception. Due to fast rotational diffusion of lipids and the additional motion of the choline group nitrogen, quadrupolar couplings are scaled down into the kHz range. Therefore, lipids can be studied by  $^{14}\text{N}$  NMR measurements.

Quadrupolar echo pulse sequence is used for  $^{14}\text{N}$  NMR measurements (Figure 2-4). The pulse sequence is starting with  $90^\circ$  pulse, continue with another  $90^\circ$  pulse at time  $\tau$  after the first pulse and end up with acquisition at time  $\tau$  after the second pulse to satisfy refocusing condition.

It has been shown that  $^{14}\text{N}$  NMR is a powerful technique to monitor changes in surface potential of membranes as well as changes in the orientation of head group of lipids in membranes upon additions of different substrates (Siminovitch, Rance et al. 1980; Lindstrom, Williamson et al. 2005).

### 2.1.4.9 $^{31}\text{P}$ - Static and MAS Exchange Experiments

The broad dynamics range of solid-state NMR also enables detection of slow, collective membrane motions. During the last decades,  $T_2$  relaxation time measurements for  $^{31}\text{P}$  and  $^2\text{H}$  nucleus were carried out to observe slow motions (Stohrer, Grobner et al. 1991; Dufourc, Mayer et al. 1992; Weisz, Grobner et al. 1992; Althoff, Heaton et al. 1996; Trouard, Nevzorov et al. 1999; Otten, Brown et al. 2000; Brown, Thurmond et al. 2001; Althoff, Frezzato et al. 2002; Althoff, Stauch et al. 2002). However these types of experiments are sensitive to a broad distribution of time scales and are therefore difficult to interpret. A better method to observe slow motions by solid state NMR is to apply exchange spectroscopy that provides information about segmentational exchanges in the time scale varying from ms to s (Spiess 1980; Rossler 1986). However, exchange experiments are known to have sensitivity and resolution problems. In order to overcome these problems, a new exchange NMR method Centerband-Only Detection of Exchange (CODEX) was developed recently, (deAzevedo, Hu et al. 1999; deAzevedo, Hu et al. 2000). CODEX experiments enable monitoring segmental reorientations of molecules on long time scales, with a better resolution and sensitivity than traditional exchange experiments.

The CODEX pulse sequence, depicted in Figure 2-12, is explained in detail in the literature (deAzevedo, Hu et al. 1999; deAzevedo, Hu et al. 2000). Basically, it is a stimulated echo experiment, with CSA recoupling pulses, which refocus magnetization after orientational exchange during the mixing time in between two recoupling periods. The reorientation of CSA tensors are observed in this experiment. After a first  $90^\circ$  pulse on the  $^{31}\text{P}$  channel, magnetization evolves during the first recoupling period, during which  $180^\circ$  pulse are applied at half rotor period time intervals. Exchange takes place during the mixing time. At the end of second recoupling period, magnetization is refocused and the FID is recorded. In the absence of motions, magnetization will be set completely refocused but decays otherwise.

During the mixing time, apart from exchange processes, there is also contribution from  $T_1$  relaxation. In order to filter out these contributions, a reference spectrum is needed by interchanging  $t_m$  and  $t_z$  durations. Therefore the ratio of peak intensities of CODEX spectrum and reference spectrum provide

information about the slow motions occur at that specific mixing time  $t_m$ .

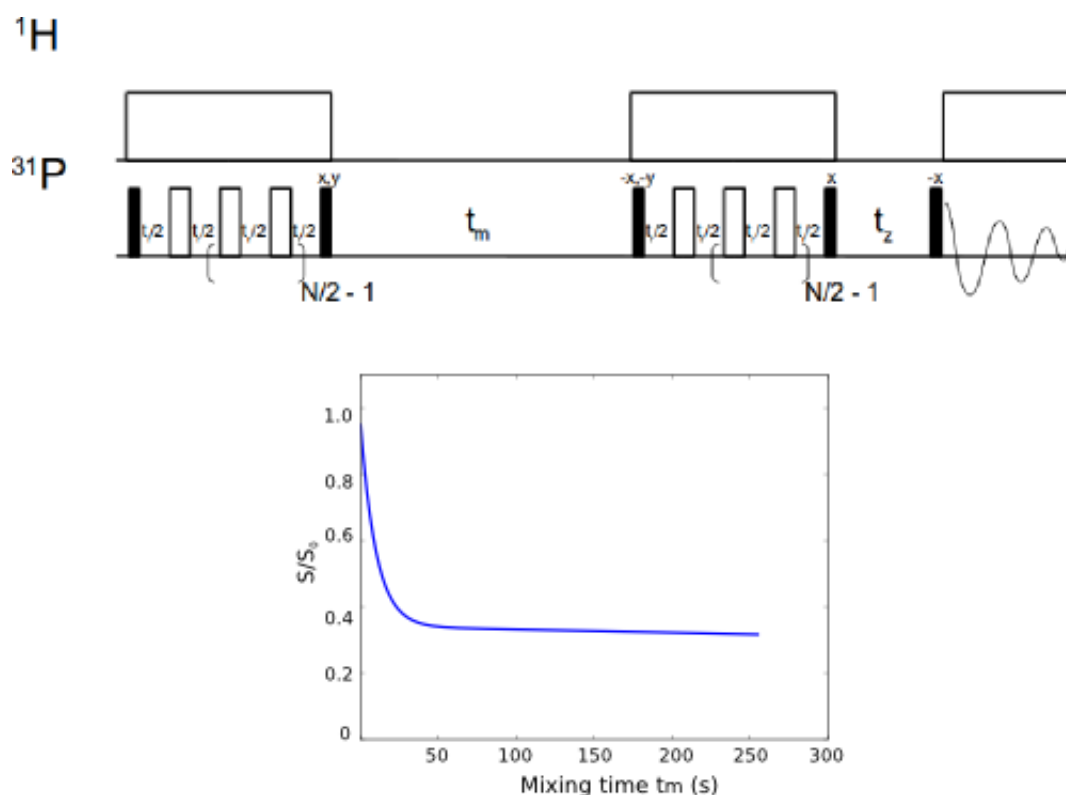


Figure 2-12:  $^{31}\text{P}$ -CODEX pulse sequence (top) and dephasing curve (bottom),  $S$  is the intensity at certain mixing time and  $S_0$  is the intensity of reference spectrum. During mixing time ( $t_m$ ), CODEX exchange takes place,  $t_m$  and  $t_z$  are interchanged to record a reference spectrum.

Another important aspect of the CODEX experiment is the effect of recoupling time on the reorientation angle of the molecules (deAzevedo, Hu et al. 2000). Therefore the variation of the number of recoupling pulses provides information about the segmental orientation of the motion. In the study of Schmidt-Rohr group, it was calculated that recoupling time variation for different orientation angles provide information about whether motions are diffusive or discrete in character (deAzevedo, Hu et al. 1999; deAzevedo, Hu et al. 2000).

Another method to obtain information on slow motions of membranes could be classical static exchange experiments. 2D static exchange experiments on  $^{31}\text{P}$  are a well suited method to investigate orientations dependent motions at slow time regime (Schmidt, Wefing et al. 1986; Wefing and Spiess 1988; Marasinghe, Buffy et al. 2005). By this method, reorientation angle distribution of motions can

be obtained if exchange of CSA tensor orientation takes place during the mixing time.

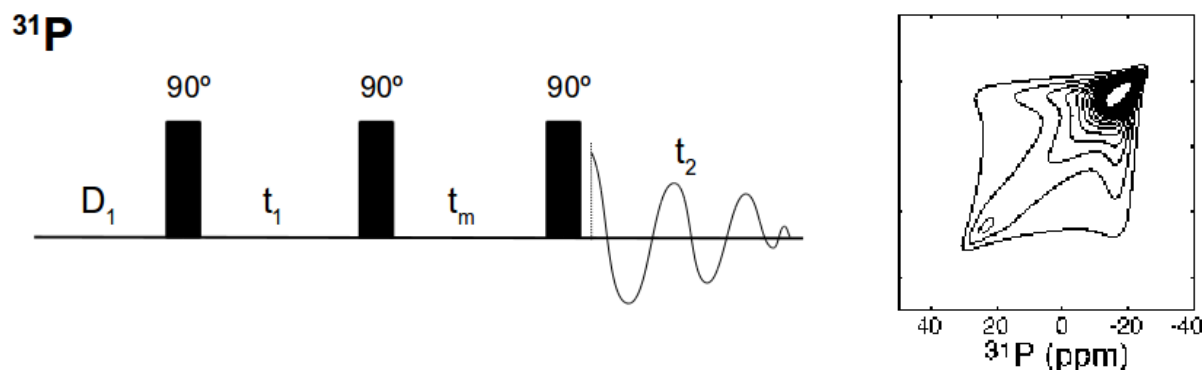


Figure 2-13:  $2D\text{-}^{31}\text{P}$  static exchange experiment pulse sequence (left) and spectral shape (right) (Marasinghe, Buffy et al. 2005), reorientation in chemical shift tensor takes place during mixing time ( $t_m$ ).

Pulse sequence and spectral shape is depicted in Figure 2-13 (Marasinghe, Buffy et al. 2005). Firstly, magnetization is aligned on the  $xy$  plane by  $90^\circ$  pulse and evolves. After that, another  $90^\circ$  pulse is applied before mixing time ( $t_m$ ). Finally, third  $90^\circ$  pulse is applied to aligned magnetization again to the  $xy$ -plane and FID is recorded during acquisition time. During  $t_m$ , reorientation in chemical shift tensor occurs. Therefore, if mixing time equals to zero, molecular orientation will not change that result in a diagonal spectrum. When mixing times are different than zero, due to orientational exchange in chemical shift tensor during mixing time, spectra deviate from pure diagonal shape with an increasing intensity of off-diagonal signal.

Time scales of this kind of experiments are in the order of milli seconds. It is known that, in this time regime, lateral diffusion in membranes is the main dynamical process that causes reorientation of molecules. In addition to lateral diffusion, it is known that, overall tumbling of membrane vesicles can affect orientation dependent motions at that time-scale (Bloom, Burnell et al. 1975). Thus, static exchange experiment can be useful to monitor the changes in lateral diffusion coefficients and vesicle tumbling of phospholipids bilayers.

## **2.2 Molecular Dynamics**

### **2.2.1 Simulation Details**

All the simulations were carried out by using GROMACS 4.0.3 package (Bekker 1993; Berendsen, Vanderspoel et al. 1995; Lindahl, Hess et al. 2001; Van der Spoel, Lindahl et al. 2005; Hess, Kutzner et al. 2008) that was installed in the cluster (intel-R xeon-R cpu e5462, 8 processors with 4 core for each processors) of Peter Guntert group in the Institute of Biophysical Chemistry, Frankfurt University, Germany. POPC and DMPC bilayers were used in this study. DMPC box consist of, 128 lipid and 3655 water molecules; POPC box consist of 128 lipid and 2460 water molecules. Figure 1-2 shows DMPC bilayer simulation box. All other details about each simulation were explained in the methods part of each chapter.

### **2.2.2 Energy Minimization**

Before starting a molecular dynamics simulation of a bilayer, an energy minimization has been carried out. It is necessary to discard any possible unnatural interactions that may create problems for further simulations. Thus, each simulation box underwent energy minimization in this work. Steep algorithm was used for energy minimization. In this method, firstly, forces and potential energies are calculated for each atom. Then, new positions of atoms are calculated. After that, new forces and energies are calculated for these new positions. If the calculated energies are lower than previous energies, new positions are accepted by the program. In this study, energy minimizations were performed by using steep algorithm with 500 steps. For the energy minimization, long range electrostatics interactions were calculated by Particle-Mesh-Ewald algorithm (Darden, York et al. 1993; Essmann, Perera et al. 1995). Both electrostatics and Van der Waals cutoffs for energy minimizations were taken as 1.0 nm.

### **2.2.3 Time Steps**

The membrane models, which were used in this study, contained 64 lipids in each monolayer. Time step for the simulations was taken as 0.002 picoseconds. GROMACS use leap-frog algorithm (Hockney, Goel et al. 1974) to update position and velocities at time intervals  $\Delta t$ . The simulations were

carried out to reach nanosecond time-scale. Lipid membranes are dynamic systems in different time-scales. Many important processes occur in longer time-scales than nanoseconds. However, with nanosecond simulations it is possible to obtain very important physicochemical properties such as order parameters, area per lipid and bilayer thickness.

#### **2.2.4 Output Options**

Since each simulation in this study has been run for the range of nanoseconds it would consume too much computational power if the output from each step were written. Instead of this, the coordinates and velocities were written to the trajectory file for each 5 picoseconds. The output frequency of saving energy information was also chosen 5 picoseconds. Energy and trajectory information were written for the whole system for each simulation box.

#### **2.2.5 Neighbor Searching**

In order to apply non-bonding forces, pairs within certain distance, which is within the specified cut-off, have to be found. Therefore, a neighbor list must be created for each molecule by using this specified cut-off value. Neighbor searching can be done by a simple algorithm or a grid algorithm (Van der Spoel, Lindahl et al. 2005). For periodic boundary conditions, grid algorithm is a better method than simple search. In this work, all the simulations were done in periodic boundary conditions, thus pair lists were generated by using grid algorithm. Atoms within 1.1 nm were used for the calculations of non-bonded pair forces. Neighbor lists were updated in each 5 steps.

#### **2.2.6 Electrostatics and Van der Waals Interactions**

Since the periodic boundary conditions were applied to the systems, Particle-mesh Ewald summation was used for coulomb interactions (Darden, York et al. 1993; Essmann, Perera et al. 1995). This method was developed to improve classical Ewald summation. In PME method, charges are defined as inside grids, which are then Fourier transformed to obtained sum for each grid. For the calculation of Van der Waals interactions, the simple cut-off method was applied. The cutoff for coulomb and VdW interactions were chosen same as the neighbor list cutoff (1.1 nm).



## 2.2.7 Temperature Coupling

The details for temperature and pressure couplings were given in the introduction chapter. In this work, all simulations were carried out at constant temperature. Temperature was coupled by Nose-Hoover algorithm (Nose 1984; Hoover 1985) for each group in the simulation boxes separately. The reference temperature was adjusted to 300 K for POPC and 310 K for DMPC, which is higher than the lipid main transition temperature. The period of controlling temperature fluctuations for the coupling was set to 0.1 ps.

## 2.2.8 Pressure Coupling

Each simulation box was coupled with Parrinello-Rahman approach, which has a similar algorithm with Nose-Hoover method, to obtain constant pressure (Parrinello and Rahman 1981; Nose and Klein 1983). Since the systems were lipid bilayers, semiisotropic coupling was applied by taking different coupling values for the z- direction and for xy plane. The pressure was set to 1 bar with 1 ps time interval and  $4.5 \times 10^{-5} \text{ bar}^{-1}$  compressibility factor.

## 2.2.9 Constraint on Bonds

Constraints were applied for bonds with H atoms. LINCS algorithm (Hess, Bekker et al. 1997) was used to calculate corrected positions of the atoms. LINCS algorithm corrects the bond lengths after an unconstrained update. In this method, correction is done in two steps. Firstly, projection of new bond on the previous bond is set as same length with previous bond. Secondly, bond lengths were further corrected due to rotational lengthening. There are several LINCS parameters that have to be set in input file. Lincs-order is the number of matrices in the matrix expansion equation in the algorithm, lincs-iter is the iteration number for correction due to rotational lengthening and Lincs-warnangle is the maximum angle to rotate the atoms for bond length correction. In this study, it was preferred to use default parameters of GROMACS. Therefore, Lincs-order was adjusted to 4, lincs-iter was set to 1 and Lincs-warnangle was chosen as 30.

## 2.2.10 Position Restraints

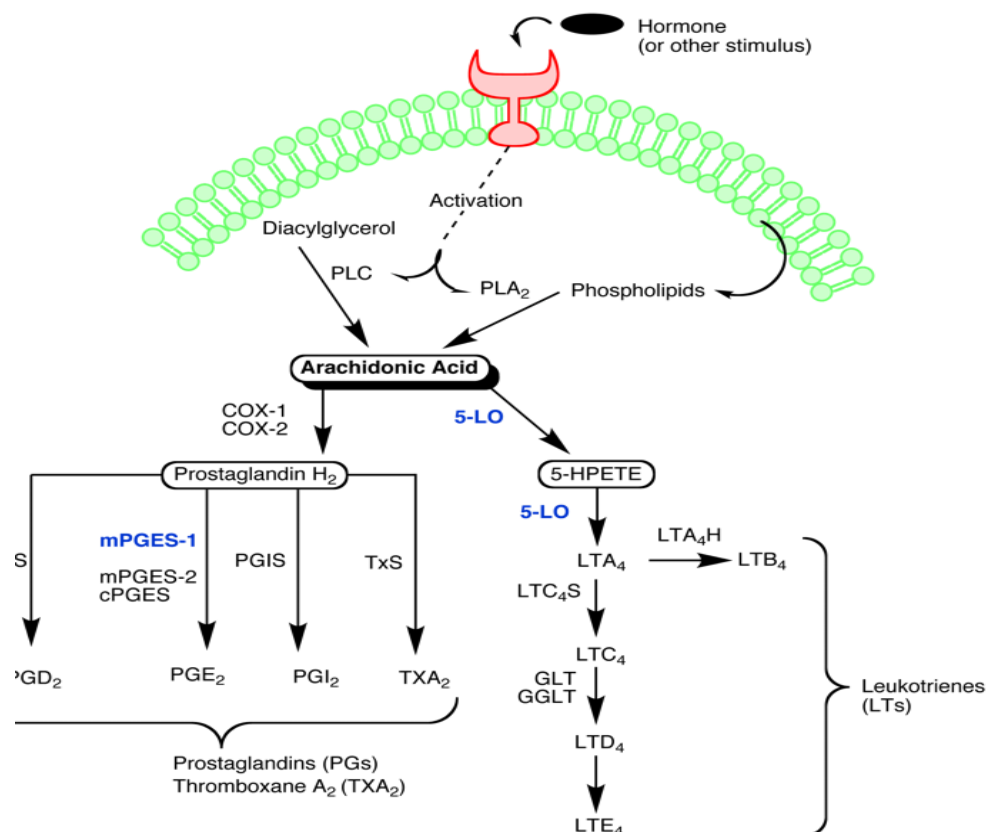
<sup>1</sup>H-MAS NOESY results are used as additional constraints to fix the position of substrates with respect to the lipids. In order to use these NMR constraints, position restraints for substrate atoms were generated. In general, for calculations of proteins, it is not common to use position restraints for implementing NOE distance informations to the calculations. For NMR experimental restraints, usage of distance restraints is much more convenient method. However for investigating drug lipid interactions, performing distance restraints is more difficult. Since there are more than one lipid molecule, fixing drug molecule at a certain distance of lipids is not possible, it will result in shrinking of bilayer around the drug molecule. Therefore, a better method will be introduced here by the usage of position restraints in the GROMACS package. Firstly, average positions for lipid atoms for the pure bilayer were calculated. After that, position restraints for drug atoms to the average position of lipid atoms were set with the information coming from <sup>1</sup>H-MAS NOESY experimental data. Details of position restraints were well explained in GROMOS manual. Basically, force constants are used for the calculation of potentials to fix atoms at certain positions. In this study, 100 kJmol<sup>-1</sup>nm<sup>-2</sup> was used as force constant.

### 3 Probing Lipid Interactions of Pirinixic Acid Derivatives

#### 3.1 Introduction

The arachidonic acid cascade has been always an important target for therapeutic studies on inflammatory diseases (Kuehl and Egan 1980; Trang 1980; Granstrom 1984; Abramson, Korchak et al. 1985). Non-steroidal anti-inflammatory drugs (NSAID) are a widely used drug class that is acting on cyclooxygenases (COX) to inhibit the formation of prostaglandins (PG) from arachidonic acid. Since PGE<sub>2</sub> cause inflammation, the inhibition of its formation by COX enzyme is strongly preventing inflammation. On the other hand, it causes the inhibition of other PGs formations (Figure 3-1) (Hieke, Greiner et al. 2011), which are necessary for homeostasis (Rainsford 2007). Therefore, NSAIDs have many side effects especially in the case of long-term use. One alternative strategy to inhibit PGE<sub>2</sub> formation can be to target mPGES-1 enzyme that is responsible the formation of PGE<sub>2</sub> from prostaglandin.

Figure 3-1:  
Schematic  
representation of  
arachidonic acid  
cascade; (Hieke,  
Greiner et al. 2011)



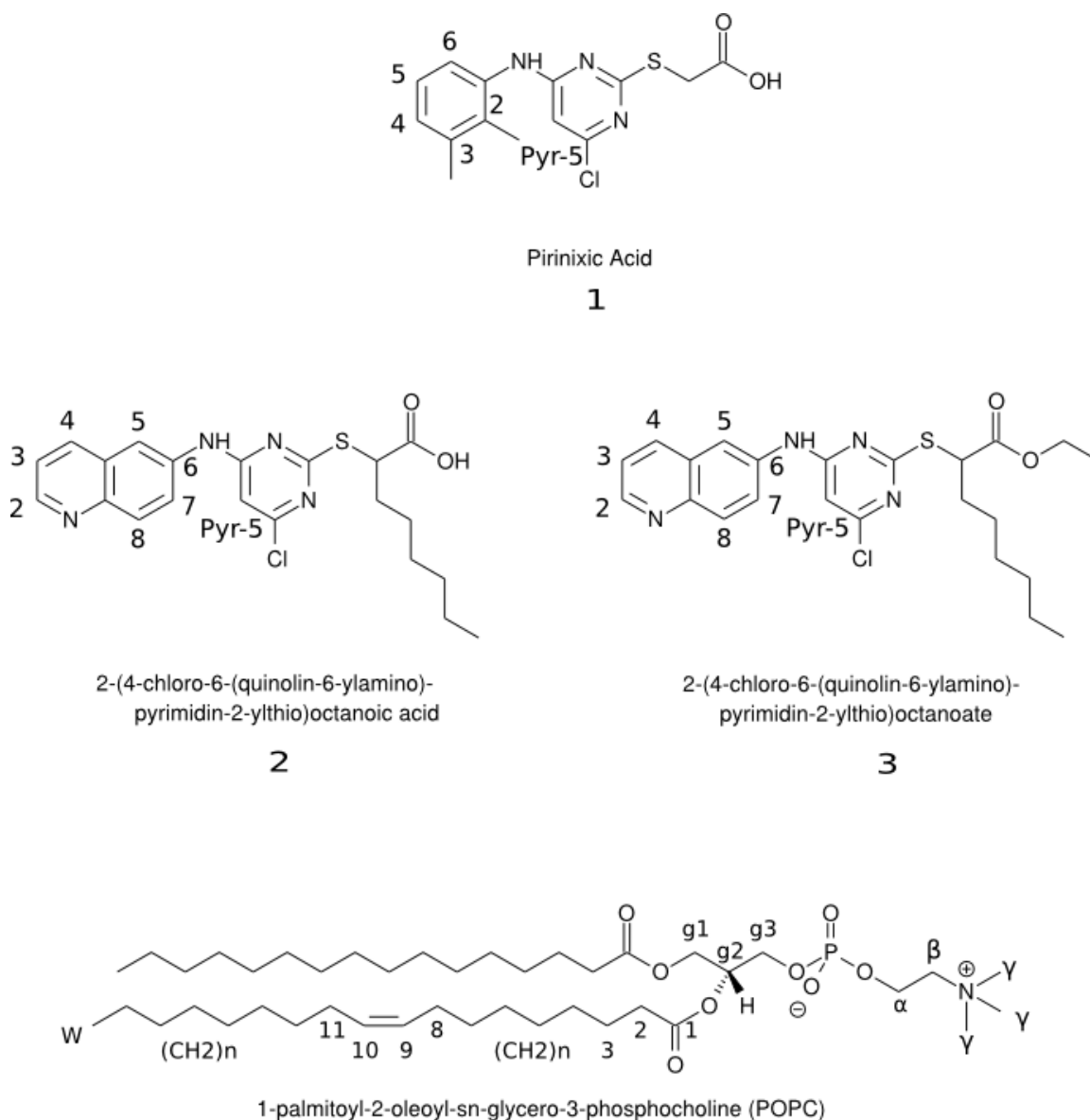


Figure 3-2: Structures and nomenclature of pirinixic acid (1), pirinixic acid derivatives (2, 3) and POPC (bottom)

Besides the formation of prostaglandin, the arachidonic acid cascade is branching out into the formation of leukotrienes (LTs) from arachidonic acid by the enzyme 5-lipoxygenase

(5-LO) (Figure 3-1). Since both LTs and PGs are mediating inflammatory processes, designing a dual inhibitor for mPGES-1 and 5-LO as therapeutic agents would be desirable. In this way, the anti-inflammatory therapeutic activity could be combined with fewer side effect (Friesen and Mancini 2008; Wang, Song et al. 2008). Pirinixic acid derivatives belong to this group of potential drugs, which showed inhibitory effects on both mPGES-1 and 5-LO product formations. The mechanism, by which pirinixic acid derivatives cause dual-inhibition of these enzymes is not yet understood. On the other hand it was shown that pirinixic acid derivatives are acting as the agonist of both the alpha and the gamma subtype of peroxisome peroliferator activated of receptor (PPAR) (Rau, Syha et al. 2008) and in this way inhibiting the LTs formation (Werz, Greiner et al. 2008).

Pirinixic acid was synthesized in 1974 by Santilli et al. (Santilli, Scotese et al. 1974), while screening pyrimidine derivatives to find more potent drugs against hyperlipidemia. Further studies were done (Koeberle, Zettl et al. 2008; Rau, Syha et al. 2008; Werz, Greiner et al. 2008; Zettl, Dittrich et al. 2009) on pirinixic acid derivatives to investigate their activities on 5-LO and mPGES-1 enzymes as well as alpha and gamma PPAR receptors in different environments.

It was revealed that n-alkyl alpha-substitution of pirinixic acid results in a decrease in 5-LO product formation in polymorphonuclear leukocytes (PMNL) (Koeberle, Zettl et al. 2008; Werz, Greiner et al. 2008). In addition, another study was done to investigate the effects of pirinixic acid derivatives on PPAR receptor activities that are closely related with 5-LO product formation (Popescu, Rau et al. 2007). It was shown that alpha substituted pirinixic acids enhance PPAR $\alpha$  and PPAR $\gamma$  agonism and inhibit cellular LT formation (Rau, Syha et al. 2008; Werz, Greiner et al. 2008). Figure 3-2 displays two potent compounds, 2-(4-chloro-6-(quinolin-6-ylamino)pyrimidin-2-ylthio)octanoic acid (compound **2**) and 2-(4-chloro-6-(quinolin-6-ylamino)pyrimidin-2-ylthio)octanoate (compound **3**). **3** was found as one of the most potent suppressors of 5-LO product formation among other derivatives they reported (Koeberle, Zettl et al. 2008; Werz, Greiner et al. 2008). They were also tested for inhibitory effects on mPGES-1 and it was

found that compound **3** is the most potent inhibitor of mPGES-1 product formation and more potent than its acidic form (compound **2**). The increased activity with n-alkyl substitution suggests that hydrophobicity is important for inhibitory effect of pirinixic acid derivatives on 5-LO and mPGES-1. Better insertion of the substances into the cell membrane could be the one reason for enhanced activity of n-alkyl substituted pirinixic acid derivatives. Therefore it is of interest to investigate the partition of compound **2** and **3** into the lipid bilayers.

### **3.1.1 Objectives**

Pirinixic acid derivatives are well-suited as potential drugs against inflammatory diseases. They are known to be dual-inhibitors for mPGES-1 and 5-LO (Koeberle, Zettl et al. 2008; Werz, Greiner et al. 2008; Hieke, Greiner et al. 2011) as well as a dual-agonist for PPAR $\alpha$  and PPAR $\gamma$  (Rau, Syha et al. 2008). Therefore, it is necessary to examine their behaviors inside the cell membranes. In this study, the motivation was to investigate configurations of compound **2** and **3** inside the artificial phospholipid membranes by using the combined methods of solid-state NMR and molecular dynamics calculations. The interactions of substrates with lipids were studied by solid-state MAS-NOESY experiments. The distance probabilities of the atoms between lipid and substrates that are coming from NOE intensities were further used as restraints for molecular dynamics simulations. Thus, the location of **2** and **3** was calculated and then visualized from the snapshots of simulation's trajectories in order to get some insight into the molecular reasons for their potency.

## **3.2 Materials and Methods**

### **3.2.1 Sample Preparation**

In this study, two pirinixic acid derivatives, namely 2-(4-chloro-6-(quinolin-6-ylamino)pyrimidin-2-ylthio)octanoic acid (**2**) and its ethyl ester (**3**), were used (Figure 3-2). Substrates were kindly provided by Prof. Dr. Manfred Schubert-Zsilavicz,

Frankfurt. Synthesis and substrate characterization have been reported by Popescu et al and Rau et al (Popescu, Rau et al. 2007; Rau, Syha et al. 2008). POPC-d31 (1-palmitoyl(d31)-2-oleoyl-sn-glycero-3-phosphocholine) was purchased from AVANTI lipid. Pirinixic acid derivatives were reconstituted inside POPC liposomes with the molar ratio of 15:1, POPC: substrates by standard liposome preparation methods as described in Chapter 2. Lipid-substrate mixtures containing 10 mg of POPC-d31 were dissolved in chloroform (5 mL). Then, solvent was evaporated by using N<sub>2</sub> stream and sample was dried further in a rotary evaporator under vacuum overnight. After removing all the solvent, lipid-substrate mixtures were obtained as thin films. They were hydrated with 1 mL water. Hydrated samples were transferred to an Eppendorf tube and pelleted. Excess water was removed and mixtures were put into the lyophilizer overnight to remove all remaining water. After this step, samples were rehydrated with 5  $\mu$ L deuterated water. Finally, 3-4 freeze-thaw cycles were performed at temperatures that were below and above the main phase transition temperatures of POPC to obtain a more homogeneous sample.

### 3.2.2 Solid State NMR

All spectra were recorded on a Bruker Avance 600 solid-state NMR instrument at 300 K with 10 kHz spinning speed. For <sup>1</sup>H-<sup>1</sup>H-MAS-NOESY experiments, mixing time for the evolution of the NOE correlations were varied from 5 to 800 ms. The recycle delay was chosen to 2s. 4096 and 512 data points were collected for the direct and indirect dimension, respectively. FID was acquired using TPPI for 256 ms in the direct and 32 ms in the indirect dimension. Spectral width of 8 kHz was used for each dimension. Spectra were processed using an exponential broadening function. Data analyses were performed by using Topspin 2.1 and CARA software (Keller 2004). In addition, all the calculations were done by using Python (<http://www.python.org/>), (Siarheyeva, Lopez et al. 2006; Maier, Schiffmann et al. 2009). Relaxation rates were calculated by full-matrix approach (explained in Chapter 1).

For <sup>1</sup>H-<sup>1</sup>H-MAS RFDR experiments, the number of 5  $\mu$ s 180° recoupling pulses during

the mixing time was varied from 48-1200. A recycle delay of 2s was used. 4096 and 512 data points were collected for the direct and indirect dimension, respectively. Acquisition time of 256 ms for direct and 32 ms for indirect dimensions were used. TPPI was used for FID acquisition. Spectral width was chosen as 8 kHz for each dimension.

### 3.2.3 Partition Coefficients

Partition coefficients (logP) were calculated by using VCCLAB (Virtual Computational Chemistry Laboratory) server (2005; Tetko, Gasteiger et al. 2005).

### 3.2.4 MD Simulations

#### 3.2.4.1 Methods

All simulations were performed by using GROMACS 4.0.3. package (Bekker 1993; Berendsen, Vanderspoel et al. 1995; Lindahl, Hess et al. 2001; Van der Spoel, Lindahl et al. 2005; Hess, Kutzner et al. 2008). The initial structure of bilayer was provided by Peter Tieleman (<http://wcm.ucalgary.ca/tieleman/downloads>) (Berger, Edholm et al. 1997; Tieleman, Forrest et al. 1998). The force-fields of both molecules were generated by using the topology server PRODRG (Schuttelkopf and van Aalten 2004), which is based on GROMOS87 force field. Analyses of the trajectories after the simulations were done by using Python.

#### 3.2.4.2 Starting Structures

2-(4-chloro-6-(quinolin-6-ylamino)pyrimidin-2-ylthio)octanoic acid and its ethyl ester were used for the simulations. The starting configuration of the POPC bilayer already equilibrated for 1.6 ns was taken provided by Peter Tieleman (<http://wcm.ucalgary.ca/tieleman/downloads>) (Tieleman, Forrest et al. 1998). It



underwent further equilibration for 50 ns until a well equilibrated pure POPC membrane was obtained. Afterwards one POPC molecule was replaced with one drug molecule in different simulation boxes for each drug. Coordinates of center of mass of the drug molecule are fixed at the coordinates of center of mass of the lipid molecule and coordinates of each atoms of the drug molecule were regenerated based on the new center of mass coordination (Falck, Patra et al. 2004). Drug molecules were placed into the lipid membrane in 3 different conformations. One last simulation box was created by deleting necessarily amount of water molecules and placing one drug molecule at its place outside the bilayer. Energy minimization was carried out for each simulation box to remove unfavorable contacts.

In summary, four different simulation boxes were created for each drug with different starting conformations of the drug molecule with respect to the POPC bilayer.

### **3.2.4.3 Force-fields**

The force-field for the POPC bilayer was a mixture of GROMOS force-field and lipid parameters (Berger, Edholm et al. 1997; Tieleman, Forrest et al. 1998). For drug molecules, force-fields were generated by giving the coordinates of drug molecules to the PRODRG server (Schuttelkopf and van Aalten 2004).

### **3.2.4.4 Simulation Parameters**

All the simulations were carried out with the parameters defined earlier. LINCS algorithm was used to constraint bonds with hydrogen atom. Periodic boundary conditions were applied in three dimensions. Long range electrostatic interactions were calculated by using PME (Particle-mesh Ewald) algorithm and cutoff for the coulomb interactions was 1.1 Å. For van der Waals interactions, 1.1 Å cutoff was implemented (Patra, Karttunen et al. 2003; Patra, Karttunen et al. 2004). Temperature for all the systems was adjusted to 300 K by using Nosé-Hoover method. The simulations were

performed at 1 bar constant pressure by using semiisotropic Parrinello-Rahman coupling scheme. 100 ns simulation was carried out for each simulation box.

### **3.2.4.5 Restraints**

Position restraints were applied to drug molecules inside the bilayer by using the lipid-drug distance constraints obtained by MAS-NOESY. The average positions of atoms of lipid throughout the trajectories were calculated and the positions of atoms of drugs were restrained to the calculated lipid's atom positions. 1000  $\text{kJmol}^{-1}\text{nm}^{-2}$  force constant were tried first to see that the atoms were fixed around the specific position. Afterwards, the force constants were chosen as 100  $\text{kJmol}^{-1}\text{nm}^{-2}$  to give some flexibility to the atoms around those specific positions. Restraints were applied only for the z-direction of the box to see the level of insertion of drugs, and their orientations along the bilayer.

### **3.2.4.6 Analysis**

After simulations, the positions of restrained atoms were calculated for the whole trajectories for each simulation box to compare the differences in between different starting configurations.

## ***3.3 Results and Discussion***

### **3.3.1 Solid State NMR**

#### **3.3.1.1 $^1\text{H}$ Chemical Shift Differences**

The aim of this study was to investigate the behavior of two pirinixic acid derivatives

incorporated inside liposomes. Pirinixic acid itself is very lipophilic compound with an aromatic backbone. Its partition coefficient ( $\log P$ , logarithm of the ratio of un-ionized solute concentration in octanol vs water) is calculated as  $3.74 \pm 0.62$ . Alpha alkyl substituted pirinixic acid derivatives are known to be more lipophilic than the lead compound (Koeberle, Zettl et al. 2008; Werz, Greiner et al. 2008). Their partition coefficients are higher than partition coefficient of pirinixic acid. Partition coefficients of  $5.73 \pm 0.89$  for compound **2** and  $6.53 \pm 0.72$  for compound **3** were found. This suggests that they may partition into the lipid bilayer and locate along the membrane. Because of this, mixtures of POPC-d31-pirinixic acid derivative samples were prepared and 1D and 2D  $^1\text{H}$ -MAS NMR experiments were applied to investigate locations and orientations of these two pirinixic acid derivatives inside POPC liposomes. Furthermore, it is of special interest to probe for differences in the lipid incorporation for both compounds.

1D-  $^1\text{H}$  NMR measurements can give valuable information about the effects of substrates on lipid resonances.  $^1\text{H}$  chemical shifts of lipids were changing with the presence of pirinixic acid derivatives. Changes in chemical shifts along the chain as well as at the head group may give an idea about substrate location inside the membrane. Chemical shift changes can give a first indication on drug-lipid interactions. Figure 3-3 shows  $^1\text{H}$  NMR spectra of pure POPC-d31 and POPC-d31-pirinixic acid derivatives mixtures. Downfield regions of mixture's spectra were zoomed in to observe aromatic peaks of compound **2** and **3**. The differences in chemical shift values of lipid resonances in the presence of **2** and **3** were plotted in Figure 3-4. In general, effects are smaller than 0.08 ppm while no significant effect in linewidth of  $^1\text{H}$  resonances is observed. It can be seen in the figure that compound **3** had an effect on head group and glycerol proton resonances as well as lipid chain resonance of POPC-d31. It changes the chemical shift of protons of both the head group and glycerol in large amount. In addition to this, **3** also had strong effect on resonances at hydrocarbon chain of lipid, including double bond protons. This is an indication that compound **3** inserted into the bilayer at a certain depth in which it can affect hydrocarbon chains of lipids. However compound **2** had small effects only on the head-group protons of lipid. It didn't change chemical shifts of chain protons significantly. This result suggests that compound **3** is located at the more hydrophobic

part of lipid bilayer while compound **2** tends to stay closer to interfacial region.

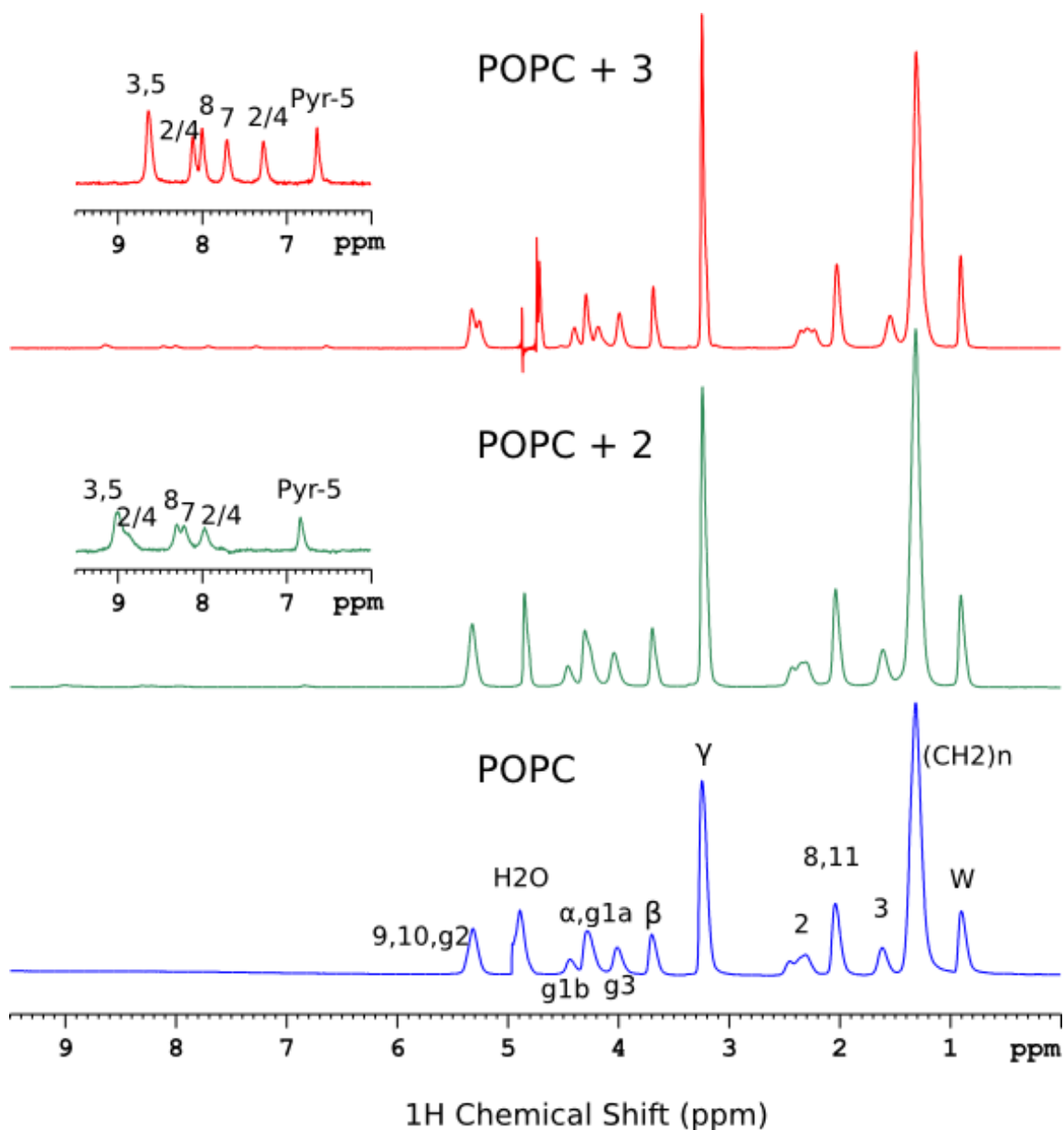


Figure 3-3: 1-dimensional  $^1\text{H}$ -MAS spectra of POPC-d<sub>31</sub> (bottom), POPC-d<sub>31</sub>-2 mixture (middle) and POPC-d<sub>31</sub>-3 mixture (top) at 300 K. The aromatic region is zoomed in to see resonances of **2** and **3**.

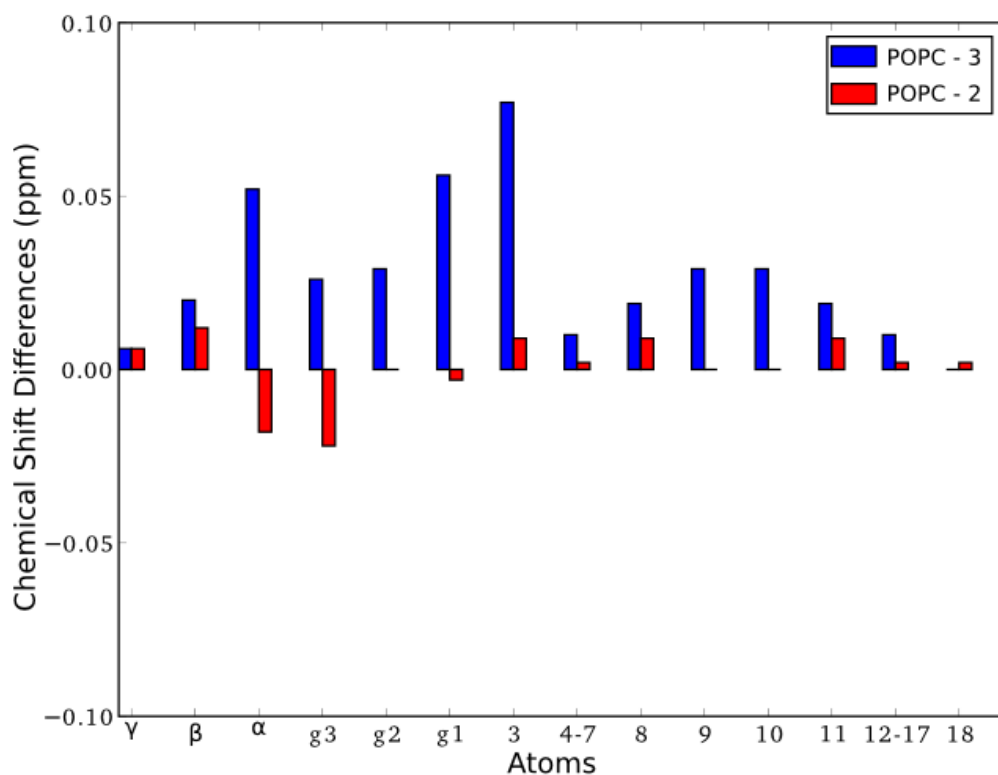


Figure 3-4:  $^1\text{H}$  chemical shift differences of pure POPC-d31, POPC-d31-2 mixture and POPC-d31-3 mixture at 300 K, x-axis shows lipid atoms along the bilayer.

### 3.3.1.2 $^1\text{H}$ -MAS NOESY

The data above indicate a stronger effect onto the lipid bilayer for compound **3** compared to **2**. To obtain a more quantitative view,  $^1\text{H}$ - $^1\text{H}$ -MAS NOESY studies were carried out, which allows obtaining further information on distribution profiles of substrates along the bilayer. Since pirinixic acid derivatives have aromatic rings, it was easy to see their peaks in  $^1\text{H}$  NMR inside POPC membrane even at low substrate concentrations. Figure 3-5, Figure 3-6 and Figure 3-7 display  $^1\text{H}$ -MAS NOESY spectra of mixtures of POPC-d31 with pirinixic acid derivatives for mixing times 50, 200, and 400 ms, respectively. POPC-d31-compound **2** spectra were chosen to show lipid region. Cross and diagonal

peaks of substrates were shown separately by zooming in the corresponding regions. At downfield region of NOESY spectra, aromatic peaks of substances can be observed. Both compound **2** and **3** show strong crosspeaks with most of lipid resonances. However as highlighted in Figure 3-5, Figure 3-6 and Figure 3-7, compound **3** had correlation mostly with lipid acyl chain protons whereas compound **2** showed crosspeaks more with lipid head group protons. This result already suggests that **3** has more contacts with the inner hydrocarbon chain than **2**.

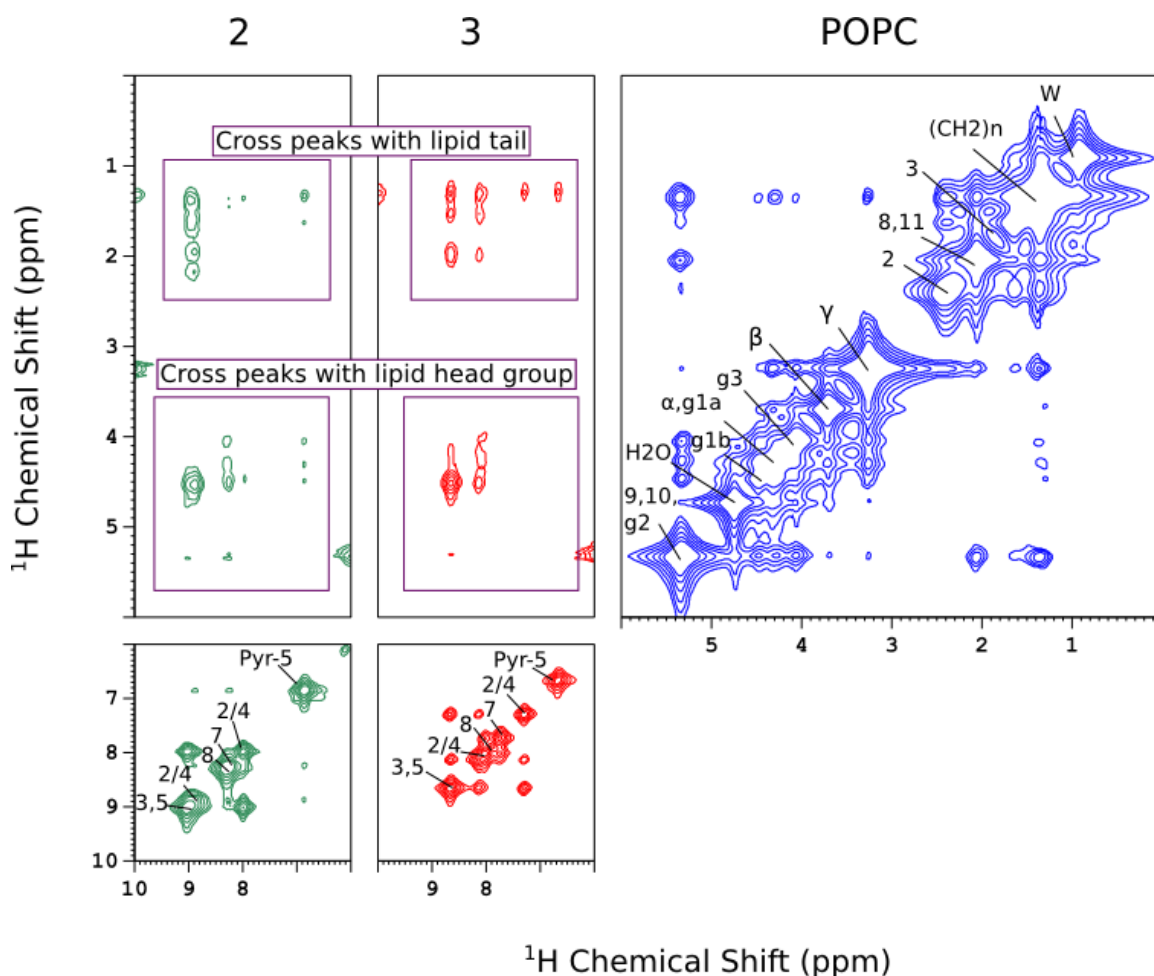


Figure 3-5:  $^1\text{H}$ -MAS NOESY spectra of POPC-d31-2 and POPC-d31-3 mixtures at 50 ms mixing time at 300 K, cross peaks of **2** and **3** with POPC head group and lipid tail were depicted in the boxes.

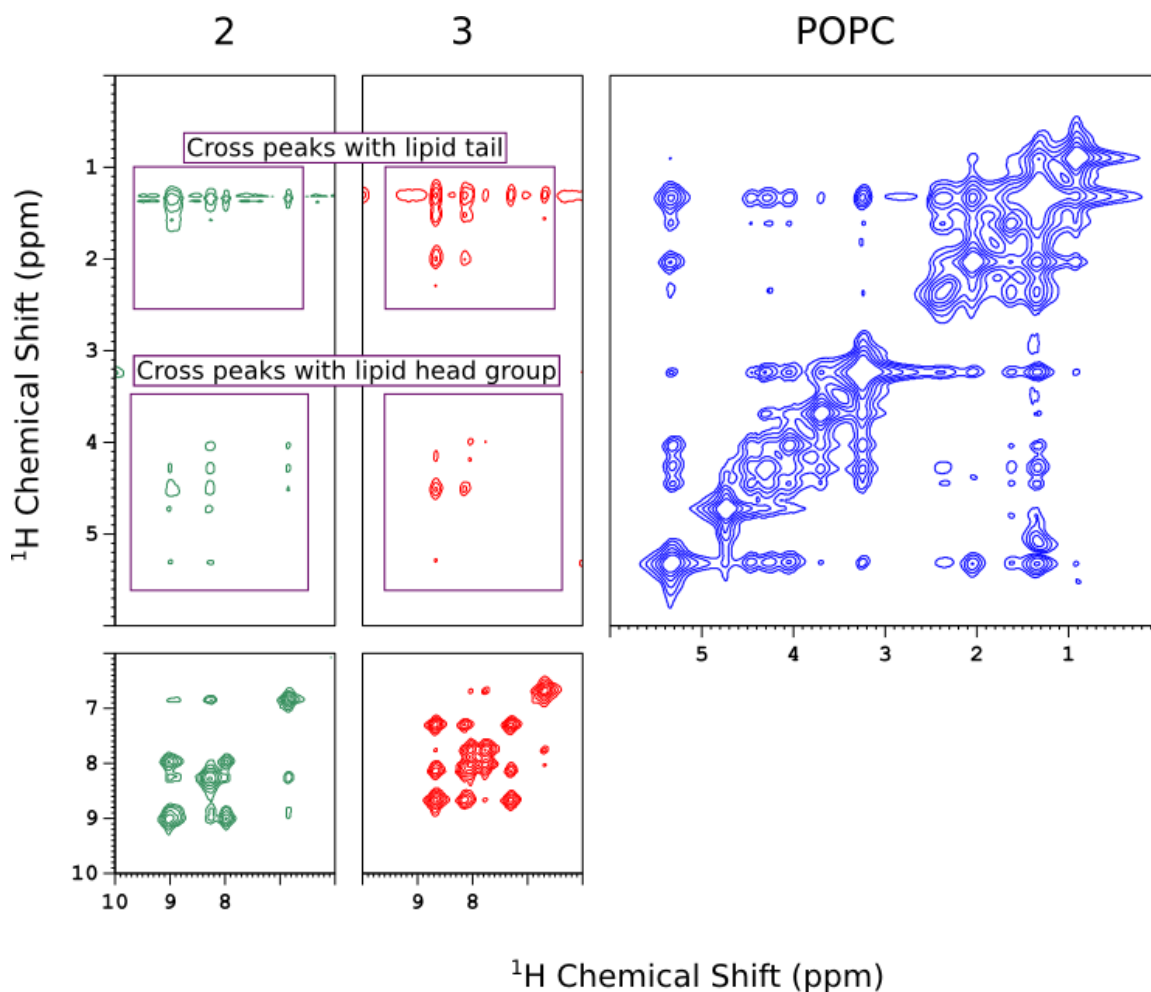


Figure 3-6:  $^1\text{H}$ -MAS NOESY spectra of POPC- $d_{31}$ -pirinixic acid derivatives mixtures at 200 ms mixing time at 300 K, crosspeaks of 2 and 3 with POPC head group and lipid tail were depicted in the boxes.

In addition, to reveal interactions between substrates and POPC by observing crosspeak intensities at NOESY spectra, distribution probabilities of substrates along the bilayer can be investigated quantitatively from cross relaxation rates. Therefore, it was necessary to record a series of spectra in different mixing times and calculate relaxation rates for each cross and diagonal peak in order to investigate the locations of these two potential drug compounds inside POPC membrane.

Cross and diagonal relaxation rates were computed by the help of full matrix approach

(Chapter 1). Buildup curves for each cross and diagonal-peaks for both lipid and substrates were plotted with measured and calculated intensity values, displayed in Figure 3-8 and Figure 3-9 for **2** and **3**, respectively. For each buildup curve, red points showed measured intensities and blue points showed calculated intensities corresponding to the specific mixing time by full matrix approach. Yellow regions in the figures show buildup curves between substrate nuclei with lipid atoms. For this analysis, more than one mixing time is needed. However, to obtain more reliable results with high precision, more than 6-8 mixing times would be necessary. From relaxation rates, distribution probabilities of substrate atoms derived from NOEs between substrate and lipid protons and displayed in Figure 3-10 and Figure 3-11 for **2** and **3**, respectively.

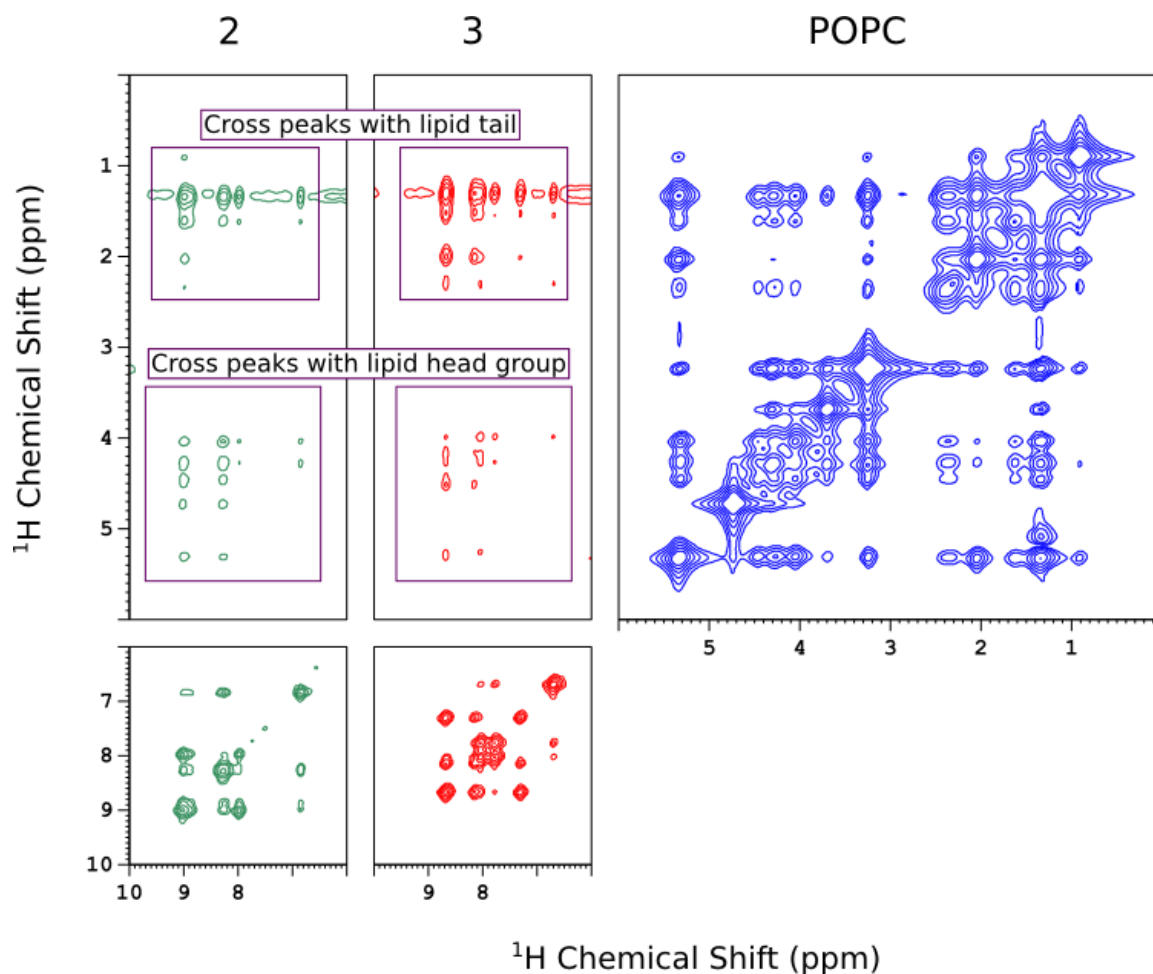


Figure 3-7:  $^1\text{H}$ -MAS NOESY spectra of POPC- $d_{31}$ -pirinixic acid derivatives mixtures at 400 ms mixing time at 300 K, crosspeaks of **2** and **3** with POPC head group and lipid tail were depicted in the boxes.



MAS NOESY Buildup Curves (POPC + 2)  
 Analysis is carried out with the full matrix approach.  
 Every subplot is scaled to its own maximum intensity.

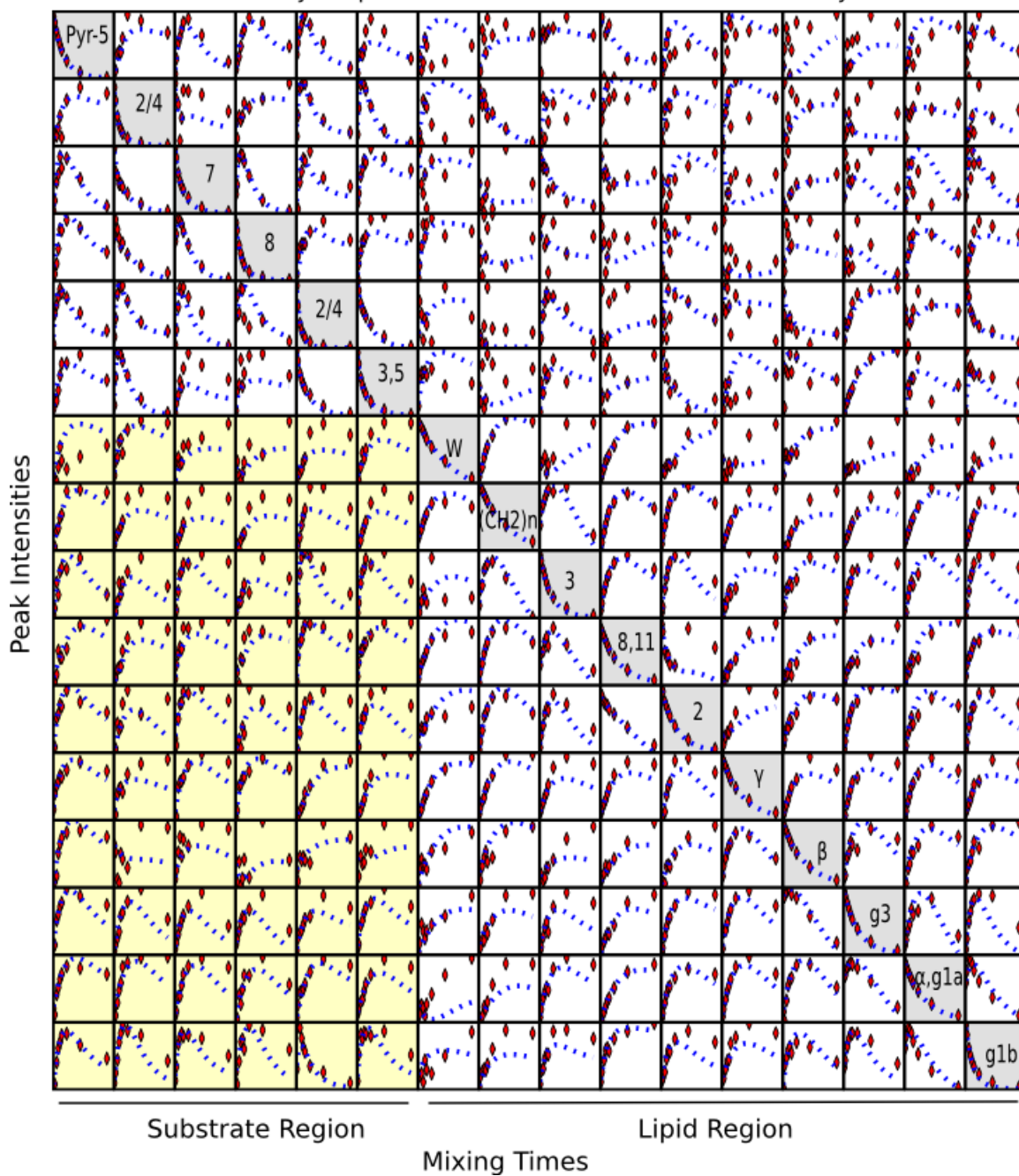


Figure 3-8: Buildup curves of  $^1\text{H}$ -MAS NOESY peak volumes of the mixture of POPC-d31 with compound 2 at 300 K; mixing times of 5-800 ms were used, yellow region shows crosspeak between 2 and POPC buildup curves.

MAS NOESY Buildup Curves (POPC + 3)  
 Analysis is carried out with the full matrix approach.  
 Every subplot is scaled to its own maximum intensity.

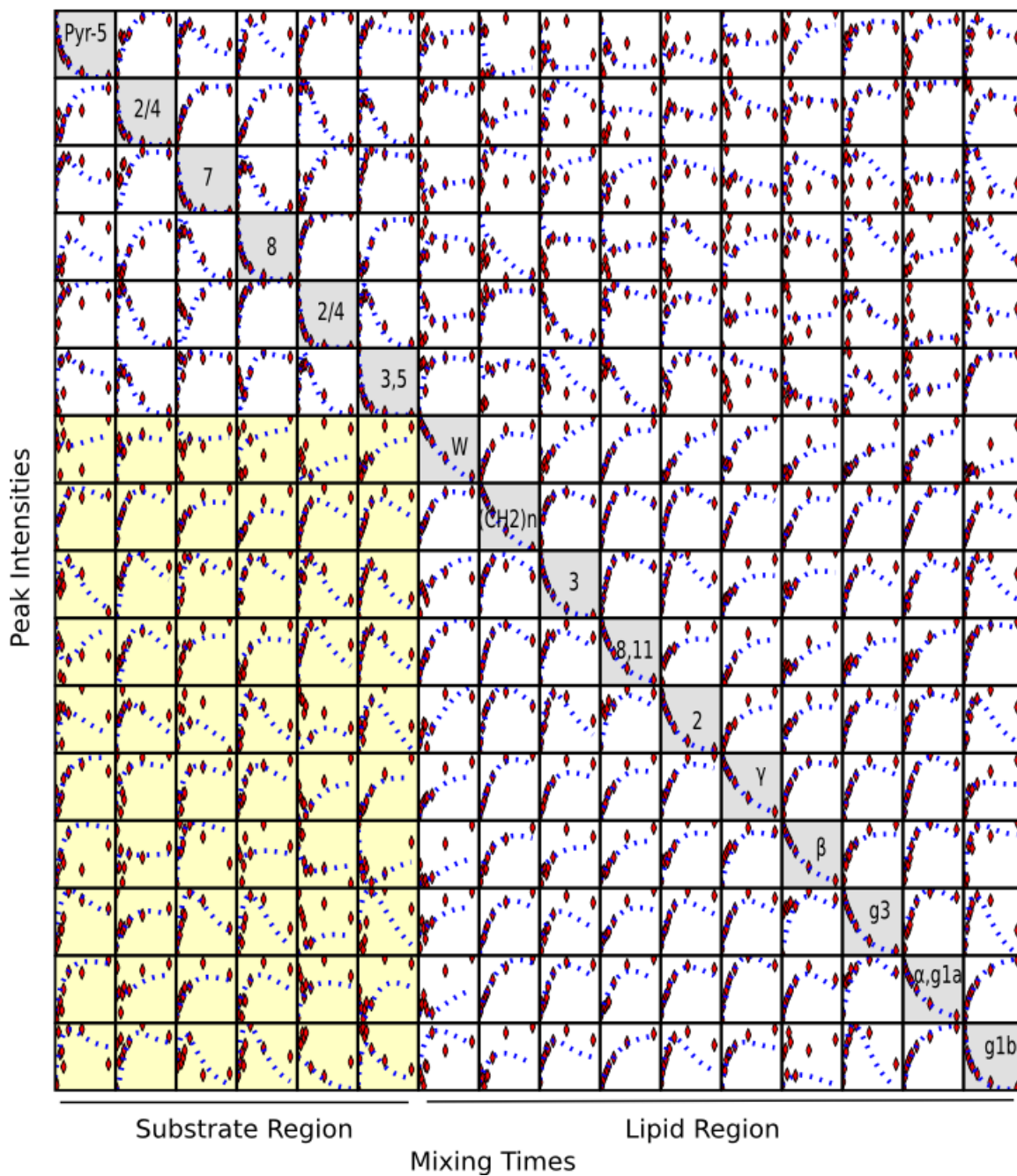


Figure 3-9: Buildup curves of  $^1\text{H}$ -MAS NOESY peak volumes of the mixture of POPC-d31 with compound 3 at 300 K; mixing times of 5-800 ms were used, yellow region shows crosspeak between 3 and POPC buildup curves.

Cross relaxation rates provide distribution profiles for substrates in lipid bilayer (Holte and Gawrisch 1997; Huster, Arnold et al. 1999). From the distribution probabilities of the two substrates, it can be easily seen that, compound **2** were strongly interacting with glycerol backbone of POPC molecules. There were also interactions with the beginning of the hydrocarbon chain but no significant interactions were observed with the protons towards to end of the chains. On the other hand, Figure 3.11 shows that compound **3** has even higher contact with hydrocarbon chains comparing with glycerol backbone. This result suggests that compound **3** was inserted into the membrane more deeply than **2**.

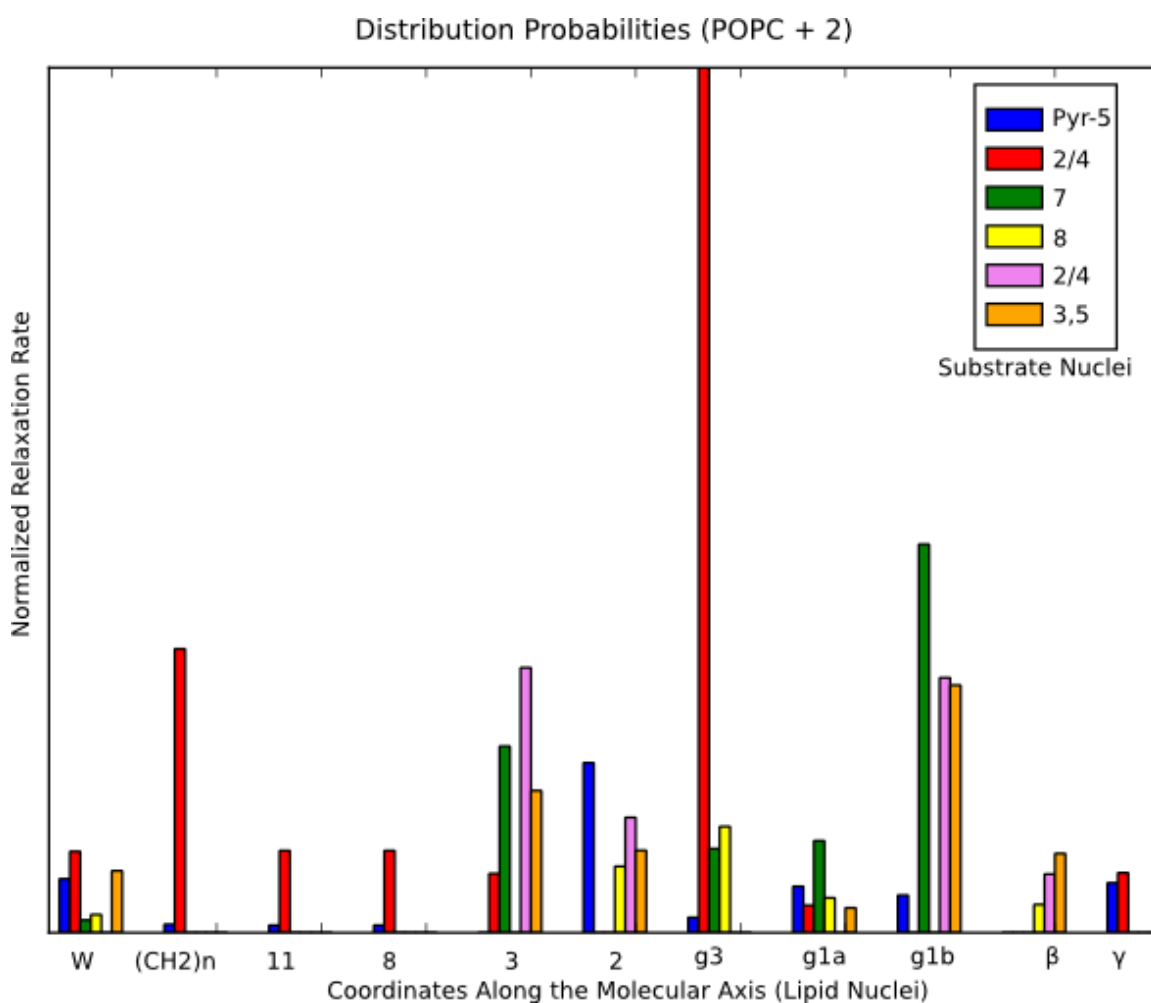
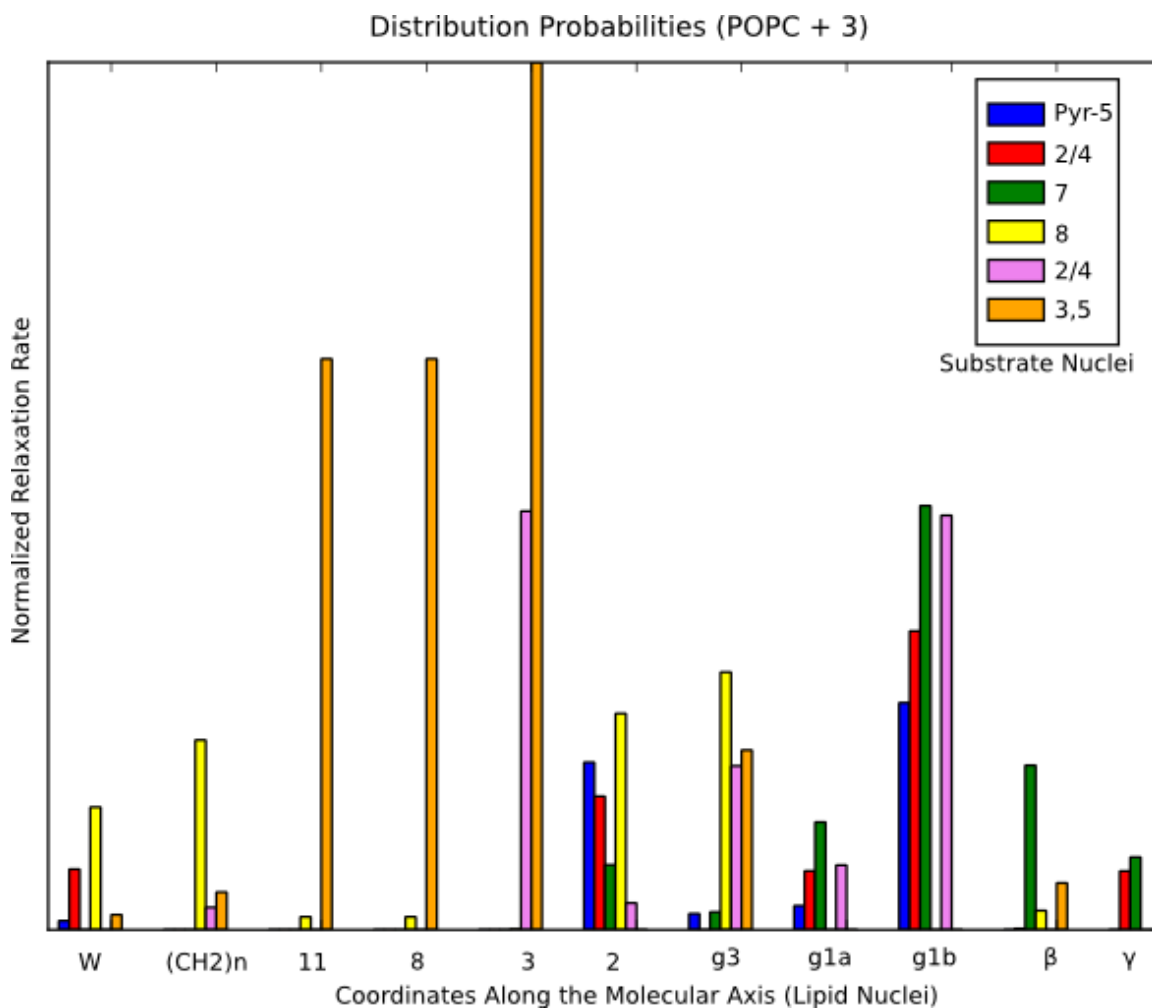


Figure 3-10: Distribution profiles of compound **2** inside POPC-d31 bilayer from  $^1\text{H}$ -MAS NOESY of the mixture of POPC-d31 with compound **2** at 300 K: in the figure legend, substrate protons at pyridine and quinoline rings were shown, 2 and 4 cannot be assigned, 3 and 5 are overlapped and other protons are well-resolved and assigned.



*Figure 3-11: Distribution profiles of compound 3 inside POPC-d31 bilayer from  $^1\text{H}$ -MAS NOESY of the mixture of POPC-d31 with compound 3 at 300: in the figure legend, substrate protons at pyridine and quinoline rings were shown, 2 and 4 cannot be assigned, 3 and 5 are overlapped and other protons are well-resolved and assigned.*

In order to see distribution profiles of two compounds along the bilayer, protons at 3,5 position of the quinoline ring of both compounds were examined in more details. Figure 3-12 displays distribution probabilities of 3,5-H of compounds **2** and **3** with POPC lipid segments. For compound **2**, distribution probability has the highest value with glycerol protons. On the contrary, compound **3** shows highest interactions with the lipid acyl chains. This result, consistent with chemical shift analysis, suggests that compound **3** was inserted into the membrane more deeply than **2**.

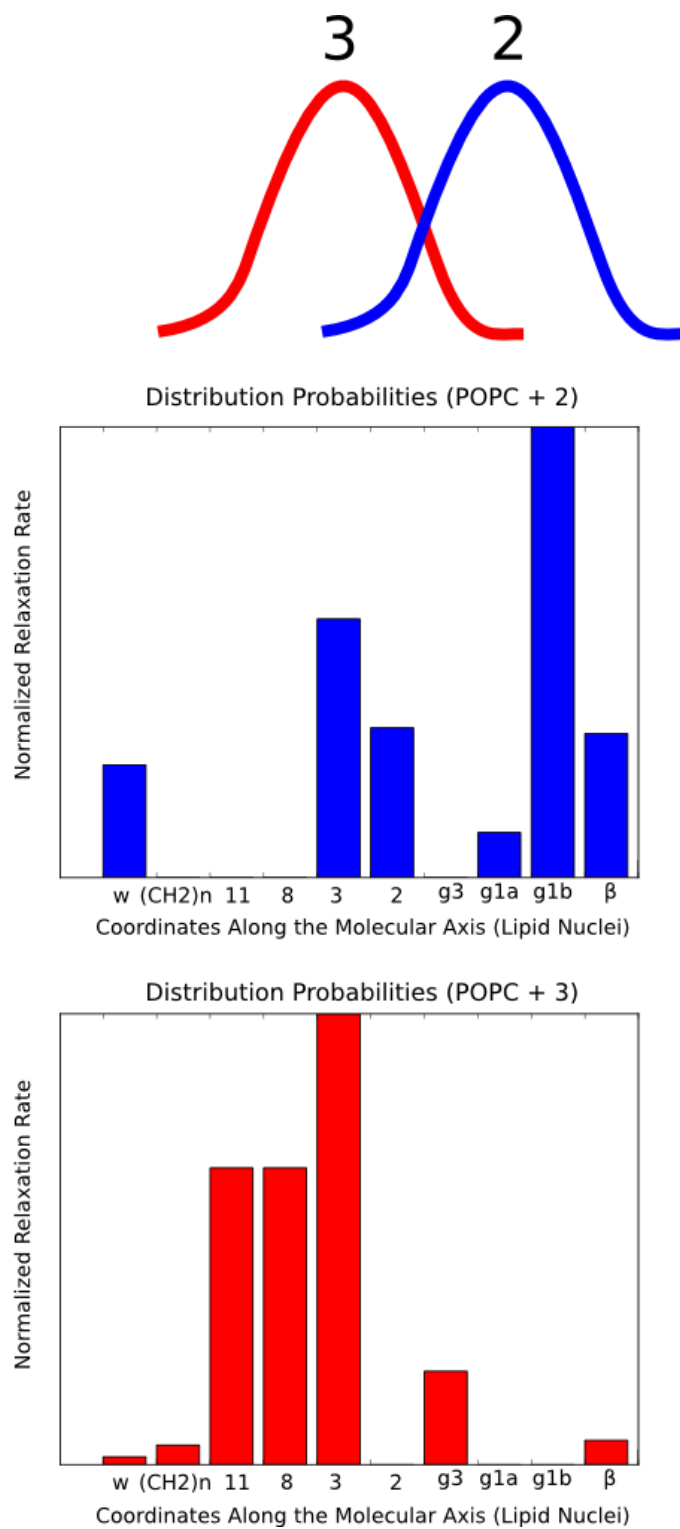


Figure 3-12: Distribution probabilities of H-3,5 of compound **2** (top) and **3** (bottom) along the bilayer calculated by  $^1\text{H}$ -MAS NOESY cross-relaxation rates at 300 K, at the top of the figure, distribution probabilities of **2** and **3** is represented.

### 3.3.1.3 <sup>1</sup>H-MAS RFDR

Recent studies (Aucoin, Camenares et al. 2009) showed that RFDR is a powerful method for studying location and orientation of small molecules inside lipid membranes. It was shown before by Aucoin et al that magnetization transfers occurs in RFDR much faster than in NOESY. The reason is that for RFDR, magnetization exchange happens directly via dipolar coupling, which is inversely proportional to  $r^3$  ( $r$  is the distance between atom), whereas the NOE follows a  $r^{-6}$  dependence. Therefore in RFDR, crosspeaks can be obtained faster even for shorter mixing times that help to save experiment time.

In this study, a series of RFDR experiments was recorded for POPC-d31-pirixinic acid derivative mixtures with mixing time from 5 ms to 125 ms. Figure 3-13 shows the lipid regions of both spectra of NOESY and RFDR of POPC-d31-2 mixture at 125 ms mixing time. At 125 ms, crosspeaks within the glycerol protons as well as within the lipid chain protons in the RFDR spectrum are more intense than in the NOESY spectrum. This fast buildup is expected due to the stronger distance dependence at the RFDR experiment. Therefore, magnetization transfer via dipolar coupling is faster than magnetization transfer via NOE, which explains the presence of more intense crosspeaks in RFDR spectra at short mixing times. Similar results were obtained for the lipid region of the spectra that are belonging to POPC-d31-3 mixture (not shown).

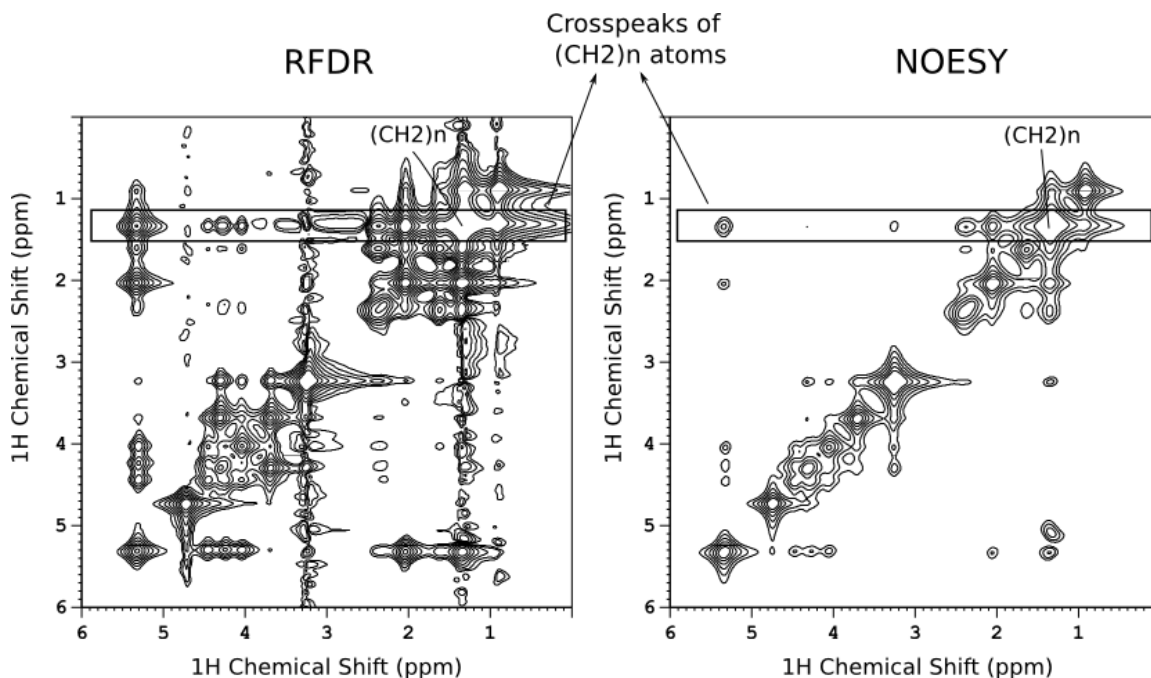


Figure 3-13: RFDR and NOESY spectra of POPC-d31 - 2 mixture for 125ms mixing time for both spectra at 300 K, inside the rectangulars, crosspeaks of large  $(CH_2)_n$  signal is highlighted.

Buildup curves for RFDR spectra were plotted after performing full matrix calculations (Chapter 1). In order to have a closer look to the buildup curves, resonance for large  $(CH_2)_n$  group was chosen and draw normalized intensities vs. mixing time plots for the diagonal peak and crosspeaks gathered from NOESY and RFDR spectra POPC-d31-2 mixture for the mixing times between 5-125 ms (Figure 3-14). This figure shows that the crosspeaks buildup at a much faster rate by using RFDR experiment. In addition, it is also clearly seen that, diagonal peaks decay faster in the case of RFDR than NOESY.

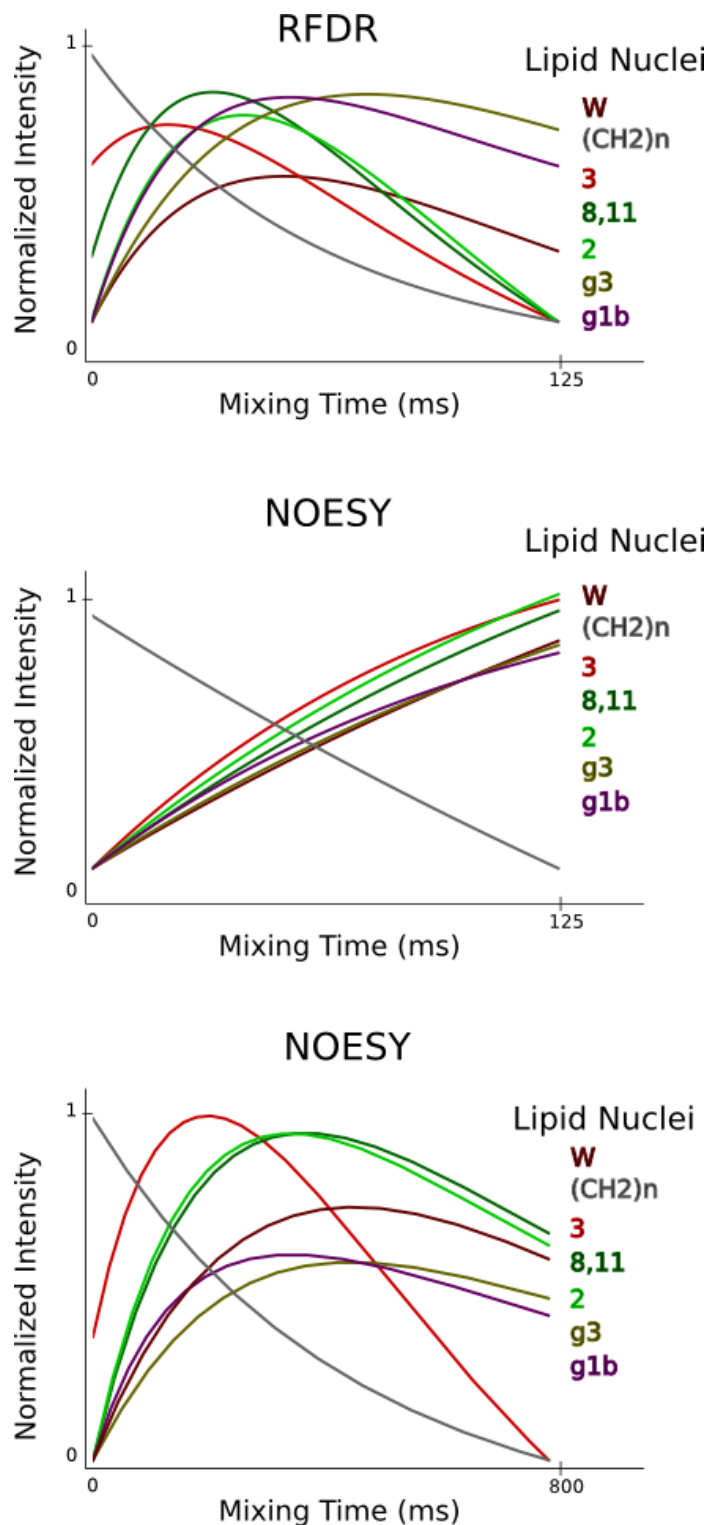


Figure 3-14: Buildup curves of diagonal-peak intensities for the resonance of  $(\text{CH}_2)_n$  and the crosspeak intensities with other lipid resonances from RFDR up to 125 ms (top), NOESY up to 125 ms (middle) and NOESY up to 800 ms (bottom) of POPC-d31 – 2 mixture at 300 K.



In addition to this, Figure 3-14 also shows that between 5-800 ms, NOESY crosspeaks buildup and diagonal peak decays in large extent compared with NOESY between 5-125 ms mixing time. Therefore, more time is needed for NOESY to observe buildup intensities. Cross relaxation rates of these atoms in the figure were also calculated for NOESY and RFDR experiments and depicted in Table 3-1. In average, the cross relaxation rates with RFDR experiments are about 7 fold higher than the cross relaxation rates with NOESY experiment. This also indicates that, RFDR provides faster magnetization transfer than NOESY experiment, as suggested by Aucoin et al (Aucoin, Camenares et al. 2009).

	Cross-Relaxation Rate with (CH <sub>2</sub> ) <sub>n</sub> Protons (1/s)					
Lipid Protons	18	8, 11	3	2	g3	g1b
NOESY	0.51	1.01	0.94	1.27	0.25	0.32
RFDR	6.13	9.53	7.74	4.23	0.94	1.11

*Table 3-1: Cross relaxation rates of lipid protons with the resonance of (CH<sub>2</sub>)<sub>n</sub> by NOESY and RFDR experiments for the POPC-2 mixture at 300 K.*

Distribution profiles for two compounds along the lipid axis by RFDR experiments were plotted in Figure 3-15 and Figure 3-16 for compound **2** and **3**, respectively. The data show a surprisingly high variation of cross relaxation rates by RFDR experiments. The differences in cross relaxation rates are larger for RFDR than for NOESY. Secondly, for both compounds, probability curves show that, interactions with hydrocarbon chain is significantly smaller than interactions with glycerol backbone. Consistent with NOESY data, it can be still observed that compound **3** shows more interactions with lipid acyl chain protons than compound **2**. However the differences in distribution profiles of two compounds are not significant as in the case of the NOESY experiments. It is known that

in the NOESY experiments magnetization transfer occurs mainly via intermolecular contact (Feller, Huster et al. 1999; Yau and Gawrisch 2000). In contrast of this, Aucoin et al showed that, in the RFDR experiments intramolecular crosspeaks are more intense than intermolecular crosspeaks (Aucoin, Camenares et al. 2009). This suggests that the NOESY experiment contains more information about lipid-substrate interactions than RFDR experiments since NOESY crosspeaks intensities are dominated intermolecular contacts. This might explain the different distribution profiles of both compounds obtained from RFDR experiments.

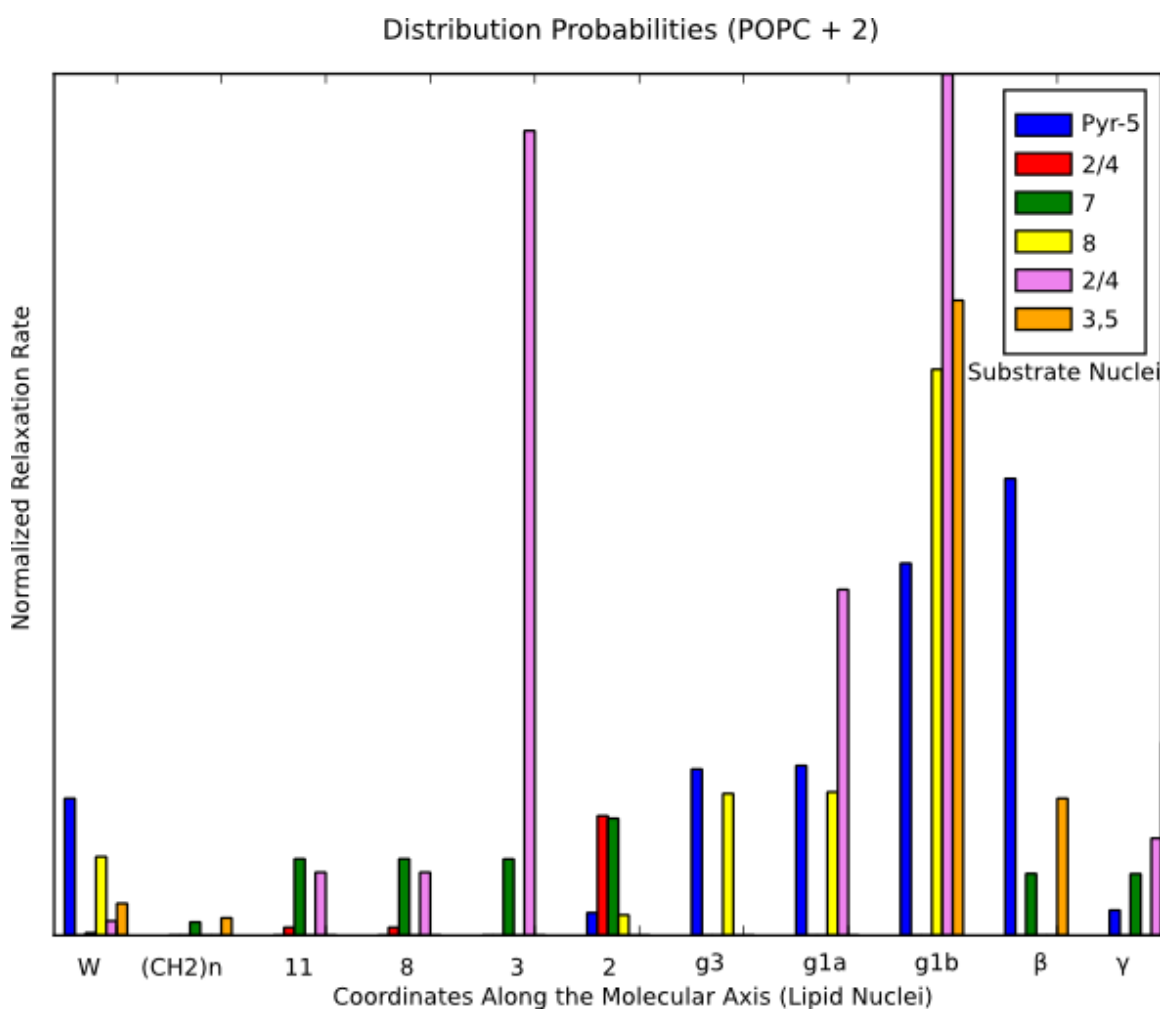


Figure 3-15: Distribution profiles of compound 2 inside POPC-d31 bilayer from  $^1\text{H}$ -MAS RFDR of the mixture of POPC-d31 with compound 2 at 300 K: in the figure legend, substrate protons at pyridine and quinoline rings were shown, 2 and 4 cannot be assigned, 3 and 5 are overlapped and other protons are well-resolved and assigned.

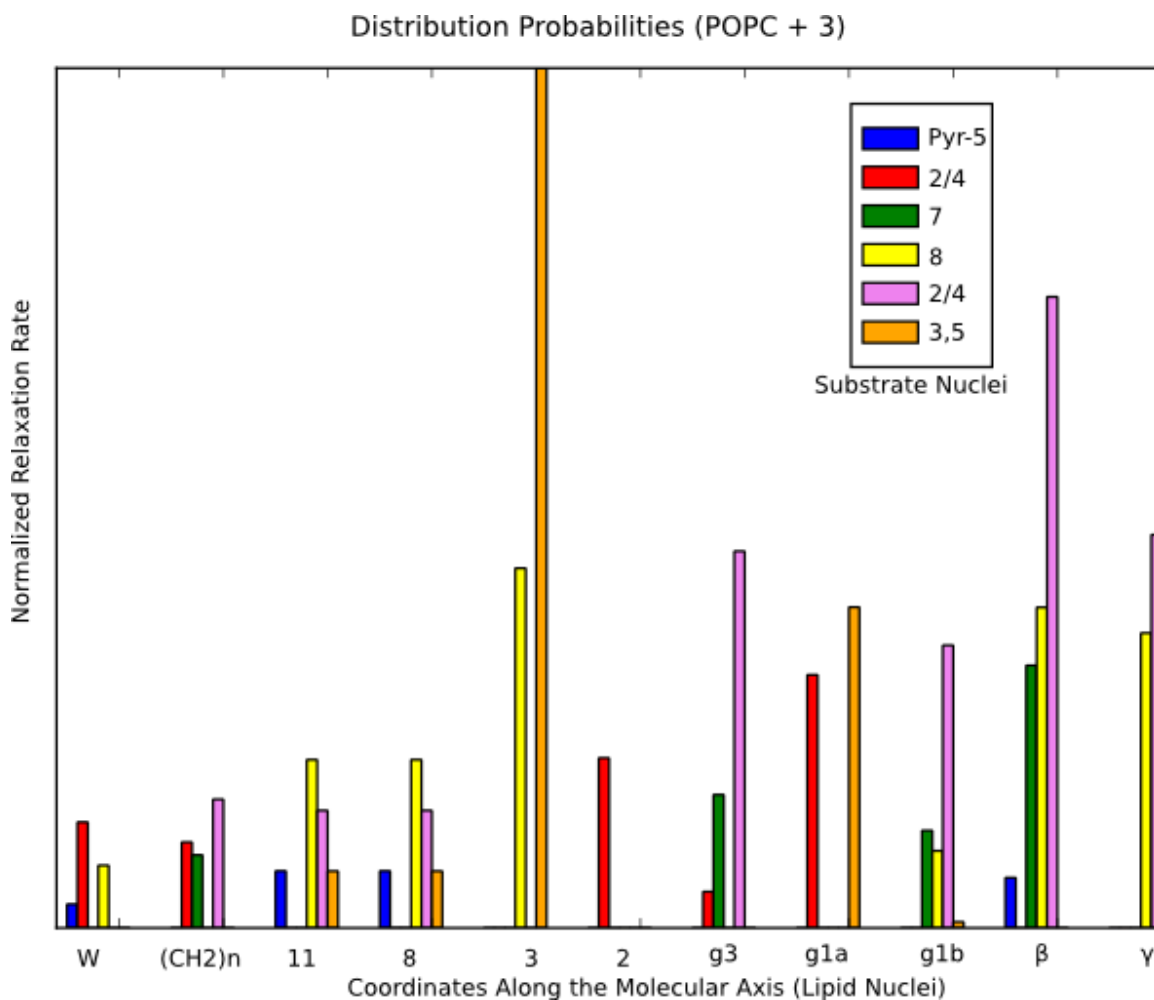


Figure 3-16: Distribution profiles of compound **3** inside POPC-d31 bilayer from  $^1\text{H}$ -MAS RFDR of the mixture of POPC-d31 with compound **3** at 300 K: in the figure legend, substrate protons at pyridine and quinoline rings were shown, 2 and 4 cannot be assigned, 3 and 5 are overlapped and other protons are well-resolved and assigned.

### 3.4 Molecular Dynamics

The aim of MD simulation was first to predict the behavior of compound **2** and **3** within the lipid bilayer and then to calculate their positions by using the NOESY peak intensities as constraints.

So far, distribution probabilities were calculated by full matrix-approach. It is also known that single mixing time can provide distribution probabilities (Holte and Gawrisch 1997; Huster, Arnold et al. 1999; Siarheyeva, Lopez et al. 2006). Although single-mixing time approach gives less accurate results than full-matrix approach, studies have shown that crosspeak intensities obtained by single mixing time method provide sufficient result in order to obtain distribution probabilities of substrates along the bilayer (Holte and Gawrisch 1997; Huster, Arnold et al. 1999; Siarheyeva, Lopez et al. 2006). Therefore,  $^1\text{H}$ -MAS NOESY peak intensities at 50 ms spectra were used to create constraints for MD calculations to find out distribution of substances along the lipid bilayer. Crosspeak intensities listed in Table 3-2 provide consistent result with cross relaxation rates (Figure 3-10 and Figure 3-11). Both crosspeak intensities and cross relaxation rate analysis showed that there are strong correlations between compound **2** and glycerol backbone of POPC whereas for compound **3**, correlations were mainly with hydrophobic tail of POPC.

The first difficulty was coming from the assignment of substrate's resonances. NOESY spectra assignments were obtained using NOESY crosspeaks and solution-state assignments in organic solvent (Popescu, Rau et al. 2007; Rau, Syha et al. 2008). It can be easily seen that quinoline and pyridine were well resolved. Thus, restraints for both rings were performed separately. However for the quinoline ring itself, the peaks for  $\text{H}_5$  and  $\text{H}_3$  overlapped at 8.7 ppm. Moreover, two peaks, at 7.3 and 8.1 ppm, couldn't be assigned. Both could belong to either  $\text{H}_2$  or  $\text{H}_4$ . Since there are many ambiguities in the chemical-shift assignment of substrates, it was not an easy task to decide about the position of restraints for MD calculations.

Firstly, for each substrate resonances, the most intense crosspeak to a lipid atom was determined from a 50 ms NOESY spectrum (Table 3-2). Second, largest crosspeak intensities for quinoline ring and pyridine ring were determined. Finally restraints were chosen according to the largest intensities that were highlighted as red in the table. Restrained sites of substrates were the same for compound **2** and **3**, namely  $\text{C}_3$  of quinoline ring and  $\text{C}_5$  of pyridine ring. Restrained sites of lipids for both substrates were

different since compound **2** has more correlation with glycerol backbone whereas compound **3** has more correlations to acyl chain protons. With the information of NOESY intensities (Table 3-2), for compound **2**, quinoline ring was restrained at the position of C<sub>3</sub> of lipid and pyridine ring was restrained at the position of C<sub>g3</sub>. For compound **3**, restrains were put in between quinoline of substrate and C<sub>8</sub> of lipid and in between pyridine of substrate and C<sub>3</sub> of lipids.

	Chemical Shift (ppm)	H <sub>18</sub>	H <sub>4-7, 12-17</sub>	H <sub>3</sub>	H <sub>8,11</sub>	H <sub>2</sub>	H <sub>γ</sub>	H <sub>β</sub>	H <sub>g3</sub>	H <sub>α, H<sub>g1a</sub></sub>	H <sub>g1b</sub>	H <sub>9,10, H<sub>g2</sub></sub>
<b>2</b> (Crosspeak intensities)												
Pyr-5	6.84			70		24			131	104		81
2/4	7.97			51					33			34
7	8.21			39					77	91		69
8	8.3			51					112	101		43
2/4	8.88			338					41			44
3,5	9			367					40			197
<b>3</b> (Crosspeak intensities)												
Pyr-5	6.64			91					61			
2/4	7.28			49	66							
7	7.71			34				32	57			
8	8			81					87			
2/4	8.11			289	182							
3,5	8.64			474	743	148						

Table 3-2: <sup>1</sup>H MAS NMR chemical-shifts of compound **2** and **3**; Crosspeak intensities between pirinixic acid derivatives and POPC for 50 ms mixing time (intensities were extracted by using CARA software); restrained sites are chosen by largest intensities highlighted in red.

The choice of the restraining force should be done carefully. It is important to have realistic forces as much as to have effective forces. In order to use optimum force constants several trials were performed. Firstly, very high force constants,  $1000 \text{ kJmol}^{-1}\text{nm}^{-2}$ , were chosen just to test the power of the restraint. With this force constant, the forces were too high for performing a realistic simulation. Then,  $10 \text{ kJmol}^{-1}\text{nm}^{-2}$  force constants were applied. However, this force was not enough to move the molecule towards the restrained site. After couple of trials it was decided to use  $100 \text{ kJmol}^{-1}\text{nm}^{-2}$  force constant that doesn't have too much force to be unrealistic but have enough effect to pull the molecule towards to restrained position.

Simulations were performed for four different conformations of substrates inside the POPC bilayer. For conformation 1 and 3, substrates were inserted perpendicular to bilayer surface by changing one lipid with substrate. For conformation 2, substrate was inserted parallel to the bilayer surface with the same method. Conformation 4 was prepared by deleting water molecules to create a hole inside bilayer and inserting substrates by fitting that hole. In Figure 3-17 and Figure 3-18, starting structures and final structures of 4 conformations for compound **2** and **3**, respectively, were displayed. It is observed that all the structures converged to a very similar structure for compound **2**. Orientation and the location of the substances for four boxes became quite similar after 100 ns simulations. For compound **3**, there are small differences in the location of substrates for 4 different boxes. This can be due to the small changes in the last snapshot of the simulation. Therefore, calculation of overall statistics of positions of substrate atoms along the bilayer throughout the trajectories can give more reliable results.

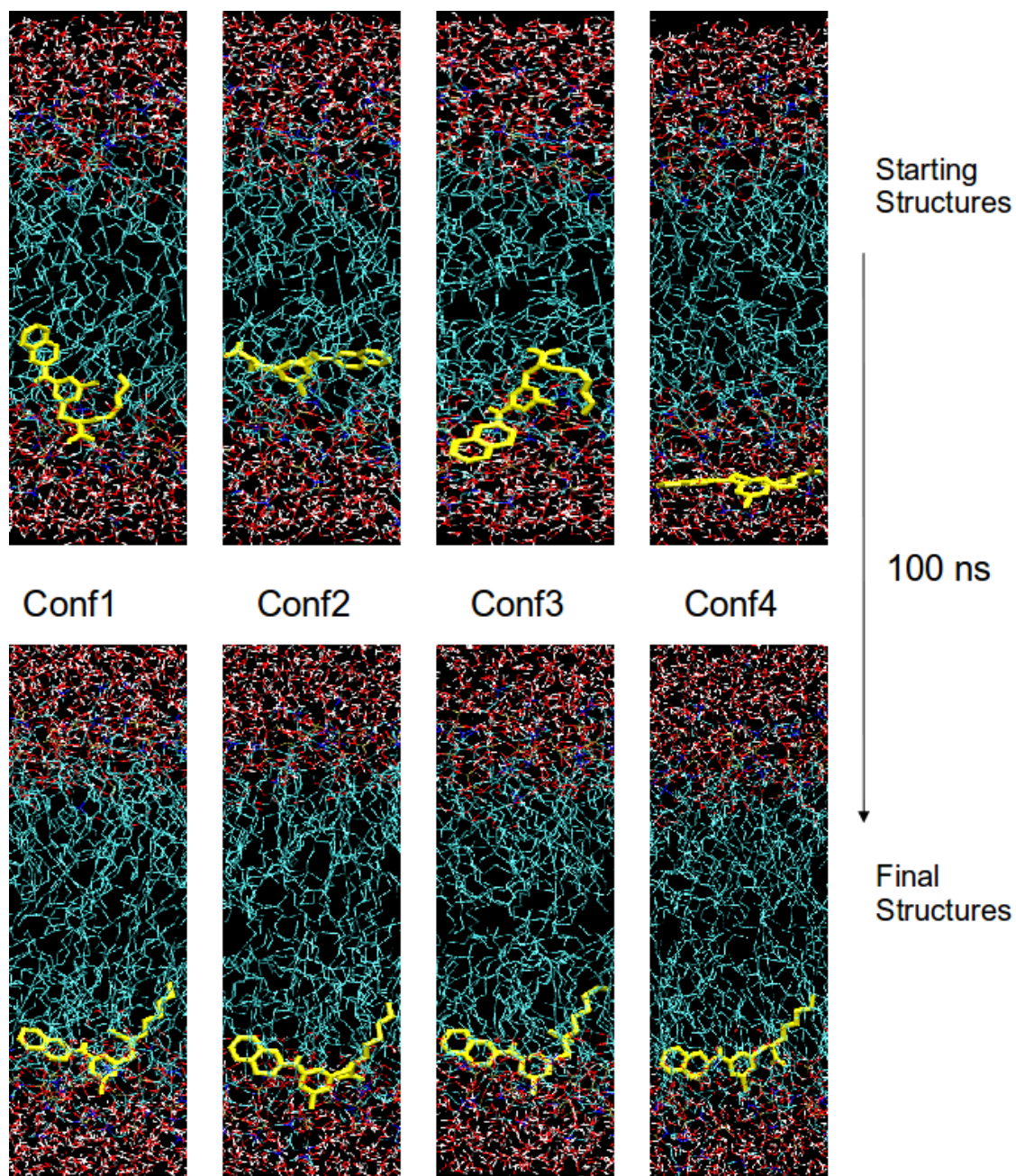


*Figure 3-17: Starting and final structures of POPC- compound 2 simulation boxes for 4 different conformations of 2 with respect to bilayer.*



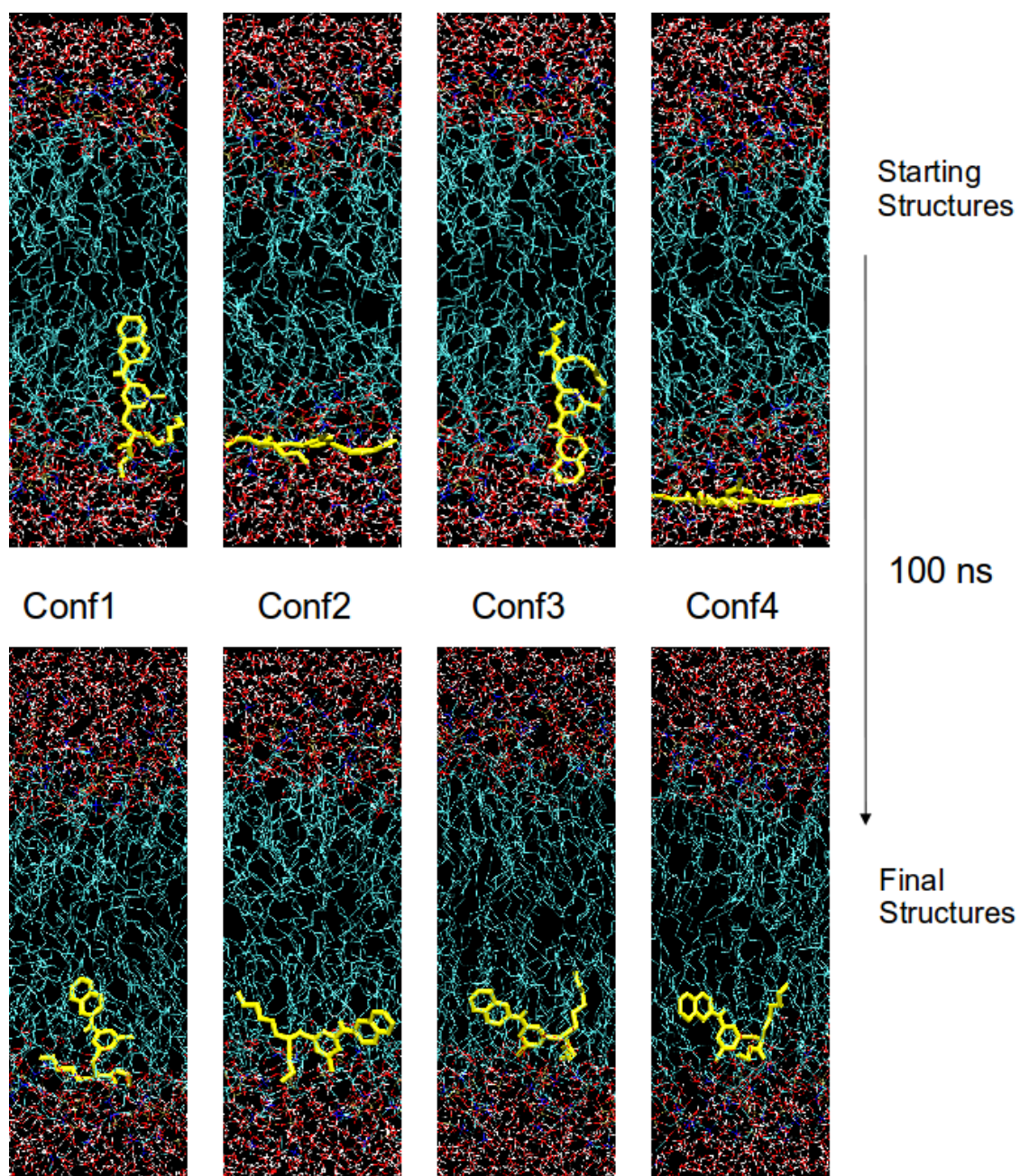


*Figure 3-18: Starting and final structures of POPC-compound 3 simulation boxes for 4 different conformations of 3 with respect to bilayer.*



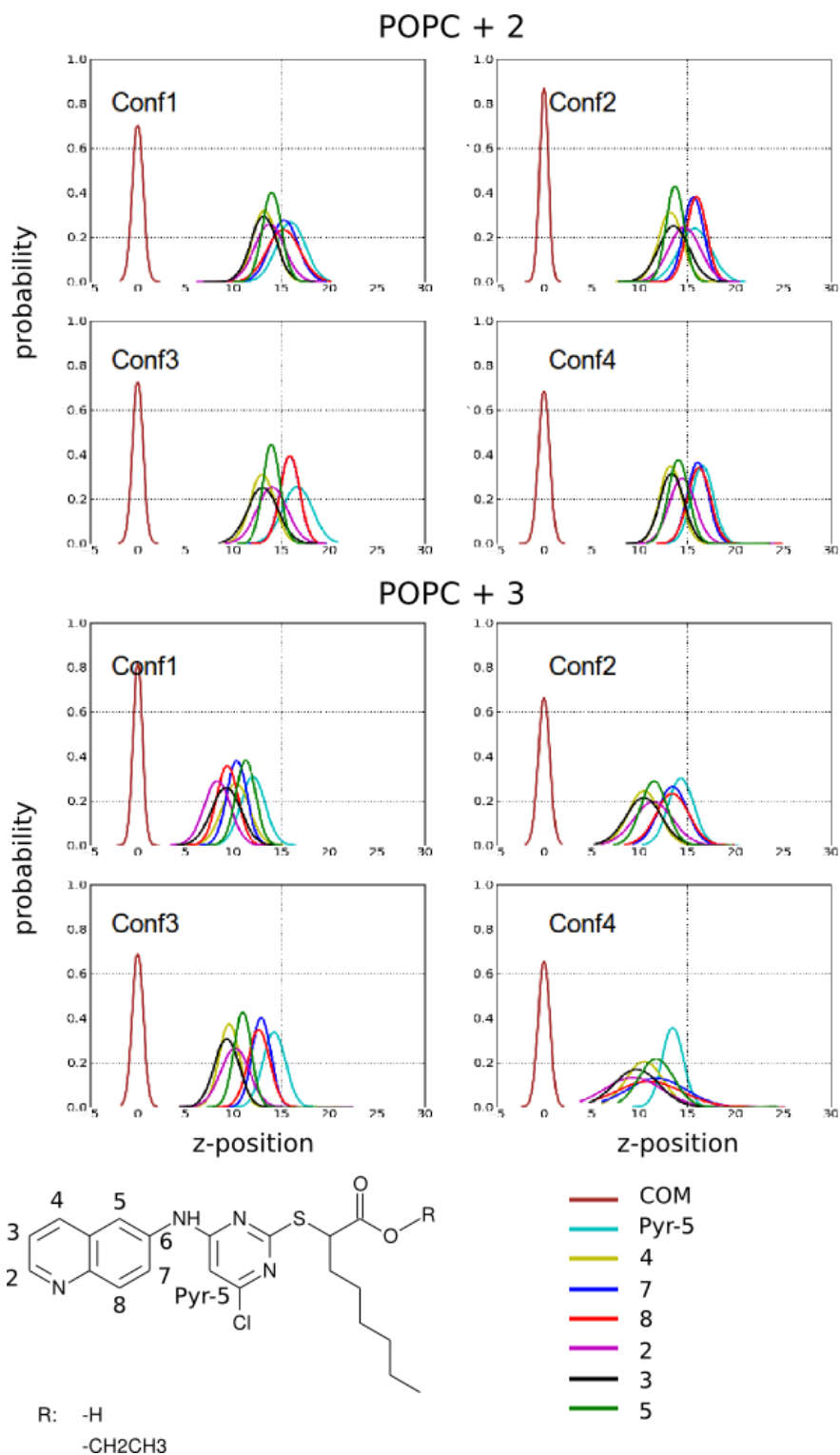


*Figure 3-19: Position distributions (Å) on z-direction of carbon atoms (names of atoms were labeled in the figure) of compound 2 and 3 with respect to bilayer center of mass (labeled as COM in the figure) for 4 different conformation of the molecules.*

Sample	<b>2</b>		<b>3</b>	
Carbon Atom Name	3	Pyr-5	3	Pyr-5
Restraint	14.4	18.15	9.76	14.4
1 <sup>st</sup> Conformation	13.17 ± 1.36	16 ± 1.50	9.23 ± 1.55	12.03 ± 1.29
2 <sup>nd</sup> Conformation	13.55 ± 1.61	15.75 ± 1.67	10.42 ± 1.88	14.31 ± 1.33
3 <sup>rd</sup> Conformation	13.06 ± 1.59	16.68 ± 1.56	9.29 ± 1.30	14.26 ± 1.19
4 <sup>th</sup> Conformation	13.37 ± 1.27	16.54 ± 1.14	9.65 ± 2.36	13.46 ± 1.13

*Table 3-3: Restraint coordinates at the beginning of simulations and average coordinates of restrained atoms throughout 100ns simulation of each conformation; coordinates were taken only for z-direction in Å unit and scaled with respect to center of mass of the bilayer.*

Figure 3-19 shows position probability distributions of aromatic atoms for two compounds with respect to the bilayer center of mass. Positions of atoms are similar for all the conformations and consistent with the restraint positions, which were set for the simulations. As can be easily seen from the figure, that atoms of compound **3** located more closely to the center of mass of bilayer than atoms of compound **2**. This finding, consistent with NMR data alone, indicates that average localization for compound **3** was towards hydrophobic core of the membrane whereas for compound **2** it was towards more interfacial part of membrane. Table 3-3 displays restraint coordinates that were extracted from 50 ns pure lipid simulation, and average coordinates of restraint atoms of pirinixic acid derivatives throughout 100 ns of simulation. Table shows that there is a variation in position of restrained atoms of compounds for different boxes. This indicates that force constants for the restraints were quite realistic, since it provided some flexibility for the restrained atoms. On the other hand, for all configurations, there were not large deviations from restrained positions.

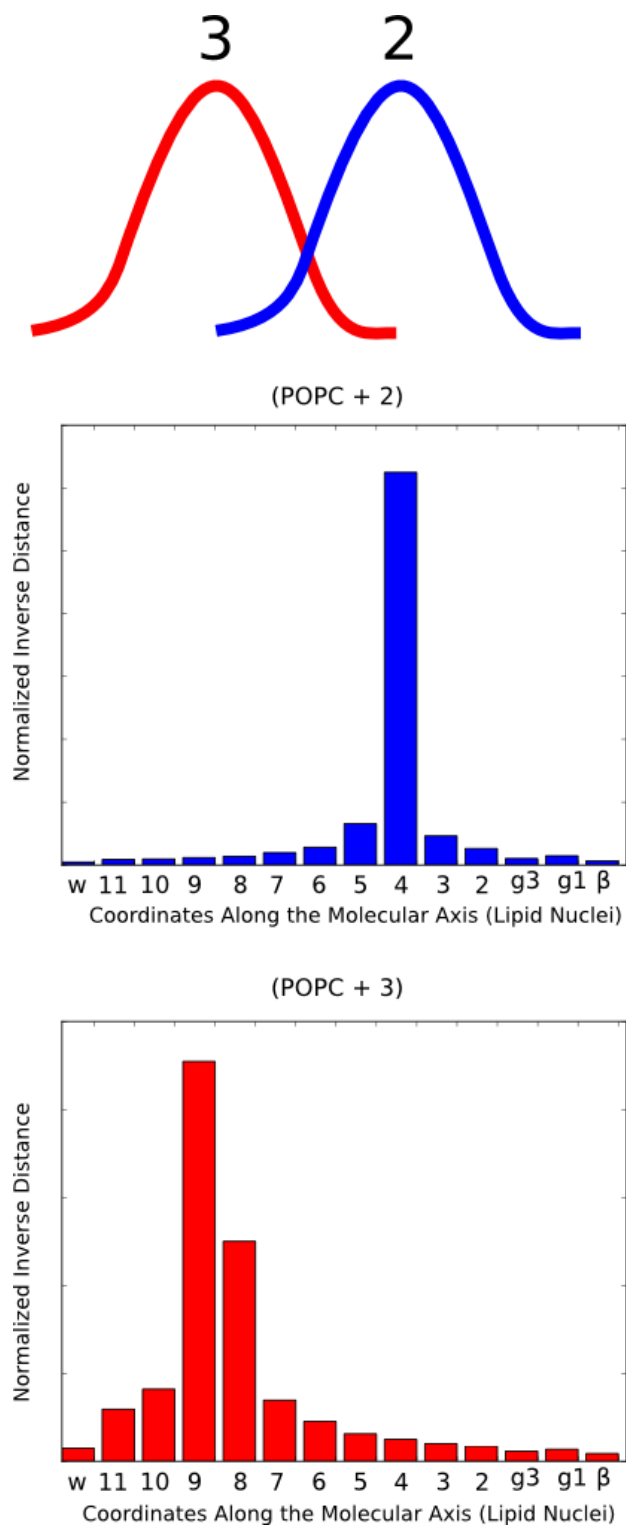
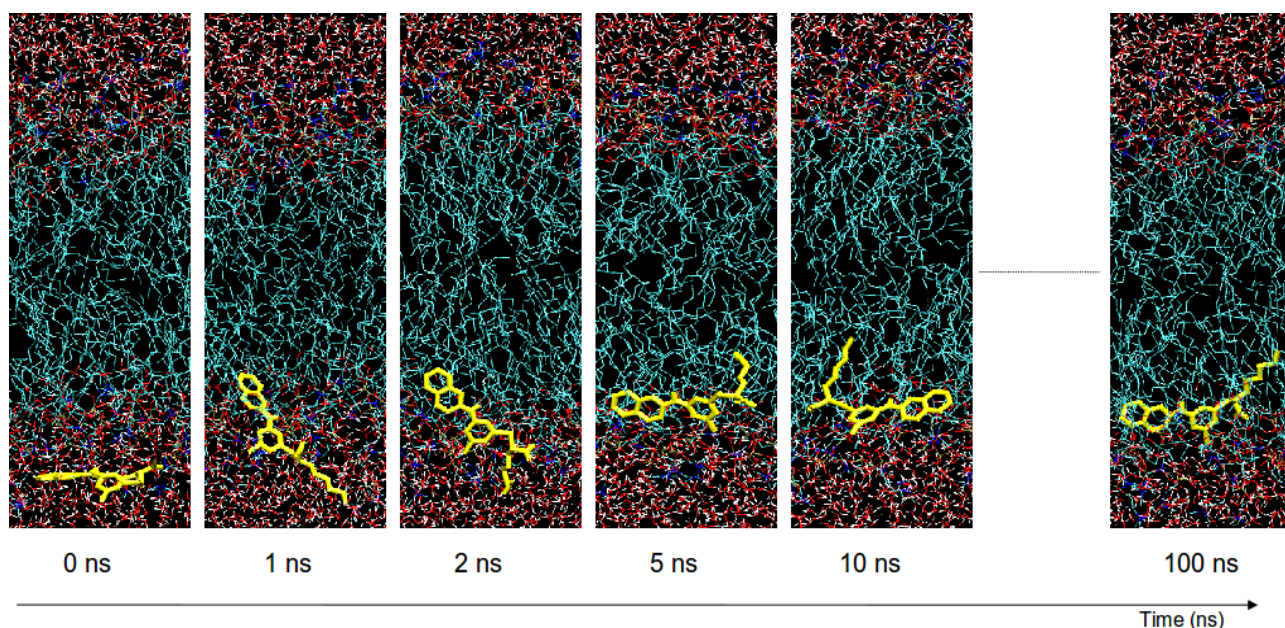


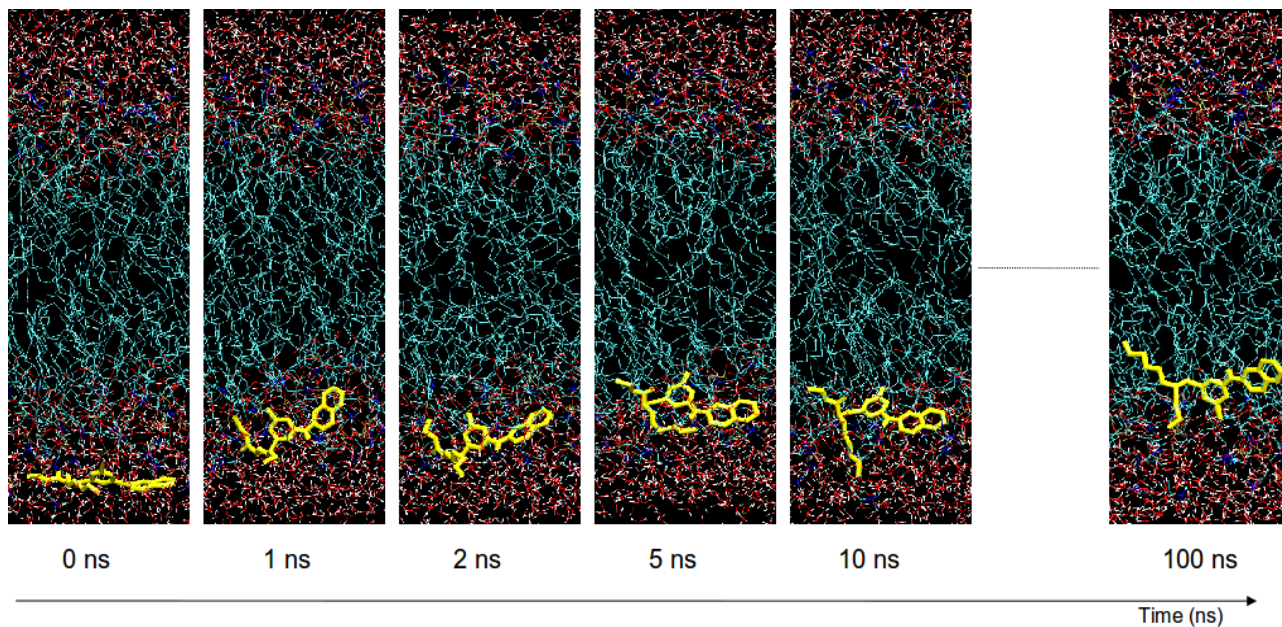
Figure 3-20: Normalized inverse distance on  $z$ -direction of simulation box between lipid atoms and carbon atom at position 3 of compound 2 (top) and 3 (bottom): calculations were done for the conformation-1, at the top of the figure, locations of 2 and 3 is represented.

Figure 3-20 displays inverse distance of carbon atom at position 3 of two compounds to the lipid atoms along the bilayer. Distances were calculated from average position of atoms at z-direction of the conformation-1 simulation box. In agreement with distribution profiles derived from NOESY relaxation rate data (Figure 3-12), Figure 3-20 showed that compound **3** is located at more inner parts of hydrocarbon chain of bilayer than compound **2**.



*Figure 3-21: Snapshots of the trajectory that show compound **2** partitioning inside POPC bilayer, partition occurs within 10 ns.*

It was also possible to monitor insertion of both compounds into the bilayer from the snapshots of trajectories of conformation-4 simulation boxes as depicted in Figure 3-21 and Figure 3-22. Insertion was so fast that, at first 10 nanoseconds, both compounds were already inserted inside the bilayer. Since both compounds were known to be very hydrophobic (they have very high partition coefficients), such a rapid insertion was expected. Hydrophobicity of two compounds as well as the application of NOE restraints resulted fast partition of substrates.



*Figure 3-22: Snapshots of the trajectory that show compound 3 partitioning inside POPC bilayer, partition occurs within 10 ns.*

### **3.5 Conclusion**

Overall results, that were gathered from both  $^1\text{H}$  chemical-shifts, 2D  $^1\text{H}$ -MAS correlation experiments, indicated that compound **3** was inserted more deeply into membrane than compound **2**. Both NOESY and chemical shift difference analysis showed that compound **3** has interactions with hydrophobic lipid chains whereas compound **2** had more interactions with the glycerol backbone. RFDR experiment provides faster magnetization but it is dominated by intra-molecular interactions. Therefore RFDR could not be used as alternative method to NOESY.

The combined usage of solid state NMR and theoretical calculations provides a more complete data insight into the lipid interaction at both substrates. It was already revealed

by NMR studies that compound **3** stays inside membrane more deeply than **2** (Figure 3-12). Molecular dynamics simulations, which were applied by using the distance information obtained from  $^1\text{H}$ -MAS NOESY intensities, also revealed statistically that both compounds **2** and **3** inserted into the bilayer quickly. **3** had stayed more close to the center of bilayer compared to **2** as consistent with NMR results. The difference in the location of two substrates can be seen easily from statistical calculations as well as from snapshots of trajectories. For future studies, location differences of these two compounds along the lipid bilayers may help to understand the differences in the potency of these two compounds on suppression of 5-LO and mPGES-1 product formation.

## 4 Characterization of Drug – Lipid Complexes by Solid-State NMR

### 4.1 Introduction

Development of drug-lipid complexes is becoming an important research area in drug design. There are different motivations for introduce drug-lipid complexes. One aim is to increase the bioavailability of drugs, which are either large in size or have low lipid solubility (Bombardelli, Curri et al. 1989; Jain, Gupta et al. 2010; Semalty, Semalty et al. 2010). Another goal of developing drug-lipid complex is to decrease gastrointestinal toxicity of non-steroidal anti-inflammatory drugs (NSAIDs) (Lichtenberger, Wang et al. 1995; Anand, Romero et al. 1999).

Figure 4-1 shows three commonly used NSAIDs structures. NSAIDs are widely used for the treatment of inflammation. They act as cyclooxygenase (COX) inhibitor and prevent prostaglandin synthesis (Funk 2001). However, NSAIDs have been reported to cause many side effects on gastrointestinal and cardiovascular systems (Jones, Rubin et al. 2008). These side effects may become even severe in case of long-term usage. Studies have shown that NSAIDs users suffer a 3-4 times more higher risk of gastrointestinal health problems compared to non-users (Gabriel, Jaakkimainen et al. 1991).

There were several studies to investigate the mechanisms of the side effects of NSAIDs (Ivey, Paone et al. 1980; Ligumsky, Golanska et al. 1983; Abramson, Korchak et al. 1985; Langenbach, Morham et al. 1995; Rainsford 2007). It is known that NSAIDs have an impact on arachidonic acid cascade (Figure 3-1) by inhibiting COX enzyme and as a result reducing prostaglandin (PGs) synthesis (Abramson, Korchak et al. 1985). Since PGE<sub>2</sub> is related with inflammation, inhibition of COX enzyme reduces inflammation. However, other PGs (PGI<sub>2</sub> and PGF<sub>2 $\alpha$</sub> ) have important functions on homeostasis. Therefore inhibition of their formation by NSAIDs causes gastrointestinal side effects (Rainsford 2007).

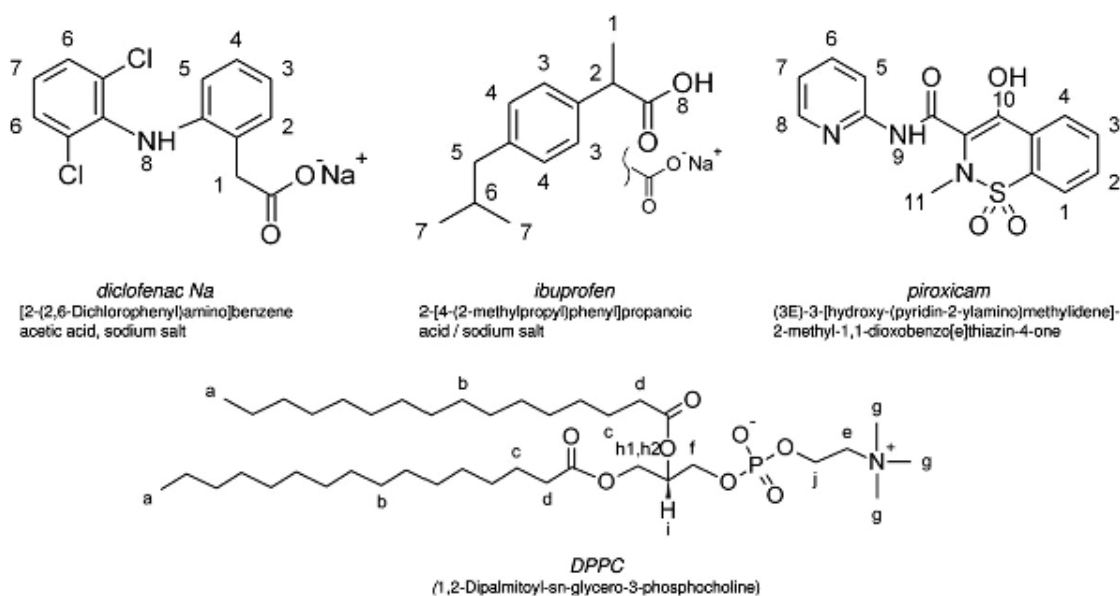


Figure 4-1: Structure and nomenclature of DPPC and drugs used in this study.

NSAIDs toxicity on gastrointestinal surface is not only related with COX enzyme inhibition. There are many evidences that NSAIDs have direct effects on gastrointestinal mucosa (Ivey, Paone et al. 1980; Ligumsky, Golanska et al. 1983; Langenbach, Morham et al. 1995). It was also shown that NSAIDs have interactions with phospholipids (Lichtenberger, Wang et al. 1995; Lucio, Bringezu et al. 2008; Moreno, Garidel et al. 2009). These interactions are known to cause disruption of phospholipids membrane on the surface of gastrointestinal mucosa and consequently protective hydrophobic layer on the mucosa is damaged (Lichtenberger, Zhou et al. 2006). In the light of these findings, the idea of preventing the injury of mucosa layer by administration of NSAIDs drugs as a preassociated lipid-drug complex (Anand, Romero et al. 1999). It has been reported that toxicity has decreased significantly ones NSAIDs have been applied in complex with lipids (Anand, Romero et al. 1999).



Although there have been several studies on these drug-lipid complexes (Lichtenberger, Wang et al. 1995; Anand, Romero et al. 1999), it is not clear yet whether NSAIDs complexed with lipids or whether they exist in isolated form inside liposomes. Studies with different techniques showed that diclofenac and ibuprofen, which are two widely used NSAIDs, are interacting with the phosphorus head group of lipids and in case of diclofenac, it was found that diclofenac changes the phase transition of lipids causing the formation of small unilamellar vesicles (Panicker, Sharma et al. 1995; Lopes, Scarpa et al. 2004; Lucio, Bringezu et al. 2008; Moreno, Garidel et al. 2009). Hence, these studies show some evidence on formation of drug-lipid complexes.

#### **4.1.1 Objectives**

It is very important to decrease side effects of NSAIDs on gastrointestinal and cardiovascular systems especially for prolonged uptake of drugs. Since it was revealed that uptake of NSAIDs in the form of lipid mixtures decreases side effects, the structural characterization of NSAIDs in liposomes is necessary to understand this effect of decrease in toxicity of drugs. Solid state NMR is a very convenient tool to investigate interactions between NSAIDs and phospholipids as well as the effects of NSAIDs on the phase transitions of membranes. It is known that the administration of NSAIDs as associated with DPPC decreased gastrointestinal damage of NSAIDs (Lichtenberger, Wang et al. 1995; Khazaeinia and Jamali 2003). Therefore, in this study, the interactions between drugs and DPPC are investigated (Huesch, Dutagaci et al. 2011). Solid state NMR was used to reveal the interactions of diclofenac, ibuprofen and piroxicam with DPPC liposomes.

## **4.2 Materials and Methods**

### **4.2.1 Sample Preparation**

1,2-dipalmitoyl-sn-glycero-3-phosphocholine (DPPC) and drug-lipid complexes (DPPC-NSAIDs, namely ibuprofen, diclofenac and piroxicam) were kindly provided by Jan Husch from Central Laboratory of German Pharmacists. Pure DPPC and 1:1/ DPPC: NSAID (molar ratio) mixtures were used for measurements. Mixtures were prepared by refluxing them in dichloromethane for three hours around 45° (not exceeding it). Then, solvent was evaporated overnight. After this step, dried mixtures were hydrated with H<sub>2</sub>O and lyophilized after hydration. For solid-state NMR measurements 20 mg of lyophilized drug-lipid mixtures were rehydrated in 10 µL D<sub>2</sub>O and transferred to 4 mm NMR rotors.

### **4.2.2 Solid State NMR**

All experiments were carried out with Bruker AVANCE 400 MHz spectrometer and a 4 mm DVT MAS probehead. Spinning rate was set to 12 kHz for <sup>1</sup>H-MAS NMR measurements. <sup>1</sup>H-MAS NOESY experiments were recorded with 4096 data-points and 512 increments. NOESY experiments were recorded at 320 K. <sup>1</sup>H NMR spectra were referenced to DSS via <sup>13</sup>C chemical shifts of adamantane. <sup>31</sup>P NMR static spectra were taken by using direct polarized Hahn echo experiment at 315 K. Chemical shift referencing was done with respect to H<sub>3</sub>PO<sub>4</sub>. Simulations of spectra were done by using Topspin 2.1 software (Bruker, Karlsruhe).

### 4.3 Results and Discussion

#### 4.3.1 1D <sup>1</sup>H MAS NMR

The structures of Diclofenac, Piroxicam, Ibuprofen and DPPC are shown in Figure 4-1. 1D <sup>1</sup>H MAS-NMR spectra of DPPC and Diclofenac, Piroxicam and Ibuprofen in mixture with DPPC are shown in Figure 4-2. Spectra are labeled according to Figure 4-1. Drug resonances of aromatic protons are found between 6 and 8 ppm. At 320 K, which is above phase transition temperature, 41°C, and 12 kHz sample rotation, well-resolved <sup>1</sup>H spectra are obtained as expected for a fluid phase lipid bilayer.

DPPC atoms	a	b	c	d	e	f	g	h <sub>1</sub>	h <sub>2</sub>	i	j
DPPC	0.91	1.33	1.63	2.37	3.70	4.02	3.26	4.31	4.44	5.29	4.44
Chemical shift difference (+diclofenac)	0.00	-0.02	-0.13	-0.15	-0.31	0.00	-0.27	n.a.	n.a.	-0.02	-0.06
Chemical shift difference (+ibuprofen)	0.00	-0.01	-0.05	-0.09	-0.06	0.01	-0.06	n.a.	n.a.	0.00	n.a.
Chemical shift difference (+piroxicam)	0.00	-0.02	-0.02	-0.02	-0.01	-0.01	-0.01	-0.01	-0.02	-0.01	-0.02
Piroxicam atoms	1	2	3	4	5	6	7	8	9	10	11
+DPPC	n.a.	7.83	7.83	7.98	8.09	7.83	7.26	8.46	n.a.	n.a.	n.a.
Diclofenac atoms	1	2	3	4	5	6	7	8	9		
+DPPC	3.61	7.26	6.76	6.85	6.32	7.22	6.85	n.a.			
Ibuprofen atoms	1	2	3	4	5	6	7	8	9		
+DPPC	1.4	3.66	7.21	7.03	2.42	1.83	0.89	n.a.			

Table 4-1: Assignment of DPPC and drugs and chemical shift differences of <sup>1</sup>H MAS NMR of DPPC in the presence of drugs; n.a.: not assignable, chemical shifts are given in ppm.

First, the effect of drugs on the lipid resonances was analyzed. While no significant change on the  $^1\text{H}$  linewidths was observed, chemical shift changes were detected. Chemical shift differences of lipids for drug-lipid mixtures and chemical shift of drugs in mixture with DPPC are summarized in Table 4-1. In the presence of diclofenac sodium,  $^1\text{H}$  chemical shifts of DPPC were mainly changed for lipid chain protons (c  $\Delta\delta$ -0.13 ppm and b d  $\Delta\delta$ -0.15 ppm) and head group (e  $\Delta\delta$ -0.31 ppm, g  $\Delta\delta$ -0.27 ppm) (Table 4-1, Figure 4-2). In addition,  $^1\text{H}$  NMR spectrum of DPPC-Diclofenac mixture gave information about conformations of lipids. Quaternary ammonium proton resonance split in the presence of diclofenac (Figure 4-2). This might be due to the existence of two different conformations. Formation of small and large sized lipid vesicle may cause the splitting in chemical shifts of the quaternary protons.

For the case of ibuprofen, the interactions with lipid were weaker compared with diclofenac. Chemical shift changes were mainly occurred only at lipid chains (e.g. d  $\Delta\delta$ -0.09 ppm) instead of head group. There was no detection of splitting at the quaternary ammonium peak. This suggests that, only bigger sized lipid vesicles were obtained in the presence of ibuprofen.

In the presence of piroxicam, no significant change in 1D spectrum was observed. Maximum change in chemical shift was not exceeding 0.02 ppm. This suggests that interactions between piroxicam and DPPC are too low to be observed in 1D  $^1\text{H}$  NMR spectrum.

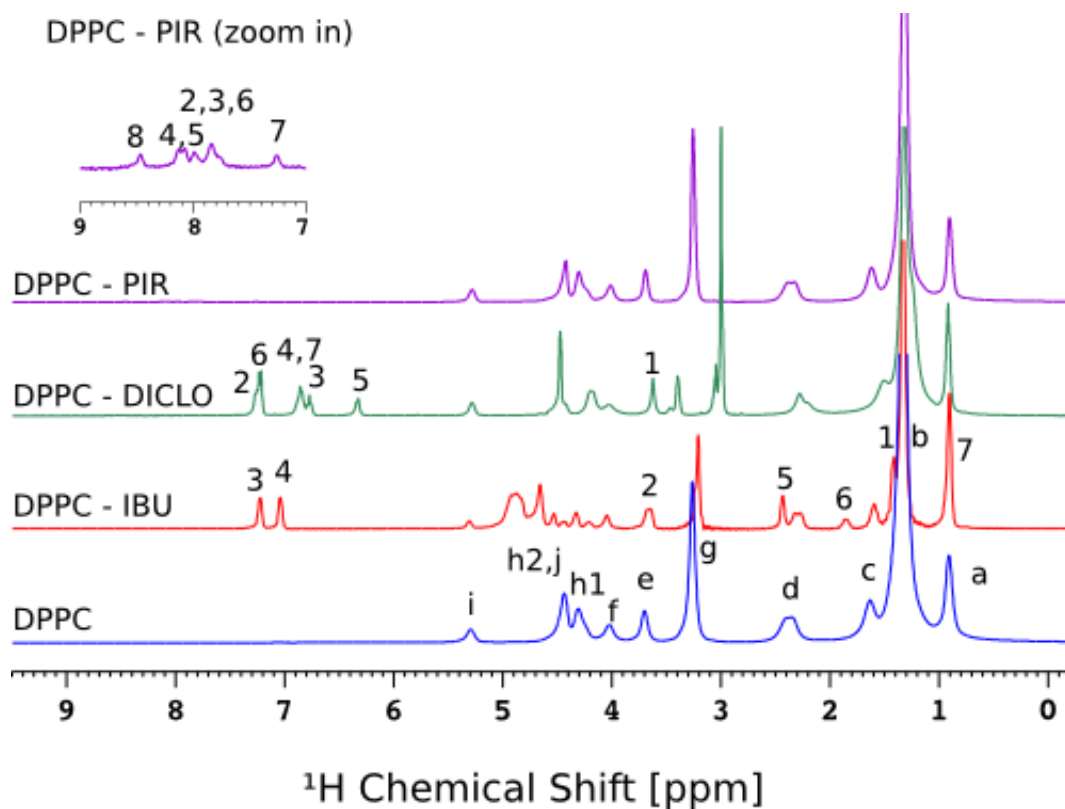


Figure 4-2:  $^1\text{H}$  NMR spectra of DPPC and mixtures of DPPC with ibuprofen (DPPC-IBU), diclofenac (DPPC-DICLO) and piroxicam (DPPC-PIR) at 320 K with 12 kHz spin rate and 16 scan number.

### 4.3.2 $^1\text{H}$ - $^1\text{H}$ -MAS NOESY NMR

To obtain direct evidence for drug-lipid interactions,  $^1\text{H}$ - $^1\text{H}$ -MAS NOESY NMR experiments as introduced in Chapter 1 and 2 were conducted. A NOESY spectrum of DPPC is shown in Figure 4-3 and a comparison of NOESY spectra of all drug-lipid complexes is shown in Figure 4-4, Figure 4-5 and Figure 4-6 for mixing times 200 ms, 400 ms and 800 ms, respectively.

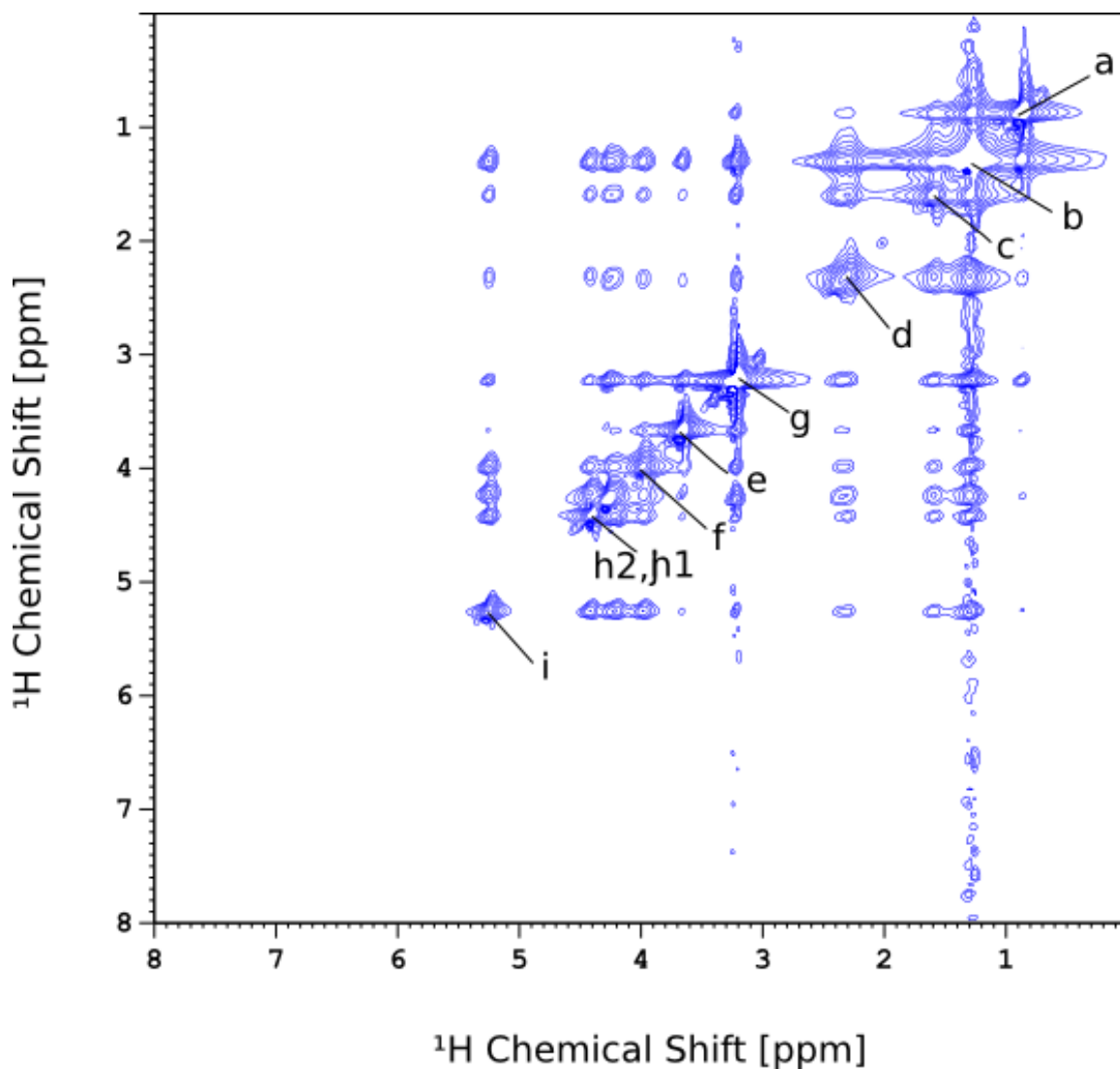


Figure 4-3:  $^1\text{H}$  MAS NOESY spectra of DPPC; spectrum were recorded at 320 K with 12 kHz spin rate and 16 scan with 300 ms mixing time.

The 2D NOESY (Figure 4-4, Figure 4-5 and Figure 4-6) spectra of diclofenac-DPPC mixture show that, there were crosspeaks of aromatic protons of diclofenac with quaternary ammonium groups and lipid tail protons as highlighted in the figure. The significant crosspeaks between DPPC and diclofenac indicate that diclofenac have strong interactions with DPPC.

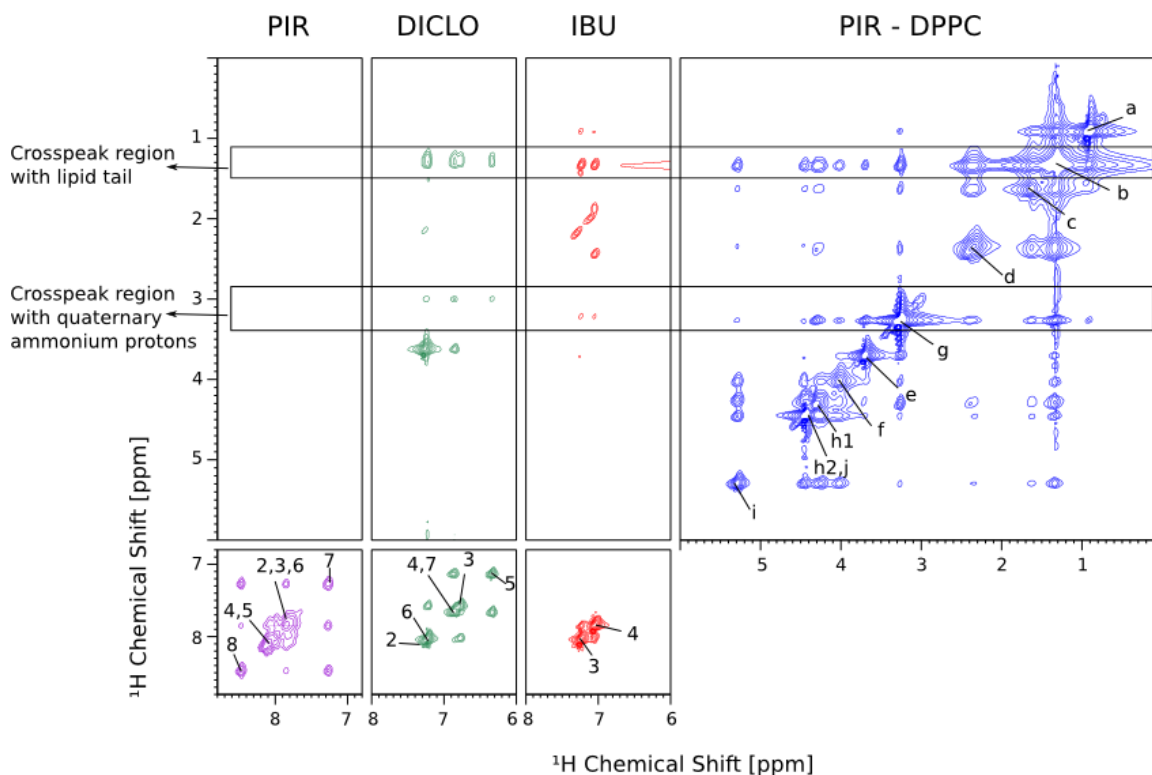


Figure 4-4:  $^1\text{H}$  MAS NOESY spectra of Piroxicam (PIR), Diclofenac (DICLO) and Ibuprofen (IBU), DPPC-Piroxicam (PIR-DPPC) spectra were chosen to show the lipid region; spectra were recorded at 320 K with 12 kHz spin rate and 16 scan with 200 ms mixing time.

Crosspeaks between ibuprofen and lipid were also quite high as in the case of diclofenac. This supports that similar to diclofenac ibuprofen has interactions with DPPC. These findings suggest that both diclofenac and ibuprofen are incorporated inside DPPC liposomes and may form drug-lipid complex.

On the other hand, in NOESY spectra, there were almost no crosspeak between lipid and piroxicam. This suggests that piroxicam tends to stay precipitated in the mixture instead of interacting with DPPC.

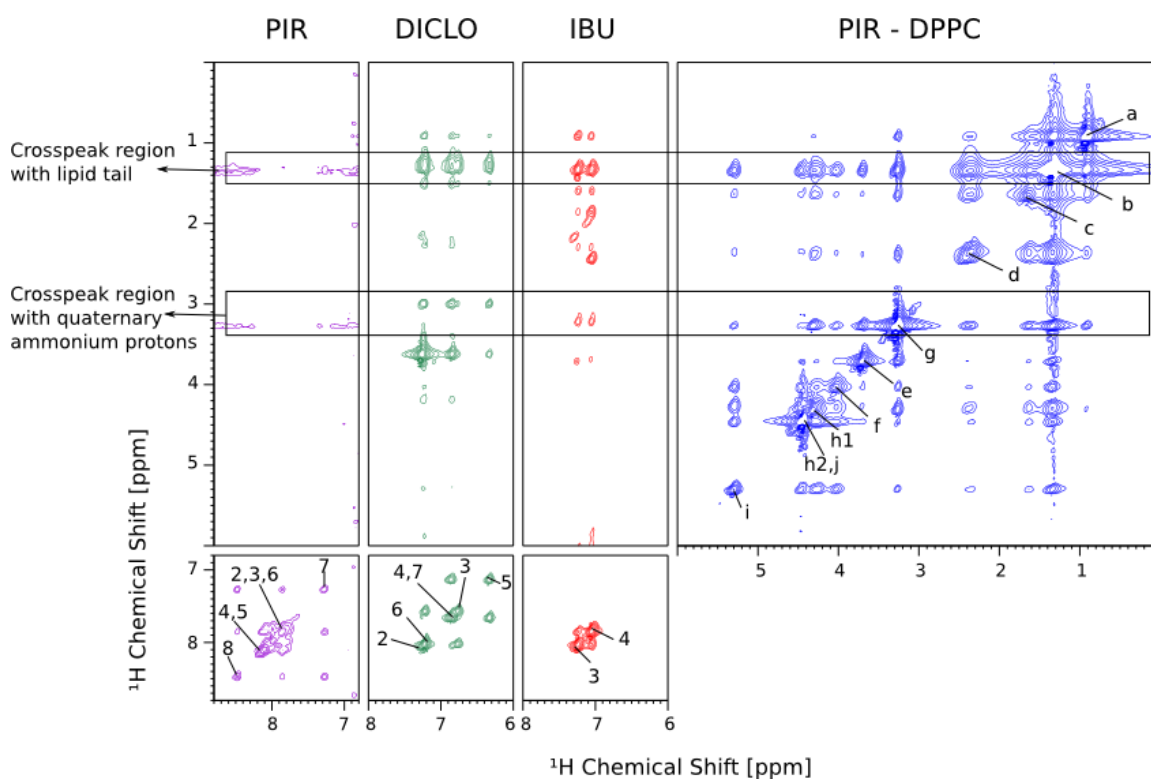


Figure 4-5:  $^1\text{H}$  MAS NOESY spectra of Piroxicam (PIR), Diclofenac (DICLO) and Ibuprofen (IBU), DPPC-Piroxicam (PIR-DPPC) spectra were chosen to show the lipid region; spectra were recorded at 320 K with 12 kHz spin rate and 16 scan with 400 ms mixing time.



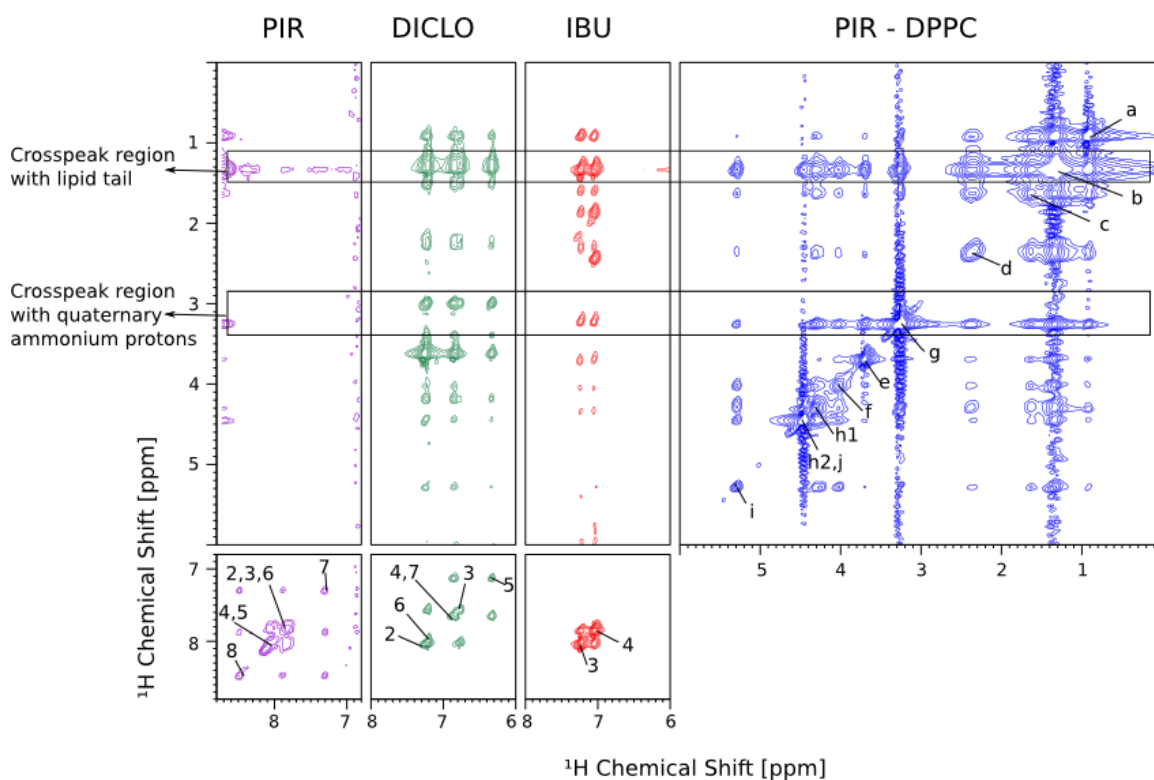


Figure 4-6:  $^1\text{H}$  MAS NOESY spectra of Piroxicam (PIR), Diclofenac (DICLO) and Ibuprofen (IBU), DPPC-Piroxicam (PIR-DPPC) spectra were chosen to show the lipid region; spectra were recorded at 320 K with 12 kHz spin rate and 16 number with 800 ms mixing time.

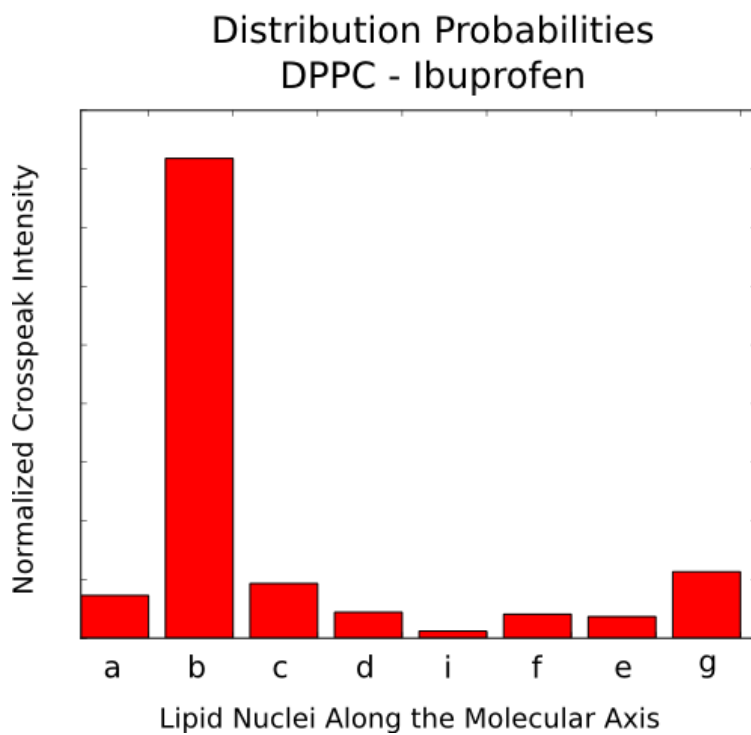
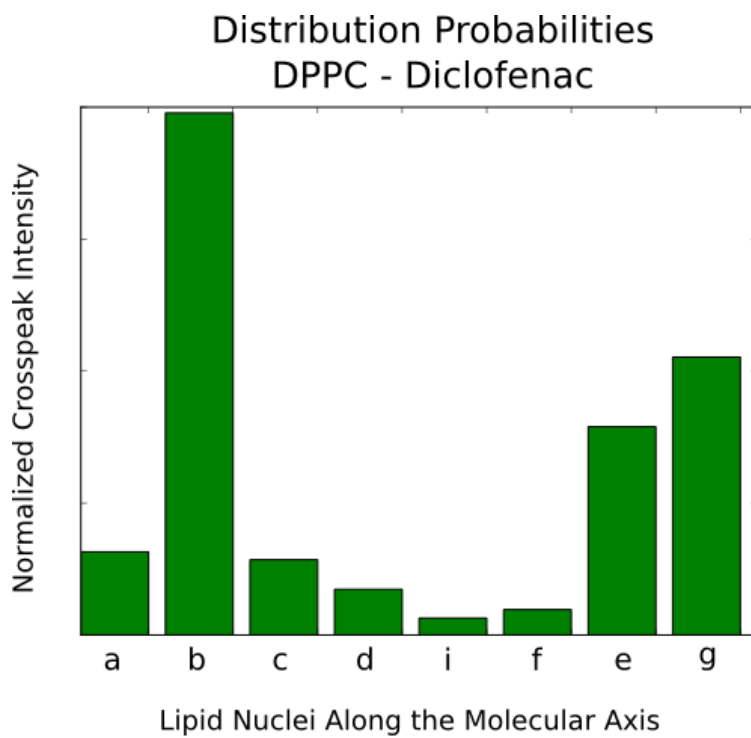


Figure 4-7: Distribution probabilities of diclofenac (5-H) and ibuprofen (4-H) along DPPC bilayer derived from  $^1\text{H}$ -MAS NOESY crosspeak intensities: at 320 K and 400 ms mixing time.

Figure 4-7 shows distribution probabilities of diclofenac and ibuprofen along the lipid bilayer. Probabilities were found from crosspeak intensities of 5-H proton of diclofenac and 4-H of ibuprofen with lipid protons from the NOESY spectra with 400 ms mixing time. Distribution probabilities can not be found for piroxicam since it didn't show significant crosspeaks with DPPC. As Figure 4-7 depicted, both diclofenac and ibuprofen has contact with lipid alkyl chain protons. In addition to this, diclofenac has interactions with also quaternary ammonium protons (g). This data suggests, in agreement with chemical shift differences, diclofenac has an effect on phosphocholine headgroup of DPPC.

### 4.3.3 Static $^{31}\text{P}$ -NMR Spectroscopy

Solid-state  $^{31}\text{P}$  NMR measurements were done on pure DPPC and drug-lipid complexes to get information about the lipid bilayer phase in the presence of drugs. At 315 K, DPPC stays in its liquid-crystalline phase.  $^{31}\text{P}$  spectra were recorded without spinning the samples. Chemical shift anisotropy ( $\delta\text{CSA}$ ) and asymmetry parameters ( $\eta$ ) were calculated from the lineshape. Both experimental and simulated spectra of four samples were displayed in Figure 4-8.

In the presence of piroxicam, the  $^{31}\text{P}$  spectra were almost identical to pure lipid ( $\delta\text{CSA} = 29$  ppm,  $\eta = 0$ ). In the case of diclofenac, lineshape of the spectrum didn't change significantly but  $\delta\text{CSA}$  reduced to 25 ppm. This indicated that diclofenac destabilizes the lipid phase. Upon addition of ibuprofen, more significant changes in  $^{31}\text{P}$  spectrum were observed. Lineshape of the spectra were largely changed that can be described by existence of two phases. One (68%) has chemical shift anisotropy of  $\delta\text{CSA} = 21$  ppm and asymmetry parameter of  $\eta = 0.2$ , and the other (32%) has chemical shift anisotropy of  $\delta\text{CSA} = 8$  ppm and asymmetry parameter of  $\eta = 1.0$ .

Results from static  $^{31}\text{P}$  NMR experiments revealed that ibuprofen and diclofenac have

significant effects on DPPC phase behavior whereas piroxicam has almost no effect. This is consistent with the previous data obtained from  $^1\text{H}$  NMR measurements.

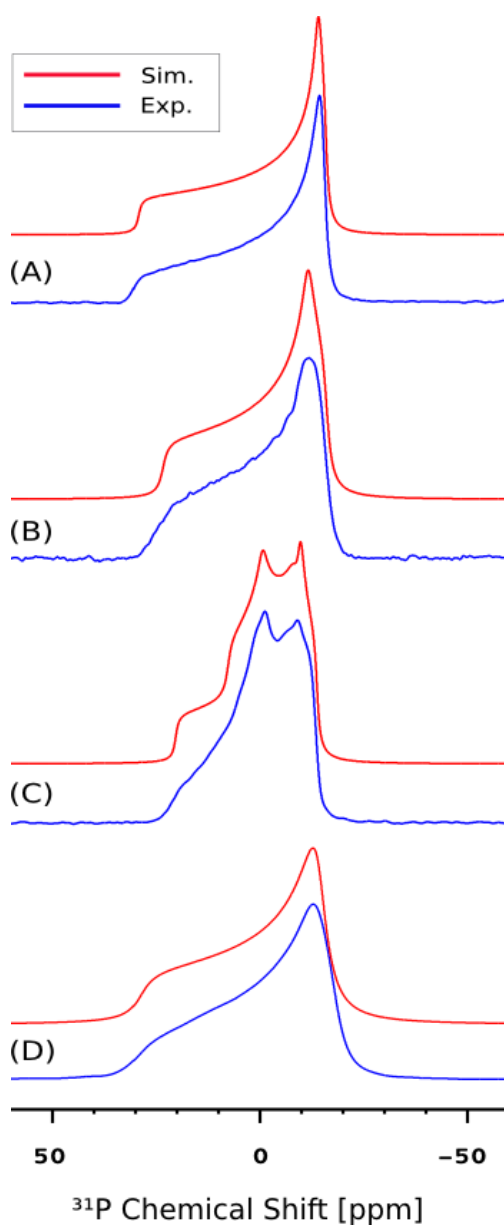


Figure 4-8: Simulated (red curve) and experimental (blue curve)  $^{31}\text{P}$  static NMR spectra of DPPC-Piroxicam (A), DPPC-Diclofenac (B), DPPC-Ibuprofen (C) and pure DPPC (D), spectra were recorded at 315 K with 512 scan number.

#### 4.3.4 Conclusion

In this study, interactions between DPPC and NSAIDs, diclofenac, ibuprofen and piroxicam, were investigated in order to understand whether drugs are incorporated into the DPPC liposomes and form drug-lipid complexes or not. 1D  $^1\text{H}$ -NMR spectra showed that ibuprofen and diclofenac have significant effects on chemical shift of DPPC protons whereas piroxicam didn't have any effects. In agreement with 1D  $^1\text{H}$ -NMR spectra,  $^1\text{H}$ -MAS NOESY spectra showed large crosspeaks of DPPC with ibuprofen and diclofenac and no significant correlation with piroxicam. Consistent with  $^1\text{H}$ -NMR results,  $^{31}\text{P}$  NMR spectra revealed that, diclofenac and ibuprofen have large effects on  $^{31}\text{P}$ -CSA of DPPC spectra while piroxicam has not shown any significant effect.

These data suggests that both diclofenac and piroxicam are incorporated inside DPPC and may form a complex with the lipid. However, in the case of piroxicam, no significant change was observed on 1D  $^1\text{H}$ -NMR and  $^{31}\text{P}$  spectra of DPPC and NOESY spectra of piroxicam-DPPC mixture didn't showed significant crosspeaks between lipid and substrate. This indicates that, opposite to diclofenac and ibuprofen, there is no indication of complex formation between piroxicam and phospholipids.

Investigations so far showed that ibuprofen and diclofenac are interacting with phospholipids (Panicker, Sharma et al. 1995; Lopes, Scarpa et al. 2004; Lucio, Bringezu et al. 2008; Moreno, Garidel et al. 2009). In agreement with literature, our solid-state NMR studies indicate strong interactions of DPPC with ibuprofen and diclofenac. On the contrary, solid state NMR studies didn't show evidence for interactions of DPPC with piroxicam. In addition to solid-state NMR, other methods such as FTIR, X-ray diffraction and photon correlation spectroscopy gave further evidences that piroxicam is not interacting with DPPC (Huesch, Dutagaci et al. 2011).

## 5 Ceramide – Lipid Bilayer Studies

### 5.1 Introduction

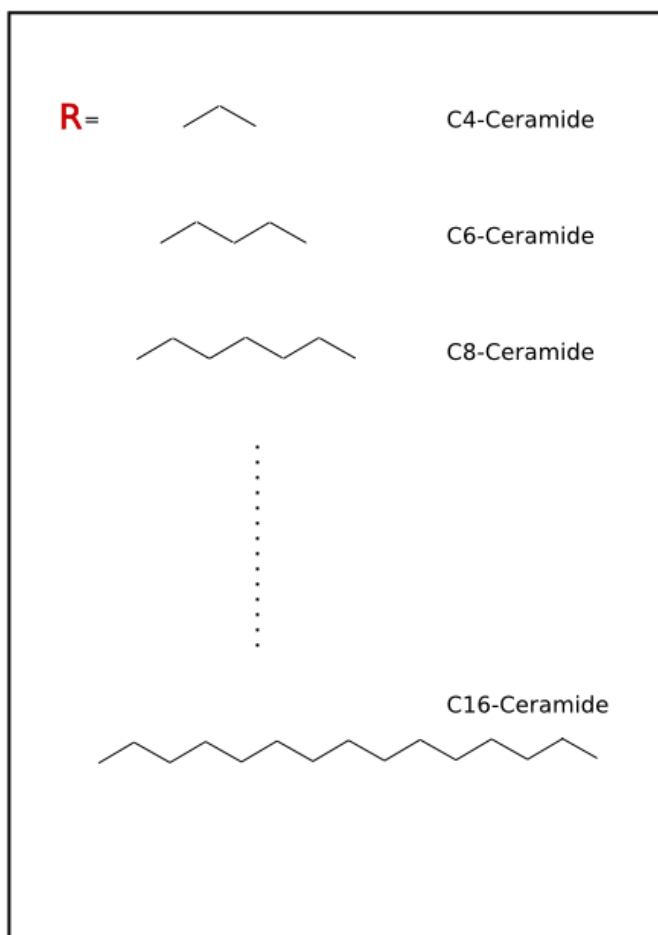
Ceramides, in other words N-acyl sphingosines, are lipid molecules, which belong to sphingolipid subclass. Ceramides have a fatty acid chain that is connected to a sphingosine base with an amide bond (Figure 5-1). Fatty acid chain length varies from 2 to 28 carbon atoms in nature and both saturated and unsaturated forms exist. Ceramides are named with their acid chain. Ceramides with acyl chain containing less than 8-10 carbon atoms are called short-chain ceramides and with acyl chain containing more than 10-12 carbon atoms are called long-chain ceramides (Sot, Aranda et al. 2005).

Free ceramides mainly occur in stratum corneum, which is the outermost layer of the skin. They are also found in membranes in small amounts as metabolites or precursor of other compounds. Ceramides are synthesized in endoplasmic reticulum and golgi from precursors serine and palmitoyl coenzyme-A, as well as, in lysosomes from sphingomyelin with the action of several enzymes, mainly, sphingomyelinase and ceramidases (Kitatani, Idkowiak-Baldys et al. 2008).

Ceramides are known to be an important bioactive sphingolipids. They act as second messenger in cell signal transduction. Hence, they are playing crucial role in inducing and modulating in many cell processes including apoptosis, differentiation, and senescence. The mechanism of physiological actions of ceramide is not completely clarified yet and thus of special interest. Recent studies indicated that ceramide functions are related with the effects of ceramide on cell membranes, especially on the membrane domains called raft. Rafts are rigid membrane domains, which are formed by clustering of sphingomyelin with cholesterol. Cholesterol is filling the hydrophobic space inside the sphingomyelin bilayer that results more close packing of sphingomyelin-cholesterol

cluster (Simons and Ikonen 1997). In the course of a signal transduction, it has been indicated by several studies that rafts are converted into larger ceramide-enriched domains by the hydrolysis of sphingomyelin into ceramide with the action of SMase (sphingomyelinase) (Gulbins, Dreschers et al. 2004). Ceramide-enriched domains are dynamically fluxing along the membrane to form larger macro-domains called ceramide-enriched platforms. It was indicated that for many receptors, ceramide macro-domains trigger capping of receptors to transmit the signaling across the membrane.

### Sphingosine Backbone



### Ceramide

*Figure 5-1: General structures of ceramides.*

Since ceramide association inside the membrane is essential for many cell processes, many studies were done to understand how ceramides behave and organize themselves in membranes (Junge, Brenner et al. 1999; Cremesti, Paris et al. 2001; Grassme, Jekle et al. 2001; Garcia-Barros, Paris et al. 2003; Gulbins and Kolesnick 2003; Bollinger, Teichgraber et al. 2005). Lateral phase separation and domain formation of ceramide inside lipid bilayers was observed by different studies (Chiantia, Kahya et al. 2006; Sot, Bagatolli et al. 2006; Boulgaropoulos, Arsov et al. 2011). They were all concluding that, ceramides induce lateral phase separation of fluid membranes into ceramide dominated gel and phospholipids dominated liquid crystalline phases. Moreover, studies on cell cultures also showed that ceramide located in cell membranes form domains (Goldschmidt-Arzi, Shimoni et al. 2011). In addition to this, the influence of ceramides on the physical properties of lipid bilayers, especially the degree of order of lipids, was studied by several groups and using a variety of techniques. Studies by fluorescence polarization technique indicated that phospholipids tend to be more ordered in the presence of ceramides (Holopainen, Lehtonen et al. 1997; Massey 2001; Silva, De Almeida et al. 2006). Besides fluorescence methods, NMR studies also indicated that ceramides increase order parameters of phospholipid chains (Huang, Goldberg et al. 1996; Hsueh, Giles et al. 2002). Ceramide effect on lipid membranes differs with the type of ceramide with different acyl chain length. Studies on the effects of short and long chain ceramides on artificial membranes revealed that membrane order is affected differently by different ceramides. In addition to this, it was observed that short chain ceramides have different effects on enzyme activities (Huang, Goldberg et al. 1998; Huang, Goldberg et al. 1999; Gidwani, Brown et al. 2003).

### **5.1.1 Objective**

Numerous studies have provided hints that ceramides have the potential to influence bulk lipid properties (Huang, Goldberg et al. 1996; Holopainen, Lehtonen et al. 1997; Massey 2001; Hsueh, Giles et al. 2002; Silva, De Almeida et al. 2006) and to induce lipid-assisted liquid crystalline domain and ceramide-assisted gel domain formations (Chiantia, Kahya et al. 2006; Sot, Bagatolli et al. 2006; Boulgaropoulos, Arsov et al. 2011). The aim of this



chapter is therefore to obtain a more atomistic insight into ceramide-lipid interactions. Thus the main three goals of this study are:

- to probe the effect of ceramides onto bulk lipid properties by measuring chain order parameters,
- to determine the chain order of the ceramides within the lipid bilayer and
- to analyse direct ceramide-lipid contacts.

MD simulations are used as a tool to predict ceramide and lipid properties. A range of different solid-state NMR experiments then verifies these predictions.

As model membranes, DMPC with ceramide C16 have been used. The obtained results are discussed in the context of previous NMR and MD studies with respect to their potential physiological meaning.

## **5.2 *Materials and Methods***

### **5.2.1 MD Simulation**

#### **5.2.1.1 Method**

All simulations were performed by using GROMACS 4.0.3. package. The initial structures of bilayer were kindly provided by Prof. Tieleman (<http://wcm.ucalgary.ca/tieleman/downloads>) (Tieleman, Forrest et al. 1998). Analyses of the trajectories after the simulations were done by using the combination of GROMACS 4.0.3 package, Python and Triangle tools.

### 5.2.1.2 Starting Structures

In this study, DMPC bilayer and bilayer mixed with ceramide molecules were simulated. DMPC bilayer contained 128 lipids and 3655 water molecules. In order to obtain DMPC bilayer with 20 % C16-Cer, 26 DMPC molecules were replaced by ceramide molecules. Starting configurations of DMPC bilayers were taken from Tieleman website (Tieleman, Forrest et al. 1998) that have been already equilibrated for 1.6 ns. For DMPC bilayer 10 ns simulation was performed for equilibration. Afterwards, DMPC molecules were replaced randomly with ceramide molecules to obtain bilayer that contain 20 % ceramide molecules. Replacement was performed by replacing DMPC molecules with ceramides according to their center of mass (Falck, Patra et al. 2004). Energy minimization was carried out for each simulation box to remove any existing bad contacts.

### 5.2.1.3 Force-fields

The force-field used for DMPC was a mixture of GROMOS force-field and lipid parameters (Berger, Edholm et al. 1997; Tieleman, Forrest et al. 1998). For ceramide, force-fields were generated in two ways. In the first way, PRODRG server was used by giving the coordinates of ceramide to the server (Schuttelkopf and van Aalten 2004). Since the charges of the head groups of ceramides, derived from server, were not compatible with the charges of DMPC head group, another force-field was created for ceramides by using DMPC as a model.

The force-field derived from the server is based on the GROMOS force-fields. However partial charges of atoms were not consistent with the charges in GROMOS force-fields (Lemkul, Allen et al. 2010). Especially for polar nuclei at the head group of ceramide, partial charges were too low that could not be compatible with the lipid head group partial charges since both lipids and ceramides have similar polar groups.

Since ceramide force-field was very inconsistent with GROMOS force-field in terms of partial charges, another force-field was derived from GROMOS by using DMPC as a

homology model. Partial charges of ceramide tails were taken directly from the tails of DMPC. For the head group, charges from GROMOS protein force-fields were implemented (Berendsen, Vandespoel et al. 1995; Lindahl, Hess et al. 2001). Bonding and non-bonding parameters were defined with the combination of lipid force-field and GROMOS87 force-field same as for lipid parameters. For the simulations of DMPC-C16-Cer mixture, the lipid-analogy force-field of C16-ceramide was used. Comparisons of the results from server and analogy forcefields can be seen in the Appendix part for POPC-Ceramide mixtures.

#### **5.2.1.4 Parameters used for the Simulations**

Simulation parameters were exactly the same as for previous simulation on POPC-pirixinic acid derivatives mixtures (Chapter 3). In order to constraint bonds with hydrogen atom LINCS algorithm was used. Periodic boundary conditions were applied in three dimensions. PME (Particle-mesh Ewald) algorithm was used to calculate long-range electrostatic interactions. For the coulomb interactions a cutoff was chosen to 1.1 A. For van der Waals interactions, a 1.1 A cutoff was implemented (Patra, Karttunen et al. 2003; Patra, Karttunen et al. 2004). Temperature for all the systems was set to 310 K by using Nosé-Hoover method. Because, the main transition temperature of DMPC is around 297K. All simulations were performed at 1 bar constant pressure by using semiisotropic Parrinello-Rahman coupling scheme. The simulations were performed for pure DMPC and 20 % of DMPC-C16-cer system for 100 ns simulations and last 90 ns of the simulations were used for the analysis.

#### **5.2.1.5 Analysis**

Trajectories were analyzed by using analysis package of GROMACS, Python programming language (<http://www.python.org/>) and Triangle program (Shewchuk 1996; Shewchuk 2002). From the trajectories of the simulations, it is possible to obtain several informations that are closely related with the membrane dynamics. Size of the boxes,

areas of bilayer planes, bilayer width, density profiles, C-H order parameters are some of them that were investigated here. Box lengths and areas of bilayer plane (xy-plane) were calculated by using `g_energy` option in GROMACS. Density profiles of the systems and water and therefore bilayer length were derived from the calculations of `g_density` algorithm. `G_order` program was used to compute order parameters for the tails of lipids and ceramide. Hydrogen bonding statistics were derived from the program `g_hbond` in GROMACS package. For pure DMPC and DMPC-C16-cer mixture, in addition to these analyses, systems were further analyzed to investigate electrostatic potential inside the bilayer by using `g_potential` program in GROMACS software. In addition to this, P-N vector orientation of DMPC lipids was also calculated. For P-N vector orientation, angle between z axis and P-N vector was calculated for each lipid throughout trajectories. The average angle gave the angle for bulk lipid. For the calculation of the P-N vector orientation for DMPC molecules, which are at close proximity with ceramide molecules, DMPC atoms were chosen with distance information between ceramide and DMPC itself. For each specific ceramide molecule, distance between oxygen attached to  $C_{g3}$  carbon atom of DMPC molecules and oxygen of hydroxyl of  $C_1$  carbon at sphingosine backbone of that certain ceramide were calculated for all DMPC molecules in one snapshot. Then, DMPC molecule with shortest distance to that specific ceramide was chosen for the calculation. This method was repeated for each ceramide. For each snapshot, DMPC molecules for P-N vector calculation were chosen again with the same method. Finally, the average P-N vector orientation for DMPC at close vicinity to ceramides was calculated by Gaussian curve for the whole trajectory. As a control, P-N vector orientations for DMPC molecules at close vicinity to randomly chosen lipids were calculated for pure DMPC bilayer.

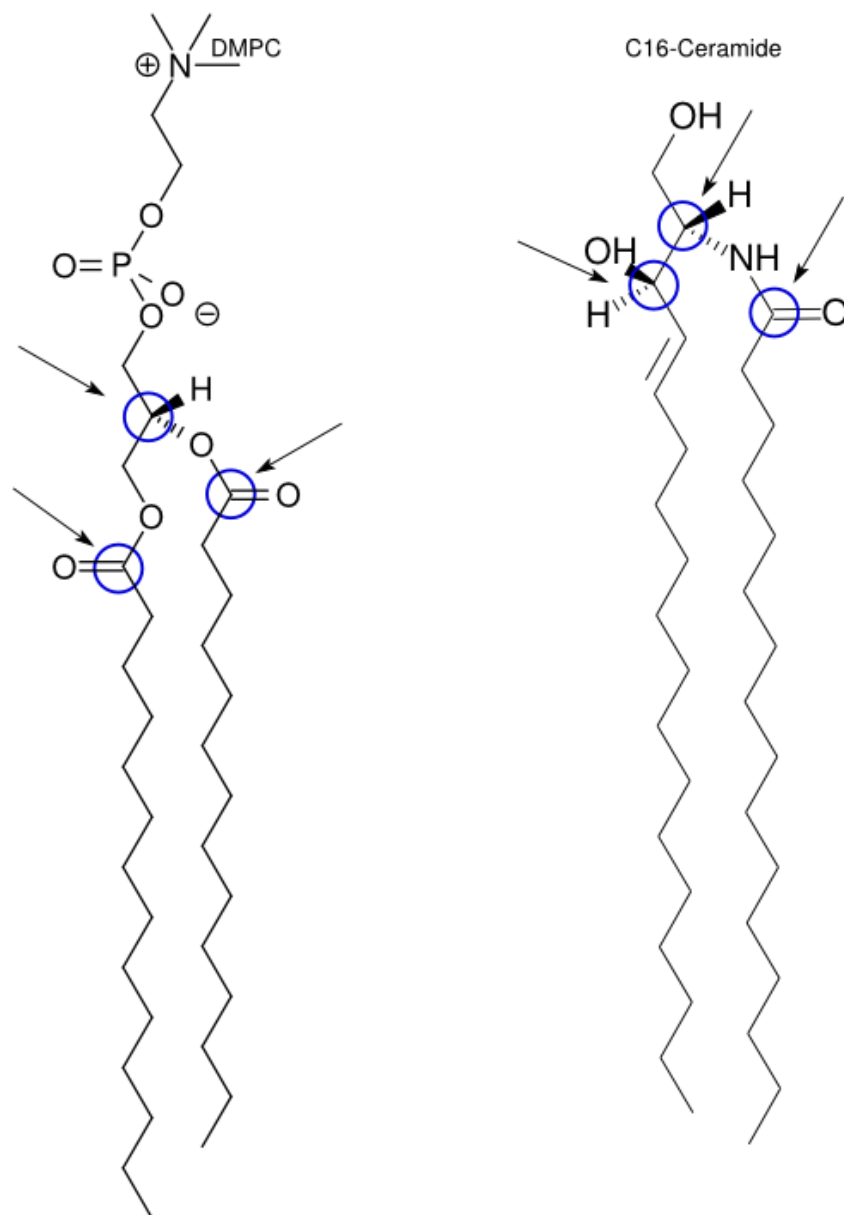


*Figure 5-2: Structures of DMPC and C16-Ceramide; atoms that were chosen for Delaunay triangulation-Voronoi tessellation were depicted inside blue circles*

Area per lipid in membranes could be calculated by dividing the area of a bilayer plane to the number of lipids at one monolayer. However, in this case, using this simple calculation might give wrong results because of the different size and dynamics of the ceramide and lipids. Therefore, a more precise method, which is called Voronoi tessellation (Voronoi 1908; Aurenhammer 1991; Shinoda and Okazaki 1998), was used for the area analysis. The projections of simulation boxes on the xy plane for each monolayer were taken from the coordinate file. Then, the coordinates of the 3 carbon atoms in between two tails of lipids and ceramides were chosen to perform Delaunay triangulation (Delaunay 1934), which creates dual triangles of voronoi polygons. The choice of atoms was done in order to represent two tails and the head group of both DMPC and Ceramide (Pandit, Vasudevan et al. 2004). For DMPC, two carbonyl carbons from two tails ( $C_1$ ) and the second carbon ( $C_{g2}$ ) in the glycerol and for ceramide,  $C_2$  and  $C_3$  on the sphingosine chain and  $C_1$  on the acyl chain were taken for the calculations (Figure 5-2). Then, areas of the dual Voronoi polygons of the triangles were calculated for each point that was corresponding to the coordinates of each carbon atom. The total area of each three atoms from the same molecule gave the area covered by that specific molecule. Probability density curves of areas for ceramide and lipids were created from all the lipids for each monolayer of each snapshot throughout the trajectories. Delaunay triangles and Voronoi diagrams were produced by using Triangle program (Shewchuk 1996; Shewchuk 2002). Area analyses were done by using Python (<http://www.python.org/>).

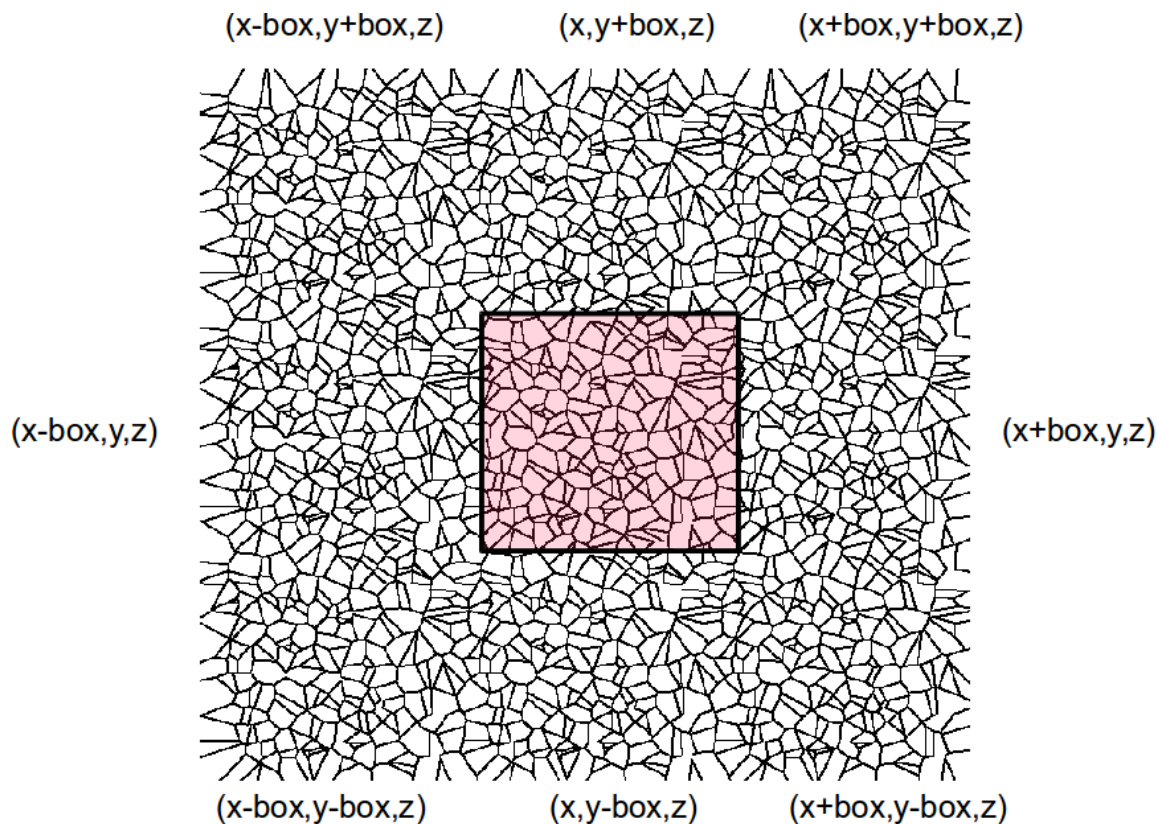


*Figure 5-3: The representation of periodicity of Voronoi diagram of a bilayer projection; at the center,  $xy$  plane of the original simulation box (highlighted as pink) locates and it is extended from each side to obtain periodicity for Voronoi tessellation.*

However, there is one drawback of this method. The areas of polygons that are at the edge of the whole diagram can be very large. To overcome this problem one box periodicity was applied from each side of the projection so the original box stayed at the middle of the whole diagram. Delaunay triangulation was performed on to the whole extended diagram, whereas area calculations were carried out only for the polygons in original simulation box at the middle of the diagram (Figure 5-3). Therefore, the edge effect of the Voronoi tessellation was able to be suppressed at a certain amount.

### 5.2.2 Sample Preparation

DMPC, DMPC-d67, DMPC-C16-Cer (20% ceramide) and DMPC-d67-C16-Cer (20% ceramide), C16-Cer were used as samples to observe dynamics of both ceramide and DMPC. Except uni-lamellar POPC and DMPC membranes all other samples were prepared with the method as described in the materials and methods chapter (Chapter 2). For uni-lamellar membranes, the preparation method described in the literature was repeated (Saleem, Lai et al. 2012). Briefly, lipids were dissolved in chloroform as usual. Then, the solvent was evaporated by using N<sub>2</sub> stream to obtain a thin film. Afterwards, lipids were suspended in the buffer that contained 200 mM sucrose, 20 mM KCl, 10 mM HEPES at pH 7.4. After applying freeze-thaw cycle, resulting suspension was extruded through 0.4 μm polycarbonate membrane. Then, LUV suspension was concentrated in a centrifuge at 5000 x g. Finally, samples were transferred to the 4 mm NMR rotor.

### 5.2.3 Solid State NMR

<sup>1</sup>H NMR spectra were recorded by Bruker Avance II 850 WB spectrometer with proton larmor frequency of 850 MHz. Samples were spinning with 10 kHz spinning speed. FID was acquired for 51 ms and 1024 data points were collected. Spectral width was set to 10 kHz. Recycle delay was chosen as 3s. Chemical shift referencing was done internally for each spectrum with respect to terminal methyl group of lipid chains at 0.89 ppm. Experiments were repeated in D<sub>2</sub>O and H<sub>2</sub>O to see exchangeable protons.

<sup>1</sup>H-MAS NOESY spectra were acquired by Bruker Avance II 850 WB spectrometer operating proton larmor frequency of 850 MHz. Sample spinning of 10 kHz was used. Mixing times were set between 5 and 800 ms. Spectral widths of 17 kHz for direct and indirect dimensions were used. FID was acquired by TPPI method with acquisition time 40 ms for direct dimension and 15 ms for indirect dimension. 1358 data points for direct dimension and 516 data points for indirect dimension were collected. Recycle delay was set 3s. Buildup curves and relaxation rates were calculated by full-matrix approach (Huster, Arnold et al. 1999; Scheidt and Huster 2008).



$^{14}\text{N}$ -MAS spectra were recorded by Bruker Avance II 850 WB spectrometer operating  $^{14}\text{N}$  larmor frequency of 262 MHz. 30000 data points were collected and FID was recorded for 60 ms. Spectral width of 250 kHz was used. Solid-echo pulse sequence was used. Delay for the echo was chosen as 0.5 ms and recycle delay was 0.2 s. Side-band analyses were done by using TOPSPIN analysis package.

Static  $^{31}\text{P}$  NMR spectra were acquired by Bruker Avance II 600 WB spectrometer operating  $^{31}\text{P}$  larmor frequency of 243 MHz. FID was acquired for 50 ms and 4994 data points were collected. 50 kHz spectral width was used. Recycle delay was chosen as 2 s. Spectral shape fitting was performed by TOPSPIN software.

Pisema experiments were performed by Bruker Avance II 850 WB spectrometer operating proton larmor frequency of 850 MHz with 10 kHz spinning speed. Spectra were acquired by States method with acquisition time 34 ms for direct dimension and 15 ms for indirect dimension. Data points of 4096 for direct dimension and 256 for indirect dimension were collected. Spectral widths of 60 kHz and 26 kHz were set for direct and indirect dimensions respectively. Recycle delay was 3 s and  $^1\text{H}$  field strength during FSLG-CP match was calculated as 42 kHz. Two  $^{13}\text{C}$  rf fields during FSLG-CP,  $\omega_{1,\text{C}}^+$  and  $\omega_{1,\text{C}}^-$ , strength was optimized by matching with  $^1\text{H}$  effective field by use of 1D-LG experiment. The difference between two  $^{13}\text{C}$  field should be  $(\omega_{1,\text{C}}^+ - \omega_{1,\text{C}}^-) = 2\omega_r$  for the first spinning side band, where  $\omega_r$  is spinning speed. Figure 5-4 shows the optimization of  $^{13}\text{C}$  rf field. Matching condition at first spinning side bands is depicted in the figure. During data processing, only cosine-modulated data were used. In order to suppress the middle peak, baseline mode were applied by obtaining signals by convolution of peaks with Gaussian function (Marion, Ikura et al. 1989).

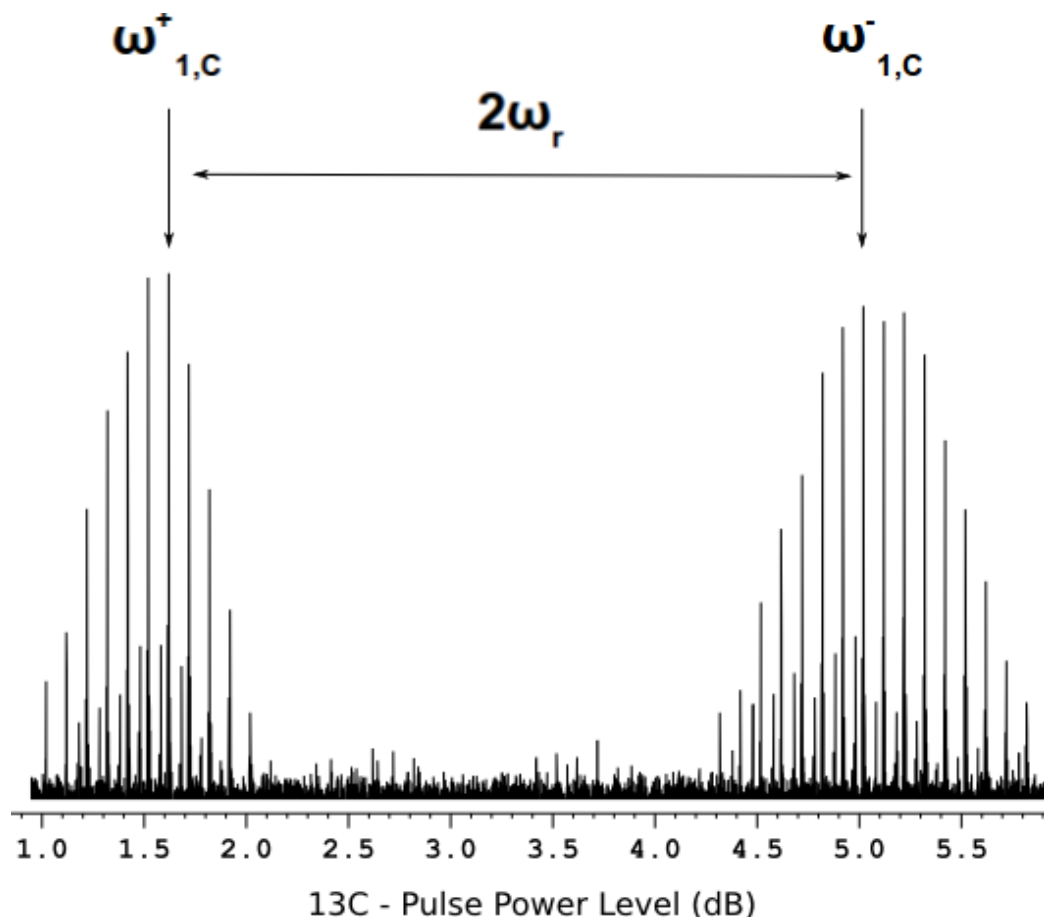


Figure 5-4: Spectrum for optimization of  $^{13}\text{C}$ -rf field for FSLG-CP conditions:  $\omega_{1,C}^+$  and  $\omega_{1,C}^-$  are  $^{13}\text{C}$  rf-fields matched with  $^1\text{H}$  efficient rf-field at spinning side bands +1 and -1, respectively;  $\omega_r$  is spinning speed (explained in methods, Chapter 2).

$^{31}\text{P}$  CODEX experiments were performed by Bruker Avance II 600 WB spectrometer operating  $^{31}\text{P}$  larmor frequency of 243 MHz with 10 kHz spinning. Spectra were acquired for 40 ms with the implementation of proton decoupling. 3992 data points were collected. Spectral width of 50 kHz was used.  $90^\circ$  pulse for  $^{31}\text{P}$  was 50 kHz and recycle delay was chosen as 3s. 14 loops were used for recoupling pulses. Mixing times were varied in between 1-100 ms.

2D static  $^{31}\text{P}$  exchange spectra were acquired by Bruker Avance II 600 WB spectrometer operating  $^{31}\text{P}$  larmor frequency of 243 MHz. 10 and 3 ms acquisition times were chosen

for direct and indirect dimensions respectively. 992 data points for the direct dimension and 300 data points for the indirect dimension were collected. Spectral width of 50 kHz was used for both dimensions. Recycle delay was chosen 3 ms and 50 kHz  $^{31}\text{P}$  pulse was applied. Experiments were repeated for 5 and 400 ms mixing times.

### **5.3 Results and Discussion**

In this study, DMPC was used as artificial lipid bilayer. DMPC is a saturated phospholipid with 14 carbon atoms at each fatty acid chain. DMPC is often used as model lipid for solid-state NMR studies and has been fully characterized. It was therefore chosen here in-depth ceramide-lipid interaction studies.

Since it is a simple and representative molecule for phospholipids, it can serve a good model for lipid bilayers. Besides that, it is also an important question how ceramides affects unsaturated lipids. Thus, POPC was also studied (see Appendix) by solid-state NMR and MD. However, for POPC bilayer, results for saturated and unsaturated chains were not consistent and thus complicated to be interpreted. Therefore, the main focus has been on analyzing DMPC bilayers with incorporated ceramides.

Ceramides vary with their fatty acid chain length. Ceramides with short chains were commonly used in the literature to see their effects on lipids, because, short chain ceramides are forming clear dispersion with water whereas long chain ceramides are not. Therefore sample preparation for short chain ceramides is easier while long chain ceramides need co-reconstitution along with lipids. However, their effects on membrane dynamics are not similar. Therefore it is important to study on ceramide molecules, which can be a model for natural ceramides. Natural ceramides contain mainly long-chained ceramides. C16-ceramide is known to be one of the main components of natural ceramides. Since long chain ceramides are more important C16-Ceramide was selected here.

### 5.3.1 MD Simulations

In order to see effects of C16-ceramide on DMPC bilayers in molecular level, MD simulations were performed on pure DMPC bilayer and DMPC bilayer contains 20 % ceramide molecules. After 100 ns simulations of both bilayers, snapshots as depicted in Figure 5-5, were already gave an idea about influences of ceramide molecules on DMPC bilayers. DMPC molecules seemed to become more packed with elongated bilayer shape in the presence of ceramide. Further analysis on area per lipid, density profiles, order parameter, radial distribution function, hydrogen bond formation, electrostatic potential across the bilayer and PN vector orientation with respect to bilayer normal will give more detailed analyses on the simulations on DMPC bilayers with and without ceramide.

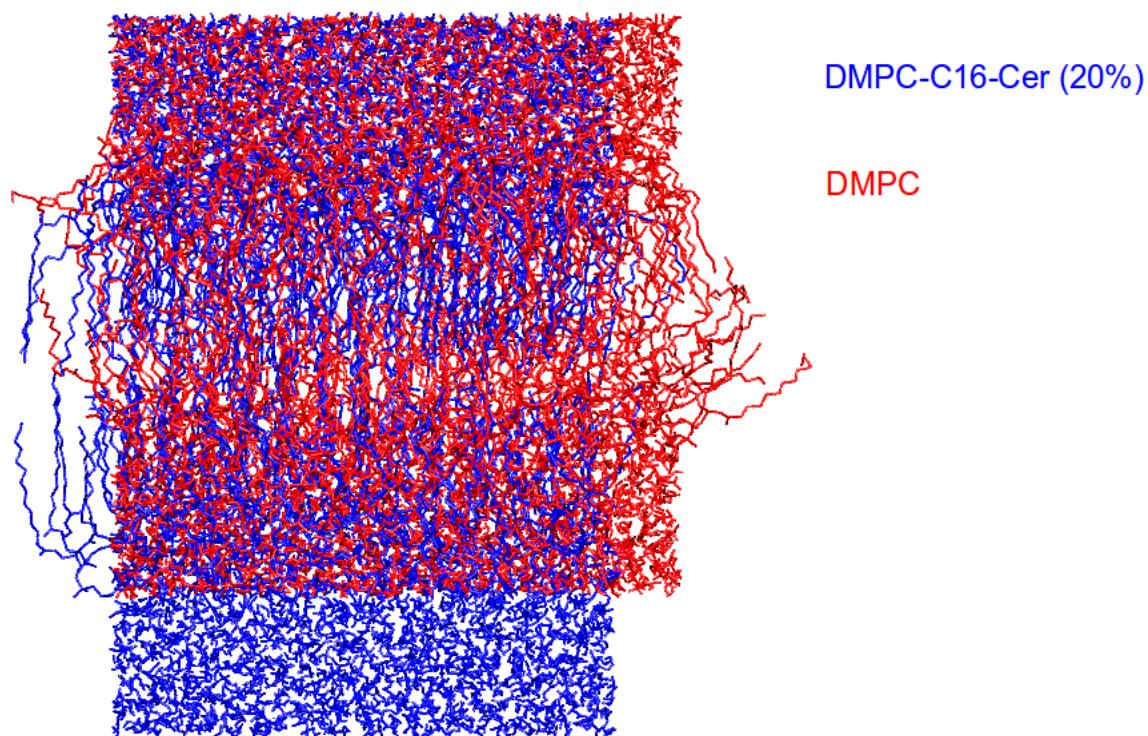


Figure 5-5: Snapshots from pure DMPC (red) and DMPC-Ceramide mixture (blue).

### 5.3.1.1 Area per Lipid

In order to calculate area per lipid, Delaunay triangulation-Voronoi tessellation dual method was applied. The xy-plane of bilayer box was chosen for calculations. For each DMPC molecule and ceramide molecule three atoms were taken. From triangles, dual polygons were calculated for each atom. Finally, areas for three polygons, which are belonging to chosen three atoms of same lipid were summed up to find the area covered by that lipid. At the end, areas for all lipids throughout the whole trajectory were plotted as area density probability curve to obtain the average areas for ceramide and DMPC separately.

In Voronoi diagrams, polygons at the side of the diagram may be too large to represent a realistic area for atoms. In order to prevent such an edge effect, one-box periodicity was applied to the bilayer projection before creating Voronoi diagrams. Therefore, only polygons inside the diagram were analyzed and as a result edge effect of the tessellation could be removed.

Figure 5-6 displays that area per lipid for DMPC was decreased with the presence of 20 % C16-cer. For the pure DMPC, area per lipid was calculated as  $61.26 \text{ \AA}^2$ , which is consistent with the value reported as 60.6 before (Kucerka, Liu et al. 2005) and it was dropped to  $53.02 \text{ \AA}^2$  for the mixture. Area per ceramide was also calculated for the mixture and it was found as  $41.43 \text{ \AA}^2$ .

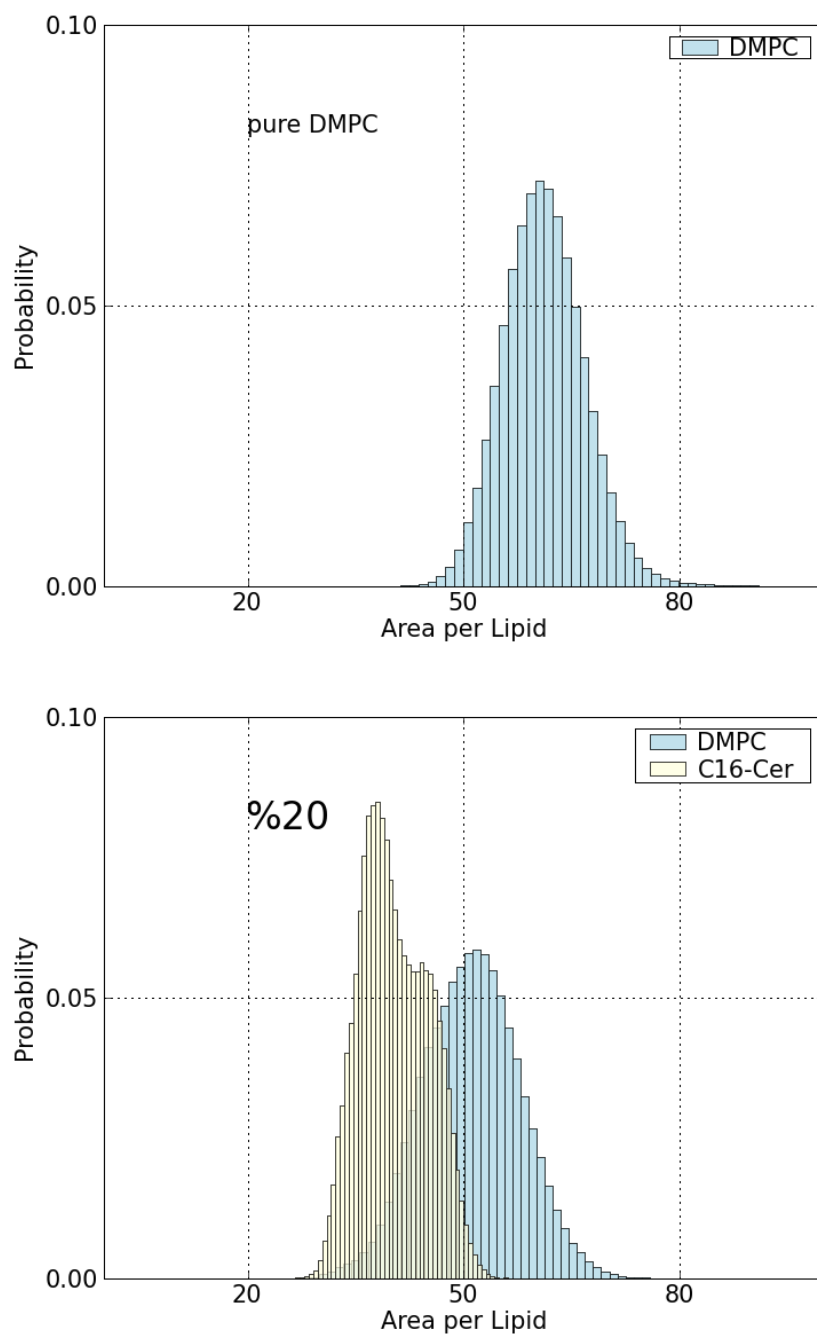


Figure 5-6: Area per lipid in DMPC bilayers: pure DMPC (top) and DMPC-C16-Cer mixture (bottom).

### 5.3.1.2 Density Profiles

Figure 5-7 shows system and water density profiles for both pure DMPC and DMPC-ceramide mixtures. Since maximum points in density profiles correspond to the phosphorus atoms for two leaflets, bilayer width can be calculated by taking the distance in between these two maximum points in density profile curves. It can be easily seen from the figures that the bilayer width of the mixture was higher than the one for pure DMPC bilayers. For the pure bilayers, it was calculated as 3.20 nm and for the mixture, it was increased up to 3.83 nm. The increase in bilayer thickness is consistent with area per lipid results. Since area per lipid decreased, DMPC molecules started to become more densely packed, which leads an elongation of the bilayer.

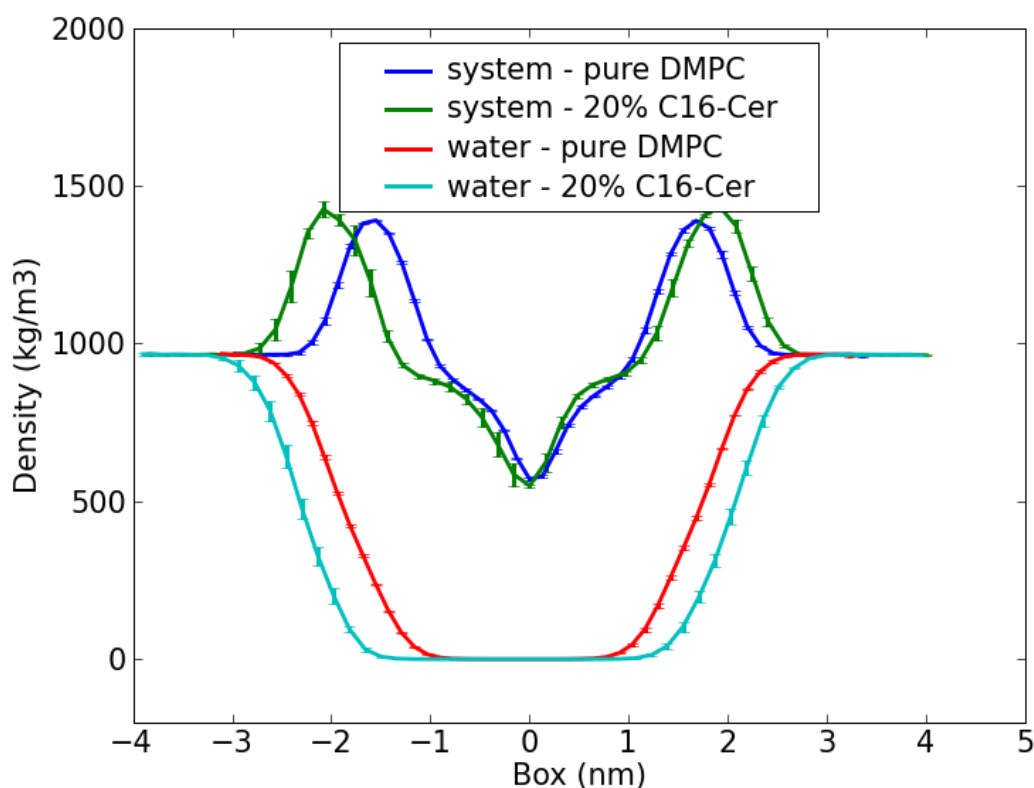


Figure 5-7: Water and system mass density profiles of pure DMPC and DMPC-C16-Cer mixture.

### 5.3.1.3 Chain Order Parameters

Order parameters of lipid chains provide information about the mobility of bond orientations with respect to bilayer normal. In general, it is defined by C-H (D) bond orientations. In this study, all the simulations were done by using united atom force-fields. Therefore, there was not any non-polar hydrogen attached to carbons. United atom simulations were performed in which carbon atoms were representing bonded hydrogens as united atoms. In this case, there are two ways to calculate C-H order parameters. In the first method, H atoms can be constructed after simulations for each snapshot of the trajectories and then C-H order parameters can be calculated with the following formula:

$$5-1 \quad S = \langle \frac{1}{2}(3\cos^2\theta - 1) \rangle$$

where  $\theta$  is the angle of C-H vector with the bilayer normal (z axis here). Second method is less time consuming. In this method, angle of  $C_{n-1}-C_{n+1}$  vector with z axis of the simulation box is computed and from this angle order parameters for  $C_n$  is calculated by using the same formula. Here, the second method was used for the analysis. More details can be found about the calculations in the GROMOS manual as well as in the literature (Chau and Hardwick 1998; D. van der Spoel 2005).

Order parameters for two acyl chains of DMPC and for acyl and sphingosine chain of ceramide were calculated. Results were displayed in the Figure 5-8. It can be easily seen that order parameters of the hydrocarbon chains of the phospholipids were increased with the presence of ceramide. Order parameters of ceramide for two chains were close to each other and higher than the order parameters of DMPC chains in pure DMPC bilayer. However, in the case of mixture, DMPC chain orders were increased and became very close to the ceramide order. This result suggests that DMPC and ceramide have an interaction that results in similar dynamics on the chains of both lipids for the 20 % DMPC-ceramide mixture.



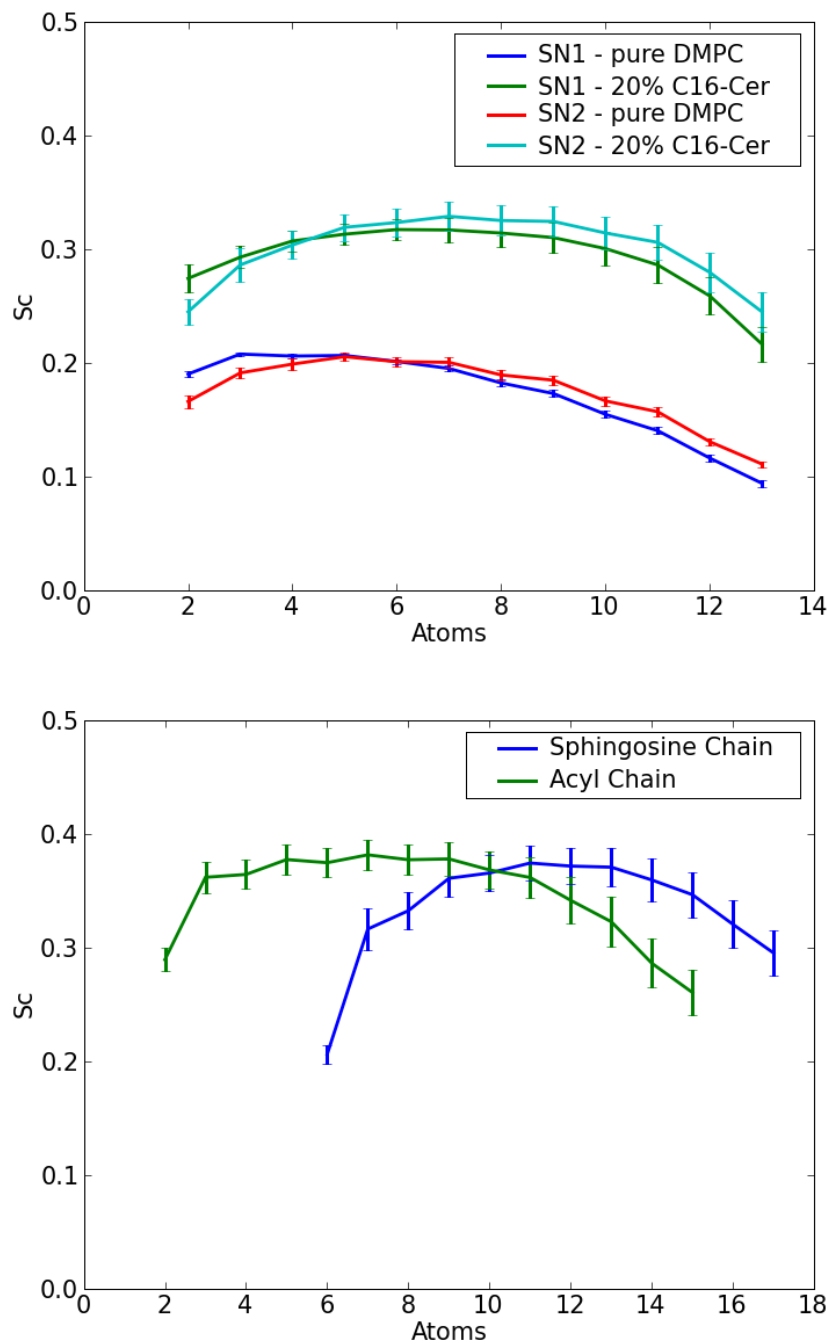


Figure 5-8: Order parameters of SN<sub>1</sub> and SN<sub>2</sub> (top) chains of DMPC for pure DMPC and DMPC-C16-Cer mixture and acyl and sphingosine (bottom) chains of ceramide for DMPC-C16-Cer mixture.

### 5.3.1.4 Hydrogen bonding

The results of DMPC-Ceramide mixture analysis show that ceramides were forming hydrogen bonds mainly with DMPC (Figure 5-9). Hydrogen bonds between ceramide and water also occurred but it was less than the number of DMPC-Ceramide hydrogen bonds. There were almost no hydrogen bonds of ceramide with ceramide itself. It was also found that number of hydrogen bonds between DMPC and water was quite high in both pure DMPC and DMPC-Cer mixture. The number of hydrogen bonds was decreased for the mixture but the decrease was proportional with the number of DMPC molecules replaced with ceramide. Therefore, this result suggests that ceramide molecules are constructing hydrogen bonds with DMPC without disturbing hydrogen bonds between DMPC and water. All the numbers of hydrogen bonds between different groups were summarized in Table 5-1.

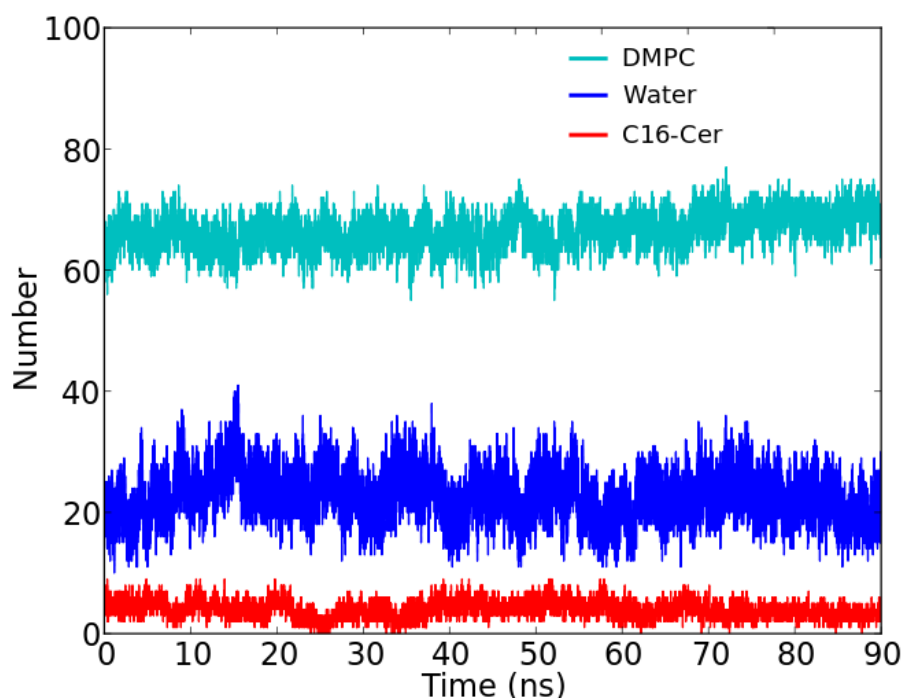


Figure 5-9: Number of H-bond that C16-Cer forms with DMPC, water, and C16-Cer itself.

	Pure DMPC	DMPC-C16-Ceramide (20%)		
Bilayer area of XY-plane (nm <sup>2</sup> )	39.56 ± 0.27	31.51 ± 0.60		
Area per lipid (Å <sup>2</sup> )	61.13 ± 0.38	51.01 ± 0.99		
Area per ceramide (Å <sup>2</sup> )	-	40.30 ± 0.55		
Bilayer width (nm)	3.23 ± 0.02	4.00 ± 0.04		
Number of H-bonds, DMPC-Water	782.71 ± 18.80	570.60 ± 16.30		
Number of H-bonds, Cer-Cer	-	4.08 ± 1.39		
Number of H-bonds, Cer-Water	-	22.61 ± 4.02		
Number of H-bonds, Cer (total)-DMPC	-	66.55 ± 2.81		
Number of H-bonds, Cer (1-OH)-DMPC	-	22.54 ± 1.63		
Number of H-bonds, Cer (3-OH)-DMPC	-	23.03 ± 1.67		
Number of H-bonds, Cer (NH)-DMPC	-	20.97 ± 1.32		
1 <sup>st</sup> RDF Maximum for DMPC-Water	0.69 ± 0.02	0.57 ± 0.05		
Electrostatic Potentials inside the bilayer	-4.94 ± 0.05	-4.93 ± 0.06		
	Pure DMPC	DMPC-C16-Ceramide (20%)	DMPC-C16-Ceramide (20%) Close Vicinity	Pure DMPC Control with random lipids
Angle of P-N vector with bilayer normal	90.11 ± 0.14	90.10 ± 0.04	91.75 ± 0.48	90.72 ± 0.78

*Table 5-1: Summary of trajectory analysis for DMPC and DMPC-C16-Cer; bilayer area, area per lipid, bilayer width, numbers of hydrogen bonds, 1st maximum of radial distribution function for DMPC-water, electrostatic potentials inside the bilayers, P-N vector orientation with respect to bilayer normal are listed.*

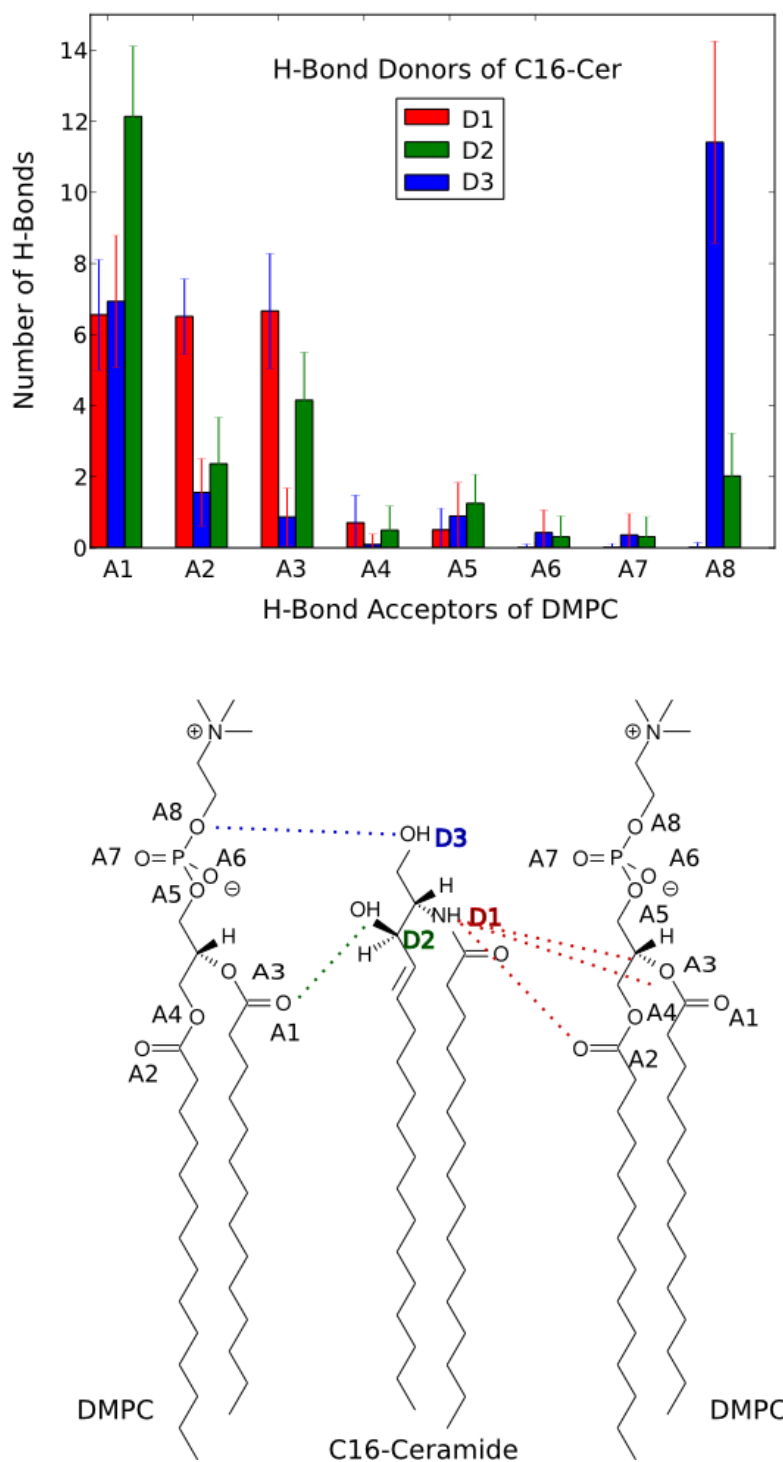


Figure 5-10: Numbers of hydrogen bonds between ceramide and DMPC: atoms denoted as D stand for H-bond donors, atoms denoted as A stand for H-bond acceptors.

Hydrogen bonding results are consistent with the order parameters results that both indicate the existence of interactions between ceramide and DMPC for the mixture. The hydrogen bonding map of ceramide between DMPC was further analyzed by looking the possible hydrogen bond donors in ceramide molecules in more detail (Figure 5-10). There are 3 hydrogen bond donors in ceramide molecule, which are NH and two OH at the sphingosine backbone. Table 5-1 shows that all three hydrogen bond donors were contributing equally to the hydrogen bonding with DMPC. As depicted in Figure 5-10, the hydroxyl group at the beginning of the sphingosine chain (D3 in the figure) was forming hydrogen bonds mainly with oxygens at the phosphorus head group (A8 in the figure) whereas amide (D1) and the other hydroxyl (D2) were forming hydrogen bonds more with the carbonyl oxygens of the DMPC chains. In other words, phosphorus head group of DMPC is interacting with the hydroxyl group of ceramide, which is at the beginning of sphingosine backbone, whereas glycerol backbone of DMPC is interacting more to the part of sphingosine backbone close to hydrocarbon chains. This suggests that not only head groups are interacting but also chains of both ceramide and DMPC were getting in close contact that might also explain the effect of ceramide on the order parameters of DMPC chains.

### 5.3.1.5 Radial Distribution Function

Radial distribution functions for water oxygen with the carbonyl carbon of SN<sub>2</sub> chain of DMPC and as well as with the carbonyl carbon of ceramide acyl chain were plotted in Figure 5-11. The distances of water to ceramide and DMPC molecules look quite similar. In addition, ceramide did not change the distances between DMPC and water. The only significant difference between radial distribution functions of DMPC for pure bilayer and the mixture was the probability to find water molecules at the radius for the first maximum. It was getting smaller for the mixture compared with the pure bilayer. It drops from 0.72 to 0.67, which is indicating that slightly less water could penetrate into the bilayer in the presence of ceramide. This result is consistent with the area per lipid result. Since area per lipid was decreasing in the presence of ceramides and the bilayer becomes more packed. Water penetration might also decrease.

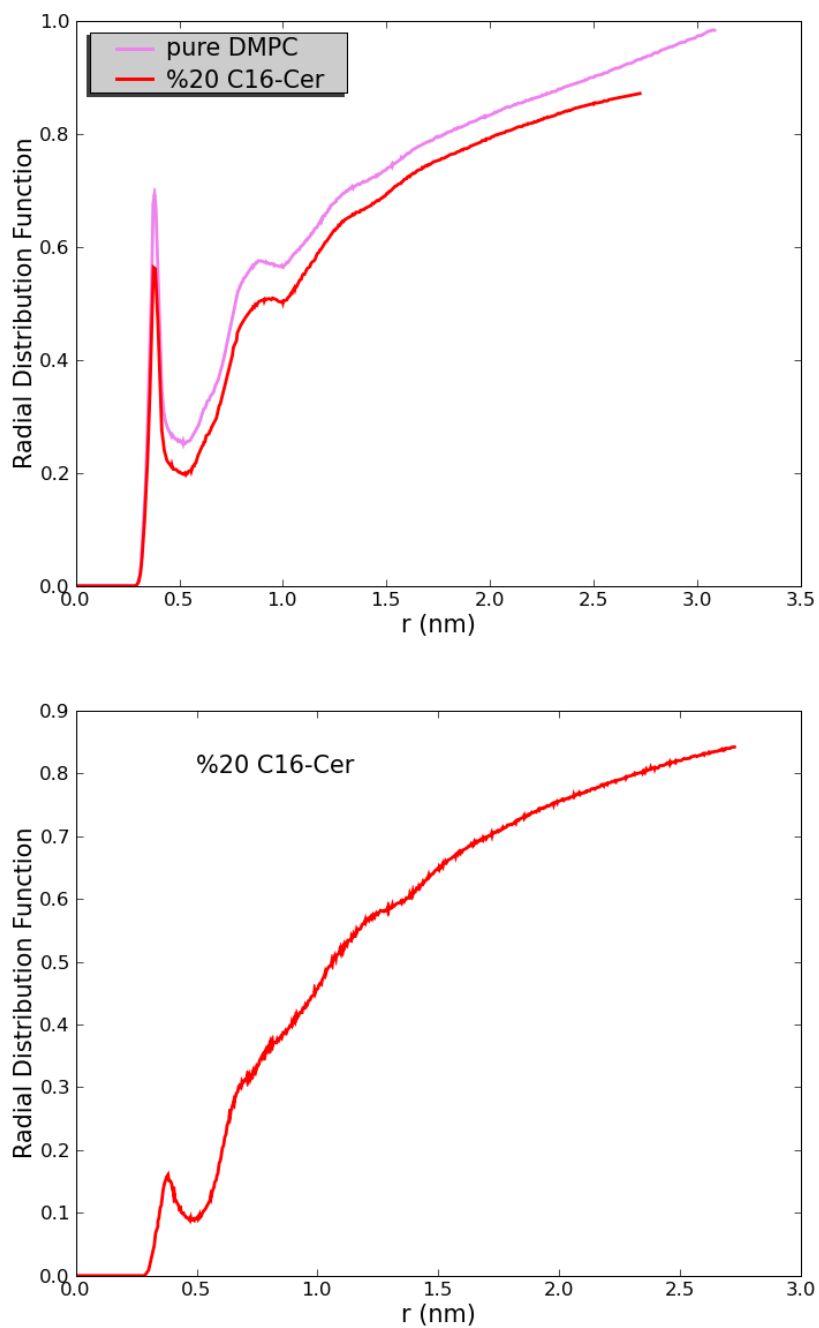


Figure 5-11: Radial distribution functions for water oxygen with carbonyl carbon of DMPC SN<sub>2</sub> chain for DMPC and DMPC-C16-Cer mixture (top) and with carbonyl carbon of ceramide acyl chain for DMPC-C16-Cer mixture (bottom).

### 5.3.1.6 Electrostatic Potential

DMPC is a zwitterionic phospholipid that has a negative phosphate and positive choline group. Therefore, the DMPC bilayer creates partial charge anisotropy for the water around the bilayer and a negative potential inside the bilayer (Figure 5-12, top graph). The analysis of two systems showed that the negative potential inside the bilayer did not change in the presence of ceramide. Charge densities were also support this conclusion. Figure 5-12 (middle and bottom graphs) displays the charge distribution of each group for both simulation boxes. Ceramide didn't have any significant effect in charge distribution of the whole system.

### 5.3.1.7 P-N Vector Orientation

The angle of the bilayer normal with the P-N vector, that is the vector between phosphorus of the phosphate group and nitrogen of the choline group at the head group of a lipid, was calculated for the whole trajectories for both systems. Therefore it could provide insight into head group orientation of lipids in the bilayer. Histograms of the P-N vector angle with the z-axis of the simulation box were displayed in Figure 5-13. Figures on top show the angles for all DMPC lipids from pure bilayer and mixture, whereas the ones at the bottom show angles of DMPC lipids that are close in distance to the ceramide molecules for each snapshot of the mixture and control analyses for DMPC by random lipids. The results show, for the mixture that the P-N vector histogram is getting broader in comparison with the pure DMPC bilayer. However, in the case of lipid molecules that were in close proximity with ceramides the orientation of PN vector are found to be different from the whole analysis of all DMPC molecules. In literature, a difference in histograms of PN vector orientations was reported for phospholipid molecules that were at close proximity of Ganglioside (sialic acid-containing glycosphingolipids) molecules (Patel and Balaji 2007). Here, histograms that were belonging to DMPC molecules at close vicinity to ceramide molecules were becoming narrow, even narrower than pure bilayer. This indicates that effects of ceramide on DMPC molecules were different according to the distance between ceramide and DMPC molecules.

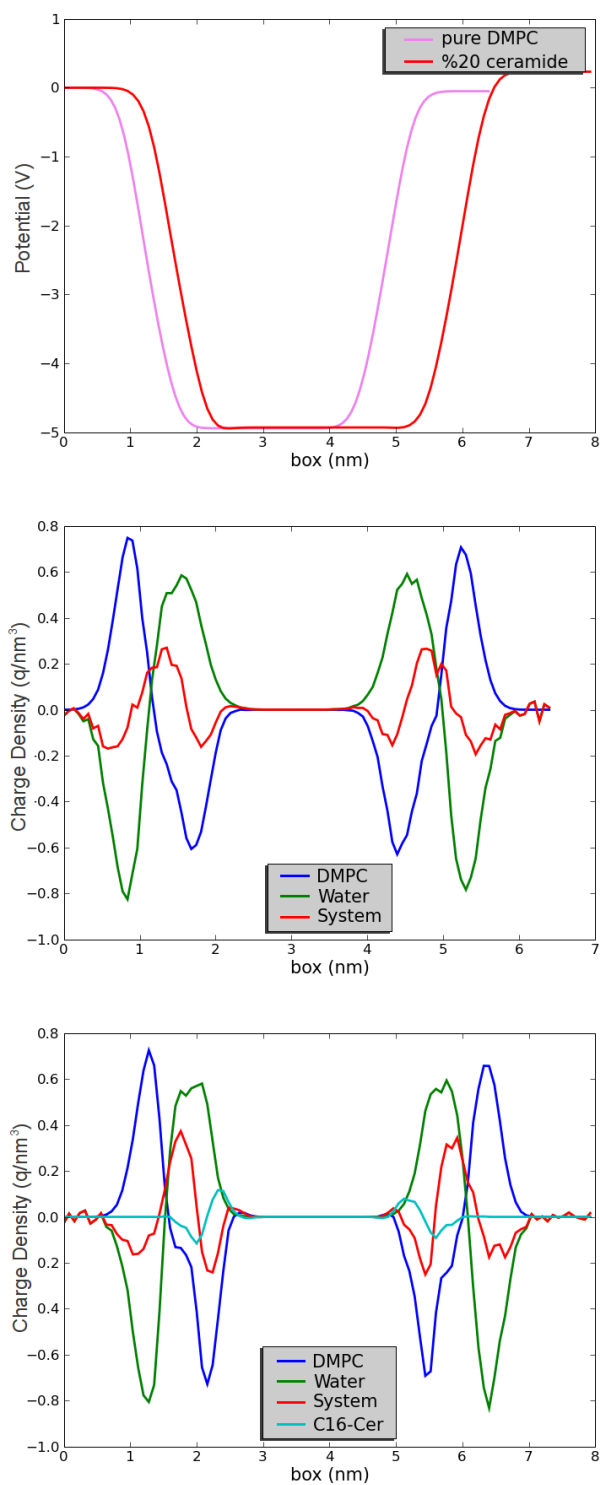


*Figure 5-12: Electrostatic Potential of DMPC(top) for DMPC and DMPC-C16-Cer; Charge Distribution of DMPC, Water and the System for DMPC bilayer (middle) and DMPC, Ceramide, Water and the System for DMPC-C16-Cer Mixture (bottom).*



In addition to this, average PN-vectors showed that pure DMPC and DMPC in the mixture had very similar PN vector orientations  $90.15^\circ$  and  $90.06^\circ$ , respectively. For the lipids molecules that were close to ceramide molecules had slightly different orientations that were calculated as  $91.75^\circ$ . This suggests that DMPC and ceramide at close distance may have interactions that result in differences in head group orientation of DMPC molecules. Hence, in agreement with order parameters and hydrogen bonding analyses, P-N vector orientation analyses provide hints on the presence of specific ceramide-DMPC interactions.

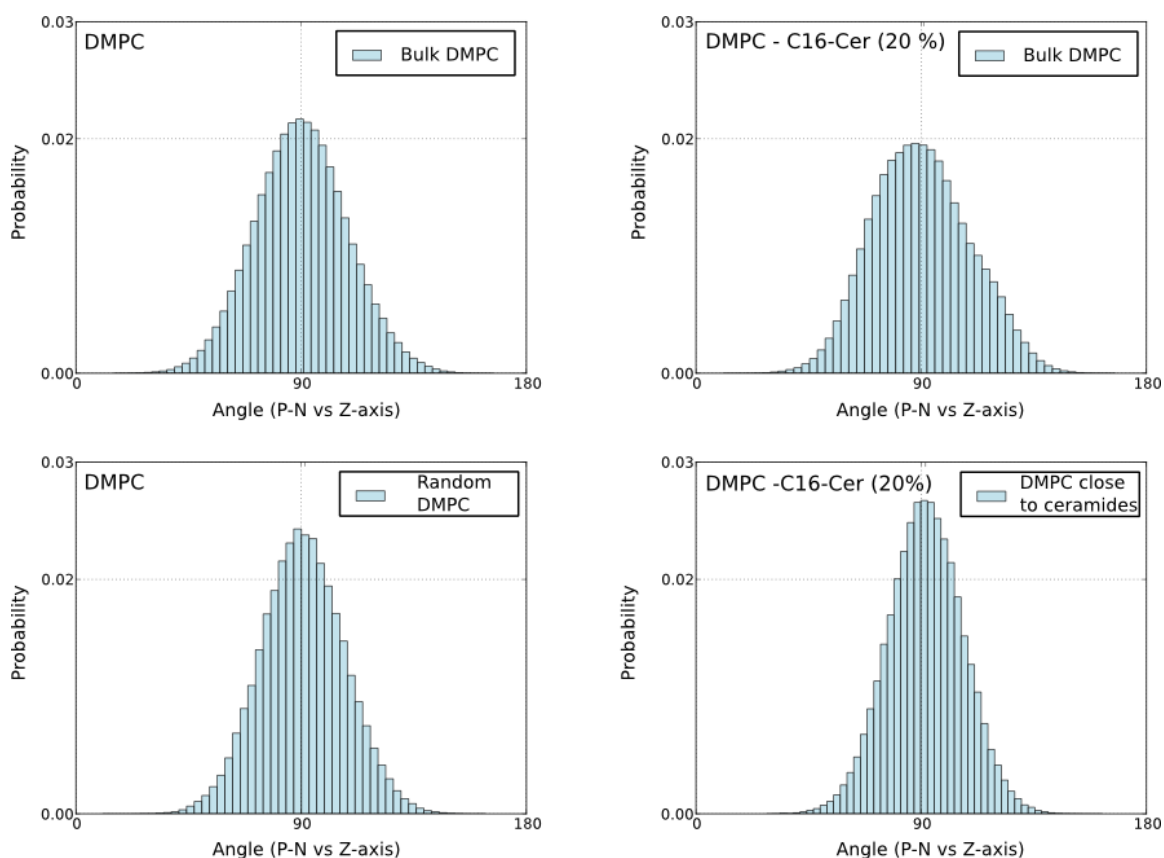


*Figure 5-13: Histograms of P-N vectors with Z axis of the simulation box for pure DMPC and DMPC-C16-Cer mixture: bulk DMPC (upperleft) and DMPC with close vicinity to random lipids (lowerleft) for DMPC bilayer; bulk DMPC (upperright) and DMPC with close vicinity to ceramides (lowerright) for DMPC-C16-Cer mixture.*

## 5.3.2 Solid State NMR

### 5.3.2.1 Static $^{31}\text{P}$ -NMR

Firstly, in order to prove that DMPC stayed in lamellar bilayer phase with the addition of ceramide, static  $^{31}\text{P}$  NMR spectra of pure DMPC and the mixture were recorded at 310K. Figure 5-14 displays that the spectra for pure lipid and the mixture look quite similar. There is not any significant disturbance of the spectral lineshape of the DMPC phosphorus. This suggests that there is not any deviation from the lamellar phase with addition of 20% C16-Ceramide into the DMPC membrane. Lineshape analysis was performed for  $^{31}\text{P}$  spectra of pure lipid and the mixture. According to spectral analysis, isotropic chemical shift values for pure lipid and for the mixture were found to be -0.88 ppm and -0.82 ppm, respectively. Chemical shift anisotropy were not changing much either, as isotropic chemical shifts. They were found 29.8 ppm for pure DMPC and 31.3 ppm for the mixture.

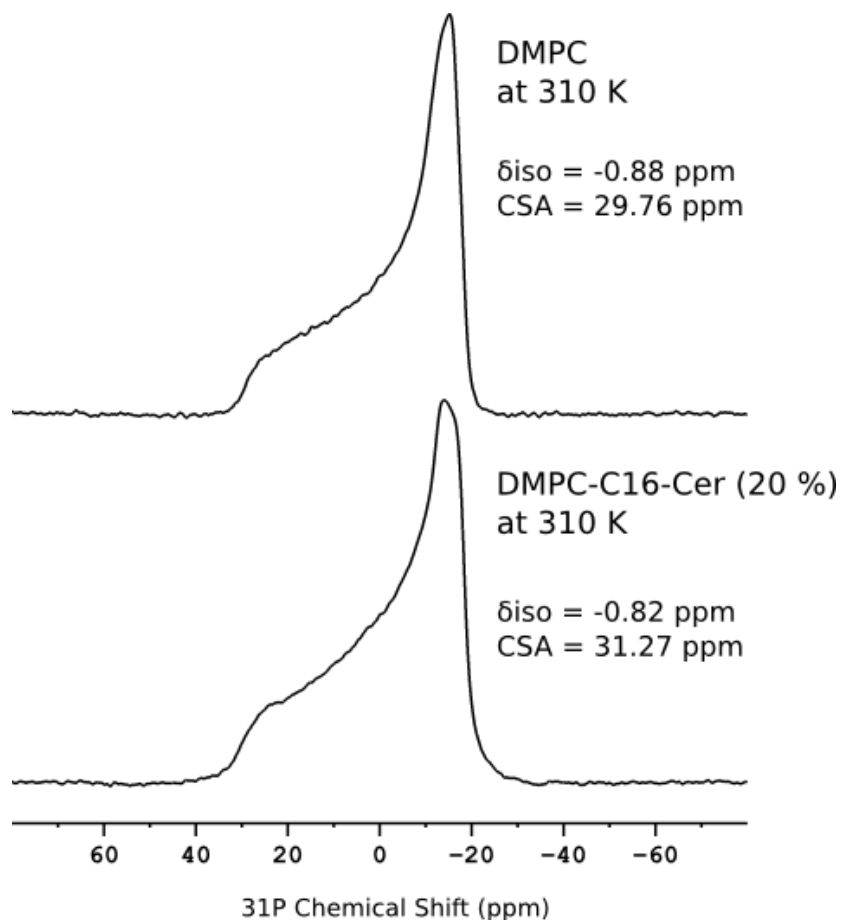
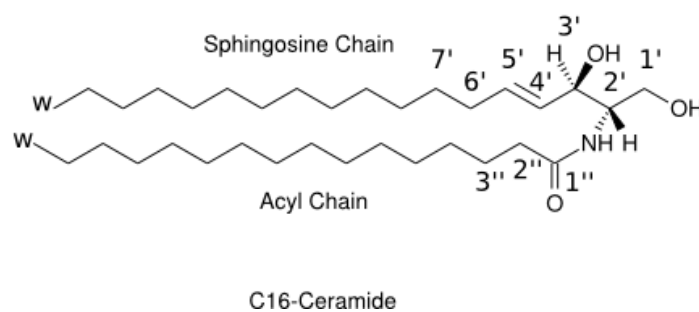
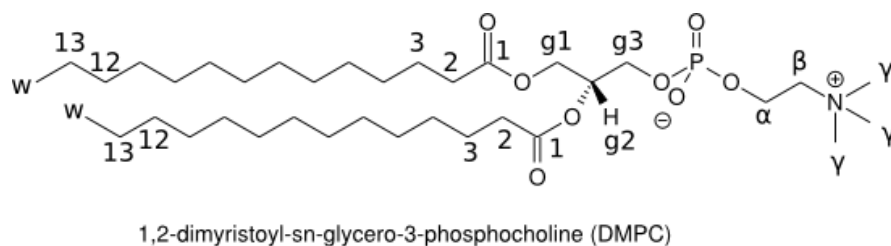


Figure 5-14:  $^{31}\text{P}$  static NMR spectra of mixture of DMPCd67- C16-Cer and DMPCd67 at 310 K: isotropic chemical shift ( $\delta_{\text{iso}}$ ) in ppm and chemical shift anisotropy (CSA) in ppm were calculated by lineshape analyses.

### 5.3.2.2 Temperature dependent $^1\text{H}$ -MAS NMR and $^1\text{H}$ -MAS NOESY

In this study, it is analysed, which are how C16-ceramide affects the properties of DMPC bilayers and whether there are specific interactions between ceramide and DMPC. Here, temperature dependent  $^1\text{H}$ -MAS NMR experiments were used to reveal effects of ceramide on the DMPC main phase transition.  $^1\text{H}$ -MAS NOESY experiments provide information on interactions between ceramide and DMPC molecules.



*Figure 5-15: Structures and assignments of DMPC and C16-Ceramide.*

$^1\text{H}$ - NMR experiments are very useful to monitor phase transition of lipids by varying the temperature. When lipids are in their liquid-crystalline phase, all proton NMR peaks are very narrow due to fast rotational diffusion of the lipids pre-averaging all anisotropic interactions. However, below the main phase transition temperature in the gel phase, lipid resonances are very broad due to restricted motions resulting in strong  $^1\text{H}$ - $^1\text{H}$  dipole couplings. Figure 5-15 displays structure and assignment of DMPC and C16-ceramide.

In order to observe ceramide effects on DMPC phase transition, pure DMPC and DMPC-C16-Cer (20 %) mixture were examined. Figure 5-16 shows phase transition profile for pure DMPC and DMPC-C16-cer (20 %) mixture. Main phase transition temperature of DMPC was higher in the presence of ceramide than the pure DMPC bilayer. Thus, this result shows that, ceramide increased phase transition temperature of DMPC.

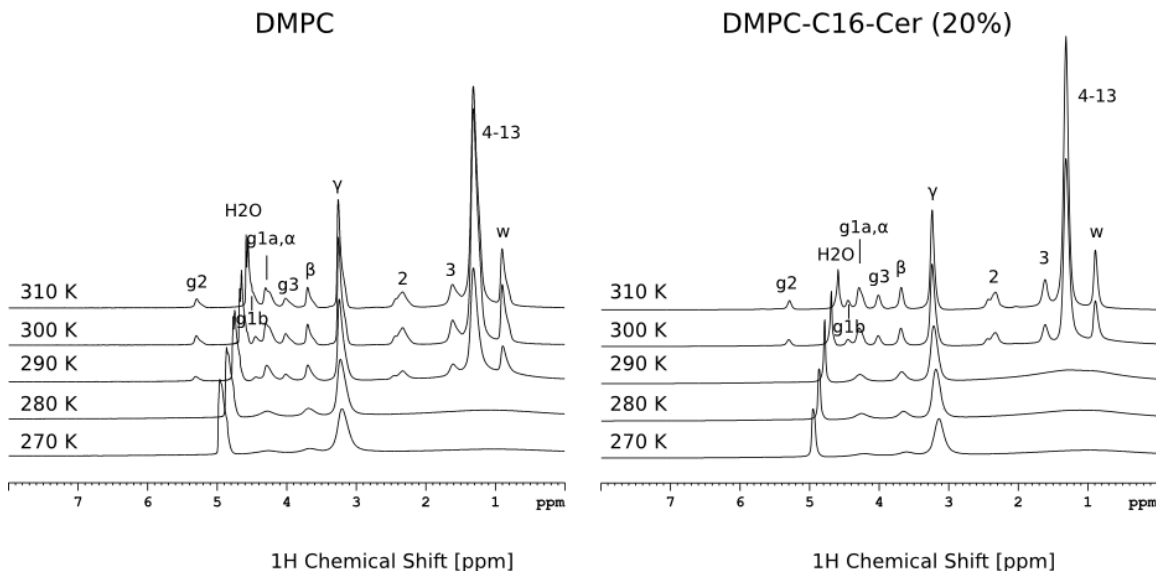


*Figure 5-16: Temperature dependent  $^1\text{H}$  NMR spectra of DMPC (left) and mixture of DMPC-C16-Cer (right). Phase transition temperature of DMPC shifted to higher temperature, from 290 K to 300 K, in the presence of C16-Cer.*

It is also of interest to monitor phase transition of C16-Cer in the DMPC bilayer. In order to see ceramide resonances, DMPC-d67 was used. In DMPC-d67, lipid protons, except in glycerol backbone, were exchanged with deuterium. Therefore in  $^1\text{H}$ -NMR measurements only ceramide peaks can be observed, except for peaks, which are belonging to glycerol protons of DMPC-d67. Figure 5-17 shows temperature dependent  $^1\text{H}$  NMR spectra of pure DMPC-d67, pure C16-Cer and mixture of DMPCd67- C16-Cer.  $^1\text{H}$  NMR assignments of ceramide peaks were done by solution-state NMR results, which were published for C18-ceramide and C16-dihydroceramide (Li, Tang et al. 2002). DMPC complete assignment for  $^1\text{H}$  nuclei by solid-state NMR was already published by different groups (Hong, Schmidt-Rohr et al. 1996; Nomura, Lintuluoto et al. 2011), which were indicated in the spectra (Figure 5-16 and Figure 5-17). It is easily seen that, for pure DMPC-d67, only glycerol peak can be observed. There are small peaks of lipid chain, which are coming from residual protons in lipid chains, which can be neglected. From glycerol protons it can be seen that, DMPC-d67 phase was sharply changed from liquid-crystalline to the gel phase in between 280-290 K.

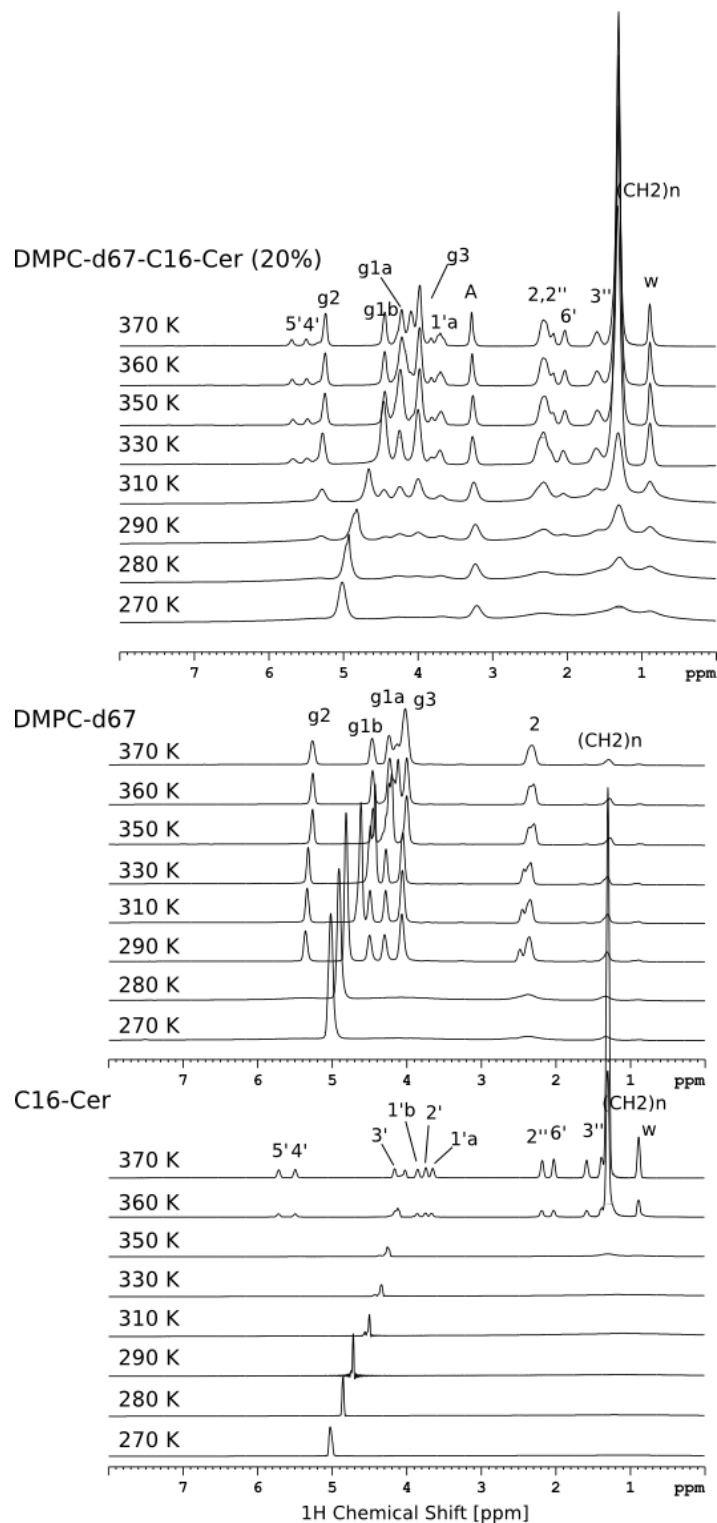


Figure 5-17: Temperature dependent  $^1\text{H}$  NMR spectra of mixture of DMPCd67- C16-Cer (top), pure DMPCd67 (middle) and pure C16-Cer (bottom). In the mixture, phase transition temperature of C16-Cer shifted to lower temperature, it follows the phase transition of DMPC.

Phase transition of pure ceramide was known to be around 90° (Shah, Atienza et al. 1995) and <sup>1</sup>H-NMR results also show very high and sharp phase transition temperature, around 360K for pure ceramide. For the mixture, since mainly ceramide peaks can be observed, the phase transition observed here is belonging to ceramide. Ceramide main phase transition temperature shifted in large extent to the lower temperature. In addition, transition occurs in a broader temperature range than pure ceramide. This suggests that, ceramide is behaving differently in DMPC bilayer than pure ceramide. Ceramides are dissolved in DMPC and follow the lipid phase transition.

<sup>1</sup>H-MAS NOESY experiments provide inter-molecular interactions between molecules. Here, ceramide inside DMPC-d67 was studied. DMPC and ceramide peaks appear in the same region in <sup>1</sup>H NMR spectrum. Therefore it is not easy to detect ceramide peaks. The advantage of using deuterated lipids is that lipid peaks are becoming invisible in <sup>1</sup>H NMR spectra so ceramide peaks can be detectable. DMPC-d67 is completely deuterated except glycerol backbone. Therefore, both ceramide peaks and DMPC glycerol peaks can be observed in NOESY spectra. In this way, interactions between DMPC and ceramide can be investigated. Figure 5-18 displays NOESY spectra of DMPC-d67 at 200 ms mixing time and Figure 5-19, Figure 5-20 and Figure 5-21 displays NOESY spectra of DMPCd67-C16-cer mixture at 50 ms, 200 ms and 400 ms mixing times respectively.

The NOESY spectra of DMPC-d67 alone (Figure 5-18) showed that mostly glycerol protons showed strong correlations. Since protons at the tails were mainly deuterated just some small peaks were observed from the residual protons at the hydrocarbon chains. Therefore for the mixture of DMPC-d67-C16-Cer, peaks for glycerol region can be assumed to be belonging to DMPC whereas peaks for the tail can be taken mainly as ceramide peaks.

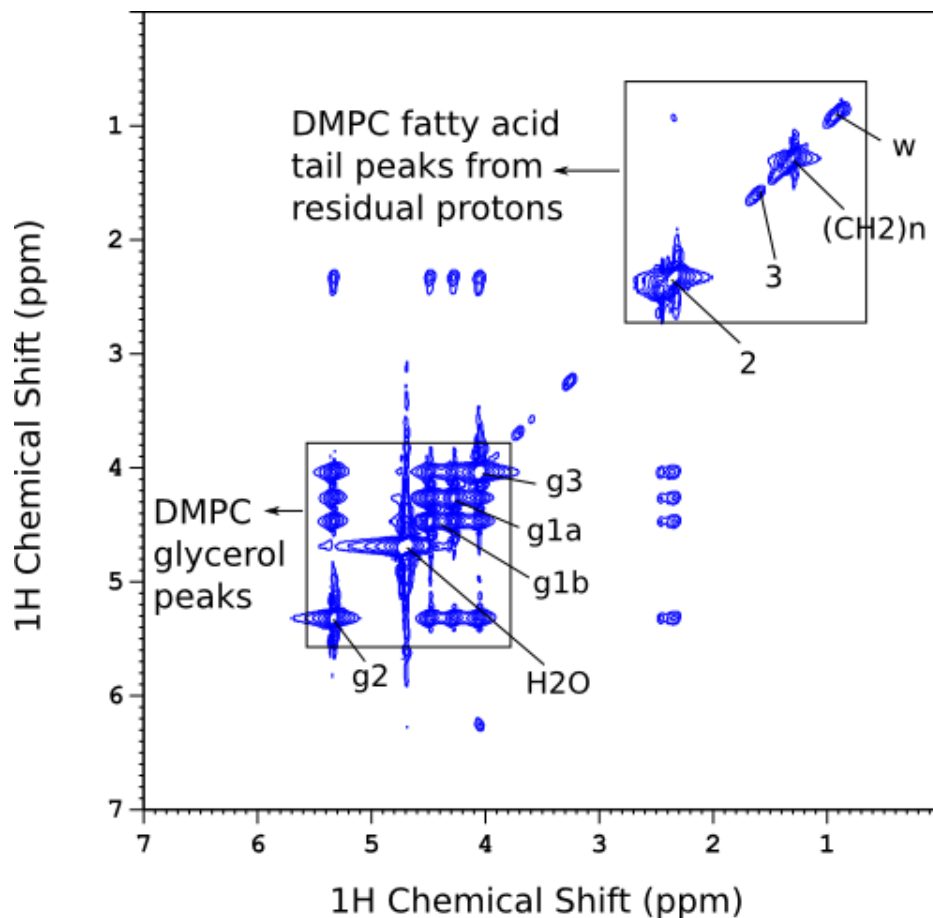


Figure 5-18:  $^1\text{H}$  MAS NOESY spectrum of DMPCd67 with 200 ms mixing time at 300 K: Glycerol peaks and residual acyl chain peaks are depicted into the rectangles.

For DMPC-d67-C16-Cer mixture, NOESY with short mixing time shows crosspeaks between DMPC nuclei that are stronger than crosspeaks between ceramide nuclei. This suggests that DMPC has faster magnetization buildup than ceramide. In order to quantify this observation, cross relaxation rates were calculated by the full-matrix approach (see Chapter 1). Buildup curves depicted in Figure 5-22, for ceramide peaks and DMPC glycerol peaks also indicate that magnetization exchange within DMPC (yellow region in the figure) is more rapid than within ceramide. This can be an indication that motions in ceramide molecules are slower than in DMPC molecules.



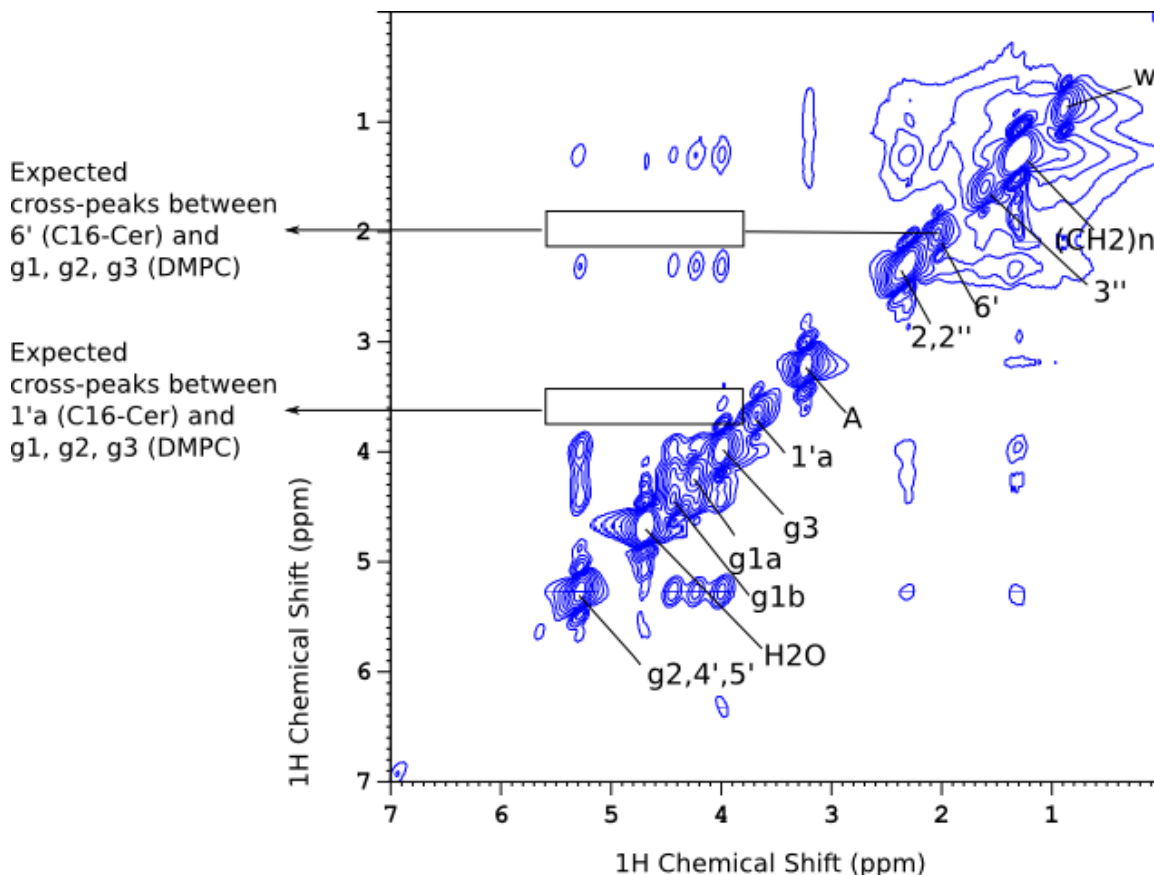


Figure 5-19: <sup>1</sup>H MAS NOESY spectrum of mixture of DMPCd67- C16-Cer with 50 ms mixing time at 300 K; boxes showed crosspeak region of g1, g2, g3 protons of DMPC with 6' and 1'a protons of C16-Cer.

The second observation of NOESY spectra is that ceramide nuclei both from tail and head group showed correlations with lipid glycerol (shown in rectangles in the spectra). This is an evidence for interactions between ceramide and DMPC molecules. Cross-relaxation rates were calculated by full matrix approach and depicted in Figure 5-23 for the nuclei, which are highlighted in NOESY spectra (Figure 5-19, Figure 5-20 and Figure 5-21). Nuclei 6'-H and 1'a-H from ceramide tail and head group, respectively, was chosen because these nuclei are belonging only to ceramides without any overlap with residual DMPC protons. Other peaks may contain some contributions from residual DMPC protons. Figure 5-23 clearly showed that 6'-H has correlations mainly with ceramide itself. However, 1'a-H showed correlations between ceramide peaks as well as between

DMPC glycerol peaks. This supports that ceramide and DMPC head groups may be interacting with each other.

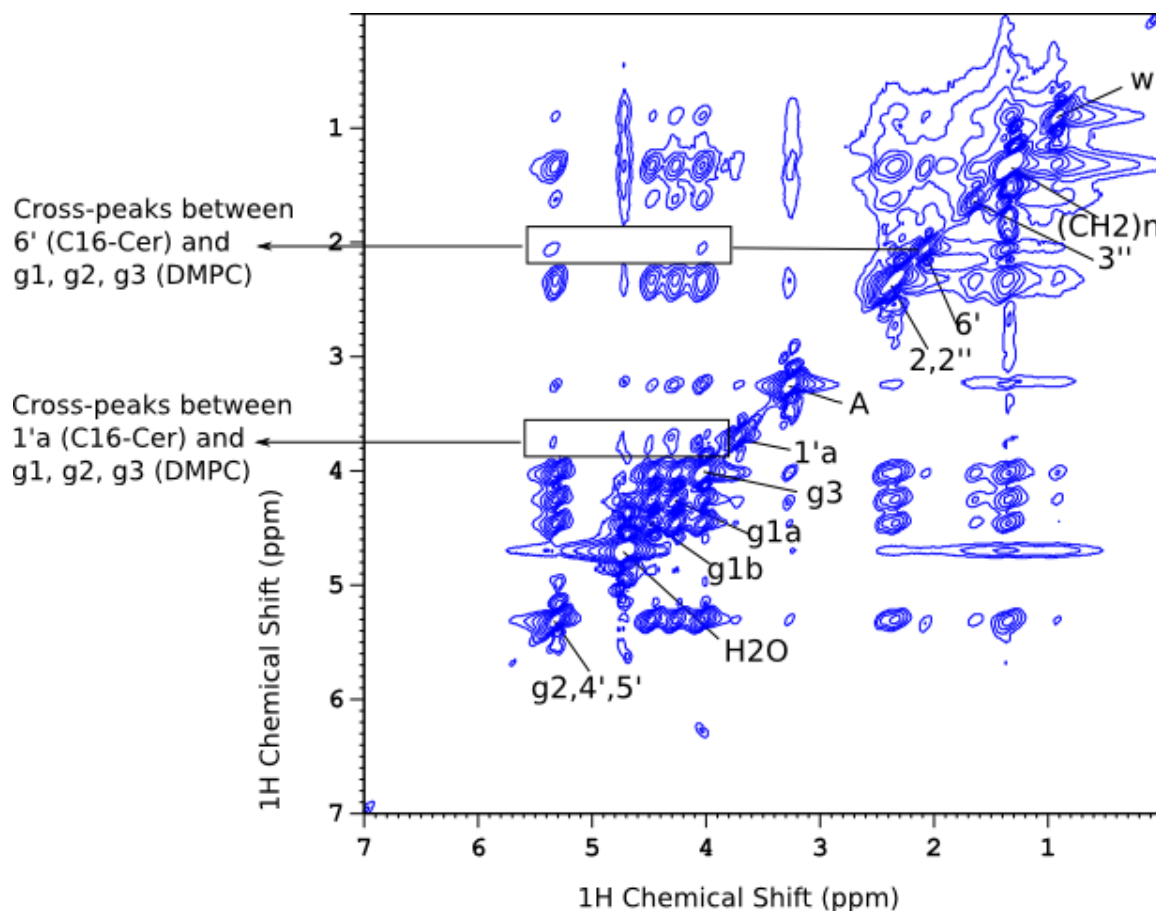


Figure 5-20:  $^1\text{H}$  MAS NOESY spectrum of mixture of DMPCd67- C16-Cer with 200 ms mixing time at 300 K; boxes showed crosspeak region of g1, g2, g3 protons of DMPC with 6' and 1'a protons of C16-Cer.

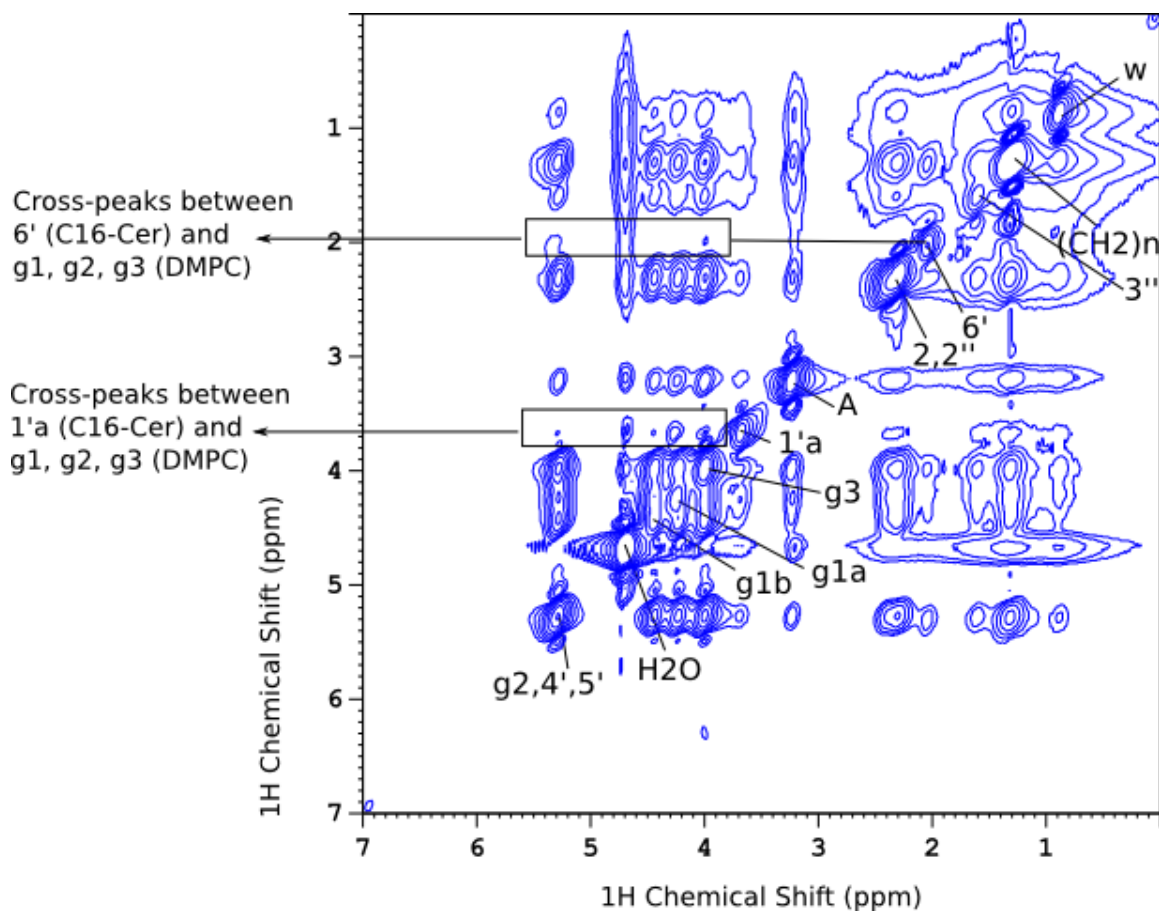


Figure 5-21:  $^1\text{H}$  MAS NOESY spectrum of mixture of DMPCd67- C16-Cer with 400 ms mixing time at 300 K; boxes showed crosspeak region of g1, g2, g3 protons of DMPC with 6' and 1'a protons of C16-Cer.

### MAS-NOESY Buildup Curves

Analysis is carried out with the full matrix approach.  
Every subplot is scaled to its own maximum intensity.

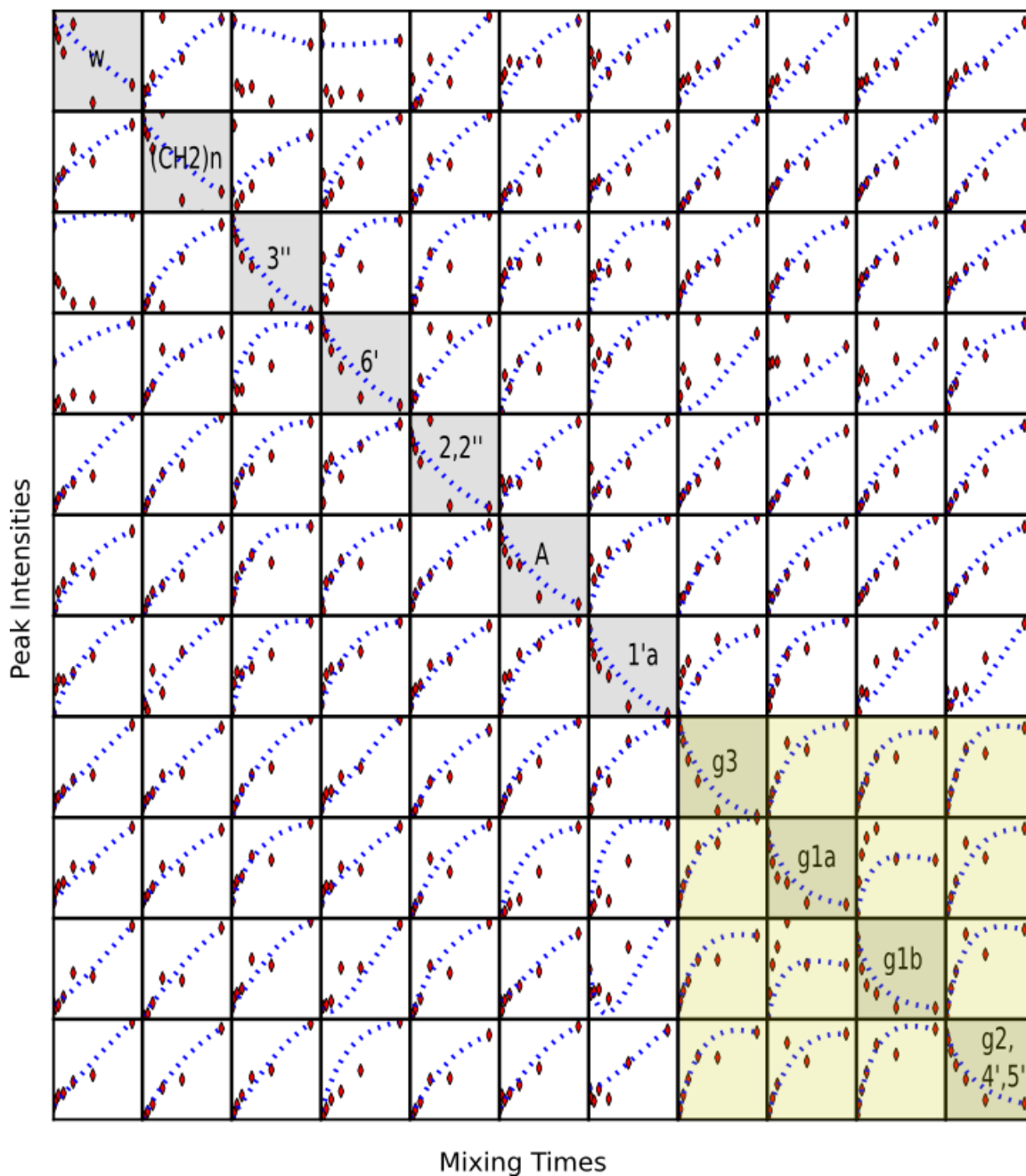
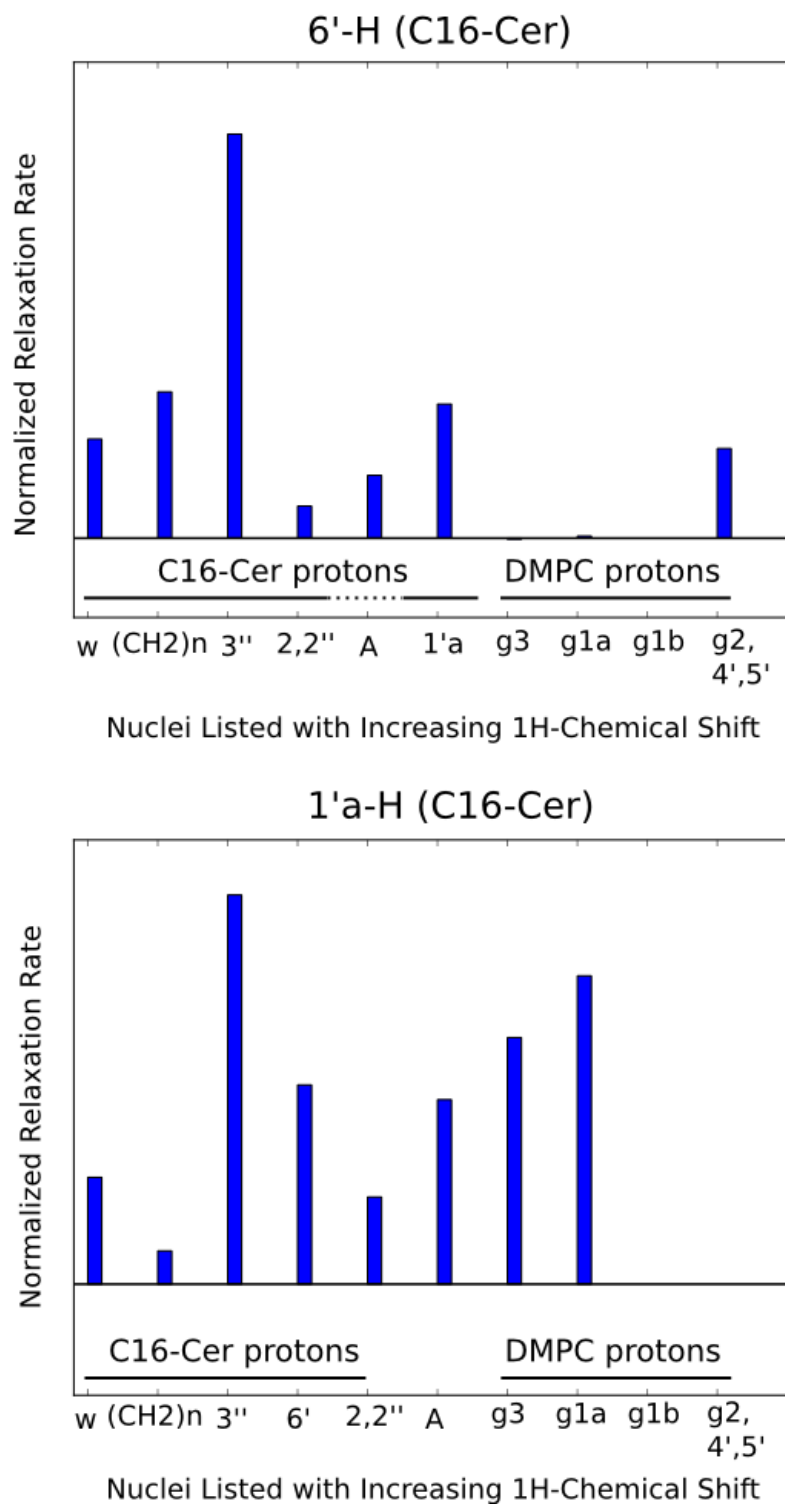


Figure 5-22: Buildup curves of peak volumes of <sup>1</sup>H-MAS NOESY of the mixture of DMPC-d<sub>67</sub>-C16-Ceramide at 300 K: The yellow region shows buildup curves at crosspeaks between DMPC glycerol backbone protons.



*Figure 5-23: Normalized cross relaxation rates of ceramide nuclei 6' (top) and 1'a (bottom) with C16-Cer and DMPC protons for the mixture of DMPCd67-C16-Cer at 300 K; C16-Cer and DMPC protons are depicted in the figure.*

However, there is one important problem here that makes interpretation of NOESY spectra difficult. Ceramide resonances partially overlap with signals from DMPC protons. Only 1'a can be unambiguously assigned. Therefore, crosspeaks observed between ceramide and DMPC glycerol protons could also partially be caused by intramolecular ceramide crosspeaks. Thus, it is difficult to reach an unambiguous result about the interactions between ceramide and DMPC molecules.

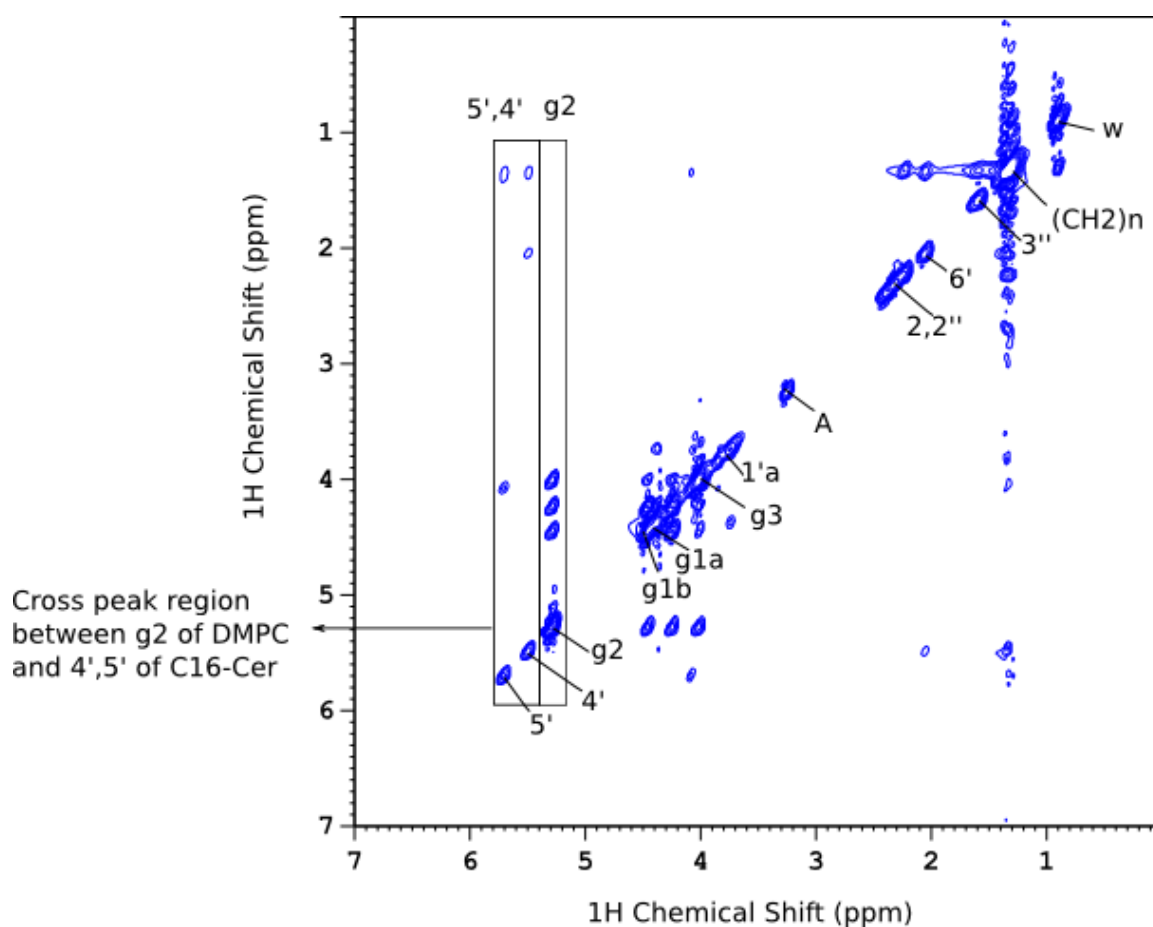


Figure 5-24:  $^1\text{H}$  MAS NOESY spectrum of mixture of DMPCd67- C16-Cer with 200 ms mixing time at 330 K: The arrow depicts, crosspeaks between DMPC g2 peak and C16-Cer double bond (4' and 5') peaks inside the rectangles.

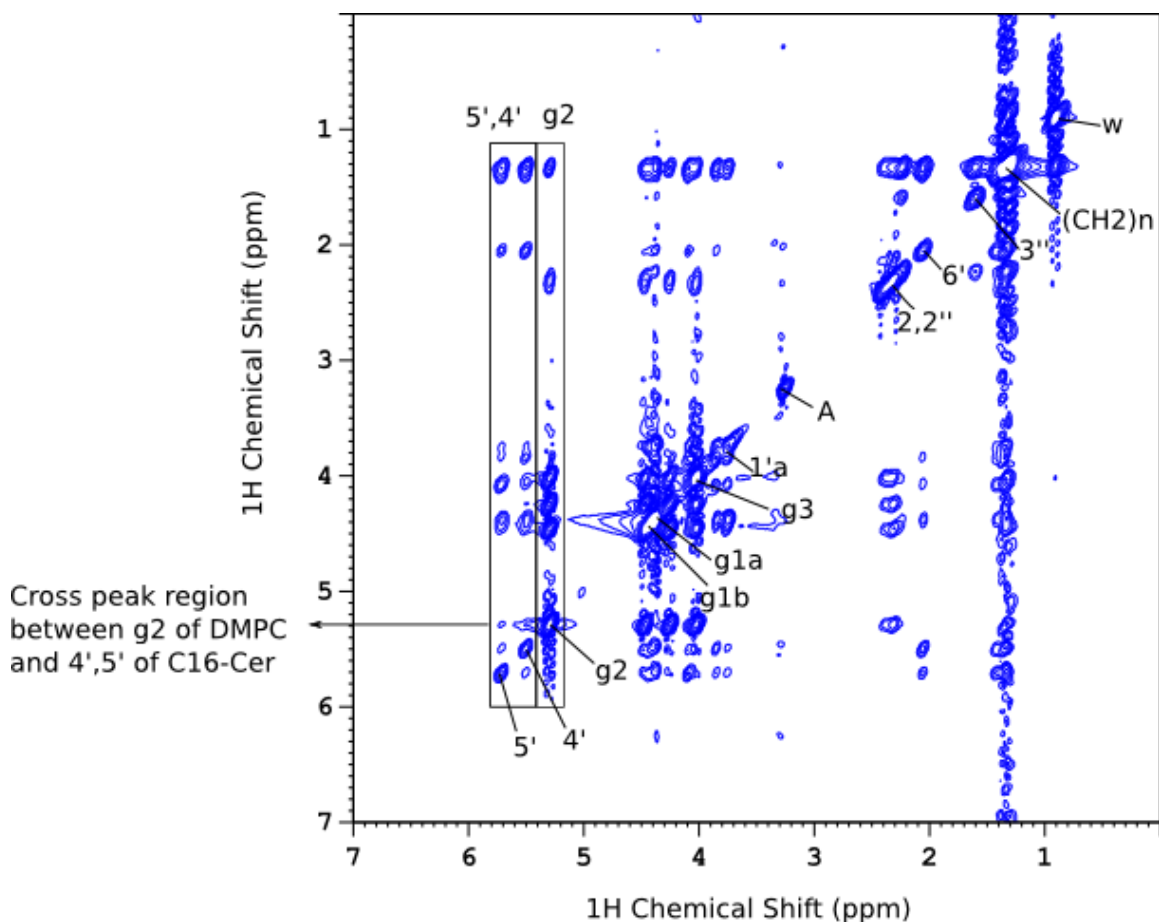


Figure 5-25:  $^1\text{H}$  MAS NOESY spectrum of mixture of DMPC-d<sub>67</sub>- C16-Cer with 800 ms mixing time at 330 K: The arrow depicts, crosspeaks between DMPC g2 peak and C16-Cer double bond (4' and 5') peaks inside the rectangles.

In order to overcome this ambiguity, NOESY experiments were repeated at 330 K. Because, from temperature dependent  $^1\text{H}$ -NMR experiments (Figure 5-17), it was known that at 330 K, two peaks, which are belonging to sphingosine double bond protons, 4' and 5', shifted to the more downfield region. As a result of the g2 proton of the glycerol backbone can be observed without any overlap with ceramide protons. Thus, this makes it possible to investigate C16-Cer – DMPC interactions without any ambiguity. NOESY spectra at different mixing times were recorded at 330 K. Figure 5-24, Figure 5-25 and Figure 5-26 displays NOESY spectra of mixture of DMPC-d<sub>67</sub>-C16-Cer for mixing time of 200 ms, 800 ms, and 1000 ms. At 300 K, it was already observed that, crosspeaks of

ceramide protons buildup very slowly. At 330 K, buildups of 4' and 5' protons were very slow. At 200 ms NOESY mixing time, they didn't show much crosspeaks. However at 800 ms, crosspeaks of 4' and 5' protons were strong. At this mixing time, as depicted in the Figure 5-25, 4' and 5' protons started to show correlations with g2 proton of DMPC. This already suggests that, ceramide and DMPC molecules are interacting with each other. In order to see crosspeaks between ceramide and DMPC better, a NOESY spectrum was recorded for a very high mixing time of 1000 ms. Figure 5-26 shows that, at this mixing time crosspeaks between DMPC g2 proton and ceramide 4' and 5' protons appeared to be very strong.

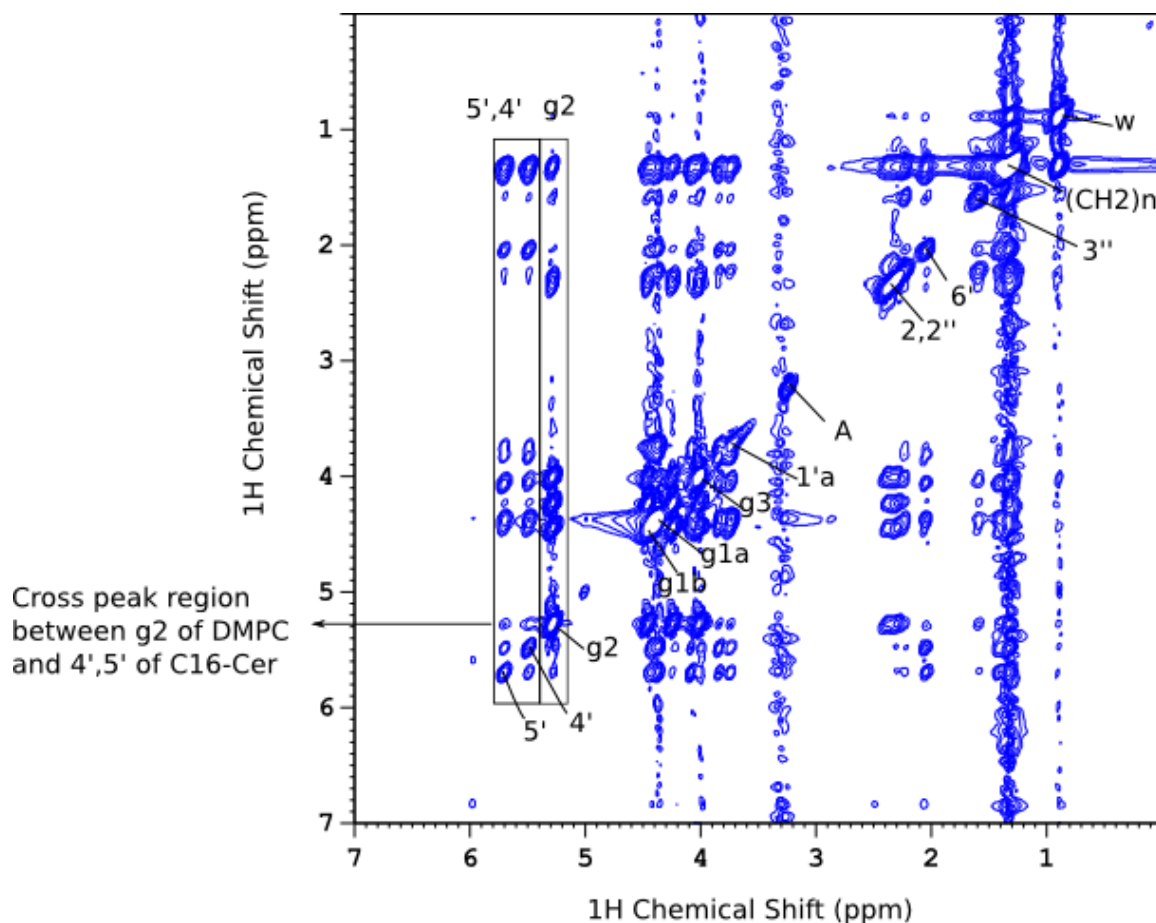
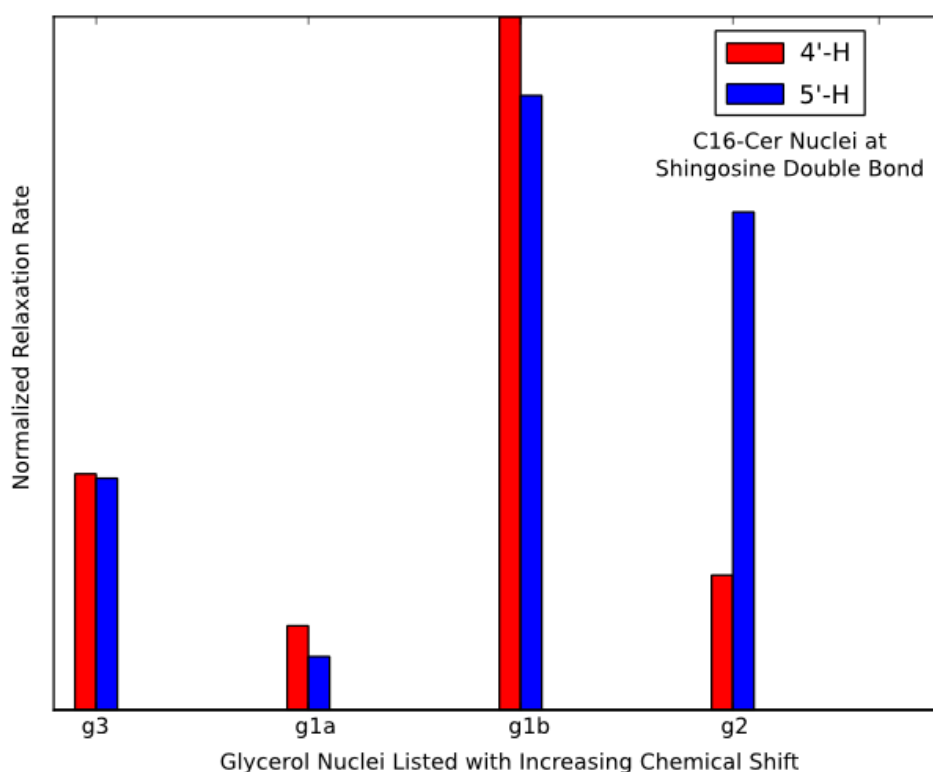


Figure 5-26: <sup>1</sup>H MAS NOESY spectrum of mixture of DMPCd67- C16-Cer with 1000 ms mixing time at 330 K: The arrow depicts, crosspeaks between DMPC g2 peak and C16-Cer double bond (4' and 5') peaks inside the rectangles.



Cross relaxation rates were also calculated for the NOESY experiments at 330 K by the full-matrix algorithm. Figure 5-27 shows relative cross relaxation rates for 4' and 5' protons with glycerol backbone protons, g1a, g1b, g2 and g3. Cross relaxation rate for g2 is comparable with other glycerol protons. This suggests that for other glycerol peaks even in the presence of ceramide-ceramide contacts, contributions from DMPC-ceramide contacts are quite high.



*Figure 5-27: Normalized cross relaxation rates of ceramide nuclei 4' and 5' with DMPC nuclei at the glycerol backbone for the mixture of DMPCd67-C16-Cer at 330 K.*

It was already shown by NOESY spectra at 300 K that for ceramide and DMPC protons intermolecular crosspeaks can be observed. As a support to this result, experiments at 330

K indicated interactions between ceramide and DMPC protons unambiguously.

Both  $^1\text{H}$ -NMR 1D spectra and the NOESY spectra reveal an additional resonance labeled 'A', which is unique to the DMPCd67-C16-cer mixture (Figure 5-17, Figure 5-19, Figure 5-20 and Figure 5-21). Relaxation rates of this peak with DMPC and C16-Cer peaks shows that A has correlations with both ceramide and DMPC resonances (Figure 5-28). This suggests that peak A could arise from either ceramide or DMPC and is shifted due to interactions between these molecules. It could be also possible that DMPC and ceramide form hydrogen bonds, so peak A might belong to H-bonded protons and indicates specific DMPC-C16-Cer interactions.

In order to investigate H-bondings between ceramide and DMPC, deuterium exchange experiments have been carried out. Figure 5-29 displays  $^1\text{H}$  NMR of pure lipid, pure ceramide and mixture in both  $\text{D}_2\text{O}$  and  $\text{H}_2\text{O}$  at 360 K. A peak was observed around 6.7 ppm, denoted as peak C, in the spectrum of the mixture in  $\text{H}_2\text{O}$ . It is characteristic peak of amide NH proton (Talbot, Vorobyov et al. 2000). Since it cannot be observed for the mixture in  $\text{D}_2\text{O}$ , it is an exchangeable peak most probably belonging to the amide proton of ceramide. In the literature, OH proton of ceramide found to be around 2.70 ppm (Li, Tang et al. 2002). However, OH peak couldn't be detected here maybe due to the overlap with other peaks around the same region. The peak A appeared in the mixture both in  $\text{H}_2\text{O}$  and  $\text{D}_2\text{O}$ . It was not observed in either pure DMPC-d67 or pure C16-Cer spectra but only spectra of the mixture. This suggests that this peak may be the result of a hydrogen bond formation between ceramide and DMPC, either with OH or NH protons of ceramide. It seems unlikely that this peak can be result of hydrogen bond of NH proton. NH proton appears around 6.7 ppm, which should be shifted more downfield in the case of H-bond formation (Yamauchi, Kuroki et al. 2000). On the other hand, peak A could be a result of H-bonded OH proton. It was reported that OH proton of ceramides appear around 2.7 ppm (Li, Tang et al. 2002). Therefore, it could be possible that, hydrogen bonded OH proton was shifted downfield to around 3.3 ppm where peak A appeared. Although, this peak can be assigned tentatively to an H-bond formation, it needs further verifications.

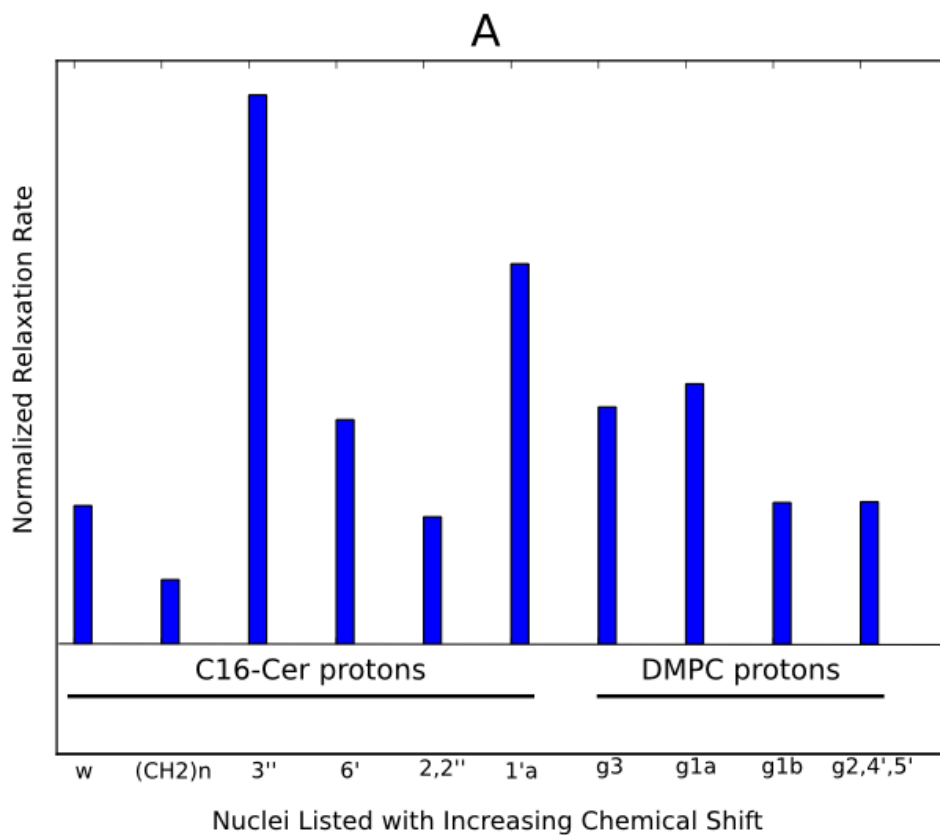


*Figure 5-28: Normalized cross relaxation rates of resonance A with C16-Cer and DMPC protons for the mixture of DMPCd67-C16-Cer at 300 K; C16-Cer and DMPC protons are depicted in the figure.*

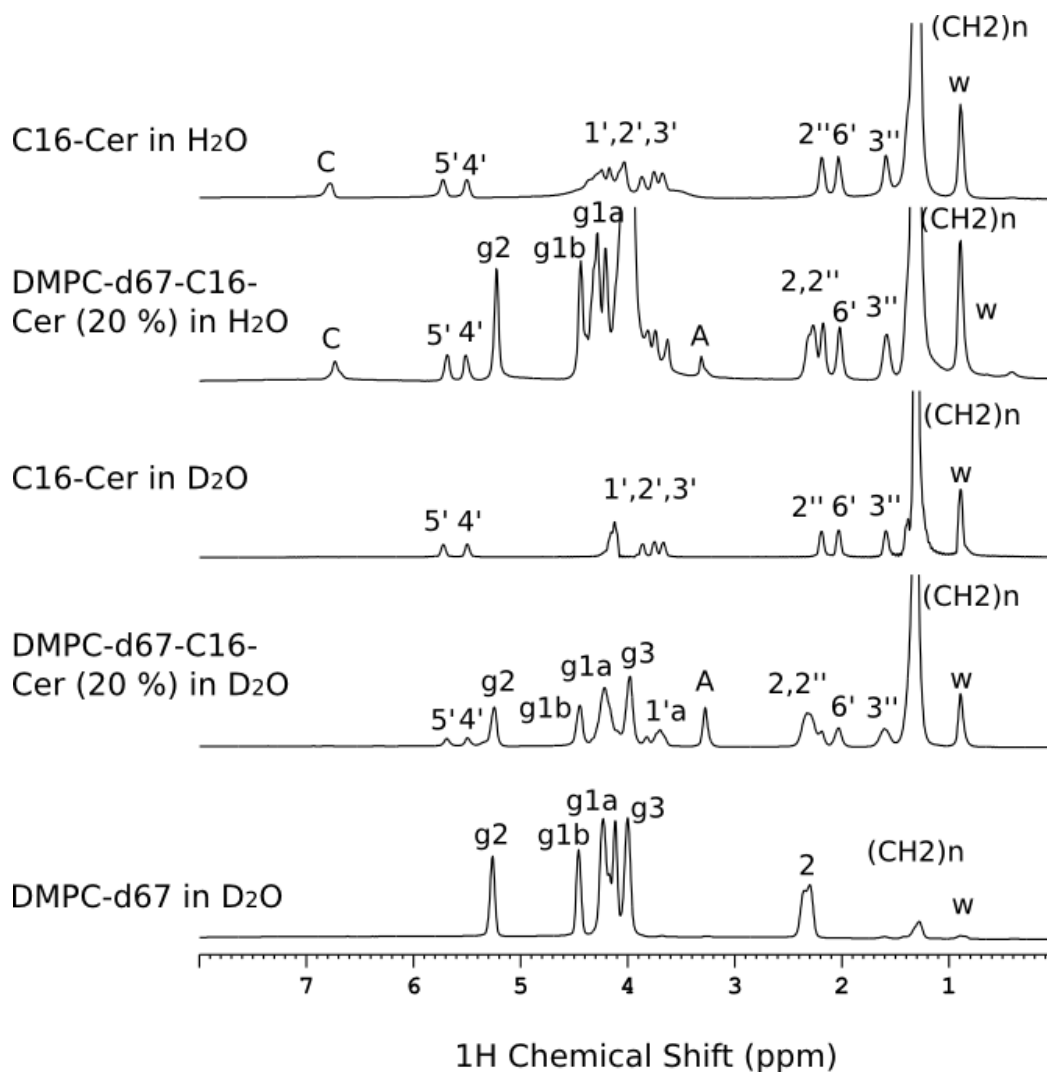


Figure 5-29:  $^1\text{H}$  NMR spectra of pure C16-Cer in H<sub>2</sub>O, mixture of DMPCd67-C16-Cer in H<sub>2</sub>O, pure C16-Cer in D<sub>2</sub>O, mixture of DMPCd67-C16-Cer in D<sub>2</sub>O and pure DMPCd67 in D<sub>2</sub>O: peak C is the exchangeable proton and peak A is seen only in the spectra of DMPC-d67-C16-Cer mixtures.

### 5.3.2.3 $^{14}\text{N}$ -MAS NMR

$^{14}\text{N}$  is a very convenient nucleus for NMR measurements with 99.6 % natural abundance. However, most of the cases it is not easy to observe it with available NMR instruments because of its large quadrupolar couplings. Fortunately, lipids that have choline head group, at liquid-crystalline phase are an exception. Due to the rotation around lipid axis as well as rotation of choline group, quadrupolar couplings are dynamically scaled.

Therefore, it is possible to observe  $^{14}\text{N}$  resonances for lipids. For this work,  $^{14}\text{N}$  MAS spectra of pure DMPC and the mixtures of DMPC with C16-Cer were recorded. The aim was to probe whether C16-Cer and DMPC can be differentiated and whether different populations can be observed. As can be seen in Figure 5-30, an isotropic peak and its sidebands were observed for pure lipid that was belonging to choline nitrogen at 300 K with 3 kHz spinning.

For the mixture, which contained 20 % C16-Cer, 2 peaks were observed at both 300 and 350 K and with 2 kHz spinning. One was belonging to the choline group of DMPC and its intensity was 7.6 times of the intensity of the small peak. Quadrupolar couplings of two peaks were calculated by side-band analyses. Quadrupolar coupling of DMPC choline group nitrogen was found to be 15 kHz for both pure DMPC and DMPC-C16-Cer mixture. Previously, quadrupolar couplings for choline group nitrogen of DMPC were reported to be the order of 10 kHz (Siminovitch, Rance et al. 1980; Siminovitch, Jeffrey et al. 1983). Thus, the quadrupolar coupling for DMPC obtained here is compatible to the quadrupolar coupling of lipid choline group nitrogen reported in the literature. Since there are only two different kinds of nitrogen, choline nitrogen of DMPC and amide nitrogen of ceramide, the second peak may be belonging to ceramide. However, it was not possible to see any nitrogen peak for the pure ceramide at very high temperature and fast spinning speed, 370 K and 15 kHz, respectively. Since in ceramide no additional motional averaging takes place as for the fast choline group rotation, quadrupolar coupling is not expected to be reduced same extent with DMPC nitrogen. Ceramide may become more flexible inside DMPC bilayer that may result an averaging in quadrupolar coupling of amide nitrogen. Even if rotational diffusion of ceramide is as fast as DMPC, averaging in quadrupolar coupling of ceramide nitrogen would be less than DMPC choline group nitrogen. Therefore, ceramide nitrogen would still have very large quadrupolar coupling and are hard to observe. In addition to this, studies on sphingomyelin was also suggesting that amide nitrogen of sphingosine has very large quadrupolar coupling, which could not be detected (Siminovitch and Jeffrey 1981).

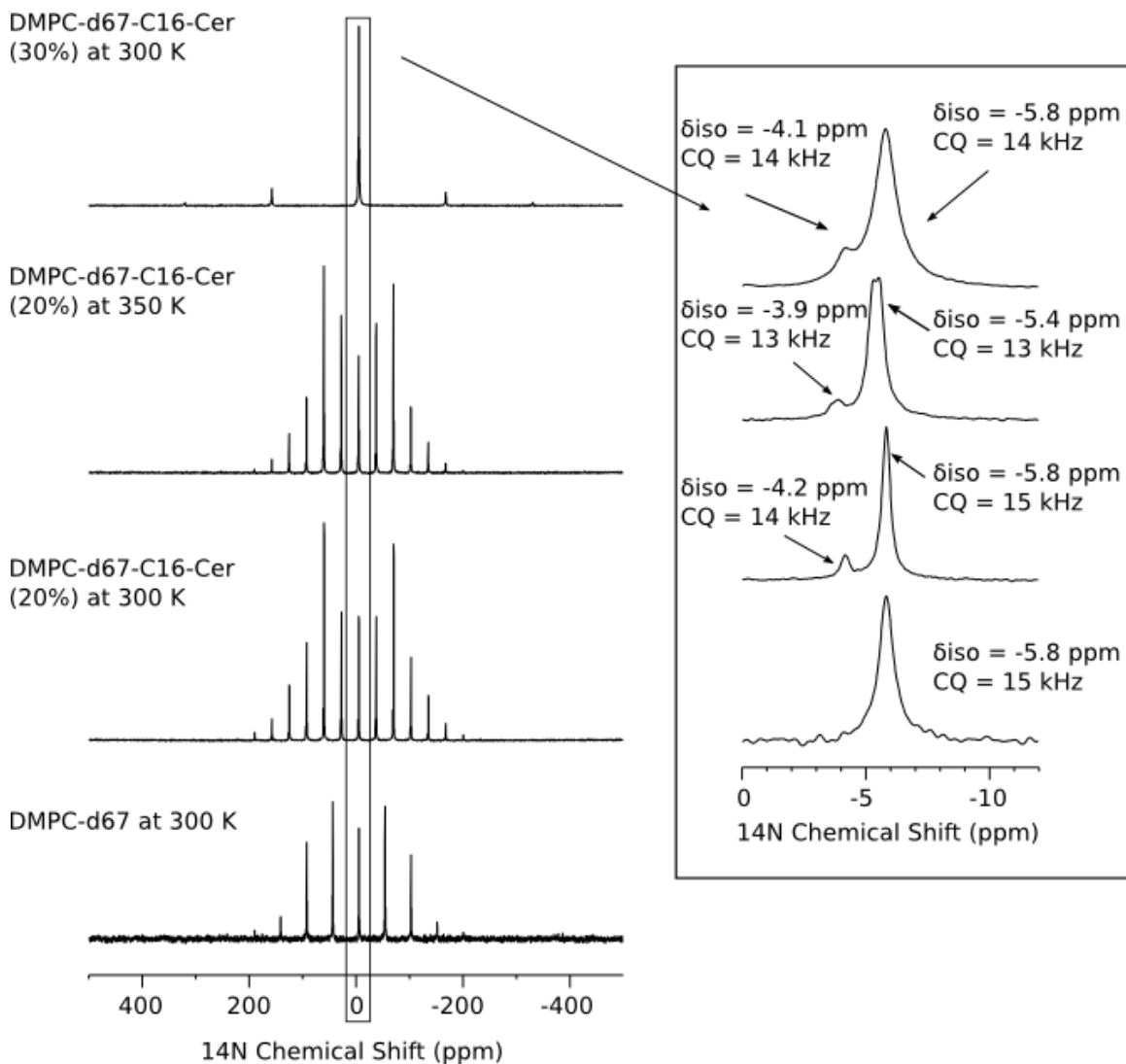


Figure 5-30:  $^{14}\text{N}$  NMR spectra of DMPCd67 at 300 K, mixture of DMPCd67- (20 %) C16-Cer at 300K and 350K and mixture of DMPCd67- (30 %) C16-Cer at 300K; isotropic chemical shift ( $\delta_{\text{iso}}$ ) in ppm and quadrupolar coupling (CQ) in kHz were calculated by side band analyses.

Therefore there are two other possibilities that might be the explanation of the appearance of the second peak. First one is the formation of two phases of DMPC in the presence of ceramide. However, the  $^{31}\text{P}$  NMR-MAS spectrum of the mixture (not shown here) showed only one isotropic peak, which suggests that there was no phase separation in the presence of ceramide. The second explanation is that the small peak can be again

belonging to choline nitrogen of DMPC molecules, which have strong interactions of ceramide. In other words, interactions between ceramide and DMPC may cause formation of DMPC-Ceramide complex. Therefore, chemical shift of choline nitrogen of this complex may be shifted. Isotropic chemical shifts and quadrupolar couplings of these two peaks, which were provided by line shape analyses were found to be very similar. This also supported that they both can belong to DMPC molecules with small differences in their head group orientation with the interaction of ceramide.

The ratio between two peaks was also supporting this hypothesis. In the mixture, DMPC to ceramide ratio is 4 to 1 whereas the ratio between big and small peaks was calculated as 7.6. This indicated that not all ceramides may form DMPC-ceramide complexes, but a certain amount of ceramides may be contributing to complex formation. Thus, ceramide molecules affect head group orientation of DMPC molecules, which are within close proximity of ceramides.

In order to see concentration dependence of  $^{14}\text{N}$  measurements, 30 % DMPCd67-C16-cer mixture were also examined at 300 K and with 10 kHz spinning. The second peak was also observed in  $^{14}\text{N}$  spectrum. The isotropic chemical shift and quadrupolar couplings of second peaks were almost same for the mixtures of 20 % and 30 % ceramide. The ratio between two peaks for 30 % ceramide mixture was calculated as 6.2. This is lower than the ratio for 20 % ceramide mixture. This shows that the second peak intensity increased with ceramide concentration. Hence, this is an indication that, increase in ceramide concentration affect head group orientation of larger number of DMPC molecules.

$^{14}\text{N}$  measurements showed two peaks of DMPC in different populations, which provide evidences for strong interactions between ceramide and DMPC molecules. P-N vector orientations calculated by MD simulations gave similar result with  $^{14}\text{N}$ -NMR experiments that ceramide change P-N vector orientation of DMPC molecules, which are at close vicinity with ceramides. There were already some hints about correlations between ceramide and DMPC from  $^1\text{H}$  NMR measurements. Therefore results from both  $^{14}\text{N}$  and  $^1\text{H}$  spectra pointing the presence of interactions between ceramide and DMPC,

which needs further studies to understand more about these interactions and possible complex formations.

#### **5.3.2.4 Dipolar Order Parameters**

The  $^1\text{H}$ -MAS data indicated differences in DMPC and C16-Cer dynamics and specific DMPC-C16-Cer interactions. Order parameters provide information on CH bond dynamics. Since solid-state NMR allows obtaining order parameters from dipolar couplings, here DMPC chain order parameters were investigated in the absence and presence of C16-ceramide.

Dipolar order parameters for DMPC and ceramide chains were investigated with the PISEMA pulse sequence (see Figure 2-7). In order to investigate order parameters of ceramide inside the mixture, DMPC-d67 was used. In this way, since DMPC chains were deuterated, it became possible to observe peaks that are belonging to ceramide chains even at low concentrations of ceramide. Order parameters of DMPC for pure lipid and the mixture were measured by using natural abundant DMPC. All measurements were repeated for 3 temperatures, 300 K, 315 K and 330 K. Figure 5-31, Figure 5-32 and Figure 5-33 show 1D slices of 2D PISEMA experiments for pure DMPC, DMPC-C16-cer and DMPCd67-C16-Cer samples, respectively, for 3 temperatures. Dipolar couplings and order parameters were calculated from dipolar splittings, which were measured from 1D slices of each peak for each sample. In order to see the difference better, order parameter profiles were plotted in Figure 5-34 for the measurements at 300 K, 315 K and 330 K. Since assignment of ceramide peaks were not known, ceramide order parameters were smoothed by assuming that order parameters were decreasing along the chain.



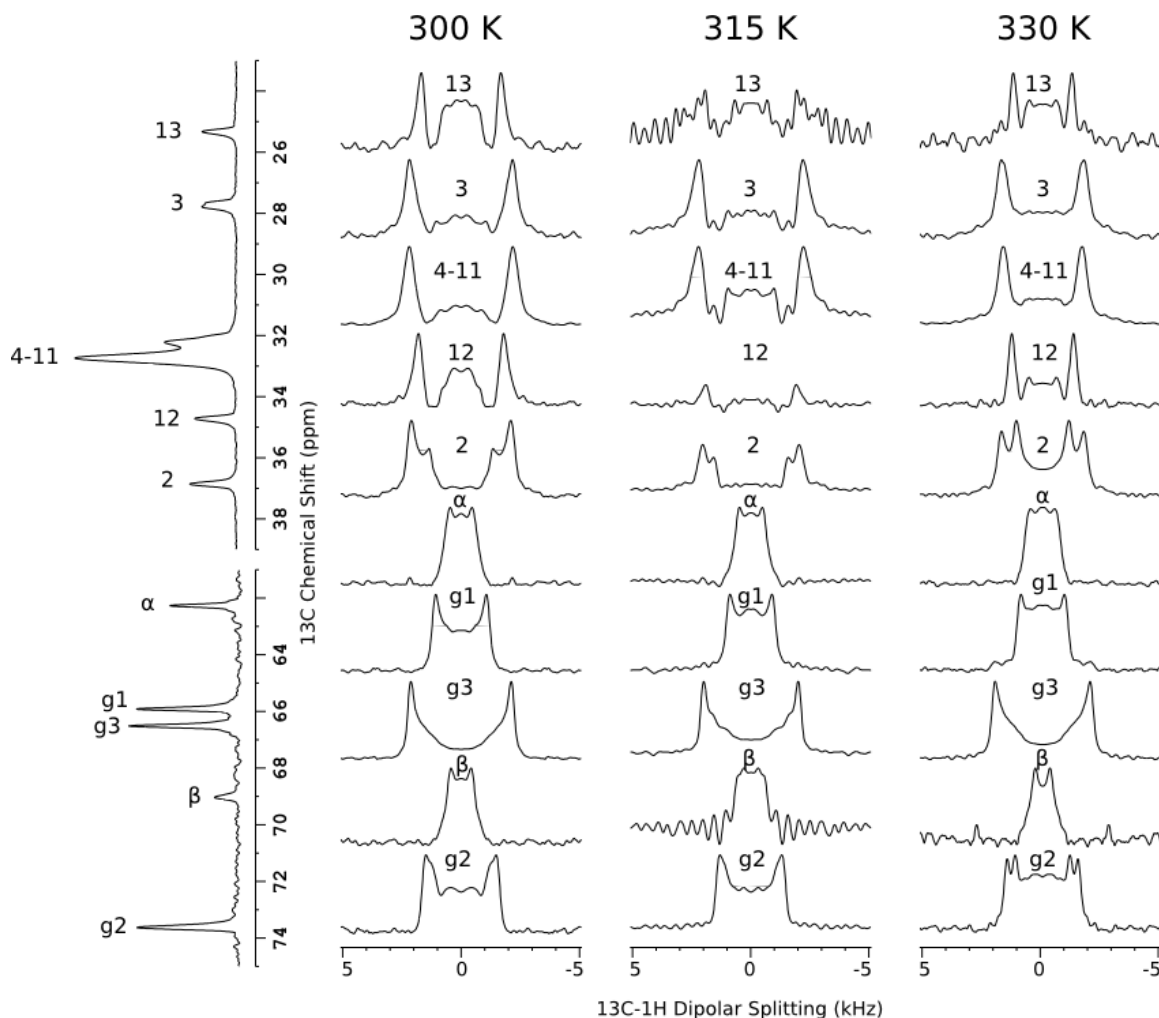


Figure 5-31: 1D slices of 2D PISEMA spectra of DMPC for the pure DMPC sample at 300 K (left), 315 K (middle) and 330 K (right).

At 300 K ceramide shows much higher order parameters than DMPC. Furthermore, pure DMPC has higher order parameters than DMPC that contained 20 % ceramide. This was an unexpected result, since results from MD simulations indicated higher order parameters for DMPC molecules in the presence of ceramide molecules (Figure 5-8). However, it is possible that, at low temperatures, DMPC and C16-Cer might not be mixed well. Temperature dependent  $^1\text{H}$ -NMR experiments showed that (Figure 5-16 and

Figure 5-17), at 300 K, DMPC is in the liquid crystalline phase whereas ceramide is in transition phase between gel to liquid crystalline phases. In such a case, ceramide would not have much effect on DMPC since they are not in the same phase.

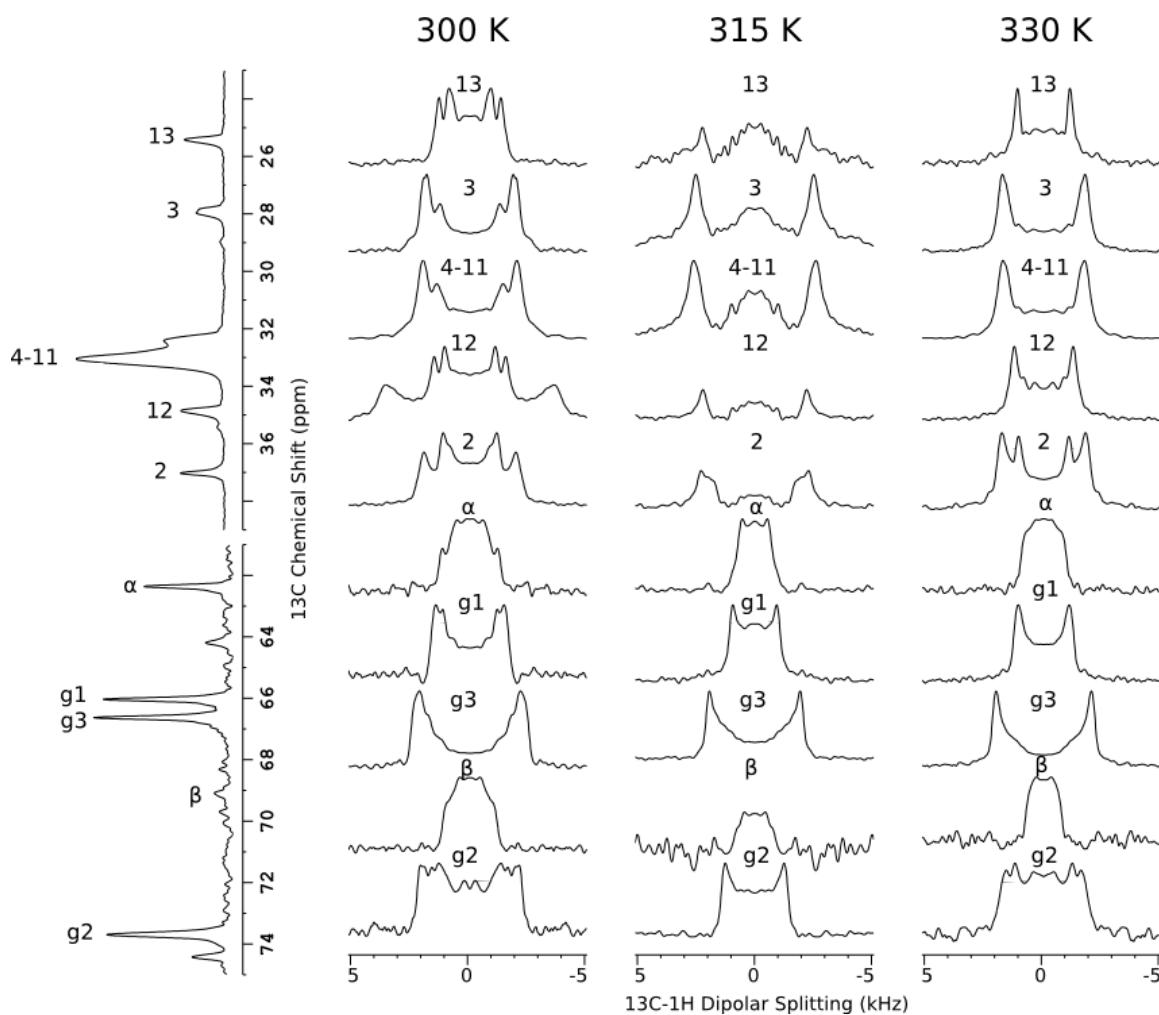
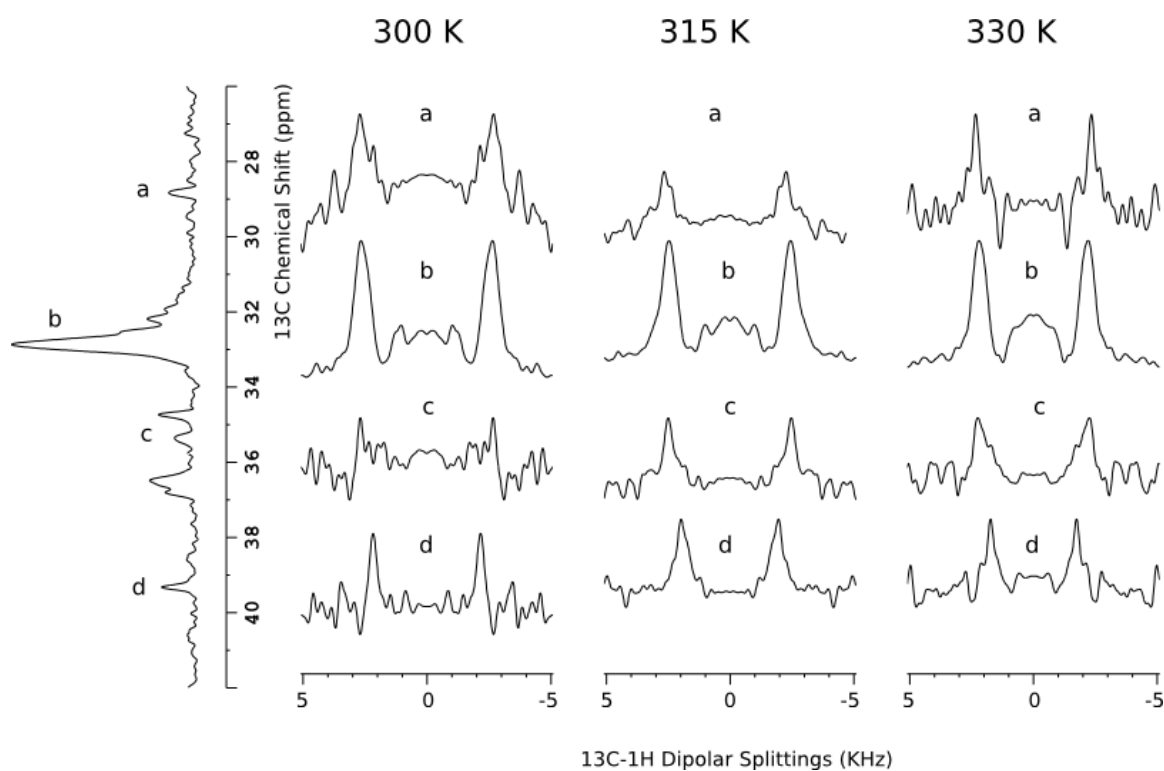


Figure 5-32: 1D slices of 2D PISEMA spectra of DMPC for the mixture of DMPC-C16-Cer at 300 K (left), 315 K (middle) and 330 K (right).

Therefore same experiments were repeated at higher temperatures, 315 K and 330 K. At 315 K, order parameters of DMPC in the mixture were higher than order parameters of pure DMPC (Figure 5-34). In the mixture, DMPC order parameters were increased in significant amount that order parameters of DMPC and ceramide became very similar. This result is quite consistent with MD simulation result. This clearly showed that, at 315 K, ceramide and DMPC mixed well that ceramide started to effect fluidity of DMPC. At, 330 K, order parameter of DMPC in the mixture started to drop down again and come close to pure DMPC order parameters. Ceramide order parameters had dropped down but not at the same extent with DMPC. Therefore, significantly higher order parameters were obtained for ceramide than DMPC in the mixture at 330 K.



*Figure 5-33: 1D slices of 2D PISEMA spectra of C16-Cer for the mixture of DMPCd67-C16-Cer at 300 K (left), 315 K (middle) and 330 K (right); a, b, c, d are C16-Cer peaks with increasing chemical shift.*

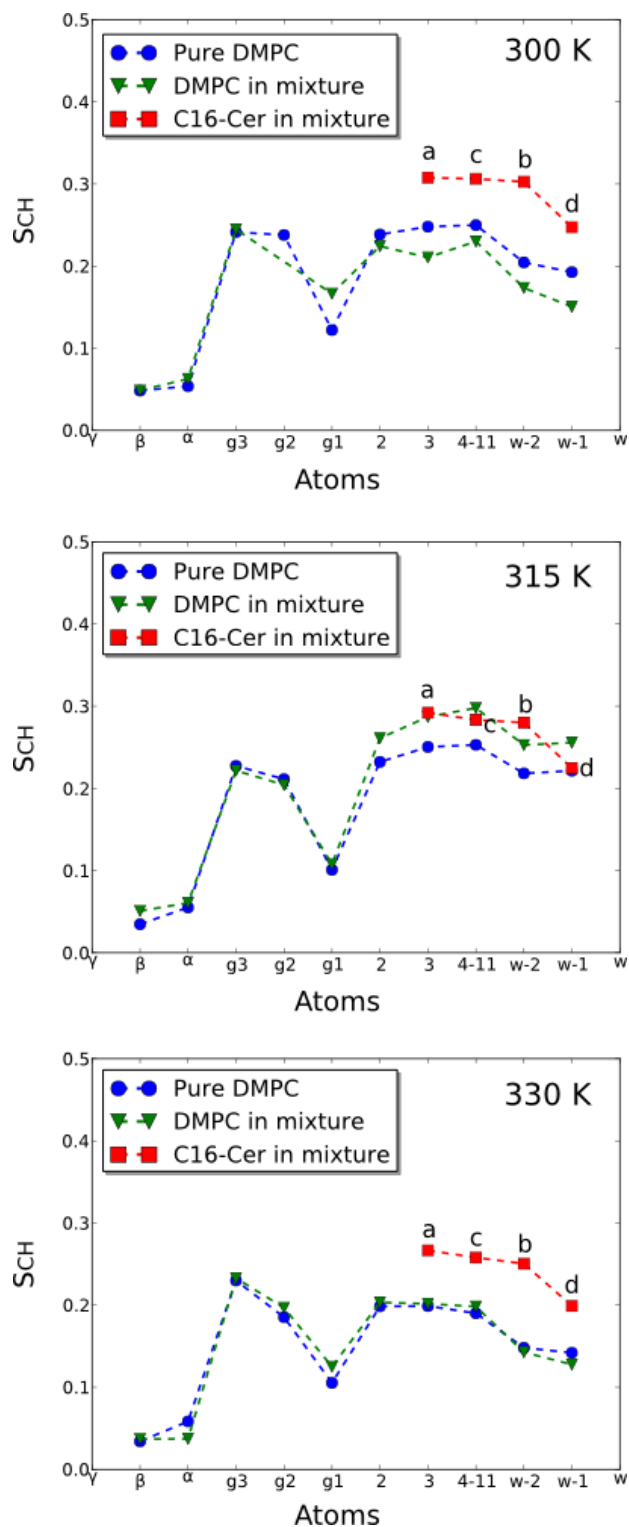


Figure 5-34: Order parameter profiles of DMPC ( in pure DMPC and DMPC- C16-Cer mixture) and C16-Cer( in DMPCd67-C16-Cer mixture) at 300 (top), 315 (middle) and 330 K (bottom); order parameters for C16-Cer peaks a, b, c and d were plotted in descending order.

These results showed that, effects of ceramides on DMPC bilayers differ with temperature. At low temperature, ceramide and DMPC is not mixed well and as a result ceramide does not have an effect on orders of DMPC chains. Just around 315 K, ceramide increases order parameters of DMPC at a certain amount that ceramide and DMPC chains are becoming very similar in terms fluidity. However, at 330 K, DMPC order parameters decreased significantly and as a result DMPC chains become more flexible than ceramide chains.

### 5.3.2.5 <sup>31</sup>P-CODEX Measurements

So far lipid motions were investigated in short time scales. As explained before, NMR exchange experiments provide informations in longer time scales up to seconds. Therefore they can be very useful to observe possible effects of ceramide on the slow motions of DMPC bilayers. Slow motion involves undulations and translational diffusion. Here, the CODEX experiment, which was explained in methods chapter, was applied to pure DMPC and DMPC-C16-Cer mixture at below and above phase transition temperature of DMPC. Figure 5-35 shows the CODEX dephasing curves for two samples at two different temperatures. At low temperature, with DMPC in the gel phase, ceramide had a strong effect on the CODEX curve of DMPC phosphorus nucleus. The rate of decay for DMPC in mixture was much slower than the one for pure DMPC. The curves show a mono-exponential decay with very different correlations times for pure DMPC and the mixture. Correlation time for DMPC was found to be 8.87 ms and for DMPC-C16-Cer was 32.53 ms, almost 4 times larger than pure DMPC, at 270K. This is an important finding that suggests that ceramide has a significant effect on slow motions of DMPC bilayer at gel phase. The nature of these motions is not quite clear. They can be caused by lateral diffusion as suggested in the literature (Marasinghe, Buffy et al. 2005; Saleem, Lai et al. 2012). However, in gel phase lateral diffusion is expected to be much slower than in fluid phase. Therefore additional motions could contribute to the CODEX dephasing at the gel phase. Another possible source for these motions could be collective membrane undulations (Goetz, Gompper et al. 1999; Otten, Brown et al. 2000). Ceramide

may have an effect on the frequencies of such undulations. However, studies on MD simulations in phospholipid gel phase showed that undulatory motions are suppressed in gel phase (Marrink, Risselada et al. 2005). Therefore, nature of slow motion of DMPC in the gel phase observed in CODEX dephasing is still not clear.

In the liquid crystalline phase, a CODEX decay curve was not obtained as expected. A continuous decrease in the intensity of the signal of the  $^{31}\text{P}$  peak with the increasing mixing time was expected. However, fluctuations in the peak intensities for DMPC  $^{31}\text{P}$  at 300 K were observed. This result indicates that there are some interfering motions in lipids at liquid crystalline phase, which cause refocusing of signal at certain mixing times.

Several test experiments were performed in order to explain the unusual fluctuations in CODEX curves. First of all, CODEX experiments with direct polarization (DP) and cross polarization (CP) were compared. The only difference of these experiments is that, in CP magnetization is transferred from proton to phosphorus whereas in DP magnetization of phosphorus is obtained by direct  $90^\circ$  pulse on phosphorus channel (Figure 2-12). With both experiments, very similar profiles were obtained. Fluctuations in CODEX curves were weaker but still observable in CP-CODEX. Then, the second change was done in phase cycling. Longer phase cycle was implemented into the pulse sequence (Wachowicz, Gill et al. 2009). There was an improvement in the dephasing curve however there were still strong fluctuations in the curve.

A series of tests were done by performing different sample preparations. All the experiments were performed on multi-lamellar DMPC vesicles, which are prepared with the standard method. Since multi-lamellar vesicles are not homogenous in vesicle size, different sizes may result in different motions and may interfere for the CODEX curves. Therefore, unilamellar vesicles were prepared in  $\text{D}_2\text{O}$  and also in sucrose buffer described in the literature (Saleem, Lai et al. 2012). In each case, CODEX curves show similar fluctuations with multi-lamellar DMPC. Same procedure was performed with also POPC and observed very similar behavior with DMPC. These results showed that, regardless of

vesicle size homogeneity, lipids have very complicated motions in the time scales that CODEX experiment is performed.

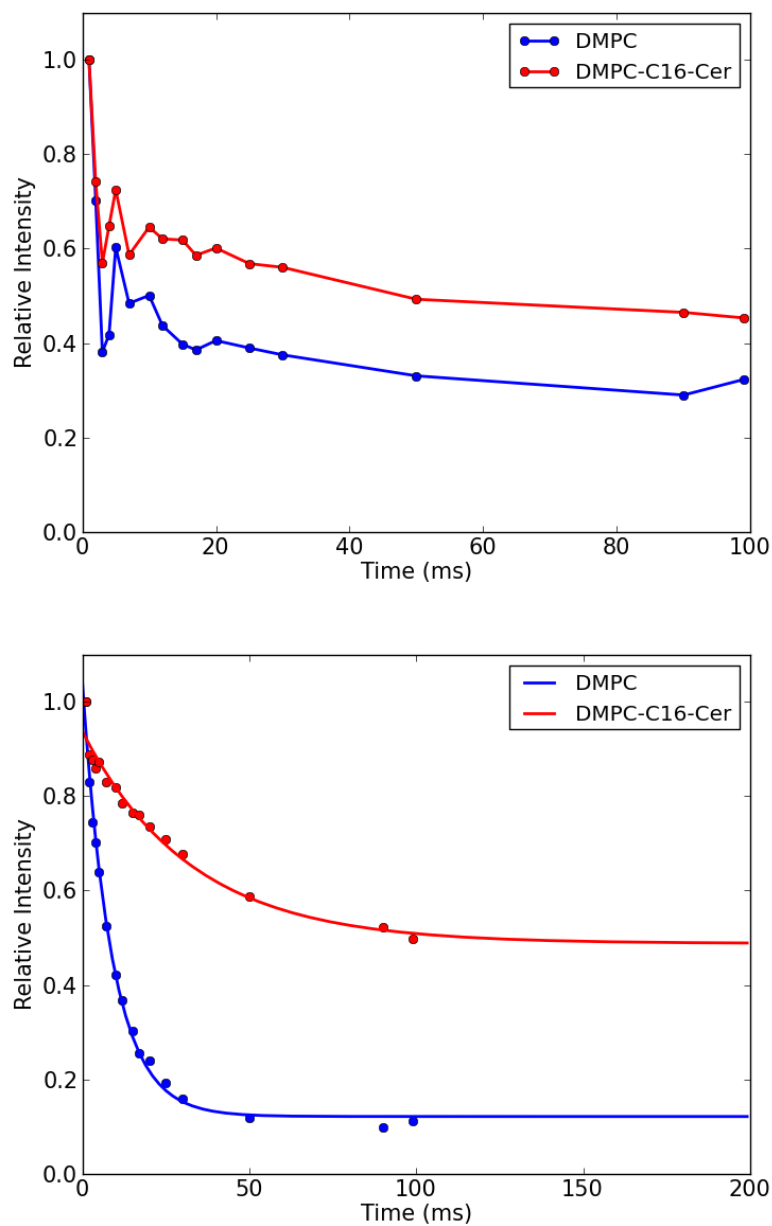


Figure 5-35 :  $^{31}\text{P}$ -CODEX dephasing curves for DMPC and DMPC-C16-Cer mixture at 300 K (top) and 270 K (bottom).

Experiments were repeated for shorter mixing times at multiples of rotor periods up to 1ms. Even for shorter times, magnetization is fluctuating with increasing mixing times. Number of recoupling pulses was varied as well as spinning speed. None of these tests provide any improvement. One interesting result was obtained by using spacers for the NMR rotors. When samples were packed thoroughly by using top and bottom inserts, it seemed that fluctuations were stronger. Without usage of any inserts, lipids were tending to stay at the wall of the rotor and it might affect the interfering motions. Therefore, the source of these jumps in magnetization can be related with orientation of samples. Further studies should be done to investigate more about this finding. However in any cases, CODEX seems not to be an appropriate method to investigate slow motions in membranes at liquid crystalline phase, since membranes have many interfering motions those make CODEX curve complicated to be interpreted.

### 5.3.2.6 $^{31}\text{P}$ Static Exchange Measurements

In addition to CODEX method,  $^{31}\text{P}$  static exchange experiments can be also useful to observe slow motions in membranes. In 1D static  $^{31}\text{P}$  experiment of lipids, typical axially symmetric spectra are observed. In 2D experiment, due to the reorientation of chemical shift tensor, the spectral shape diverted from diagonal ellipsoid. Here 2D  $^{31}\text{P}$  exchange spectra were recorded for DMPC and DMPC-C16-Cer mixture at below and above phase transition temperature for 5 ms and 400 ms mixing times to see the exchange for short and long mixing times.

Figure 5-36 shows that for DMPC both for liquid crystalline and gel phase, exchange occur for long mixing time. It was also depicted with CODEX experiments that DMPC showed some slow motions at gel phase. However, for liquid crystalline phase, CODEX could not give a satisfying answer about motions due to the strange fluctuation at high



temperatures. In static exchange spectra of DMPC, there is no significant off-diagonal intensity at 5 ms whereas at 400 ms, large off-diagonal signals were observed. This experiment was repeated for 600 ms mixing time (not shown). It was very similar with 400 ms mixing time that suggest that most of the exchange happens within 400 ms.

Figure 5-37 shows exchange spectra of DMPC in the presence of ceramide. At short mixing times, no significant exchange has been observed as in the case of pure DMPC. At longer mixing time, off-diagonal peaks appears for both phases. For liquid crystalline phase, the shape of spectrum was disrupted although 1D experiment gave a perfect typical spectrum with no difference with pure DMPC. This strange shape might be due to some hardware imperfections. For the gel phase, spectral lineshape looks like normal off-diagonal exchange spectrum, which was not much different than pure DMPC. This can be an indication that in both pure DMPC and DMPC-C16-Cer mixture, reorientation due to the slow motions occurs at low temperature. CODEX results suggested that ceramide has a large effect on DMPC dynamics at slow motional regimes at gel phase. It is not easy to extract similar kind of results for static 2D exchange experiments by just looking at the spectra. Further analyses are needed to find out correlation times for pure DMPC and DMPC-C16-Cer bilayers. However, consistent with CODEX results, it is clear that in gel phase, DMPC show some slow motions that cause off-diagonal peaks in  $^{31}\text{P}$  static exchange spectra.

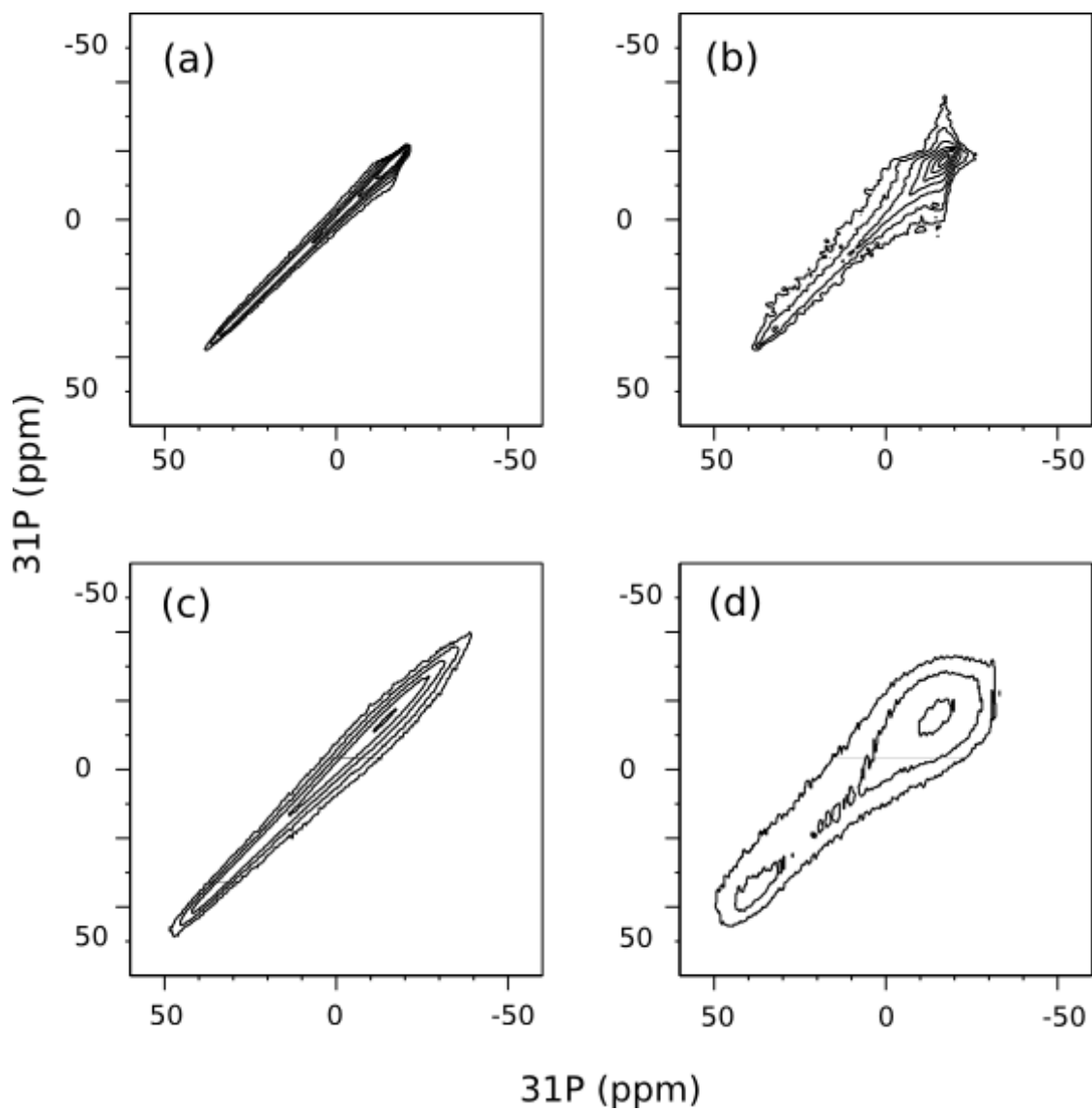


Figure 5-36: 2D  $^{31}\text{P}$  exchange spectra of DMPC bilayer: at 300K with  $t_m$  equals 5 ms (a) and 400 ms (b), at 270K with  $t_m$  equals 5 ms (c) and 400 ms (d).

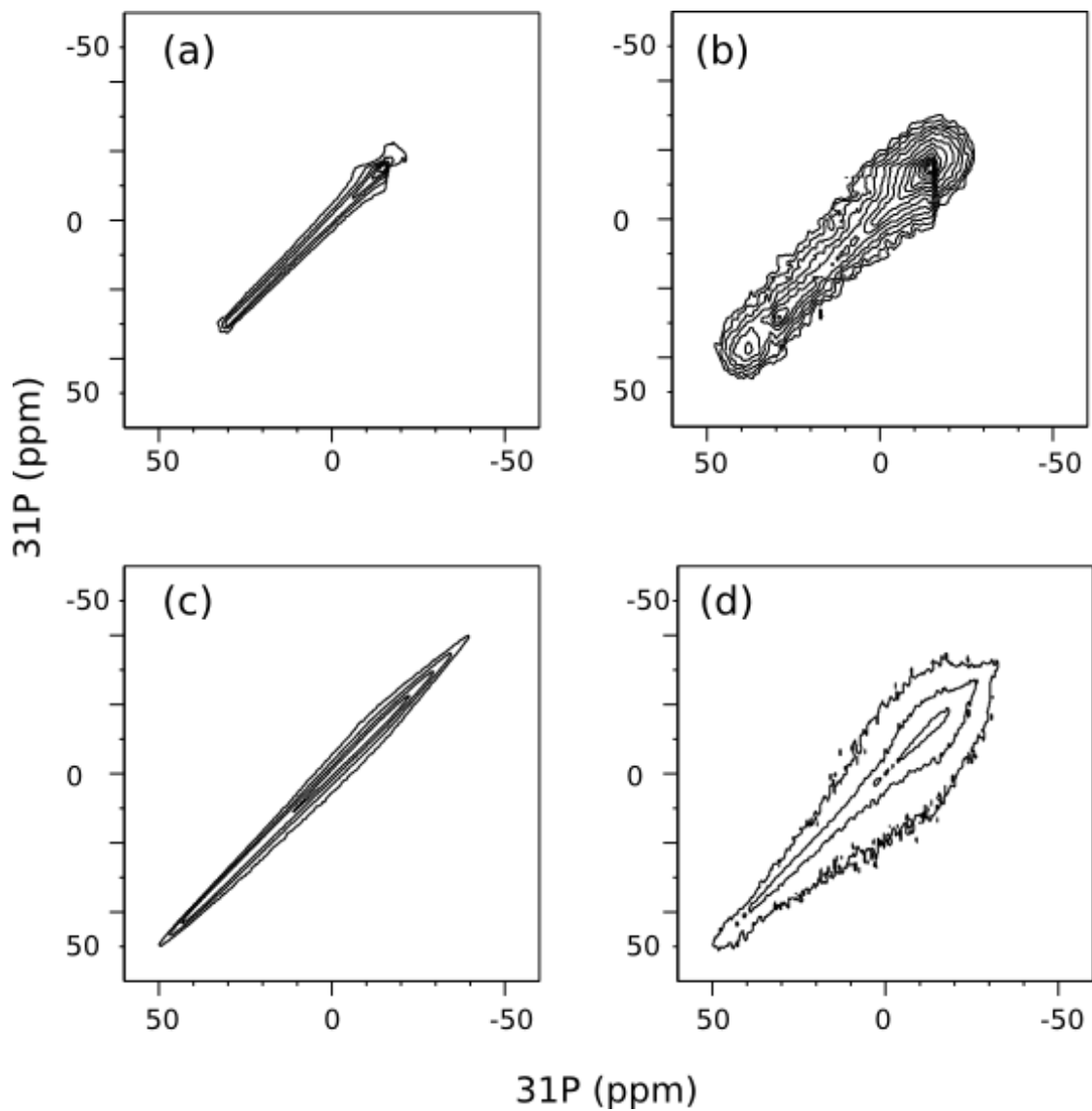


Figure 5-37:  $2D$   $^{31}\text{P}$  exchange spectra of DMPC-C16-Cer mixture: at 300K with  $t_m$  equals 5 ms (a) and 400 ms (b), at 270K with  $t_m$  equals 5 ms (c) and 400 ms (d).

## 5.4 Conclusion

Ceramides are known to play key roles in many cell processes. In this study, influences of ceramides on the biophysics of lipid bilayers were investigated by using MD simulations and various solid-state NMR techniques in order to get more atomistic view on ceramide-lipid interactions. Results from both MD calculations and NMR measurements clearly showed that ceramide and lipids have strong interactions. MD simulations revealed that ceramide and DMPC molecules form H-bonds between sphingosine and glycerol backbone. This finding was supported by  $^1\text{H}$ -MAS NOESY experiments, which unambiguously showed that glycerol backbone of DMPC had contact with ceramide protons. In addition, in  $^1\text{H}$  spectra of ceramide mixture with DMPC-d67 showed an additional peak, which was an outcome of ceramide-DMPC interactions.

Supporting this data, MD simulations showed that ceramides have effects on the P-N vector orientation of DMPC molecules, which are at close proximity to ceramide molecules. In consistent with this finding,  $^{14}\text{N}$  NMR spectra of mixture showed an additional peak, which can be a further evidence of DMPC-ceramide contacts. This suggests that DMPC-ceramide interactions cause a shift in  $^{14}\text{N}$  resonance of DMPC molecules at close contact with ceramide.

Furthermore, it was indicated by MD simulations that ceramide increased the rigidity of DMPC by increasing chain order parameters. Moreover, PISEMA experiments showed that order parameters of DMPC were significantly increased in the mixture with ceramide at 315 K. At this temperature, order parameters of both ceramide and DMPC chains were quite similar and higher than pure DMPC order parameters. This result is consistent with MD simulations results in which it was observed that DMPC became more ordered in the presence of ceramide.

MD simulations showed that ceramide did not have any significant effect on electrostatic potential of DMPC bilayer. It was also supported by  $^{14}\text{N}$ -MAS experiments that ceramide did not change DMPC choline group nitrogen quadrupolar coupling, which is very

sensitive to electrostatic potential. Thus, NMR results also indicate that ceramide did not affect electrostatic potential of DMPC bilayer.

It was reported before by several studies (Huang, Goldberg et al. 1996; Holopainen, Lehtonen et al. 1997; Massey 2001; Hsueh, Giles et al. 2002; Silva, De Almeida et al. 2006) that ceramide increase order parameters of phospholipids. Here, consistent with literature, both MD simulations and solid-state NMR experiments give similar result that DMPC chains became more ordered in the presence of ceramide. In addition to this, several studies indicated hydrogen bond formation between ceramide and water and ceramide itself (Pascher 1976; Li, Tang et al. 2002; Anishkin, Sukharev et al. 2006) as well as ceramide with sphingomyelin (Holopainen, Subramanian et al. 1998; Metcalf and Pandit 2012). Here, as a first time, MD simulations clearly showed DMPC-ceramide hydrogen bond formation and specific interaction sites of ceramide and DMPC due to hydrogen bonding. Various solid-state NMR experiments also supported this finding by giving strong evidences on DMPC-ceramide interactions.

## 6 Investigation of Hydrophobic Polarizing Agents for DNP

### 6.1 Introduction

This chapter deals with the membrane incorporation of a DNP polarizing agents. Dynamic Nuclear Polarization (DNP) is a method to enhance NMR signals via polarization transfer from electrons to protons by using microwave irradiation. Since gyromagnetic ratio of electrons is much higher than protons, very large enhancements can be achieved by DNP at optimum conditions. Theoretically, maximum enhancement is directly related with the ratio of gyromagnetic ratios of electron and nucleus.

Paramagnetic polarizing agents are used as magnetization sources. DNP is especially useful for solid-state NMR on membrane proteins. It is therefore important to consider interactions between these polarizing agents and the membranes. Mono radicals and recently biradicals have been largely used (Hu, Yu et al. 2004; Song, Hu et al. 2006). It is known that polarization transfer is related with electron-electron dipolar coupling (Wollan 1976; Wollan 1976; Goldman 2008). Recent studies have shown that biradicals such as TOTAPOL (Song, Hu et al. 2006) allow a very efficient signal enhancement due to their strongly coupled electrons. Furthermore, it was suggested that the relative g-tensor orientation of both radicals with respect to each other is of importance as demonstrated for bTbk, which yielded an even higher enhancement than TOTAPOL. Matsuki and co-workers (Matsuki, Maly et al. 2009) reported bTbk first time. They compared the enhancement profile of bTbk with TOTAPOL (structures were given in Figure 6-1) that has relatively flexible orientations of two radicals with respect to each other. They obtained around 1.4 enhancement factor of bTbk over TOTAPOL.

A limitation so far has been its hydrophobicity, which might restrict its application. Matsuki et. al. that reported that the maximum amount of water that btbk could be solved was 23 % in DMSO. On the other hand, this could also be of advantage in case of

membrane protein samples if bTbk would partition into lipid bilayer. Lipid membranes as well as membrane proteins that are reconstituted in membranes can be studied by DNP in the presence of a hydrophobic biradical such as bTbk. A first report of a membrane study with bTbk was published by Salnikov et al in 2010 (Salnikov, Rosay et al. 2010). They showed DNP on a trans-membrane model protein that was reconstituted in oriented membrane. In this first report, they already obtained 18 fold enhancements in CP-MAS  $^{15}\text{N}$  spectra by using 40% of bTbk. The enhancement efficiency may be related with the location and orientation of bTbk inside bilayers. Therefore it becomes important to investigate where bTbk stays inside membranes to understand enhancement profile of bTbk for DNP measurements.

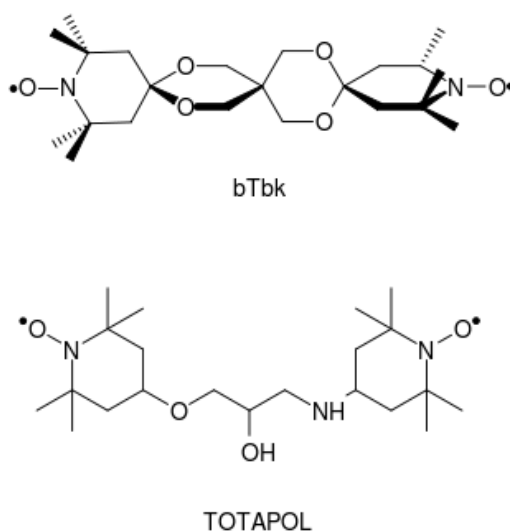


*Figure 6-1: Structures of bTbk (top) and TOTAPOL (bottom)*

### 6.1.1 Objectives

Application of DNP methods on membrane is an ongoing research. It is necessary to design new polarizing agents for lipid environment as well as to understand their behavior inside membranes. BTbk is the first reported lipid soluble polarizing agent that enhanced  $^{15}\text{N}$  spectra 18 fold (Salnikov, Rosay et al. 2010). It is known to be much more

effective than TOTAPOL (Song, Hu et al. 2006) and hydrophobicity of bTbk can make it even more useful for insertion to lipid bilayers. Therefore, in this study, it is research of interest to investigate the location and orientation of bTbk inside lipid bilayer by using molecular dynamics simulations together with solid-state NMR measurements (solid state NMR spectra were recorded and resulting data were kindly donated by Yeansin Ong)

## **6.2 Materials and Methods**

### **6.2.1 Sample Preparation**

Pure DMPC and 100:1 / DMPC-bTbk mixture were prepared as described before (Chapter 2). In order to dissolve lipids, trifluoroethanol were used as solvent. After solvent was evaporated samples were rehydrated by D<sub>2</sub>O.

### **6.2.2 Solid-State NMR**

600 MHz solid state NMR instrument were used to record spectra. <sup>1</sup>H-T<sub>1</sub> measurements were recorded by using saturation recovery experiment by observing <sup>13</sup>C resonances to obtained more resolved spectra for calculation of each T<sub>1</sub> values.

### **6.2.3 Molecular Dynamics**

All simulations were done using GROMACS 4.0.3 package. The initial structure of DMPC bilayer was taken from Tieleman website. The analyses of the trajectories after the simulations were done by using Python

#### **6.2.3.1 Starting Structures**

Bis-TEMPO-bisketal was used for the simulations. Starting configuration of DMPC



bilayer was taken from Tieleman website (Tieleman, Forrest et al. 1998) that has been already equilibrated for 1.6 ns. It was further underwent simulation for 10 ns for equilibration. BTbk molecule was placed into the lipid membrane in 4 different conformations as in the case of pirinixic acid derivatives. As usual, energy minimization was carried out for each simulation box to get rid of any existing bad contacts.

### **6.2.3.2 Force-fields**

The force-field for the DMPC bilayer was a mixture of GROMOS87 force-field and lipid parameters (Berger, Edholm et al. 1997; Tieleman, Forrest et al. 1998). Force-field of bTbk was generated based on GROMOS87 force field except ether bonds and nitroxide radical. Parameters for ether were taken from extended GROMOS force fields that were reported in Horta et al (Horta, Fuchs et al. 2011). Nitroxide bonding and non-bonding parameters were taken from Barone et al (Barone, Bencini et al. 1998).

### **6.2.3.3 Simulation Parameters**

All the simulations were carried out with the run parameters defined earlier. Same algorithms and same ensembles that were used for pirinixic acid derivatives were used here as well. Temperature of DMPC bilayer was chosen as 300K. 40 ns simulations were carried out for each simulation box.

### **6.2.3.4 Analysis**

After simulations, the positions of center of mass of btbk were calculated for the whole trajectories for each simulation box to compare the differences in between different starting configurations.

### **6.3 Results and Discussion**

The importance of bTbk was explained in the introduction part. It is very hydrophobic polarizing agent and it is assumed to prefer staying in lipid phase. Therefore it can be useful to use bTbk while measuring lipids with DNP to increase the magnetization enhancement. The aim of this study to understand how bTbk is partitioning in lipid membrane as well as where it sits inside lipid bilayer by performing MD simulations. The first aim was to perform NOESY experiments in order to get some distance information between lipids and bTbk. Therefore, it could be possible to put some restraints. However, nitroxide radical has a paramagnetic effect inside lipid membrane that cause quenching of NMR peaks. Thus, all the simulations were performed without any NMR distance information.

In spite of absence of NOESY data, saturation recovery experiment was recorded to observe effect of bTbk on relaxation time of DMPC protons. Figure 6-2 displays  $^1\text{H}$   $T_1$  values of DMPC atoms for pure DMPC and DMPC-bTbk mixtures. As can be easily seen from the figure, bTbk had a significant effect on relaxations times of  $^1\text{H}$  atoms of DMPC for both head group and hydrocarbon chains. This result suggests that bTbk has interactions almost all parts of lipids. The effects of bTbk are higher for the atoms at the end of hydrocarbon chains. This may be an indication that bTbk tends to stay more around the inner hydrophobic part of the bilayer instead of interfacial surface of the membrane.

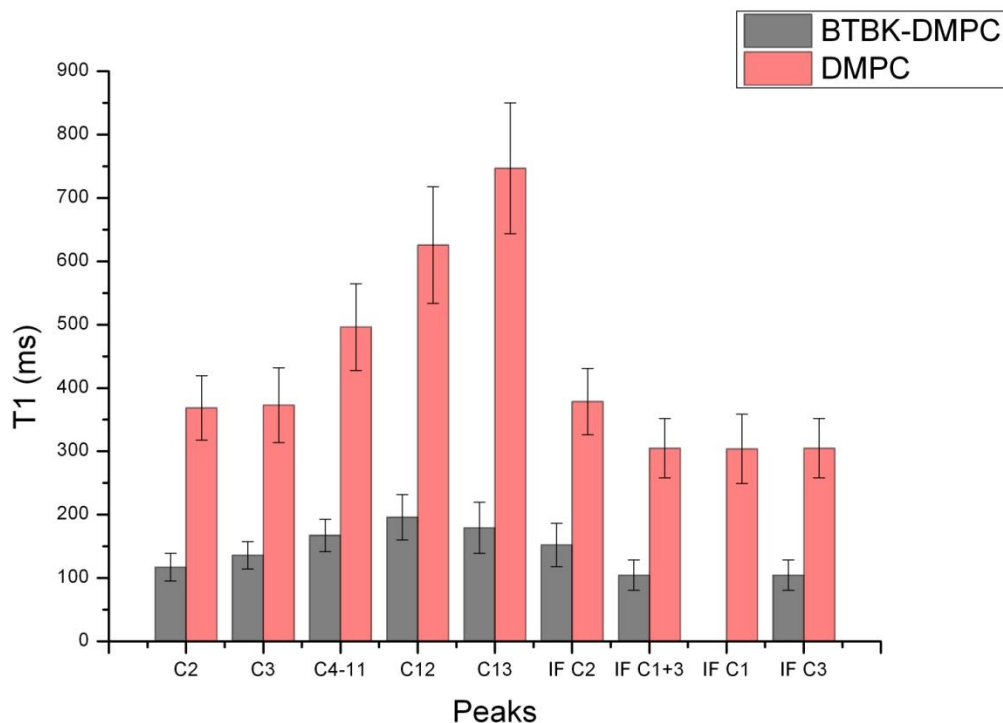


Figure 6-2:  $^1\text{H}$ - $T_1$  values for pure DMPC and DMPC-bTbk mixture (Yeansin Ong, 2011): spectra are recorded by Bruker 600WB Avance II at 300 K by saturation recovery experiment.

In order to have more clues about the location of bTbk inside bilayers molecular dynamics simulations on DMPC bilayers was performed, which contain one bTbk molecule with different starting configurations. Figure 6-3 shows starting and final structures of 4 bilayers with different bTbk conformations. It can be easily recognized that, after 40 ns simulation, bTbk stayed inside the bilayer with various different orientations for each of 4 different starting conditions. The orientation of it was almost parallel to the bilayer (perpendicular to the bilayer normal) for starting conformation 3 and 4 whereas for starting conformations 1 and 2 it stays with an angle less than  $90^\circ$  to the bilayer normal.

Since these were only the last snapshots more statistical analysis were done. In order to have more quantitative data the position on z-axis (bilayer normal) of center of mass of bTbk molecule with respect to bilayer center of mass and position on z-axis of C1 and C14 atoms of DMPC molecules for the last 30 ns were calculated. Figure 6-4 shows clearly that bTbk tends to stay at almost same place for 4 different starting conditions. The average center of mass of bTbk stayed with higher proximity to the carbonyl groups of lipid chains than the end of the chains. This suggested that btbk stays more along the hydrocarbon chains of lipids relatively closer to beginning part of the chains than the middle of the bilayer. The numerical values of positions of center of mass of bTbk as well as C1 and C14 atoms of DMPC with respect to center of mass of bilayer were summarized in Table 6-1.

	1 <sup>st</sup> Conformation (Å)	2 <sup>nd</sup> Conformation (Å)	3 <sup>rd</sup> Conformation (Å)	4 <sup>th</sup> Conformation (Å)
C1	13.09 ± 0.30	13.18 ± 0.30	13.1 ± 0.32	13.19 ± 0.24
C14	1.95 ± 0.54	2.05 ± 0.55	2.02 ± 0.50	2.04 ± 0.50
Btbk COM	8.89 ± 1.21	8.74 ± 1.34	8.6 ± 1.70	9.32 ± 1.28

*Table 6-1: Average positions on z-direction of C1 and C14 atoms of DMPC and center of mass of bTbk for 4 different starting conformations; positions are in Å and are calculated with respect to the center of mass of bilayer.*

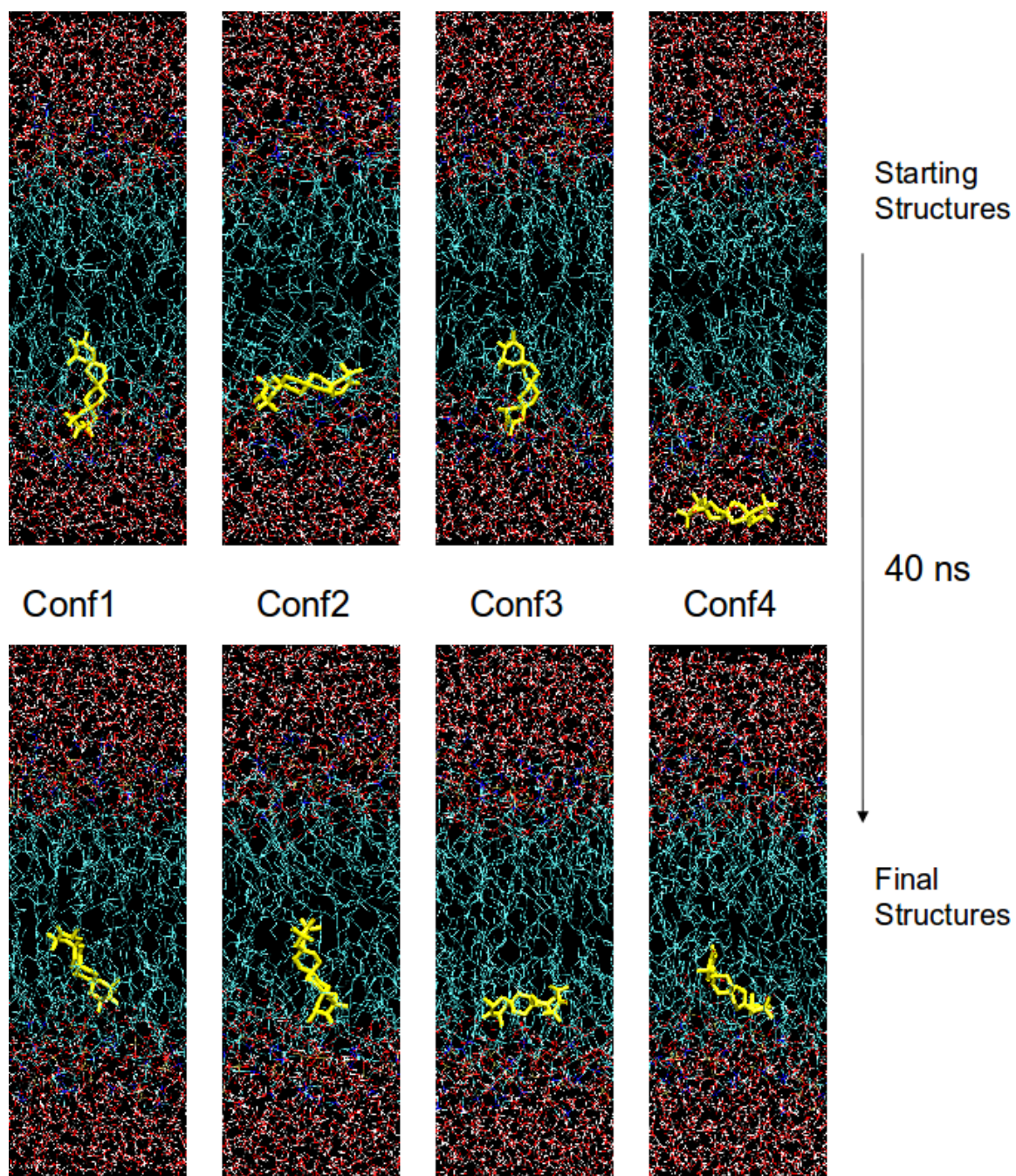


*Figure 6-3: Starting and final structures of DMPC-bTbk simulation boxes for 4 different conformation of bTbk.*

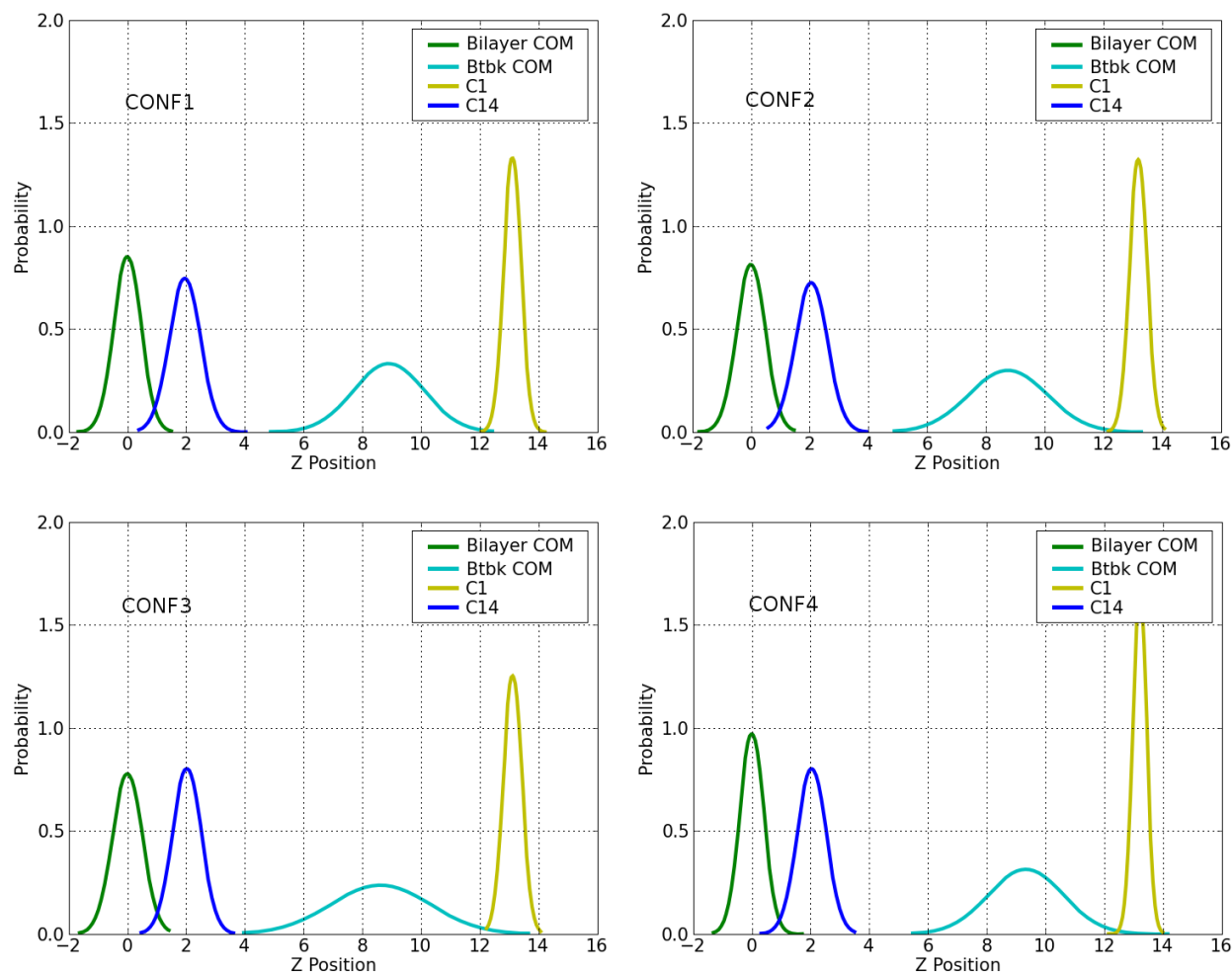


*Figure 6-4: Center of mass of bTbk (labeled as bTbk COM) with respect to bilayer center of mass (labeled as Bilayer COM in the figure) and two carbon atoms (C1 and C14) of DMPC SN1 chains for 4 different conformations of bTbk. Z-positions are in Å and are scaled with the average position of the center of mass of the bilayer.*

It is also amazing to see how fast bTbk molecule was inserted inside the bilayer as depicted in Figure 6-5. For the fourth configuration, in less than 10 nanosecond, bTbk partitioned inside the bilayer and stayed at very similar location with the bTbk molecules in other three simulation boxes in which bTbk molecules were already inside the bilayers from the beginning of the simulations. This shows, even without distance information from NMR, DMPC bilayers with bTbk converged relatively stable structures after 40 nanosecond at 300 K.



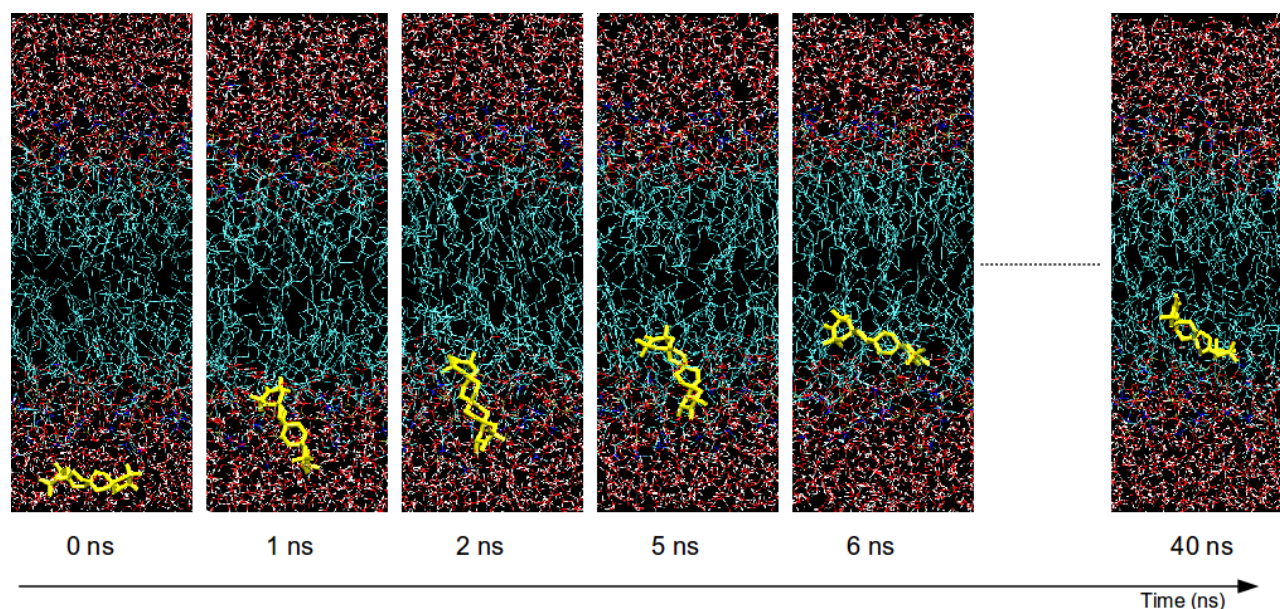


*Figure 6-5: Snapshots of the trajectory that shows bTbk partitioning inside DMPC bilayer*

## 6.4 Conclusion

It is important to investigate how bTbk partitions into the lipid bilayer, whether close to interfacial area of bilayer or at the more hydrophobic inner parts of the membranes, in order to investigate the differences in efficiency of polarization enhancements of DNP experiments. NMR relaxation time studies showed that bTbk had stronger interactions with hydrocarbon chains of bilayer than with the head groups of lipids. In addition to NMR results, molecular dynamics simulations gave an idea about the location of the bTbk inside DMPC bilayer. Statistical analysis of the simulations indicated that, similar to NMR results, bTbk stayed inside bilayer closer to the hydrophobic part of the lipids than the interfacial part. However, the orientation of bTbk was more complicated to be discovered.  $^1\text{H-T}_1$  analysis suggests that bTbk tends more towards an orientation parallel to membrane plane, since  $T_1$  of chain protons reduced more with the presence of bTbk. It is difficult to extract a similar result from MD simulations. From the snapshots of

trajectories for four different starting structures, it was shown that bTbk orientations were varied randomly from parallel to perpendicular to the bilayer normal. Maybe, longer simulations are needed to achieve more converged orientation of bTbk with respect to bilayer normal.



## 7 Conclusion and Outlook

In this study, biophysics of lipid membranes in the absence and presence of different kind of substrates were studied. It was of interest to investigate the changes in structure and dynamics of membranes in different temperatures as well as in different time-scales. Thus, the main focus of this study was to maintain a general procedure to monitor biophysical properties of phospholipid membranes, which cover time scales from nanoseconds to seconds, via different NMR techniques with the help of theoretical calculations.

For small molecules, the first important information to find the location of substrates inside membranes by investigating interaction sites of substrates with lipid molecules via different NMR techniques, namely  $^1\text{H}$  chemical-shift analysis,  $^1\text{H}$ - $^1\text{H}$ -MAS NOESY and  $^1\text{H}$ - $^1\text{H}$ -MAS RFDR experiments. For NSAID's, NOESY experiments were performed just to depict whether any interactions occurred or not between drugs and DPPC molecules, without doing any further analysis. Results showed that Ibuprofen and diclofenac had strong interactions with lipid molecules whereas piroxicam showed no interactions with lipids. For pirinixic acid derivatives, more detailed work was done by using  $^1\text{H}$  chemical-shift difference analysis,  $^1\text{H}$ - $^1\text{H}$ -MAS NOESY and  $^1\text{H}$ - $^1\text{H}$ -MAS RFDR experiments. Furthermore, in this study, the help of molecular dynamics simulations was used in order to understand the difference in between two different pirinixic acid derivatives. Molecular dynamics simulations were performed by using the distance information that was obtained from NMR measurements. The combined data from all experiments and simulations clearly showed that compound **3** was more deeply inserted inside the bilayer than compound **2**.

The second question was to investigate the phase behavior of liposomes in the presence of small molecules. The most common method for this is to use  $^{31}\text{P}$  NMR techniques and interpret the differences in the shape of static spectrum. For NSAID's,  $^{31}\text{P}$  static experiments indicated that ibuprofen and diclofenac had an impact of DPPC phase while

piroxicam had no effect.

Not only with small molecules but also signaling lipids, namely ceramides, were studied to observe their effects on phospholipids. Ceramide-membrane interactions are huge and ongoing research area. It is known that they have key roles in many signaling processes in biological cells. Therefore, in this study, ceramides contained a large space, since NMR methods and MD simulations can provide many information of membrane biophysics in the presence of ceramides. Different NMR methods were used to investigate the effect of ceramides on the dynamics of DMPC. Each NMR experiment related with motions in different time scales, so the main focus was to be able to cover wide range of time scales with various kind of experiments.

For DMPC-Ceramide system, molecular dynamics simulations were performed for pure DMPC bilayer and DMPC-C16-Cer mixture, which contain 20 % ceramide molecules. From the analysis of the area per lipid, order parameters and density profiles, it was found that ceramide had an ordering effect on DMPC bilayer. In addition to this, hydrogen bond analysis revealed that DMPC was forming hydrogen bonds with ceramide molecules. Moreover, PN vector orientation analysis showed that DMPC molecules, which were at close proximity to ceramide, had slightly different PN vector orientation from bulk lipids. This might be caused by DMPC molecules that formed hydrogen bonds with ceramide. These findings point at the presence of strong interaction between ceramide and DMPC molecules.

Solid-state NMR experiments were done in order to validate simulation results. Firstly, order parameters, which were calculated from dipolar couplings, showed that ceramide increased order parameters of DMPC at 315 K. This supports the MD simulation data. Secondly,  $^1\text{H}$ -MAS NOESY experiments showed significant correlation between ceramide and DMPC protons. This is an indication that ceramide and DMPC have interactions as MD simulations also showed. In addition to this, further analysis on  $^1\text{H}$  and  $^{14}\text{N}$  NMR spectra point the existence of additional peaks that can be result of interactions of DMPC and Ceramide. Thirdly,  $^{31}\text{P}$  NMR exchange experiments with and

without MAS were performed to obtain informations on slow motions in DMPC membranes in the absence and presence of ceramide. CODEX experiments gave reliable results just for gel phase of membrane. It was observed that ceramide increase correlations time of  $^{31}\text{P}$  CODEX curve of DMPC at low temperatures. This result indicates that ceramide has decrease motions of DMPC in slow time regimes at gel phase. Static exchange experiments gave the information for both DMPC and DMPC-C16-ceramide mixtures. Exchange has occurred for both temperatures below and above phase transition temperature consistent with CODEX data. However, further spectral shape analyses should be done in order to calculate correlations times for pure DMPC and mixture to have a better comparison with the CODEX data.

## 8 Appendix

### 8.1 Solid State NMR Studies on POPC – Ceramide Systems

#### 8.1.1 Dipolar Order Parameters

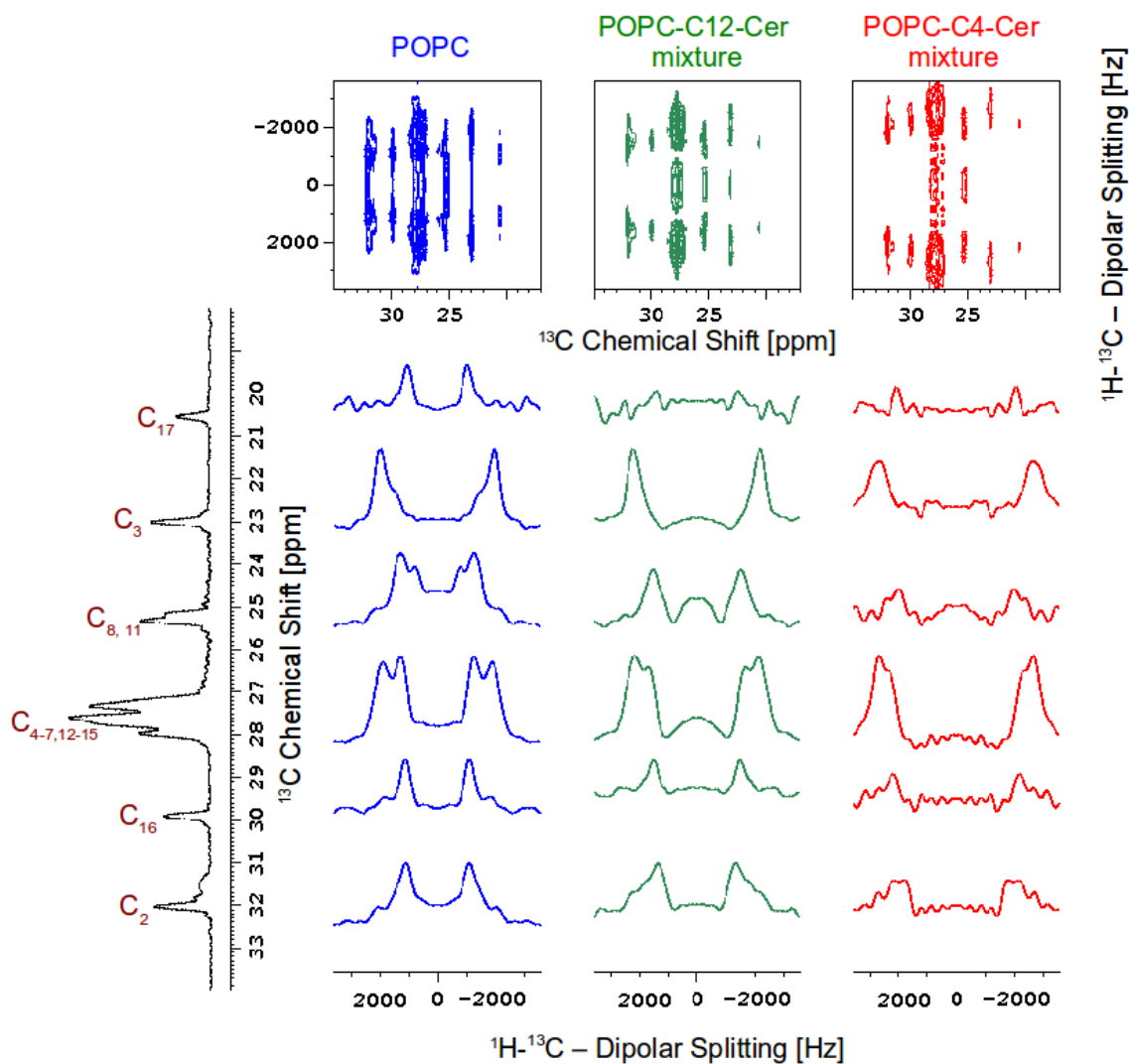


Figure 8-1: 1D spectra of POPC extracted from 2D FSLG-CP spectrum for pure POPC (left), mixture of POPC-C12-Cer (10 % C12-Cer) (middle) and mixture of POPC-C4-Cer (10 % C4-Cer) (right): Spectra were recorded by BRUKER 600 WB Avance II spectrometer at 300 K.

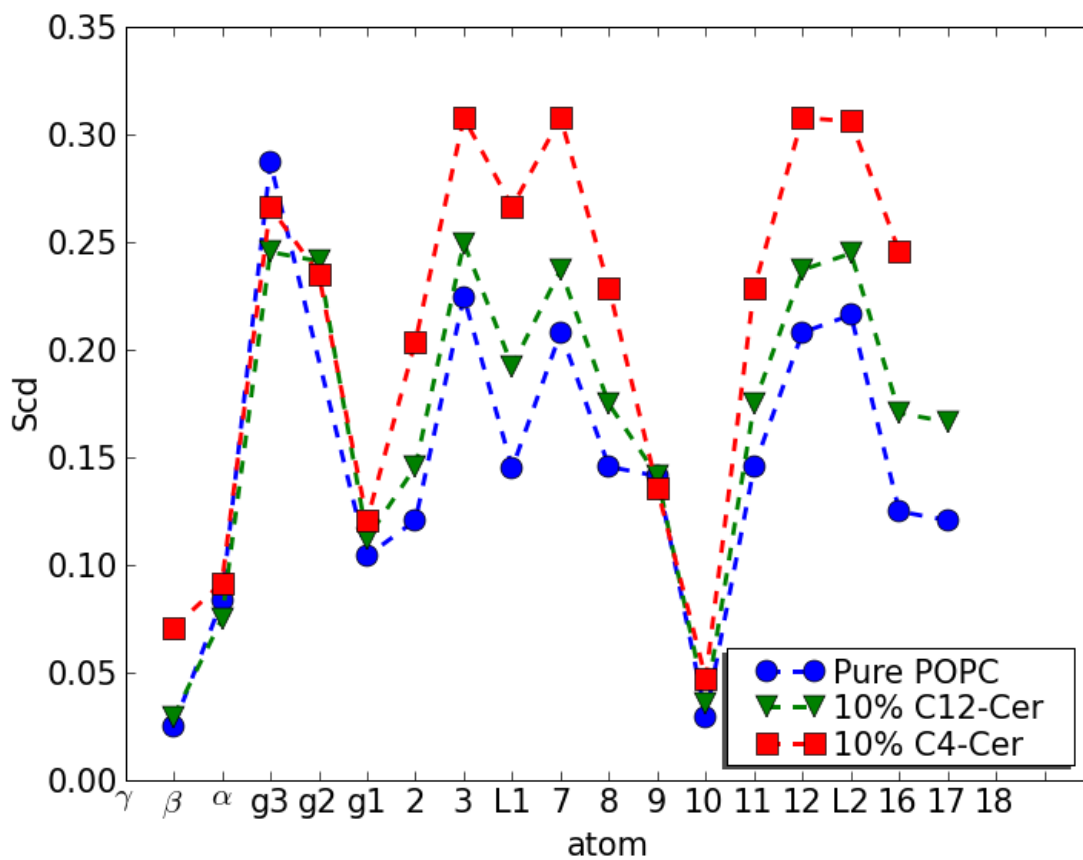


Figure 8-2: Order parameters profiles of POPC-d31 from samples of pure POPC and the mixture of POPC with C4-, C12-Ceramides (10 % ceramide concentration for each mixture) calculated from FSLG-CP spectra, which were recorded by BRUKER 600 WB Avance II spectrometer at 300 K. (L1 stands for the peak  $C_{4-7,12-15}$ )

### 8.1.2 Quadrupolar Order Parameters

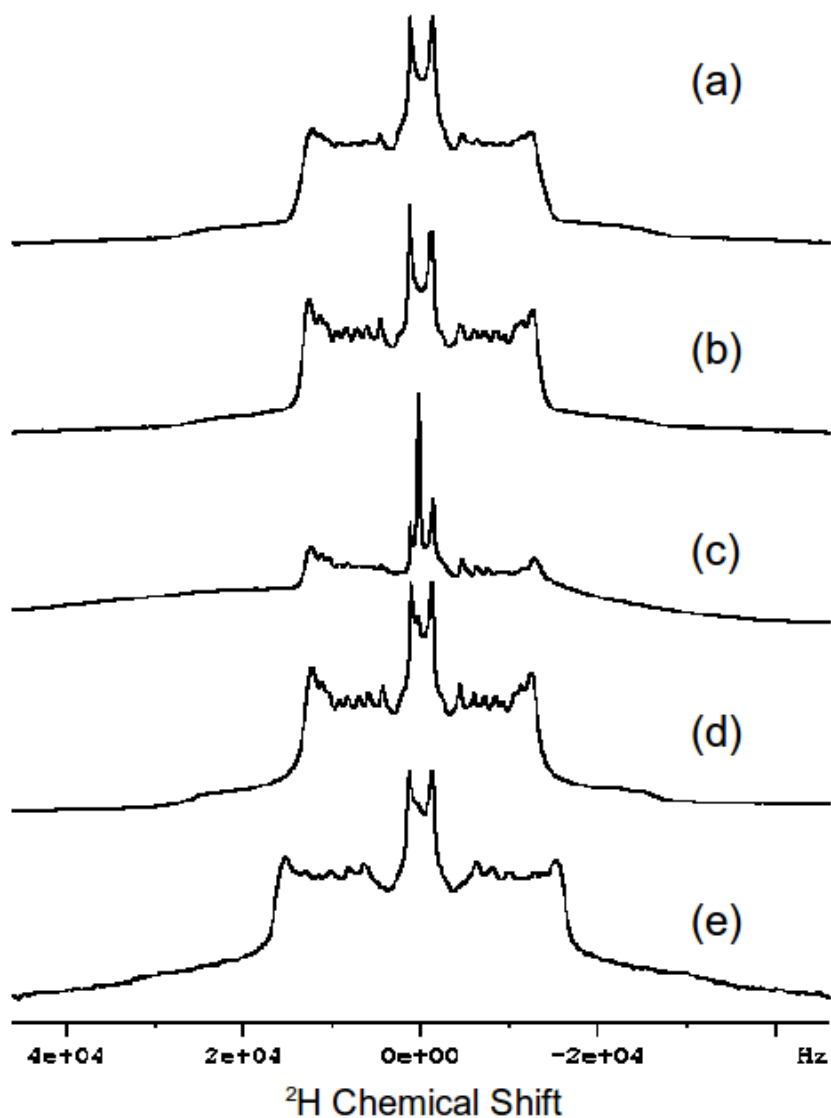


Figure 8-3:  $^2\text{H}$  Spectra of samples of pure POPC-d31 (a), mixture of POPC-d31 with C4, C12, C16-Ceramides (b, c, d, respectively; 10 % ceramide concentration for each mixture) and POPC with C16-Ceramide-d31 (e). Spectra were recorded by BRUKER 600 WB Avance II spectrometer at 300 K.

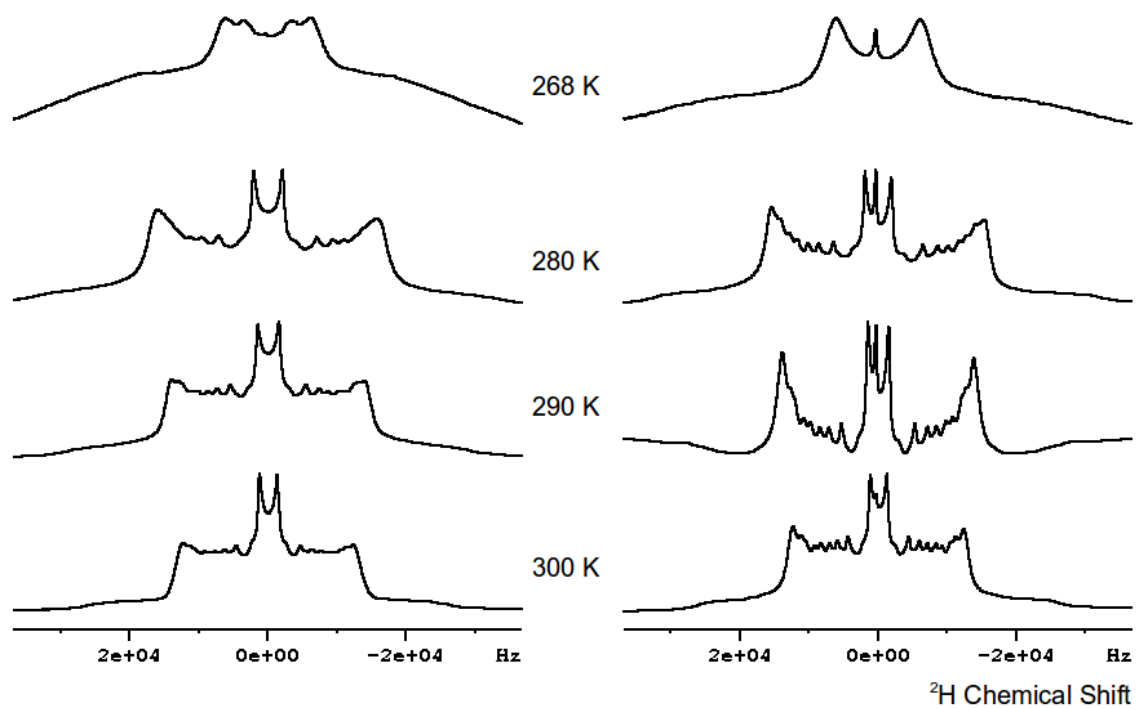


Figure 8-4: Temperature dependent  $^2\text{H}$  NMR spectra of samples of pure POPC-d31 (left) and the mixture of POPC-d31 with C16-Ceramide (10 % C16-Ceramide) (right), Spectra were recorded by BRUKER 600 WB Avance II spectrometer.

### 8.1.3 $^{31}\text{P}$ -NMR

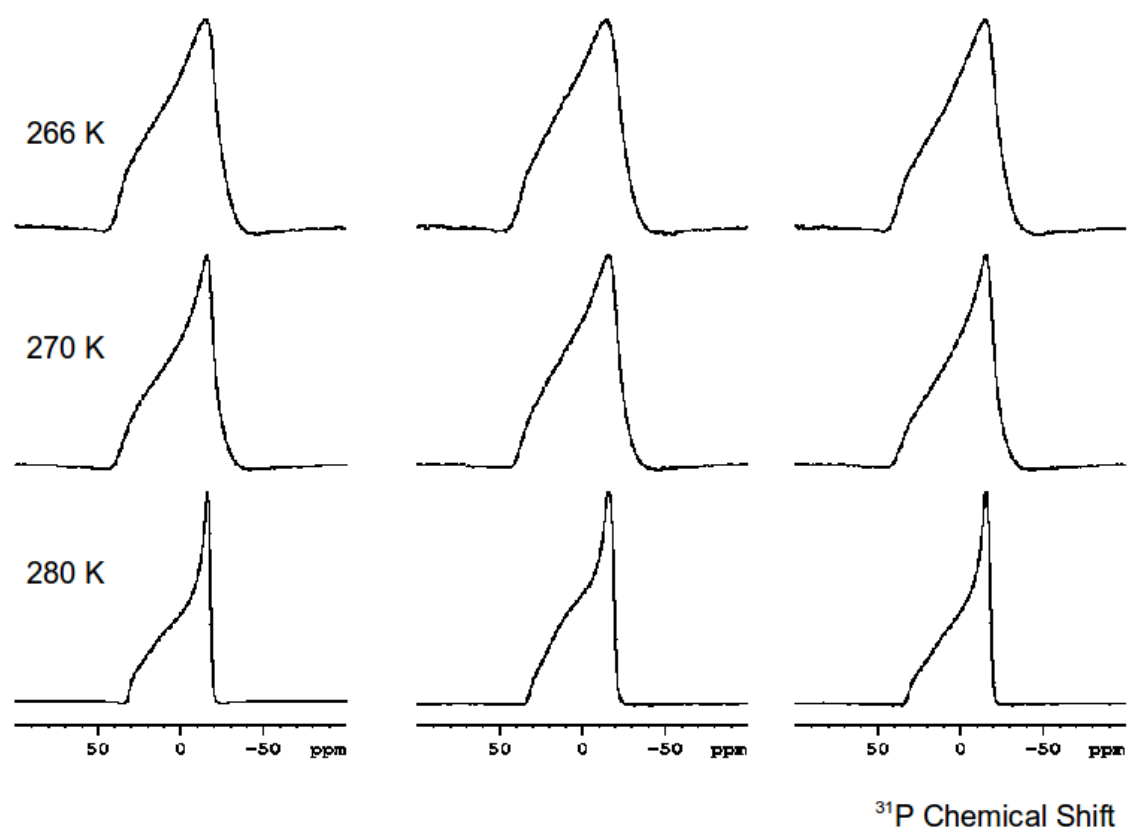


Figure 8-5: Temperature dependent  $^{31}\text{P}$  static spectra of samples of pure POPC-d31 (left), mixture of POPC-d31 with C4, C12-Ceramides (middle, right, respectively, 10 % ceramide concentration for each mixture), Spectra were recorded by BRUKER 400 WB Avance II spectrometer.



### 8.1.4 Spin-Lattice Relaxation Times at Laboratory Frame

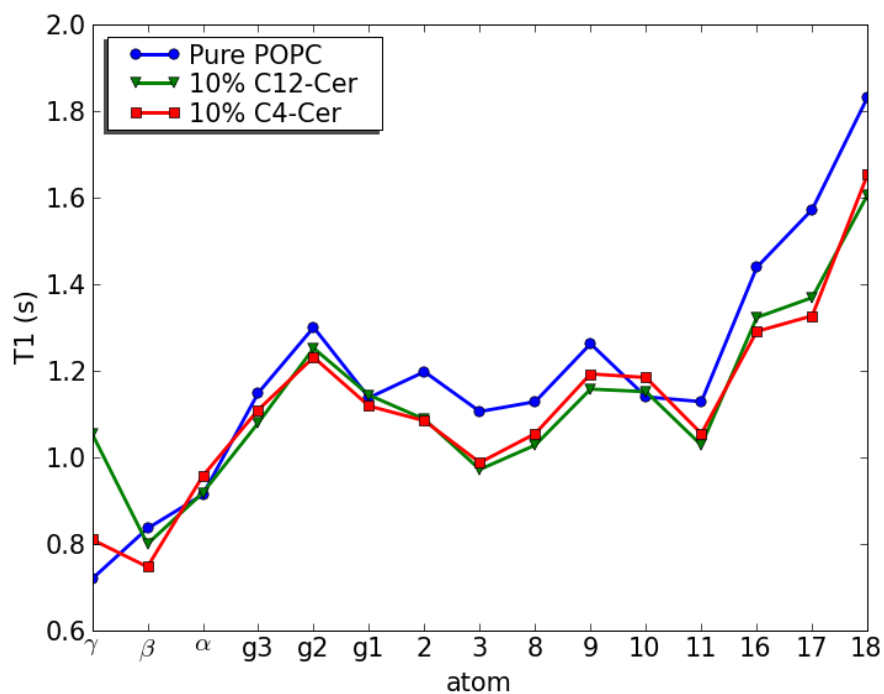


Figure 8-6: Spin-lattice relaxation times for  $^1\text{H}$  of pure POPC-d31, mixture of POPC-d31 with C4, C12, and C16-Ceramides (10 % ceramide concentration for each mixture). Saturation recovery experiment was used to measure relaxation times, spectra were recorded by BRUKER 850 WB Avance II spectrometer at 300 K.

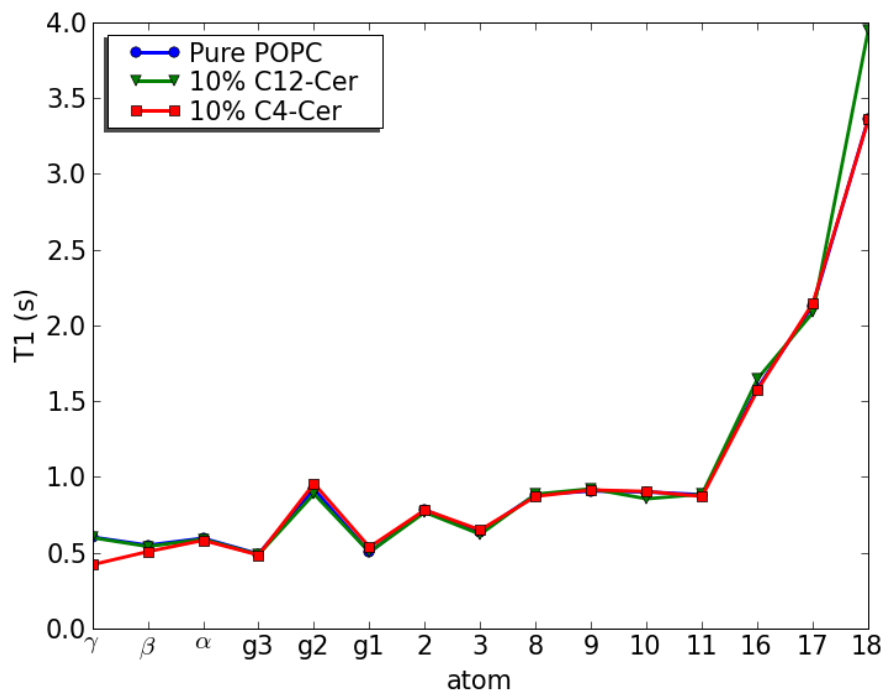


Figure 8-7: Spin-lattice relaxation times for  $^{13}\text{C}$  of pure POPC-d31, mixture of POPC-d31 with C4, C12, and C16-Ceramides (10 % ceramide concentration for each mixture). Decay experiment was used to measure relaxation times, spectra were recorded by BRUKER 850 WB Avance II spectrometer at 300 K.

### 8.1.5 Spin-Lattice Relaxation Times at Rotating Frame

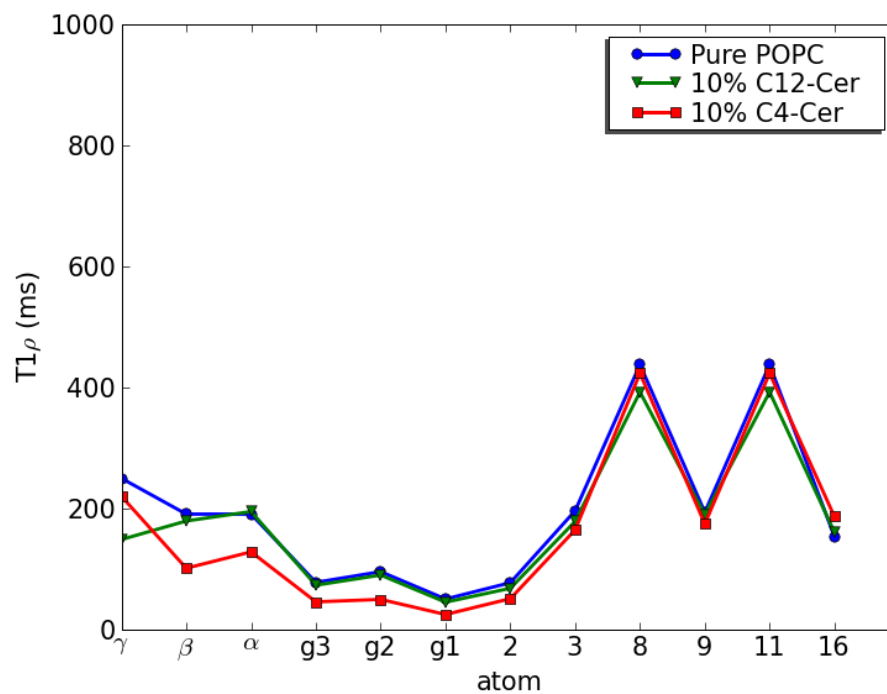


Figure 8-8: Spin-lattice relaxation times in rotating frame for  $^{13}\text{C}$  of pure POPC-d31, mixture of POPC-d31 with C4, C12, and C16-Ceramides (10 % ceramide concentration for each mixture). Spectra were recorded by BRUKER 850 WB Avance II spectrometer at 300 K.

	C $\gamma$	C $\beta$	C $\alpha$	Cg3	Cg2	Cg1	C2	C3	C4-7, 12-15	C8-11	C9	C10	C16	C17	C18
POPC at 310K – 850 MHz															
$^1\text{H-T}_1$	0.77	0.92	0.86	0.98	1.27	1.09	1	0.99	1.3	1.14	1.29	1.33	1.68	1.79	2.22
$^{13}\text{C-T}_1$	0.27	0.35	0.44	0.36	0.63	0.37	0.46	0.54	0.86	0.64	0.66	0.49	1.28	1.45	1.77
POPC-C4-Cer at 310K-850 MHz															
$^1\text{H-T}_1$	0.75	0.91	0.94	0.98	1.18	1.05	0.99	0.92	1.08	1.06	1.21	1.27	1.35	1.52	1.85
$^{13}\text{C-T}_1$	0.25	0.35	0.44	0.35	0.67	0.38	0.46	0.52	0.87	0.65	0.67	0.5	1.33	1.59	1.77
POPC-C12-Cer at 310K-850 MHz															
$^1\text{H-T}_1$	1	0.93	0.89	1.03	1.16	1.04	0.95	0.97	1.12	1.04	1.17	1.19	1.33	1.49	1.85
$^{13}\text{C-T}_1$	0.26	0.36	0.48	0.39	0.68	0.39	0.51	0.55	0.92	0.69	0.77	0.53	1.47	1.75	1.84
POPC at 310K – 600 MHz															
$^1\text{H-T}_1$	0.8	0.89	0.76	0.75	0.97	0.82	0.8	0.75	1.01	0.91	1.32	1.14	1.39	1.45	1.84
$^{13}\text{C-T}_1$	0.23	0.31	0.37	0.25	0.45	0.27	0.36	0.38	0.75	0.53	0.67	0.53	1.11	1.38	1.7
POPC-C4-Cer at 310K – 600 MHz															
$^1\text{H-T}_1$	0.82	0.7	0.69	0.76	0.93	0.8	0.78	0.7	0.94	0.87	0.99	1.08	1.12	1.23	1.45
$^{13}\text{C-T}_1$	0.21	0.26	0.34	0.27	0.5	0.31	0.39	0.37	0.83	0.52	0.65	0.49	1.12	1.55	1.79
POPC-C12-Cer at 310K – 600 MHz															
$^1\text{H-T}_1$	0.88	0.74	0.71	0.76	0.93	0.81	0.76	0.71	0.94	0.87	1.01	0.99	1.21	1.28	1.5
$^{13}\text{C-T}_1$	0.22	0.27	0.34	0.27	0.47	0.28	0.37	0.42	0.75	0.54	0.66	0.47	1.15	1.36	1.68
POPC at 300K – 850 MHz															
$^1\text{H-T}_1$	0.72	0.84	0.91	1.15	1.3	1.14	1.2	1.11	1.18	1.13	1.26	1.14	1.44	1.57	1.83
$^{13}\text{C-T}_1$	0.6	0.55	0.59	0.49	0.92	0.5	0.78	0.64	1.02	0.88	0.91	0.9	1.58	2.13	3.36
$^{13}\text{C-T}_{1p}$	0.25	0.19	0.19	0.08	0.1	0.05	0.08	0.2	0.22	0.44	0.19	0.82	0.15	n.d.	n.d.
POPC-C4-Cer at 300K – 850 MHz															
$^1\text{H-T}_1$	0.81	0.75	0.96	1.11	1.23	1.12	1.08	0.99	1.1	1.05	1.19	1.18	1.29	1.33	1.65

$^{13}\text{C-T}_1$	0.42	0.51	0.58	0.48	0.95	0.54	0.78	0.65	1.01	0.87	0.91	0.9	1.57	2.15	3.36
$^{13}\text{C-T}_{1\rho}$	0.22	0.1	0.13	0.05	0.05	0.02	0.05	0.16	0.26	0.42	0.17	0.33	0.19	n.d.	n.d.
POPC-C12-Cer at 300K – 850 MHz															
$^1\text{H-T}_1$	1.05	0.8	0.92	1.08	1.25	1.14	1.09	0.97	1.07	1.03	1.16	1.15	1.32	1.37	1.61
$^{13}\text{C-T}_1$	0.6	0.54	0.59	0.49	0.89	0.5	0.77	0.62	1	0.88	0.92	0.85	1.65	2.08	3.95
$^{13}\text{C-T}_{1\rho}$	0.15	0.18	0.19	0.07	0.09	0.04	0.07	0.18	0.21	0.39	0.19	0.98	0.16	n.d.	n.d.

*Table 8-1:  $^1\text{H}$ -, and  $^{13}\text{C-T}_1$  and  $^{13}\text{C-T}_{1\rho}$  for three sample, pure POPC and mixtures of POPC-C4-Cer and POPC-C12-Cer (10 % ceramide concentration for each mixture), at different external magnetic fields and temperatures; all the values are in seconds.*

## 8.2 MD Studies on POPC – Ceramide Systems

### 8.2.1 Area per Lipid

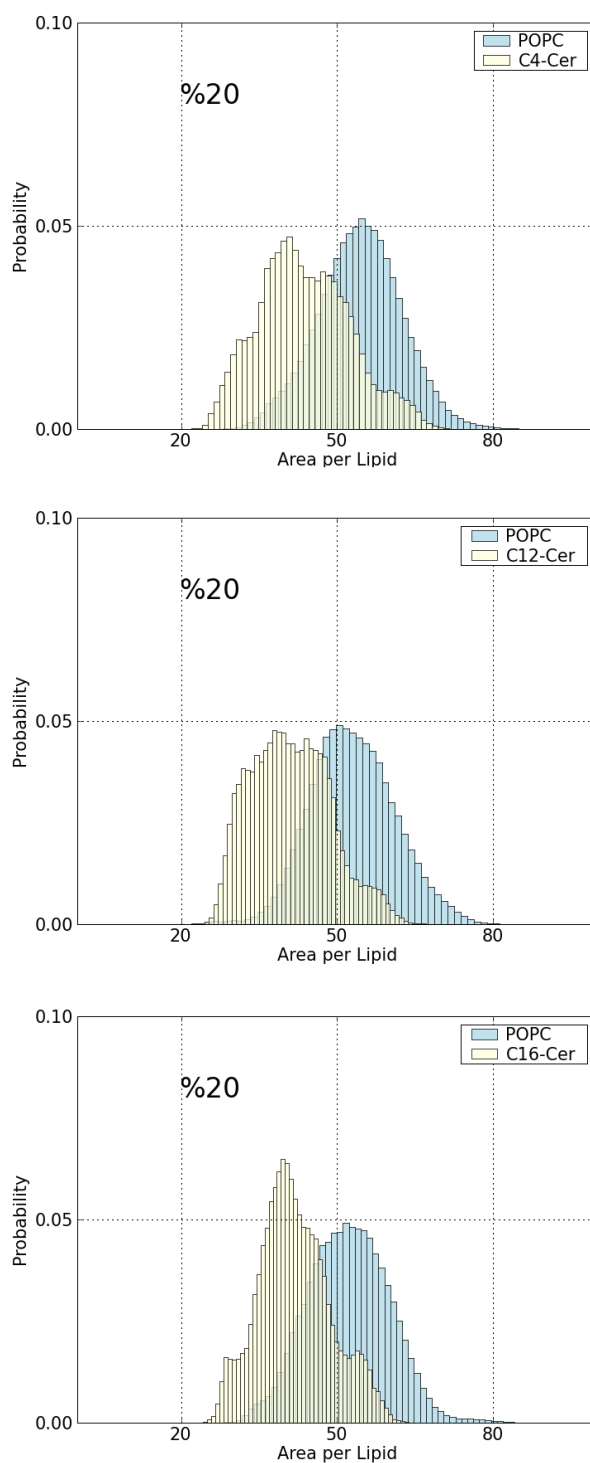


*Figure 8-9: Area per lipid of POPC-ceramide systems with analogy force-field (each simulation was performed for 10 ns at 300 K).*

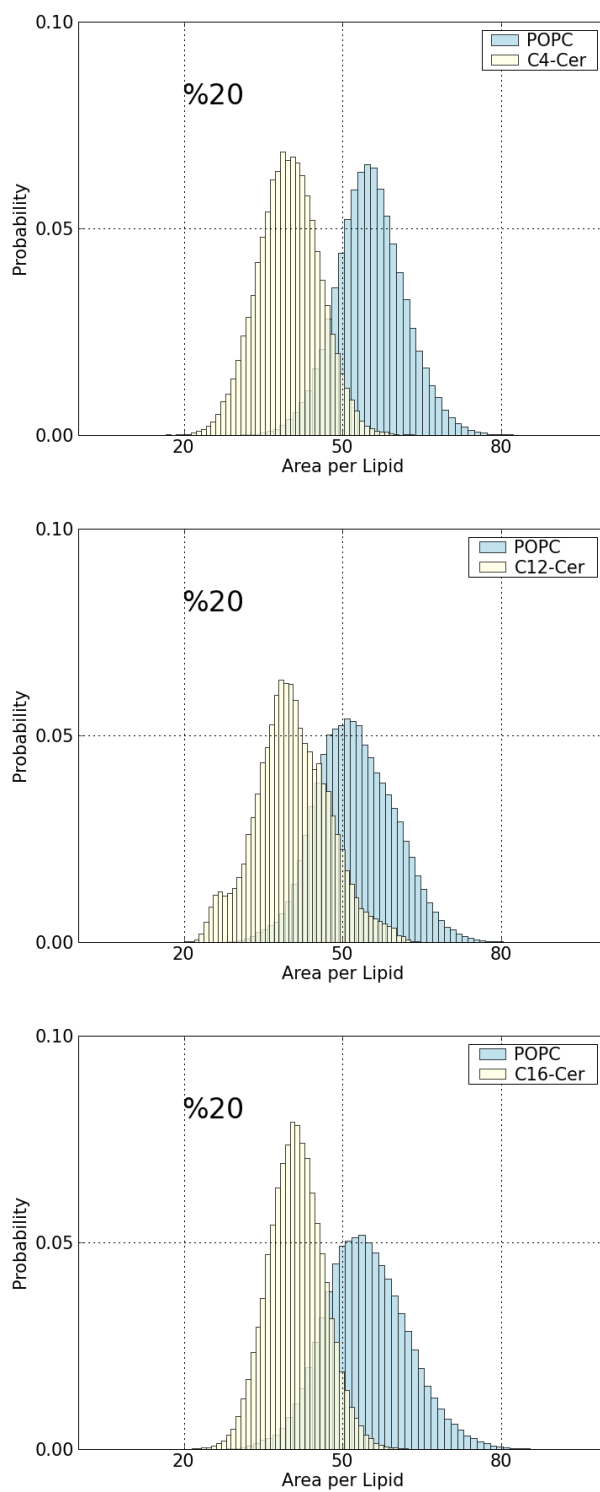


*Figure 8-10: Area per lipid of POPC-ceramide systems with server force-field, (each simulation was performed for 10 ns at 300 K).*

## 8.2.2 Density Profile

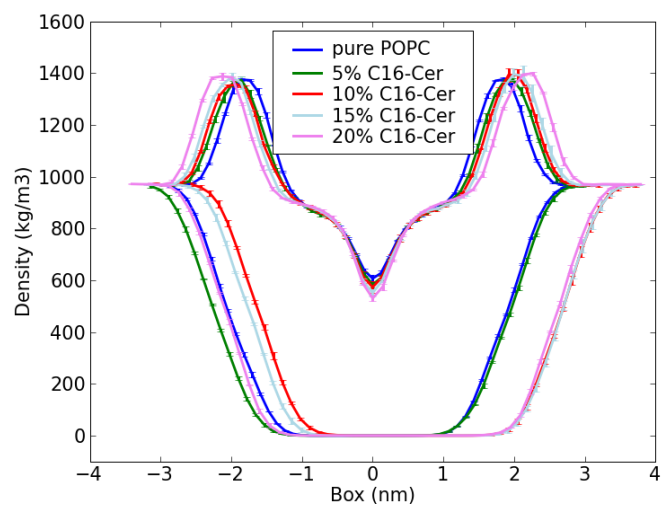
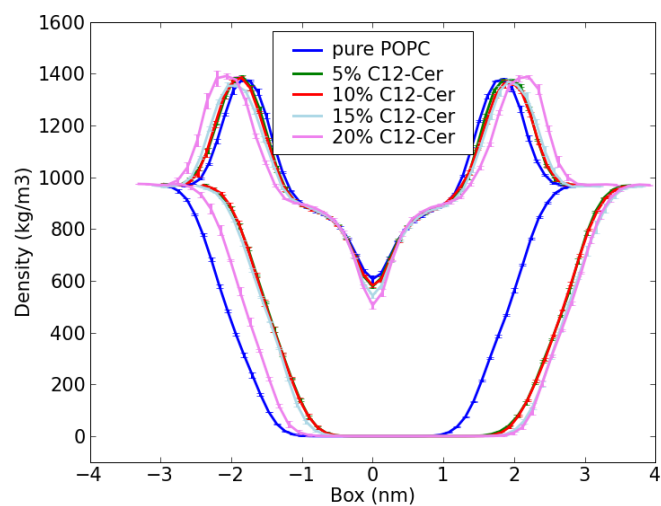
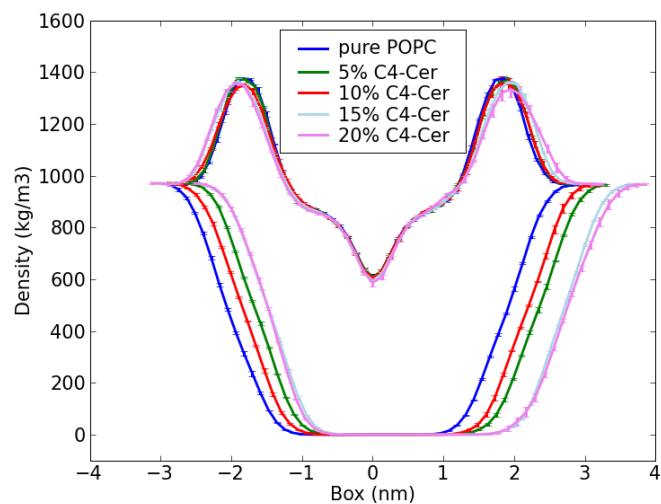


*Figure 8-11: Density profiles of POPC-Ceramide systems in different ceramide concentration with analogy force-fields: lower curves displays water density, higher curves displays system density (each simulation was performed for 10 ns at 300 K).*



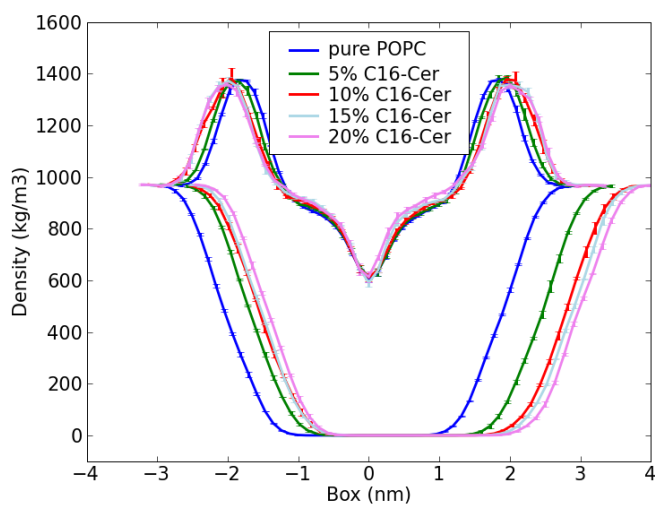
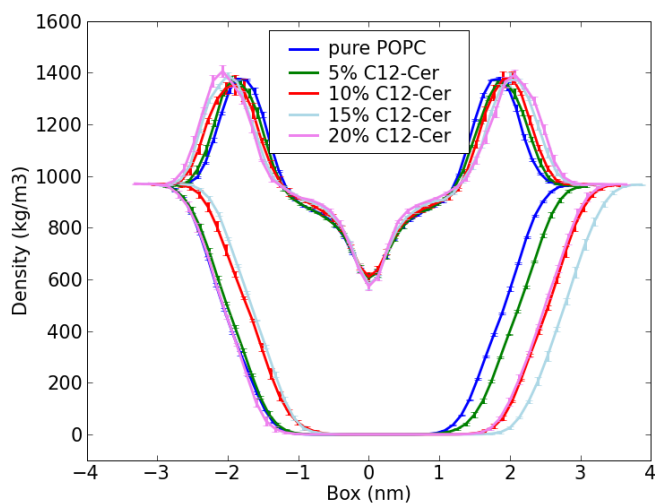
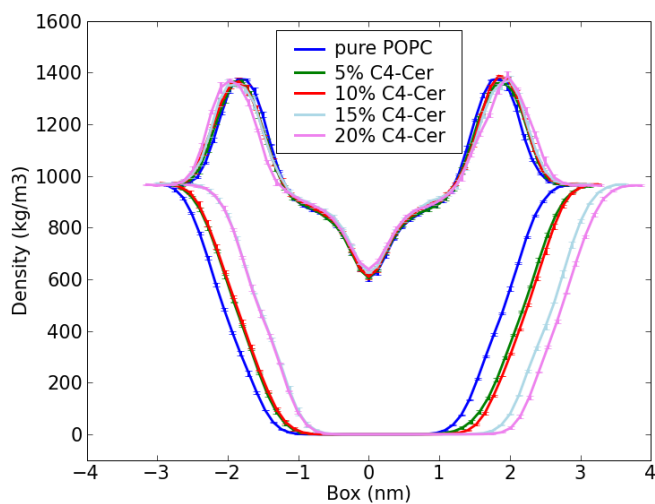


*Figure 8-12: Density profiles of POPC-Ceramide systems in different ceramide concentration with server force-fields: lower curves displays water density, higher curves displays system density (each simulation was performed for 10 ns at 300 K).*

### 8.2.3 Chain Order Parameters

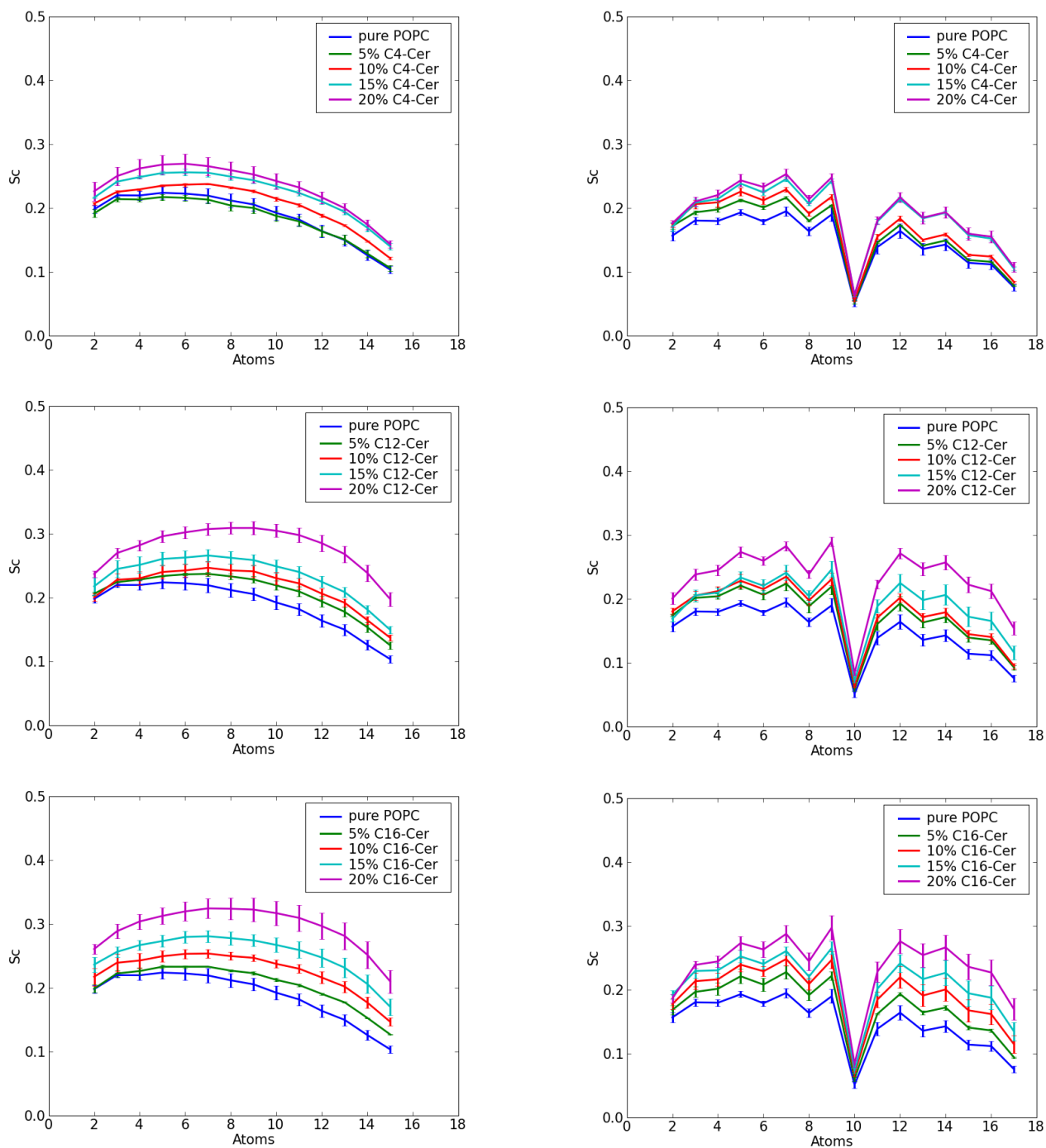


Figure 8-13: Order parameters of  $SN_1$  and  $SN_2$  chains of POPC for POPC-ceramide systems with analogy force-fields (each simulation was performed for 10 ns at 300 K).

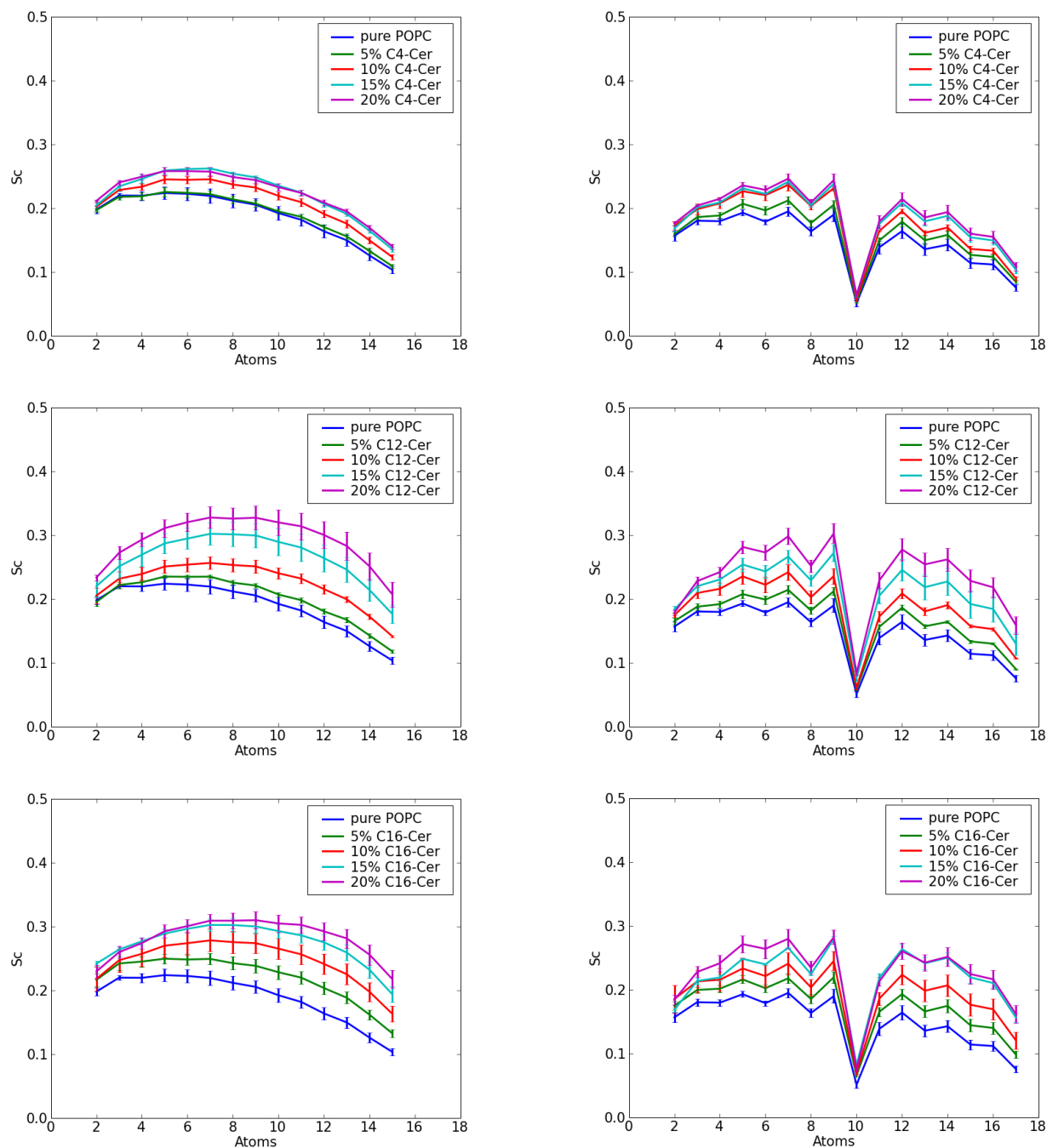


Figure 8-14: Order parameters of SN<sub>1</sub> and SN<sub>2</sub> chains of POPC for POPC-ceramide systems with server force-fields (each simulation was performed for 10 ns at 300 K).

		Percentage of Ceramide	Area of XY-Plane (nm <sup>2</sup> )	Area per Lipid (Å <sup>2</sup> )	Bilayer Width (nm)	1 <sup>st</sup> RDF Maximum for POPC-Water	
	POPC	0	40.0 ± 0.5	62.3 ± 0.6	3.67 ± 0.04	1.07 ± 0.02	
Analogy	C4-Cer	5	38.9 ± 0.2	60.5 ± 0.3	3.77 ± 0.08	1.06 ± 0.02	
		10	37.0 ± 0.2	58.5 ± 0.2	3.7 ± 0.05	1.04 ± 0.01	
		15	34.9 ± 0.3	55.9 ± 0.4	3.81 ± 0.04	0.97 ± 0.01	
		20	33.8 ± 0.4	54.4 ± 0.6	3.86 ± 0.07	0.93 ± 0.01	
	C12-Cer	5	38.0 ± 0.4	59.4 ± 0.6	3.77 ± 0.06	0.99 ± 0.01	
		10	37.0 ± 0.6	58.9 ± 0.7	3.8 ± 0.1	1.08 ± 0.01	
		15	35.5 ± 0.8	56.8 ± 1.1	3.89 ± 0.17	0.96 ± 0.05	
		20	32.7 ± 0.6	53 ± 0.8	4.27 ± 0.13	0.93 ± 0.05	
	C16-Cer	5	38.2 ± 0.4	59.7 ± 0.5	3.88 ± 0.06	1.03 ± 0.04	
		10	36.2 ± 0.7	57.2 ± 1.0	3.97 ± 0.07	0.98 ± 0.04	
		15	34.6 ± 0.8	55.2 ± 1.2	4.03 ± 0.07	0.97 ± 0.07	
		20	32.4 ± 0.8	52.2 ± 1.3	4.4 ± 0.07	0.89 ± 0.06	
	Server	C4-Cer	5	38.6 ± 0.2	60.5 ± 0.4	3.77 ± 0.13	1.04 ± 0.01
			10	36.6 ± 0.3	58.7 ± 0.3	3.69 ± 0.07	1.01 ± 0.03
			15	35.2 ± 0.4	56.8 ± 0.6	3.88 ± 0.01	1 ± 0.04
			20	33.7 ± 0.5	55.2 ± 0.7	3.94 ± 0.04	0.96 ± 0.01
C12-Cer		5	38.4 ± 0.3	60.2 ± 0.5	3.85 ± 0.05	1.03 ± 0.02	
		10	36.4 ± 0.7	57.8 ± 0.9	3.93 ± 0.02	0.98 ± 0.06	
		15	34.2 ± 1.0	55.1 ± 1.3	4.04 ± 0.03	0.92 ± 0.06	
		20	32.4 ± 0.8	52.5 ± 1.2	4.14 ± 0.09	0.91 ± 0.04	
C16-Cer		5	37.7 ± 0.4	59 ± 0.7	3.85 ± 0.09	0.97 ± 0.03	
		10	35.9 ± 1.0	56.9 ± 1.6	3.95 ± 0.09	1.05 ± 0.04	
		15	34.1 ± 0.4	54.8 ± 0.5	3.98 ± 0.09	0.95 ± 0.02	
		20	33.5 ± 0.7	54.4 ± 1.4	4.02 ± 0.16	0.95 ± 0.07	

*Table 8-2: Bilayer area, area per lipid, bilayer width, 1st maximum of radial distribution function for POPC-water of pure POPC and POPC-Ceramide mixtures in different ceramide concentrations for two different force-fields.*

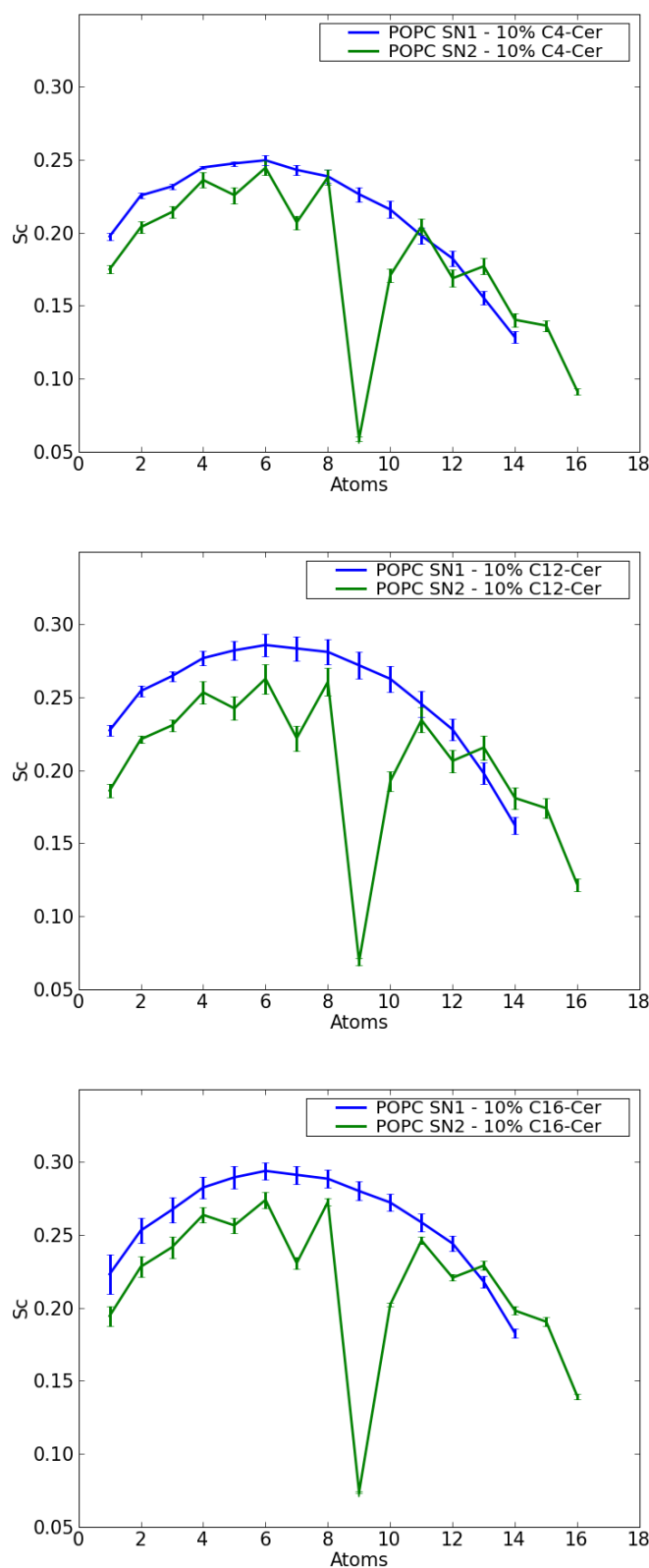


Figure 8-15: Order parameters of  $SN_1$  and  $SN_2$  chains of POPC for 10% of POPC-ceramide systems from last 90 ns of 180 ns long simulations with server force-fields for ceramides at 300 K.

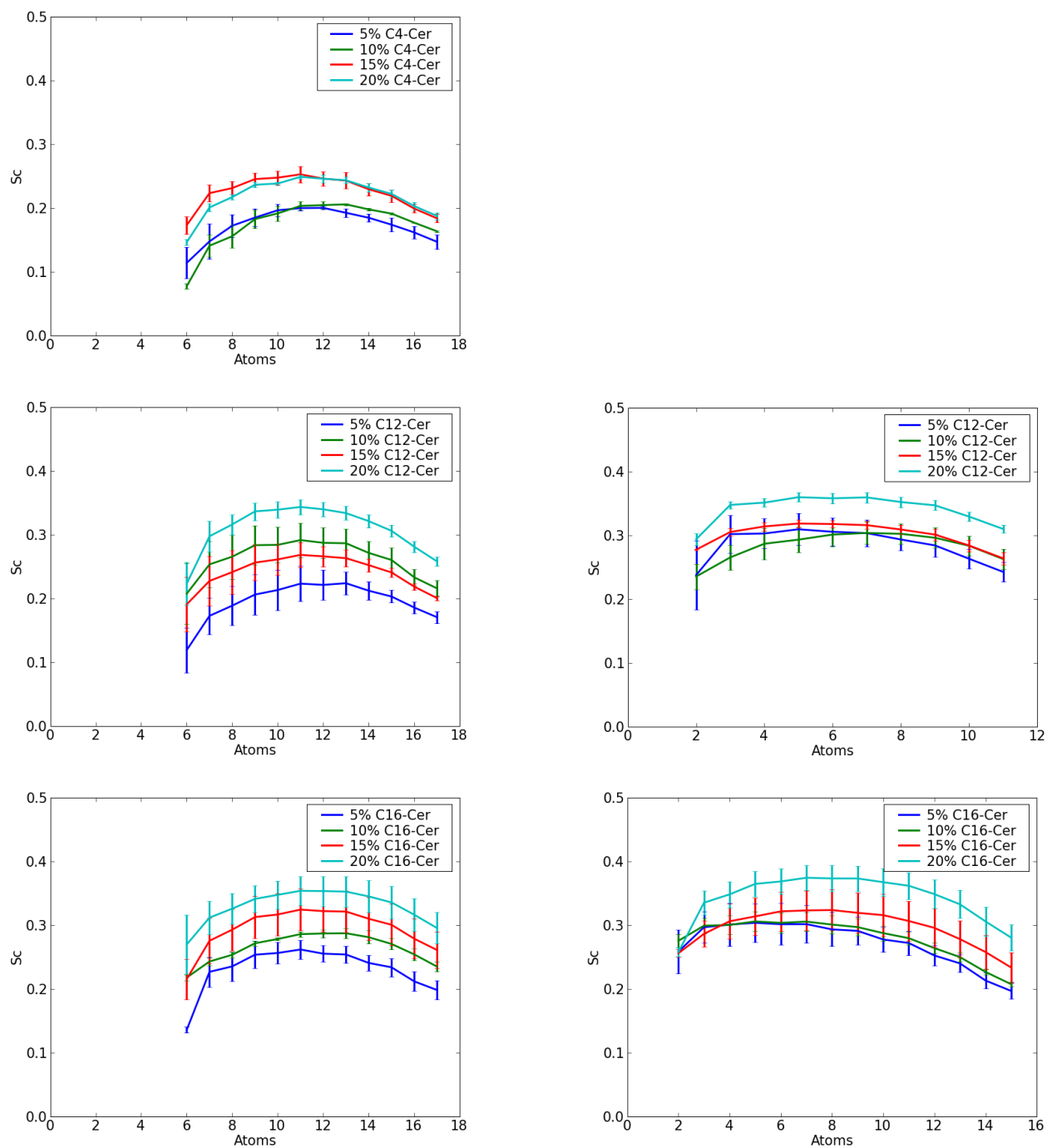


Figure 8-16: Order parameters of acyl and sphingosine chains of ceramide for POPC-ceramide systems with analogy force-fields (each simulation was performed for 10 ns at 300 K).

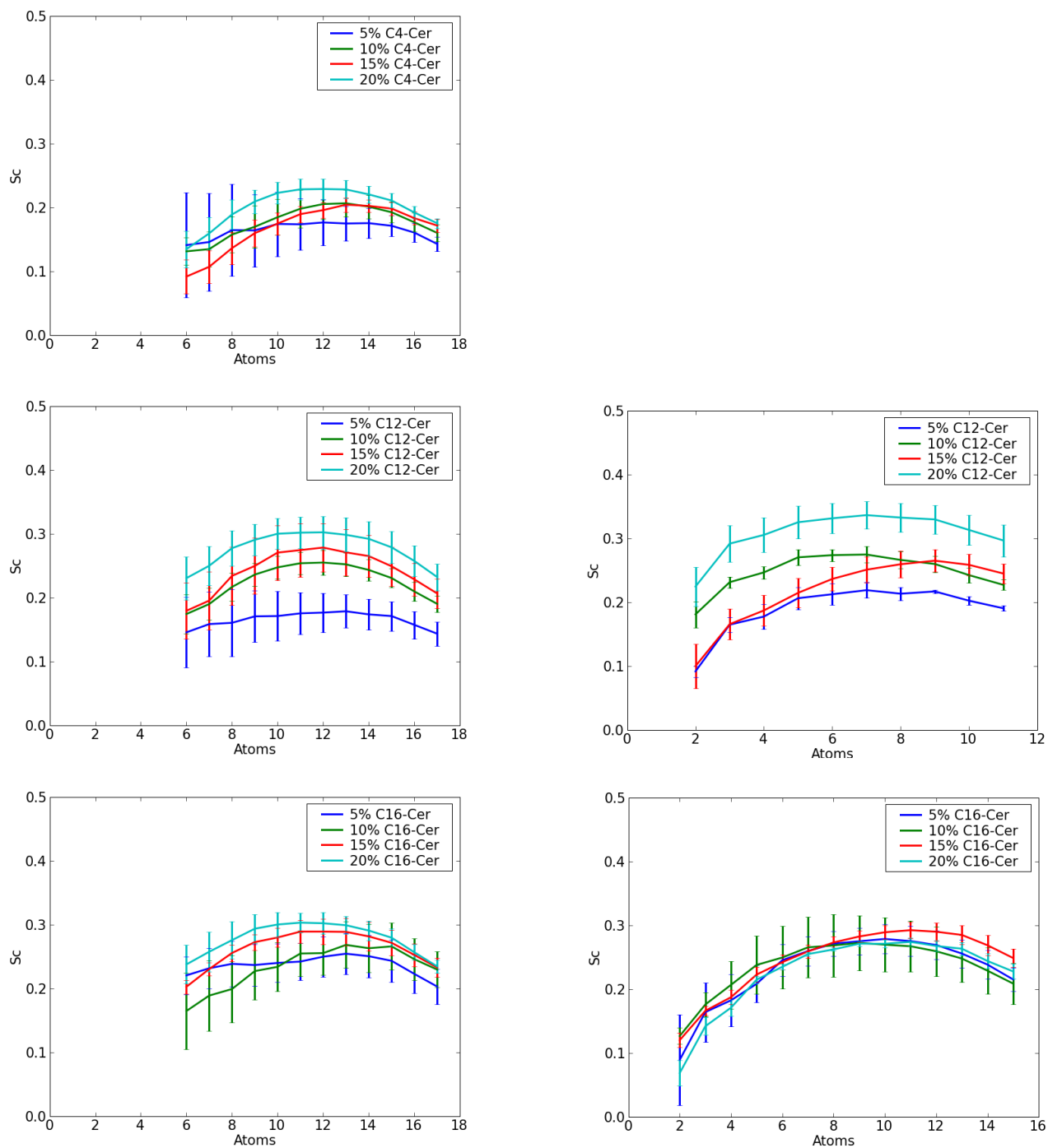


Figure 8-17: Order parameters of acyl and sphingosine chains of ceramide for POPC-ceramide systems with server force-fields (each simulation was performed for 10 ns at 300 K).

### 8.2.4 Hydrogen-bonding

		Percentage of Ceramide	Number of H-bonds POPC-Water	Number of H-bonds POPC-Cer	Number of H-bonds Cer-Water	Number of H-bonds Cer-Cer	
	POPC	0	812.8 ± 17.5	-	-	-	
Analogy	C4-Cer	5	777.3 ± 14.9	13.2 ± 1.4	6.1 ± 2.1	1.4 ± 0.9	
		10	727.3 ± 16.5	28.6 ± 3.7	14.8 ± 4.2	2.8 ± 1.7	
		15	671.3 ± 16.9	43.6 ± 3.6	16.2 ± 4.7	4.7 ± 1.3	
		20	629.1 ± 15.2	60.4 ± 6.2	22.1 ± 6.9	6.5 ± 1.8	
	C12-Cer	5	752.6 ± 18.2	15.6 ± 1.7	4.8 ± 2.3	0.6 ± 0.7	
		10	724.4 ± 15.5	34.3 ± 3.0	9.5 ± 4.2	1.7 ± 1.3	
		15	677.8 ± 18.4	43.7 ± 4.5	16.9 ± 6.3	4.1 ± 1.5	
		20	614.1 ± 20.0	61.6 ± 6.4	23.0 ± 7.3	6.2 ± 2.3	
	C16-Cer	5	757.9 ± 18.7	14.1 ± 2.2	6.5 ± 2.8	0.9 ± 0.8	
		10	711.0 ± 19.9	31.4 ± 3.5	12.1 ± 4.1	2.0 ± 1.3	
		15	669.3 ± 23.1	43.7 ± 4.4	18.2 ± 4.7	3.5 ± 1.5	
		20	612.7 ± 19.9	57.9 ± 6.0	25.6 ± 7.9	5.7 ± 2.0	
	Server	C4-Cer	5	777.9 ± 15.9	1.4 ± 1.3	1.0 ± 1.1	0.1 ± 0.4
			10	733.5 ± 16.0	3.8 ± 1.8	1.8 ± 1.5	0.3 ± 0.6
			15	700.1 ± 16.6	4.7 ± 2.0	3.0 ± 2.1	0.5 ± 0.7
			20	649.9 ± 15.4	7.9 ± 2.6	3.8 ± 2.5	0.7 ± 0.9
C12-Cer		5	775.4 ± 16.3	2.3 ± 1.5	1.2 ± 1.1	0.2 ± 0.4	
		10	727.5 ± 20.1	4.7 ± 2.0	2.6 ± 1.7	0.4 ± 0.7	
		15	678.1 ± 23.9	5.6 ± 2.2	3.4 ± 2.2	1.0 ± 1.1	
		20	629.6 ± 21.2	10.8 ± 3.2	5.7 ± 2.7	1.0 ± 1.1	
C16-Cer		5	758.9 ± 17.8	2.0 ± 1.4	1.3 ± 1.2	0.1 ± 0.4	
		10	720.9 ± 22.9	4.0 ± 1.8	2.6 ± 1.7	0.4 ± 0.7	
		15	681.0 ± 17.2	7.0 ± 2.4	4.2 ± 2.3	1.1 ± 1.1	
		20	651.3 ± 16.9	9.2 ± 2.7	5.1 ± 2.6	1.4 ± 1.2	

*Table 8-3: Number of hydrogen-bonds between ceramide with POPC, water and ceramide itself and between POPC and water for pure POPC and POPC-Ceramide mixtures in different ceramide concentrations for two different force-fields.*



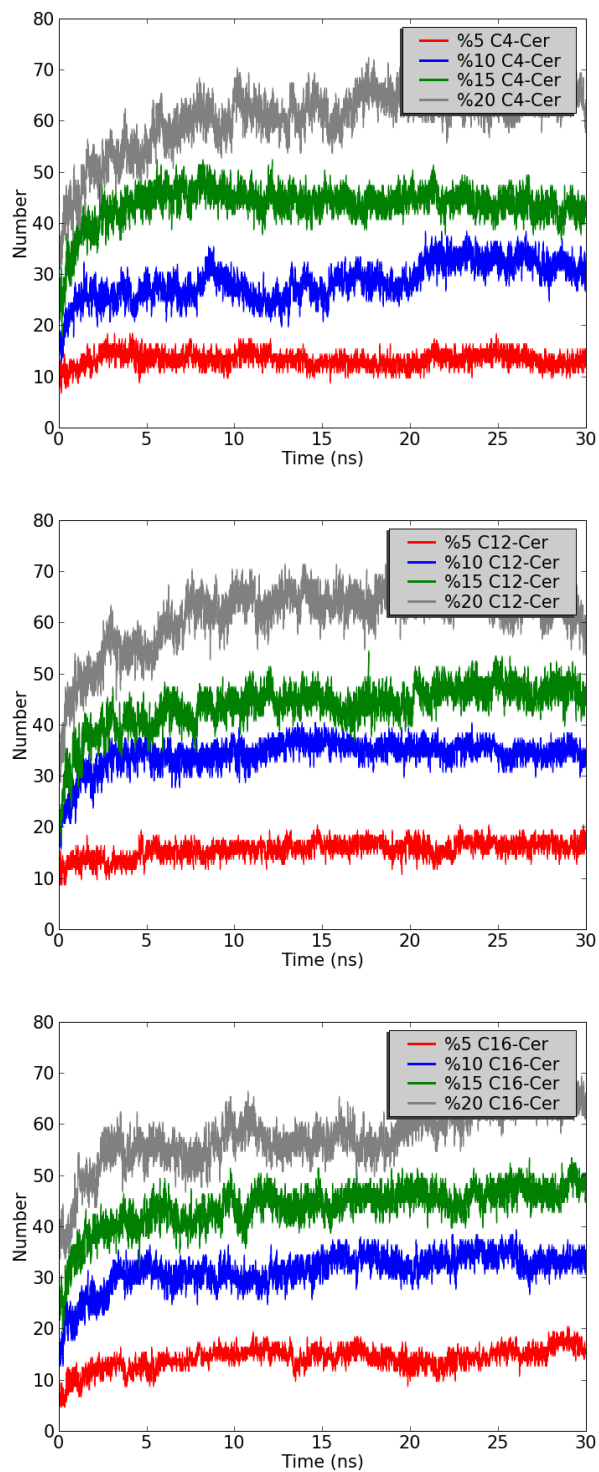


Figure 8-18: Number of hydrogen bonds between POPC and ceramides for POPC-ceramide systems with analogy force-fields (each simulation was performed for 10 ns at 300 K).

## 8.2.5 Radial Distribution Function

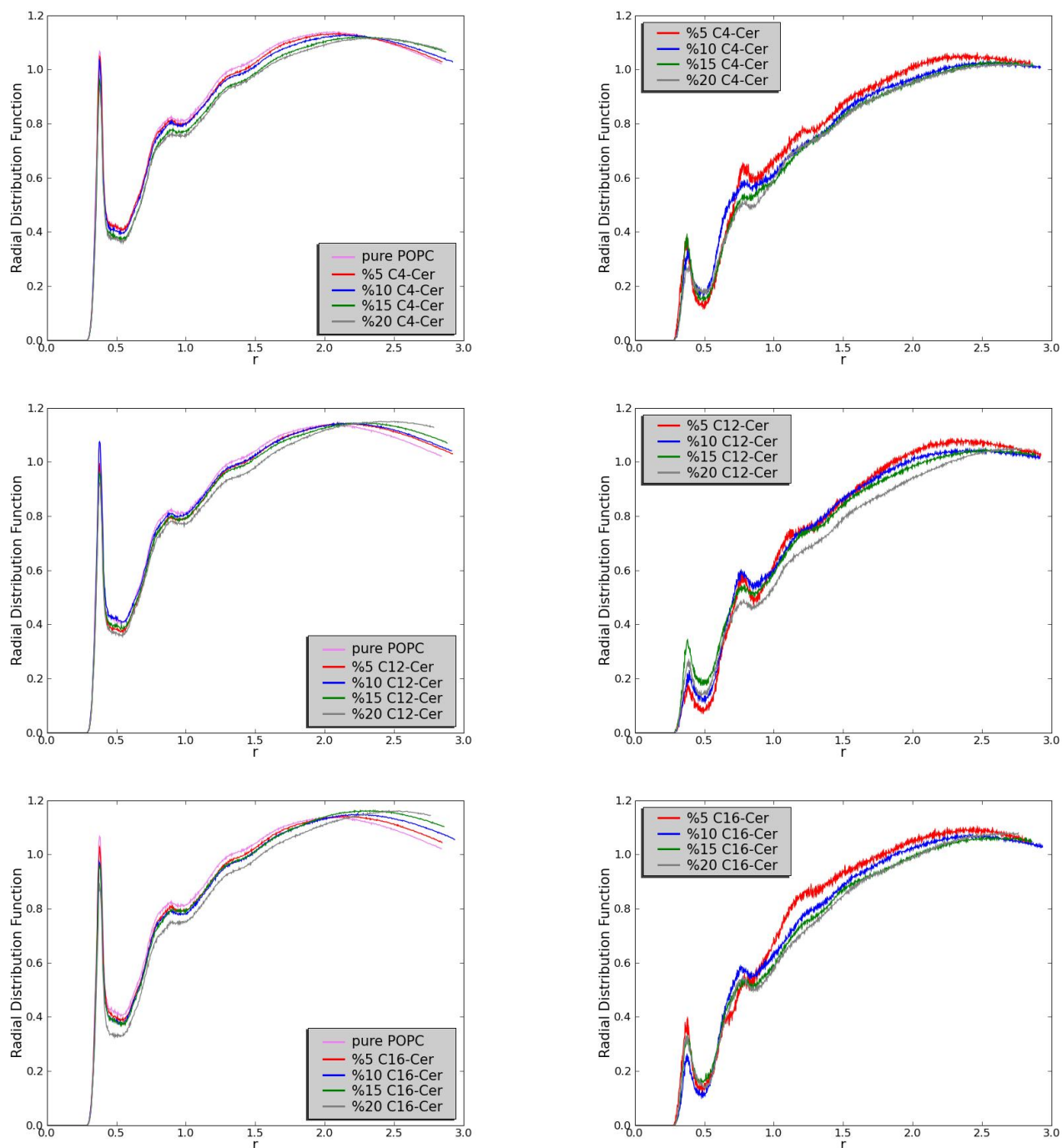


Figure 8-19: Radial distribution functions for water oxygen with carbonyl carbon of POPC SN<sub>2</sub> chain (left) and carbonyl carbon of ceramide acyl chain (right) for POPC-ceramide systems with analogy force-fields (each simulation was performed for 10 ns at 300 K).

## References

- (2005). "VCCLAB, virtual computational chemistry laboratory." from <http://www.vcclab.org>.
- Abramson, S., H. Korchak, et al. (1985). "Modes of action of aspirin-like drugs." Proceedings of the National Academy of Sciences of the United States of America **82**(21): 7227-7231.
- Althoff, G., D. Frezzato, et al. (2002). "Transverse nuclear spin relaxation studies of viscoelastic properties of membrane vesicles. I. Theory." Journal of Physical Chemistry B **106**(21).
- Althoff, G., N. J. Heaton, et al. (1996). "NMR relaxation study of collective motions and viscoelastic properties in biomembranes." Colloids and Surfaces a-Physicochemical and Engineering Aspects **115**.
- Althoff, G., O. Stauch, et al. (2002). "Transverse nuclear spin relaxation studies of viscoelastic properties of membrane vesicles. Ii. Experimental results." Journal of Physical Chemistry B **106**(21).
- Anand, B. S., J. J. Romero, et al. (1999). "Phospholipid association reduces the gastric mucosal toxicity of aspirin in human subjects." American Journal of Gastroenterology **94**(7): 1818-1822.
- Andrew, E. R., A. Bradbury, et al. (1959). "Removal of dipolar broadening of nuclear magnetic resonance spectra of solids by specimen rotation." Nature **183**(4678): 1802-1803.
- Anishkin, A., S. Sukharev, et al. (2006). "Searching for the molecular arrangement of transmembrane ceramide channels." Biophysical Journal **90**(7): 2414-2426.
- Aucoin, D., D. Camenares, et al. (2009). "High-resolution H-1 MAS RFDR NMR of biological membranes." Journal of Magnetic Resonance **197**(1): 77-86.
- Aurenhammer, F. (1991). "Voronoi diagrams - a survey of a fundamental geometric data structure." Computing Surveys **23**(3).
- Barone, V., A. Bencini, et al. (1998). "Assessment of a combined qm/mm approach for the study of large nitroxide systems in vacuo and in condensed phases." Journal of the American Chemical Society **120**(28): 7069-7078.
- Bekker, H., Berendsen, H. J. C., Dijkstra, E. J., Achterop, S., van Drunen, R., van der Spoel, D., Sijbers, A., Keegstra, H., Reitsma, B., Renardus, M. K. R. (1993). "Gromacs: A parallel computer for molecular dynamics simulations." Physics Computing **92**: 257-261.
- Berendsen, H. J. C., J. P. M. Postma, et al. (1984). "Molecular-dynamics with coupling to an external bath." Journal of Chemical Physics **81**(8): 3684-3690.
- Berendsen, H. J. C., D. Vandespoel, et al. (1995). "GROMACS - a message-passing parallel molecular-dynamics implementation." Computer Physics Communications **91**(1-3).
- Berger, O., O. Edholm, et al. (1997). "Molecular dynamics simulations of a fluid bilayer of dipalmitoylphosphatidylcholine at full hydration, constant pressure, and constant temperature." Biophysical Journal **72**(5): 2002-2013.
- Bjelkmar, P., P. S. Niemela, et al. (2009). "Conformational changes and slow dynamics through microsecond polarized atomistic molecular simulation of an integral kv1.2 ion channel." Plos Computational Biology **5**(2).

- Bloom, M., E. E. Burnell, et al. (1975). "Nuclear magnetic-resonance line-shapes in lipid bilayer model membranes." Chemistry and Physics of Lipids **14**(2): 107-112.
- Bollinger, C. R., V. Teichgraber, et al. (2005). "Ceramide-enriched membrane domains." Biochimica Et Biophysica Acta-Molecular Cell Research **1746**(3): 284-294.
- Bombardelli, E., S. B. Curri, et al. (1989). "Complexes between phospholipids and vegetal derivatives of biological interest." Fitoterapia **60**: 1-9.
- Boulgaropoulos, B., Z. Arsov, et al. (2011). "Stable and unstable lipid domains in ceramide-containing membranes." Biophysical Journal **100**(9): 2160-2168.
- Brown, D. A. and E. London (1998). "Structure and origin of ordered lipid domains in biological membranes." Journal of Membrane Biology **164**(2): 103-114.
- Brown, M. F. (1996). Membrane structure and dynamics studied with NMR spectroscopy. Membrane structure and dynamics. K. M. Merz and B. Roux, Birkhäuser: 175-252.
- Brown, M. F., R. L. Thurmond, et al. (2001). "Composite membrane deformation on the mesoscopic length scale." Physical Review E **64**(1).
- Chau, P. L. and A. J. Hardwick (1998). "A new order parameter for tetrahedral configurations." Molecular Physics **93**(3): 511-518.
- Chiantia, S., N. Kahya, et al. (2006). "Effects of ceramide on liquid-ordered domains investigated by simultaneous afm and fcs." Biophysical Journal **90**(12): 4500-4508.
- Cremesti, A., F. Paris, et al. (2001). "Ceramide enables fas to cap and kill." Journal of Biological Chemistry **276**(26): 23954-23961.
- D. van der Spoel, E. L., B. Hess, A. R. van Buuren, E. Apol, P. J. Meulenhoff, D. P. Tieleman, A. L. T. M. Sijbers, K. A. Feenstra, R. van Drunen and H. J. C., Berendsen, H. J. C. (2005). "Gromacs user manual version 4.0."
- Darden, T., D. York, et al. (1993). "Particle mesh ewald - an n.Log(n) method for ewald sums in large systems." Journal of Chemical Physics **98**(12): 10089-10092.
- Davis, J. H. (1979). "Deuterium magnetic-resonance study of the gel and liquid-crystalline phases of dipalmitoyl phosphatidylcholine." Biophysical Journal **27**(3): 339-358.
- Davis, J. H., M. Auger, et al. (1995). "High resolution H-1 nuclear magnetic resonance of a transmembrane peptide." Biophysical Journal **69**(5): 1917-1932.
- Davis, J. H., K. R. Jeffrey, et al. (1976). "Quadrupolar echo deuteron magnetic-resonance spectroscopy in ordered hydrocarbon chains." Chemical Physics Letters **42**(2): 390-394.
- deAzevedo, E. R., W. G. Hu, et al. (1999). "Centerband-only detection of exchange: Efficient analysis of dynamics in solids by NMR." Journal of the American Chemical Society **121**(36): 8411-8412.
- deAzevedo, E. R., W. G. Hu, et al. (2000). "Principles of centerband-only detection of exchange in solid-state nuclear magnetic resonance, and extension to four-time centerband-only detection of exchange." Journal of Chemical Physics **112**(20): 8988-9001.
- Delaunay, B. (1934). "Sur la sphère vide." Izvestia Akademii Nauk SSSR, Otdelenie Matematicheskikh i Estestvennykh Nauk **7**: 793-800.
- Dufourc, E. J., C. Mayer, et al. (1992). "Dynamics of phosphate head groups in

- biomembranes - comprehensive analysis using P-31 nuclear-magnetic-resonance lineshape and relaxation-time measurements." Biophysical Journal **61**(1).
- Dvinskikh, S. V., V. Castro, et al. (2005). "Efficient solid-state NMR methods for measuring heteronuclear dipolar couplings in unoriented lipid membrane systems." Physical Chemistry Chemical Physics **7**(4): 607-613.
- Dvinskikh, S. V., H. Zimmermann, et al. (2003). "Heteronuclear dipolar recoupling in liquid crystals and solids by pisema-type pulse sequences." Journal of Magnetic Resonance **164**(1): 165-170.
- Dvinskikh, S. V., H. Zimmermann, et al. (2005). "Heteronuclear dipolar recoupling in solid-state nuclear magnetic resonance by amplitude-, phase-, and frequency-modulated lee-goldburg cross-polarization." Journal of Chemical Physics **122**(4).
- Egberts, E. and H. J. C. Berendsen (1988). "Molecular-dynamics simulation of a smectic liquid-crystal with atomic detail." Journal of Chemical Physics **89**(6): 3718-3732.
- Epand, R. M. (1998). "Lipid polymorphism and protein-lipid interactions." Biochimica Et Biophysica Acta-Reviews on Biomembranes **1376**(3): 353-368.
- Essmann, U., L. Perera, et al. (1995). "A smooth particle mesh ewald method." Journal of Chemical Physics **103**(19): 8577-8593.
- Falck, E., M. Patra, et al. (2004). "Lessons of slicing membranes: Interplay of packing, free area, and lateral diffusion in phospholipid/cholesterol bilayers." Biophysical Journal **87**(2): 1076-1091.
- Feller, S. E., D. Huster, et al. (1999). "Interpretation of NOESY cross-relaxation rates from molecular dynamics simulation of a lipid bilayer." Journal of the American Chemical Society **121**(38): 8963-8964.
- Friesen, R. W. and J. A. Mancini (2008). "Microsomal prostaglandin e-2 synthase-1 (mPGES-1): A novel anti-inflammatory therapeutic target." Journal of Medicinal Chemistry **51**(14).
- Funk, C. D. (2001). "Prostaglandins and leukotrienes: Advances in eicosanoid biology." Science **294**(5548): 1871-1875.
- Gabriel, S. E., L. Jaakkimainen, et al. (1991). "Risk for serious gastrointestinal complications related to use of nonsteroidal antiinflammatory drugs - a metaanalysis." Annals of Internal Medicine **115**(10): 787-796.
- Gan, Z. H. (2000). "Spin dynamics of polarization inversion spin exchange at the magic angle in multiple spin systems." Journal of Magnetic Resonance **143**(1): 136-143.
- Garcia-Barros, M., F. Paris, et al. (2003). "Tumor response to radiotherapy regulated by endothelial cell apoptosis." Science **300**(5622): 1155-1159.
- Gidwani, A., H. A. Brown, et al. (2003). "Disruption of lipid order by short-chain ceramides correlates with inhibition of phospholipase d and downstream signaling by fc epsilon ri." Journal of Cell Science **116**(15): 3177-3187.
- Goetz, R., G. Gompper, et al. (1999). "Mobility and elasticity of self-assembled membranes." Physical Review Letters **82**(1): 221-224.
- Goldman, M. (2008). "Overview of spin temperature, thermal mixing and dynamic nuclear polarization." Applied Magnetic Resonance **34**(3-4): 219-226.
- Goldschmidt-Arzi, M., E. Shimoni, et al. (2011). "Intracellular localization of organized lipid domains of c16-ceramide/cholesterol." Journal of Structural Biology **175**(1): 21-30.
- Granstrom, E. (1984). "The arachidonic-acid cascade prostaglandins thromboxanes and

- leukotrienes." Inflammation **8**(SUPPL): S15-S26.
- Grassme, H., A. Jekle, et al. (2001). "Cd95 signaling via ceramide-rich membrane rafts." Journal of Biological Chemistry **276**(23): 20589-20596.
- Gulbins, E., S. Dreschers, et al. (2004). "Ceramide, membrane rafts and infections." Journal of Molecular Medicine-Jmm **82**(6): 357-363.
- Gulbins, E. and R. Kolesnick (2003). "Raft ceramide in molecular medicine." Oncogene **22**(45): 7070-7077.
- Hess, B., H. Bekker, et al. (1997). "LINCS: A linear constraint solver for molecular simulations." Journal of Computational Chemistry **18**(12): 1463-1472.
- Hess, B., C. Kutzner, et al. (2008). "GROMACS 4: Algorithms for highly efficient, load-balanced, and scalable molecular simulation." Journal of Chemical Theory and Computation **4**(3).
- Hieke, M., C. Greiner, et al. (2011). "A novel class of dual mPGES-1/5-LO inhibitors based on the alpha-naphthyl pirinixic acid scaffold." Bioorganic & Medicinal Chemistry Letters **21**(5): 1329-1333.
- Hockney, R. W., S. P. Goel, et al. (1974). "Quiet high-resolution computer models of a plasma." Journal of Computational Physics **14**(2): 148-158.
- Holopainen, J. M., J. Y. A. Lehtonen, et al. (1997). "Lipid microdomains in dimyristoylphosphatidylcholine-ceramide liposomes." Chemistry and Physics of Lipids **88**(1): 1-13.
- Holopainen, J. M., M. Subramanian, et al. (1998). "Sphingomyelinase induces lipid microdomain formation in a fluid phosphatidylcholine/sphingomyelin membrane." Biochemistry **37**(50): 17562-17570.
- Holte, L. L. and K. Gawrisch (1997). "Determining ethanol distribution in phospholipid multilayers with MAS-NOESY spectra." Biochemistry **36**(15): 4669-4674.
- Hong, M., K. Schmidt-Rohr, et al. (1996). "Conformational constraints on the headgroup and sn-2 chain of bilayer DMPC from NMR dipolar couplings." Biochemistry **35**(25): 8335-8341.
- Hoover, W. G. (1985). "Canonical dynamics - equilibrium phase-space distributions." Physical Review A **31**(3): 1695-1697.
- Horta, B. A. C., P. F. J. Fuchs, et al. (2011). "New interaction parameters for oxygen compounds in the GROMOS force field: Improved pure-liquid and solvation properties for alcohols, ethers, aldehydes, ketones, carboxylic acids, and esters." Journal of Chemical Theory and Computation **7**(4): 1016-1031.
- Hsueh, Y. W., R. Giles, et al. (2002). "The effect of ceramide on phosphatidylcholine membranes: A deuterium NMR study." Biophysical Journal **82**(6): 3089-3095.
- Hu, K. N., H. H. Yu, et al. (2004). "Dynamic nuclear polarization with biradicals." Journal of the American Chemical Society **126**(35): 10844-10845.
- Huang, H. W., E. M. Goldberg, et al. (1996). "Ceramide induces structural defects into phosphatidylcholine bilayers and activates phospholipase a(2)." Biochemical and Biophysical Research Communications **220**(3): 834-838.
- Huang, H. W., E. M. Goldberg, et al. (1998). "Ceramide perturbs the structure of phosphatidylcholine bilayers and modulate the activity of phospholipase a(2)." European Biophysics Journal with Biophysics Letters **27**(4): 361-366.
- Huang, H. W., E. M. Goldberg, et al. (1999). "Ceramide modulate protein kinase c activity and perturb the structure of phosphatidylcholine/phosphatidylserine

- bilayers." Biophysical Journal **77**(3): 1489-1497.
- Huesch, J., B. Dutagaci, et al. (2011). "Structural properties of so-called NSAID-phospholipid-complexes." European Journal of Pharmaceutical Sciences **44**(1-2): 103-116.
- Huster, D., K. Arnold, et al. (1999). "Investigation of lipid organization in biological membranes by two-dimensional nuclear overhauser enhancement spectroscopy." Journal of Physical Chemistry B **103**(1): 243-251.
- Ivey, K. J., D. B. Paone, et al. (1980). "Acute effect of systemic aspirin on gastric-mucosa in man." Digestive Diseases and Sciences **25**(2): 97-99.
- Jain, N., B. P. Gupta, et al. (2010). "Phytosome: A novel drug delivery system for herbal medicine." International Journal of Pharmaceutical Sciences and Drug Research **2**(4): 224-228.
- Janiak, M. J., D. M. Small, et al. (1979). "Temperature and compositional dependence of the structure of hydrated dimyristoyl lecithin." Journal of Biological Chemistry **254**(13): 6068-6078.
- Jeener, J., B. H. Meier, et al. (1979). "Investigation of exchange processes by 2-dimensional NMR-spectroscopy." Journal of Chemical Physics **71**(11): 4546-4553.
- Joachim K. Seydel, M. W. (2002). Drug-membrane interactions: Analysis, drug distribution, modeling, Wiley-VCH.
- Jones, G. P. (1966). "Spin-lattice relaxation in rotating frame - weak-collision case." Physical Review **148**(1): 332-&.
- Jones, R., G. Rubin, et al. (2008). "Gastrointestinal and cardiovascular risks of nonsteroidal anti-inflammatory drugs." American Journal of Medicine **121**(6): 464-474.
- Junge, S., B. Brenner, et al. (1999). "Intracellular mechanisms of I-selectin induced capping." Cellular Signalling **11**(4): 301-308.
- Keeler, J. (2005). Understanding NMR spectroscopy. Chichester, John Wiley
- Keller, R. (2004). The computer aided resonance assignment tutorial CANTINA Verlag.
- Khazaeinia, T. and F. Jamali (2003). "A comparison of gastrointestinal permeability induced by diclofenac-phospholipid complex with diclofenac acid and its sodium salt." Journal of pharmacy & pharmaceutical sciences : a publication of the Canadian Society for Pharmaceutical Sciences, Societe canadienne des sciences pharmaceutiques **6**(3): 352-9.
- Kiihne, S. R., K. B. Geahigan, et al. (1999). "Distance measurements in multiply labeled crystalline cytidines by dipolar recoupling solid state NMR." Journal of Physical Chemistry A **103**(20): 3890-3903.
- Kinnunen, P. K. J. (1996). "On the molecular-level mechanisms of peripheral protein-membrane interactions induced by lipids forming inverted non-lamellar phases." Chemistry and Physics of Lipids **81**(2): 151-166.
- Kitatani, K., J. Idkowiak-Baldys, et al. (2008). "The sphingolipid salvage pathway in ceramide metabolism and signaling." Cellular Signalling **20**(6): 1010-1018.
- Koeberle, A., H. Zettl, et al. (2008). "Pirinixic acid derivatives as novel dual inhibitors of microsomal prostaglandin e(2) synthase-1 and 5-lipoxygenase." Journal of Medicinal Chemistry **51**(24): 8068-8076.
- Koenig, B. W., H. H. Strey, et al. (1997). "Membrane lateral compressibility determined

- by NMR and x-ray diffraction: Effect of acyl chain polyunsaturation." Biophysical Journal **73**(4): 1954-1966.
- Kolesnick, R. N., F. M. Goni, et al. (2000). "Compartmentalization of ceramide signaling: Physical foundations and biological effects." Journal of Cellular Physiology **184**(3): 285-300.
- Kucerka, N., Y. F. Liu, et al. (2005). "Structure of fully hydrated fluid phase DMPC and dlpc lipid bilayers using x-ray scattering from oriented multilamellar arrays and from unilamellar vesicles." Biophysical Journal **88**(4).
- Kucerka, N., S. Tristram-Nagle, et al. (2005). "Structure of fully hydrated fluid phase lipid bilayers with monounsaturated chains." Journal of Membrane Biology **208**(3): 193-202.
- Kuehl, F. A. and R. W. Egan (1980). "Prostaglandins, arachidonic-acid, and inflammation." Science **210**(4473): 978-984.
- Lafleur, M., B. Fine, et al. (1989). "Smoothed orientational order profile of lipid bilayers by H-2-nuclear magnetic-resonance." Biophysical Journal **56**(5).
- Langenbach, R., S. G. Morham, et al. (1995). "Prostaglandin-synthase-1 gene disruption in mice reduces arachidonic acid-induced inflammation and indomethacin-induced gastric-ulceration." Cell **83**(3): 483-492.
- Leach, A. R. (2001). Molecular dynamics simulation methods. Molecular modelling: Principles and applications  
Pearson Education Limited: 353-406.
- Lee, M. and W. I. Goldberg (1965). "Nuclear-magnetic-resonance line narrowing by a rotating rf field." Physical Review **140**(4A): 1261-&.
- Lemkul, J. A., W. J. Allen, et al. (2010). "Practical considerations for building GROMOS-compatible small-molecule topologies." Journal of Chemical Information and Modeling **50**(12): 2221-2235.
- Li, L., X. P. Tang, et al. (2002). "Conformational characterization of ceramides by nuclear magnetic resonance spectroscopy." Biophysical Journal **82**(4): 2067-2080.
- Lichtenberger, L. M., Z. M. Wang, et al. (1995). "Nonsteroidal antiinflammatory drugs (nsaids) associate with zwitterionic phospholipids - insight into the mechanism and reversal of NSAID-induced gastrointestinal injury." Nature Medicine **1**(2): 154-158.
- Lichtenberger, L. M., Y. Zhou, et al. (2006). "NSAID injury to the gastrointestinal tract: Evidence that nsaids interact with phospholipids to weaken the hydrophobic surface barrier and induce the formation of unstable pores in membranes." Journal of Pharmacy and Pharmacology **58**(11): 1421-1428.
- Ligumsky, M., E. M. Golanska, et al. (1983). "Aspirin can inhibit gastric-mucosal cyclooxygenase without causing lesions in rat." Gastroenterology **84**(4): 756-761.
- Lindahl, E., B. Hess, et al. (2001). "GROMACS 3.0: A package for molecular simulation and trajectory analysis." Journal of Molecular Modeling **7**(8): 306-317.
- Lindstrom, F., P. T. F. Williamson, et al. (2005). "Molecular insight into the electrostatic membrane surface potential by N-14/P-31 MAS NMR spectroscopy: Nociceptin-lipid association." Journal of the American Chemical Society **127**(18): 6610-6616.
- Lippert, J. L. and Peticola, W. I. (1971). "Laser raman investigation of effect of cholesterol on conformational changes in dipalmitoyl lecithin multilayers - (gel-liquid crystal transition/noncooperative/transition temperature)." Proceedings of the



- National Academy of Sciences of the United States of America **68**(7): 1572-&
- Lopes, L. B., M. V. Scarpa, et al. (2004). "Studies on the encapsulation of diclofenac in small unilamellar liposomes of soya phosphatidylcholine." Colloids and Surfaces B-Biointerfaces **39**(4): 151-158.
- Lucio, M., F. Bringezu, et al. (2008). "Binding of nonsteroidal anti-inflammatory drugs to DPPC: Structure and thermodynamic aspects." Langmuir **24**(8): 4132-4139.
- Lundbaek, J. A., A. M. Maer, et al. (1997). "Lipid bilayer electrostatic energy, curvature stress, and assembly of gramicidin channels." Biochemistry **36**(19): 5695-5701.
- Macura, S., Y. Huang, et al. (1981). "Two-dimensional chemical-exchange and cross-relaxation spectroscopy of coupled nuclear spins." Journal of Magnetic Resonance **43**(2): 259-281.
- Maier, T. J., S. Schiffmann, et al. (2009). "Cellular membranes function as a storage compartment for celecoxib." Journal of Molecular Medicine-Jmm **87**(10): 981-993.
- Marasinghe, P. A. B., J. J. Buffy, et al. (2005). "Membrane curvature change induced by an antimicrobial peptide detected by P-31 exchange NMR." Journal of Physical Chemistry B **109**(46): 22036-22044.
- Marcelja, S. (1974). "Chain ordering in liquid-crystals .2. Structure of bilayer membranes." Biochimica Et Biophysica Acta **367**(2): 165-176.
- Marion, D., M. Ikura, et al. (1989). "Improved solvent suppression in one-dimensional and two-dimensional NMR-spectra by convolution of time-domain data." Journal of Magnetic Resonance **84**(2).
- Marrink, S. J., H. J. Risselada, et al. (2005). "Simulation of gel phase formation and melting in lipid bilayers using a coarse grained model." Chemistry and Physics of Lipids **135**(2): 223-244.
- Marrink, S. J., H. J. Risselada, et al. (2007). "The martini force field: Coarse grained model for biomolecular simulations." Journal of Physical Chemistry B **111**(27): 7812-7824.
- Marsh, D. (2008). "Protein modulation of lipids, and vice-versa, in membranes." Biochimica Et Biophysica Acta-Biomembranes **1778**(7-8): 1545-1575.
- Massey, J. B. (2001). "Interaction of ceramides with phosphatidylcholine, sphingomyelin and sphingomyelin/cholesterol bilayers." Biochimica Et Biophysica Acta-Biomembranes **1510**(1-2): 167-184.
- Matsuki, Y., T. Maly, et al. (2009). "Dynamic nuclear polarization with a rigid biradical." Angewandte Chemie-International Edition **48**(27): 4996-5000.
- McIntosh, T. J. and S. A. Simon (1986). "Area per molecule and distribution of water in fully hydrated dilauroylphosphatidylethanolamine bilayers." Biochemistry **25**(17): 4948-4952.
- Metcalf, R. and S. A. Pandit (2012). "Mixing properties of sphingomyelin ceramide bilayers: A simulation study." Journal of Physical Chemistry B **116**(15): 4500-4509.
- Moreno, M. M., P. Garidel, et al. (2009). "The membrane-activity of ibuprofen, diclofenac, and naproxen: A physico-chemical study with lecithin phospholipids." Biochimica Et Biophysica Acta-Biomembranes **1788**(6): 1296-1303.
- Mouritsen, O. G. and K. Jorgensen (1998). "A new look at lipid-membrane structure in relation to drug research." Pharmaceutical Research **15**(10): 1507-1519.

- Nagle, J. F. (1980). "Theory of the main lipid bilayer phase-transition." Annual Review of Physical Chemistry **31**: 157-195.
- Nagle, J. F. and S. Tristram-Nagle (2000). "Structure of lipid bilayers." Biochimica Et Biophysica Acta-Reviews on Biomembranes **1469**(3): 159-195.
- Nagle, J. F., R. T. Zhang, et al. (1996). "X-ray structure determination of fully hydrated l(alpha) phase dipalmitoylphosphatidylcholine bilayers." Biophysical Journal **70**(3): 1419-1431.
- Nelson, D. L. and M. M. Cox (2005). Lehninger principles of biochemistry, W.H. Freeman and Company.
- Nomura, K., M. Lintuluoto, et al. (2011). "Hydration and temperature dependence of C-13 and H-1 NMR spectra of the DMPC phospholipid membrane and complete resonance assignment of its crystalline state." Journal of Physical Chemistry B **115**(50): 14991-15001.
- Nose, S. (1984). "A molecular-dynamics method for simulations in the canonical ensemble." Molecular Physics **52**(2): 255-268.
- Nose, S. and M. L. Klein (1983). "Constant pressure molecular-dynamics for molecular-systems." Molecular Physics **50**(5): 1055-1076.
- Otten, D., M. F. Brown, et al. (2000). "Softening of membrane bilayers by detergents elucidated by deuterium NMR spectroscopy." Journal of Physical Chemistry B **104**(51).
- Overhauser, A. W. (1953). "Paramagnetic relaxation in metals." Physical Review **89**(4): 689-700.
- Pandit, S. A., S. Vasudevan, et al. (2004). "Sphingomyelin-cholesterol domains in phospholipid membranes: Atomistic simulation." Biophysical Journal **87**(2): 1092-1100.
- Panicker, L., V. K. Sharma, et al. (1995). "Interaction of aspirin with DPPC in the lyotropic, dppc-aspirin-H<sub>2</sub>O/D<sub>2</sub>O membrane." Molecular Crystals and Liquid Crystals Science and Technology Section a-Molecular Crystals and Liquid Crystals **260**: 611-621.
- Parrinello, M. and A. Rahman (1981). "Polymorphic transitions in single-crystals - a new molecular-dynamics method." Journal of Applied Physics **52**(12): 7182-7190.
- Pascher, I. (1976). "Molecular arrangements in sphingolipids conformation and hydrogen-bonding of ceramide and their implication on membrane stability and permeability." Biochimica Et Biophysica Acta **455**(2): 433-451.
- Patel, R. Y. and P. V. Balaji (2007). "Characterization of the conformational and orientational dynamics of ganglioside gmi in a dipalmitoylphosphatidylcholine bilayer by molecular dynamics simulations." Biochimica Et Biophysica Acta-Biomembranes **1768**(6): 1628-1640.
- Patra, M., M. Karttunen, et al. (2003). "Molecular dynamics simulations of lipid bilayers: Major artifacts due to truncating electrostatic interactions." Biophysical Journal **84**(6).
- Patra, M., M. Karttunen, et al. (2004). "Lipid bilayers driven to a wrong lane in molecular dynamics simulations by subtle changes in long-range electrostatic interactions." Journal of Physical Chemistry B **108**(14).
- Popescu, L., O. Rau, et al. (2007). "Quinoline-based derivatives of pirinixic acid as dual ppar alpha/gamma agonists." Archiv Der Pharmazie **340**(7): 367-371.

- Rainsford, K. D. (2007). "Anti-inflammatory drugs in the 21st century." Sub-cellular biochemistry **42**.
- Rau, O., Y. Syha, et al. (2008). "Alpha-alkyl substituted pirinixic acid derivatives as potent dual agonists of the peroxisome proliferator activated receptor alpha and gamma." Archiv Der Pharmazie **341**(3): 191-195.
- Raya, J., A. Bianco, et al. (2002). "Proton dipolar recoupling in resin-bound peptides under high-resolution magic angle spinning." Journal of Magnetic Resonance **157**(1): 43-51.
- Rosler, E. (1986). "Two-dimensional exchange NMR analyzed in the time domain." Chemical Physics Letters **128**(3).
- Rothman, J. E. (1973). "Molecular basis of mesomorphic phase-transitions in phospholipid systems." Journal of Theoretical Biology **38**(1): 1-16.
- Saleem, Q., A. Lai, et al. (2012). "Lateral diffusion of bilayer lipids measured via P-31 codex NMR." Chemistry and Physics of Lipids **165**(7): 721-730.
- Salmon, A., S. W. Dodd, et al. (1987). "Configurational statistics of acyl chains in polyunsaturated lipid bilayers from H-2 NMR." Journal of the American Chemical Society **109**(9): 2600-2609.
- Salnikov, E., M. Rosay, et al. (2010). "Solid-state NMR spectroscopy of oriented membrane polypeptides at 100 k with signal enhancement by dynamic nuclear polarization." Journal of the American Chemical Society **132**(17): 5940-+.
- Santilli, A. A., A. C. Scotese, et al. (1974). "Potent antihypercholesterolemic agent - 4-chloro-6-(2,3-xylidino)-2-pyrimidinylthio acetic acid (wy-14643)." Experientia **30**(10): 1110-1111.
- Scheidt, H. A. and D. Huster (2008). "The interaction of small molecules with phospholipid membranes studied by H-1 NOESY NMR under magic-angle spinning." Acta Pharmacologica Sinica **29**(1): 35-49.
- Scheidt, H. A., A. Pampel, et al. (2004). "Investigation of the membrane localization and distribution of flavonoids by high-resolution magic angle spinning NMR spectroscopy." Biochimica Et Biophysica Acta-Biomembranes **1663**(1-2): 97-107.
- Schiller, J., M. Muller, et al. (2007). "P-31 NMR spectroscopy of phospholipids: From micelles to membranes." Current Analytical Chemistry **3**(4): 283-301.
- Schindler, H. and J. Seelig (1975). "Deuterium order parameters in relation to thermodynamic properties of a phospholipid bilayer - statistical mechanical interpretation." Biochemistry **14**(11): 2283-2287.
- Schlick, T. (2002). Molecular modeling and simulation : An interdisciplinary guide, Springer
- Schmidt, C., S. Wefing, et al. (1986). "Dynamics of molecular reorientations - direct determination of rotational angles from two-dimensional NMR of powders." Chemical Physics Letters **130**(1-2): 84-90.
- Schuttelkopf, A. W. and D. M. F. van Aalten (2004). "PRODRG: A tool for high-throughput crystallography of protein-ligand complexes." Acta Crystallographica Section D-Biological Crystallography **60**: 1355-1363.
- Seelig, J. (1977). "Deuterium magnetic-resonance - theory and application to lipid-membranes." Quarterly Reviews of Biophysics **10**(3).
- Seelig, J. and N. Waespesarcevic (1978). "Molecular order in cis and trans unsaturated phospholipid bilayers." Biochemistry **17**(16): 3310-3315.

- Semalty, A., M. Semalty, et al. (2010). "Supramolecular phospholipids-polyphenolics interactions: The phytosome (r) strategy to improve the bioavailability of phytochemicals." Fitoterapia **81**(5): 306-314.
- Shah, J., J. M. Atienza, et al. (1995). "Structural and thermotropic properties of synthetic c16-0 (palmitoyl) ceramide - effect of hydration." Journal of Lipid Research **36**(9): 1936-1944.
- Shewchuk, J. R. (1996). Triangle: Engineering a 2d quality mesh generator and Delaunay triangulator. Applied computational geometry: Towards geometric engineering. M. C. L. a. D. Manocha, Springer-Verlag. **1148**: 203--222.
- Shewchuk, J. R. (2002). "Delaunay refinement algorithms for triangular mesh generation." Computational Geometry-Theory and Applications **22**(1-3).
- Shinoda, W. and S. Okazaki (1998). "A Voronoi analysis of lipid area fluctuation in a bilayer." Journal of Chemical Physics **109**(4).
- Siarheyeva, A., J. J. Lopez, et al. (2006). "Localization of multidrug transporter substrates within model membranes." Biochemistry **45**(19): 6203-6211.
- Silva, L., R. F. M. De Almeida, et al. (2006). "Ceramide-platform formation and -induced biophysical changes in a fluid phospholipid membrane." Molecular Membrane Biology **23**(2): 137-U2.
- Siminovitch, D. J. and K. R. Jeffrey (1981). "Orientational order in the choline headgroup of sphingomyelin - a N-14-NMR study." Biochimica Et Biophysica Acta **645**(2): 270-278.
- Siminovitch, D. J., K. R. Jeffrey, et al. (1983). "A comparison of the headgroup conformation and dynamics in synthetic analogs of dipalmitoylphosphatidylcholine." Biochimica Et Biophysica Acta **727**(1): 122-134.
- Siminovitch, D. J., M. Rance, et al. (1980). "The use of wide-line nitrogen-N-14 NMR as a probe in model membranes." Febs Letters **112**(1): 79-82.
- Simons, K. and E. Ikonen (1997). "Functional rafts in cell membranes." Nature **387**(6633).
- Singer, S. J. and G. L. Nicolson (1972). "Fluid mosaic model of structure of cell-membranes." Science **175**(4023): 720-&.
- Smit, B., P. A. J. Hilbers, et al. (1990). "Computer-simulations of a water oil interface in the presence of micelles." Nature **348**(6302): 624-625.
- Sodickson, D. K., M. H. Levitt, et al. (1993). "Broad-band dipolar recoupling in the nuclear-magnetic-resonance of rotating solids." Journal of Chemical Physics **98**(9).
- Solomon, I. (1955). "Relaxation processes in a system of 2 spins." Physical Review **99**(2): 559-565.
- Song, C. S., K. N. Hu, et al. (2006). "TOTAPOL: A biradical polarizing agent for dynamic nuclear polarization experiments in aqueous media." Journal of the American Chemical Society **128**(35): 11385-11390.
- Sot, J., F. J. Aranda, et al. (2005). "Different effects of long- and short-chain ceramides on the gel-fluid and lamellar-hexagonal transitions of phospholipids: A calorimetric, NMR, and x-ray diffraction study." Biophysical Journal **88**(5): 3368-3380.
- Sot, J., L. A. Bagatolli, et al. (2006). "Detergent-resistant, ceramide-enriched domains in sphingomyelin/ceramide bilayers." Biophysical Journal **90**(3): 903-914.

- Spiess, H. W. (1980). "Deuteron spin alignment - a probe for studying ultraslow motions in solids and solid polymers." Journal of Chemical Physics **72**(12): 6755-6762.
- Stejskal, E. O., J. Schaefer, et al. (1977). "Magic-angle spinning and polarization transfer in proton-enhanced NMR." Journal of Magnetic Resonance **28**(1): 105-112.
- Stohrer, J., G. Grobner, et al. (1991). "Collective lipid motions in bilayer-membranes studied by transverse deuteron spin relaxation." Journal of Chemical Physics **95**(1).
- Szoka, F. and D. Papahadjopoulos (1980). "Comparative properties and methods of preparation of lipid vesicles (liposomes)." Annual Review of Biophysics and Bioengineering **9**: 467-508.
- Talbott, C. M., I. Vorobyov, et al. (2000). "Conformational studies of sphingolipids by NMR spectroscopy. Ii. Sphingomyelin." Biochimica Et Biophysica Acta-Biomembranes **1467**(2): 326-337.
- Tardieu, A., V. Luzzati, et al. (1973). "Structure and polymorphism of hydrocarbon chains of lipids - study of lecithin-water phases." Journal of Molecular Biology **75**(4): 711-&.
- tenGrotenhuis, E., R. A. Demel, et al. (1996). "Phase behavior of stratum corneum lipids in mixed langmuir-blodgett monolayers." Biophysical Journal **71**(3): 1389-1399.
- Tetko, I. V., J. Gasteiger, et al. (2005). "Virtual computational chemistry laboratory - design and description." Journal of Computer-Aided Molecular Design **19**(6): 453-463.
- Tieleman, D. P., L. R. Forrest, et al. (1998). "Lipid properties and the orientation of aromatic residues in ompf, influenza m2, and alamethicin systems: Molecular dynamics simulations." Biochemistry **37**(50): 17554-17561.
- Tieleman, D. P., S. J. Marrink, et al. (1997). "A computer perspective of membranes: Molecular dynamics studies of lipid bilayer systems." Biochimica Et Biophysica Acta-Reviews on Biomembranes **1331**(3): 235-270.
- Trang, L. E. (1980). "Prostaglandins and inflammation." Seminars in Arthritis and Rheumatism **9**(3): 153-190.
- Trouard, T. P., A. A. Nevzorov, et al. (1999). "Influence of cholesterol on dynamics of dimyristoylphosphatidylcholine bilayers as studied by deuterium NMR relaxation." Journal of Chemical Physics **110**(17).
- Van der Spoel, D., E. Lindahl, et al. (2005). "GROMACS: Fast, flexible, and free." Journal of Computational Chemistry **26**(16): 1701-1718.
- van Rossum, B. J., C. P. de Groot, et al. (2000). "A method for measuring heteronuclear (H-1-C-13) distances in high speed MAS NMR." Journal of the American Chemical Society **122**(14): 3465-3472.
- Vanderploeg, P. and H. J. C. Berendsen (1982). "Molecular-dynamics simulation of a bilayer-membrane." Journal of Chemical Physics **76**(6): 3271-3276.
- Vanderploeg, P. and H. J. C. Berendsen (1983). "Molecular-dynamics of a bilayer-membrane." Molecular Physics **49**(1): 233-248.
- Vangunsteren, W. F. and H. J. C. Berendsen (1990). "Computer-simulation of molecular-dynamics - methodology, applications, and perspectives in chemistry." Angewandte Chemie-International Edition in English **29**(9): 992-1023.
- Veiga, M. P., J. L. R. Arrondo, et al. (1999). "Ceramides in phospholipid membranes: Effects on bilayer stability and transition to nonlamellar phases." Biophysical

- Journal **76**(1): 342-350.
- Vermeer, L. S., B. L. de Groot, et al. (2007). "Acyl chain order parameter profiles in phospholipid bilayers: Computation from molecular dynamics simulations and comparison with H-2 NMR experiments." European Biophysics Journal with Biophysics Letters **36**(8): 919-931.
- Voronoi, G. F. (1908). "Nouvelles applications des paramètres continus à la théorie de formes quadratiques." Journal für die reine und angewandte Mathematik **134**: 198-287.
- Wachowicz, M., L. Gill, et al. (2009). "Polyolefin blend miscibility: Polarization transfer versus direct excitation exchange NMR." Macromolecules **42**(2): 553-555.
- Wang, M., W. L. Song, et al. (2008). "Microsomal prostaglandin e synthase-1 inhibition in cardiovascular inflammatory disease." Journal of Internal Medicine **263**(5).
- Wefing, S. and H. W. Spiess (1988). "Two-dimensional exchange NMR of powder samples .1. 2-time distribution-functions." Journal of Chemical Physics **89**(3): 1219-1233.
- Weisz, K., G. Grobner, et al. (1992). "Deuteron nuclear-magnetic-resonance study of the dynamic organization of phospholipid cholesterol bilayer-membranes - molecular-properties and viscoelastic behavior." Biochemistry **31**(4).
- Werz, O., C. Greiner, et al. (2008). "Novel and potent inhibitors of 5-lipoxygenase product synthesis based on the structure of pirinixic acid." Journal of Medicinal Chemistry **51**(17): 5449-5453.
- Wesolowska, O., K. Michalak, et al. (2011). "Direct visualization of phase separation induced by phenothiazine-type antipsychotic drugs in model lipid membranes." Molecular Membrane Biology **28**(2): 103-114.
- Wiener, M. C. and S. H. White (1992). "Structure of a fluid dioleoylphosphatidylcholine bilayer determined by joint refinement of x-ray and neutron-diffraction data .3. Complete structure." Biophysical Journal **61**(2): 434-447.
- Wohlert, J. and O. Edholm (2006). "Dynamics in atomistic simulations of phospholipid membranes: Nuclear magnetic resonance relaxation rates and lateral diffusion." Journal of Chemical Physics **125**(20).
- Wollan, D. S. (1976). "Dynamic nuclear-polarization with an inhomogeneously broadened esr line .1. Theory." Physical Review B **13**(9).
- Wollan, D. S. (1976). "Dynamic nuclear-polarization with an inhomogeneously broadened esr line .2. Experiment." Physical Review B **13**(9).
- Wu, C. H., A. Ramamoorthy, et al. (1994). "High-resolution heteronuclear dipolar solid-state NMR-spectroscopy." Journal of Magnetic Resonance Series A **109**(2): 270-272.
- Yamauchi, K., S. Kuroki, et al. (2000). "The amide proton NMR chemical shift and hydrogen-bonded structure of peptides and polypeptides in the solid state as studied by high-frequency solid-state H-1 NMR." Chemical Physics Letters **324**(5-6): 435-439.
- Yau, W. M. and K. Gawrisch (2000). "Lateral lipid diffusion dominates NOESY cross-relaxation in membranes." Journal of the American Chemical Society **122**(16): 3971-3972.
- Yellin, N. and I. W. Levin (1977). "Hydrocarbon chain trans-gauche isomerization in phospholipid bilayer gel assemblies." Biochemistry **16**(4): 642-647.

- Zettl, H., M. Dittrich, et al. (2009). "Novel pirinixic acids as ppar alpha preferential dual ppar alpha/gamma agonists." Qsar & Combinatorial Science **28**(5): 576-586.
- Zhou, Y., J. F. Hancock, et al. (2010). "The nonsteroidal anti-inflammatory drug indomethacin induces heterogeneity in lipid membranes: Potential implication for its diverse biological action." Plos One **5**(1): 8.

## List of Abbreviations

5-LO: 5-lipoxygenase

bTbk: Bis-TEMPO-bisketal

Cer : Ceramide

CIS: Induced chemical shift

CODEX: Centerband-Only Detection of Exchange

COX: cyclooxygenase

CP: Cross polarization

CSA:Chemical shift anisotropy

DEPE: 1-palmitoyl-2-stearoyl-(14-doxy)-*sn*-glycero-3-phosphocholine

DMPC: 1,2-dimyristoyl-*sn*-glycero-3-phosphocholine

DNP: Dynamic Nuclear Polarization

DPPC: 1,2-dipalmitoyl-*sn*-glycero-3-phosphocholine

DSS: 4,4-dimethyl-4-silapentane-1-sulfonic acid

FID: Free induction decay

FSLG-CP: Frequency switched Lee Goldberg cross-polarization

GUV: Giant unilamellar vesicles

IR: Infrared spectroscopy

LG: Lee Goldberg

LTs: leukotrienes

MAS: Magic angle spinning

MD: Molecular dynamics

mPGES-1: Microsomal prostaglandin E synthase-1

na: not assignable

nd: not determined

NMR: Nuclear magnetic resonance

NOE: Nuclear Overhauser effect

NOESY: Nuclear Overhauser effect spectroscopy

NPT: constant pressure and temperature

NSAIDs: Non-steroidal anti-inflammatory drugs



NVT: constant volume and temperature

PGE2: Prostaglandin E2

PGs: Prostaglandins

PISEMA: Polarization inversion spin exchange at magic angle

PMNL: polymorphonuclear leukocytes

POPC: 1-palmitoyl-2-oleoyl-*sn*-glycero-3-phosphocholine

PPAR's: Peroxisome proliferator activated of receptors

QUAD: Quadrupolar moment

rf: Radiofrequency

RFDR: Radiofrequency driven dipolar recoupling

SMase: Sphingomyelinase

SN: Nucleophilic Substitution

TEMPO: (2,2,6,6-Tetramethylpiperidin-1-yl)oxyl

TOTAPOL: 1-(TEMPO-4-oxy)-3-(TEMPO-4-amino)propan-2-ol

TPPI: Time proportional phase incrementation

VdW: van der Waals

## List of Figures

- Figure 1-1: Phase transition diagram of a binary DMPC-Water system: L, lamellar phase;  $L_{\beta}$ , gel phase;  $L_{\alpha}$ , liquid crystalline phase;  $P_{\beta}$ , rippled gel phase; C, hydrated crystalline phase; (Janiak, Small et al. 1979). ..... 10
- Figure 1-2: Structure of a DMPC lipid bilayer as illustrated by a united-atom MD simulation. The bilayer width, i.e head-to-head distance of 3.2 nm is illustrated on the right as a mass-density profile plotted across the bilayer. .... 12
- Figure 1-3: Schematic representation of NMR parameters, which can be extracted from phospholipids and which report on bilayer structure and dynamics: information on lipid chain order and dynamics can be obtained in form of order parameters from C-H dipole couplings or C-D deuterium quadrupole couplings.  $T_1$  is the spin-lattice relaxation time in laboratory frame and  $T_{1\rho}$  is spin-lattice relaxation time in rotating frame along the acyl chains. The  $^{31}\text{P}$  CSA and  $^{14}\text{N}$  quadrupole coupling are sensitive parameters for the lipid phase and for charge effects at the membrane surface. In addition  $^1\text{H}$  chemical shifts of all sites in the lipids offer insight into lipid-lipid interactions via 2D NOESY-MAS NMR correlation spectroscopy. .... 13
- Figure 1-4: Accessibility of motions occurring in lipid membranes by solid-state NMR experiments and by MD simulations. .... 15
- Figure 1-5: The basic-principle of magic angle spinning NMR: Rotating samples about the magic angle with respect to external magnetic field (left), averages anisotropic NMR interactions if the sample rotation rate exceeds the size of the anisotropy as illustrated here for the case of chemical shift anisotropy (right). Without sample rotations, the full CSA tensor is observed, if the spinning speed smaller than the CSA; spinning sidebands occur and if the spinning speed exceeds the size of the CSA, only the isotropic chemical shift remains. Simulations shown here correspond to  $^{31}\text{P}$ -spectra of DPPC static, slow spinning (2 kHz) and fast spinning (10 kHz) (Schiller, Muller et al. 2007). .... 18
- Figure 1-6: Lipid polymorphism and typical  $^{31}\text{P}$ -lineshapes. Simulations of static  $^{31}\text{P}$  NMR line shapes are shown for a dry powder sample (a), liquid crystalline phase (b), inverted hexagonal phase (c) and liquid crystalline phase under MAS (c); The spectra were simulated based on principle CSA tensor values taken from Schiller et al. (Schiller, Muller et al. 2007) ..... 22
- Figure 1-7: Schematic representation of NOE transitions between energy levels of two spins.  $W_0$ ,  $W_1$  and  $W_2$  denote zero quantum, single quantum and double quantum transitions, respectively. .... 26
- Figure 2-1: Structures of lipid: POPC, DPPC, DMPC, POPC-d31 and DMPC-d67. .... 36
- Figure 2-2: Pulse sequence (left) and spectral shape (right) of NOESY experiment. Magnetization transfer between nuclei takes place during mixing time ( $t_m$ ). .... 38
- Figure 2-3: Pulse sequence (left) and spectral shape (right) of RFDR experiment. Magnetization transfer between nuclei takes place by application of recoupling pulses at rotor period ( $t_{\text{rotor}}$ ) during mixing time ( $t_m$ ). .... 39
- Figure 2-4:  $^2\text{H}$ -NMR quadrupolar echo pulse sequence (left) and a static quadrupolar spectrum (right),  $\tau$  is the delay to refocus the signal.  $\Delta\nu$  is the quadrupolar splitting. .... 40
- Figure 2-5: Representation of effective magnetic field at the rotating frame at Lee-

Goldburg condition.....	41
Figure 2-6: Schematic representation of FSLG - $^1\text{H}$ pulses .....	42
Figure 2-7: FSLG-CP pulse sequence (left) and spectral shape (right).....	43
Figure 2-8: Pulse sequences to measure $T_1$ relaxation times of $^1\text{H}$ (left) and saturation recovery curve (right); $S_0$ is the maximum intensity, $n$ times $90^\circ$ pulses are repeated to saturate magnetization, delay time $\tau$ is varied to observe recovery.....	44
Figure 2-9: Pulse sequences to measure $T_1$ relaxation times of $^{13}\text{C}$ (left) and decay curve (right); $S_0$ is the maximum intensity, delay time $\tau$ is varied to observe magnetization delay.....	45
Figure 2-10: Pulse sequence to measure $T_1$ relaxation time in rotating frame for $^{13}\text{C}$ nucleus (left) and decay curve (right); $S_0$ is the maximum intensity. Pulse length $\tau$ is varied to observe relaxation process.....	47
Figure 2-11: $^{31}\text{P}$ NMR Hahn echo pulse sequence (left) and static spectral shape (right), $\tau$ is the delay to refocus the signal.....	48
Figure 2-12: $^{31}\text{P}$ -CODEX pulse sequence (top) and dephasing curve (bottom), $S$ is the intensity at certain mixing time and $S_0$ is the intensity of reference spectrum. During mixing time ( $t_m$ ), CODEX exchange takes place, $t_m$ and $t_z$ are interchanged to record a reference spectrum.....	50
Figure 2-13: 2D- $^{31}\text{P}$ static exchange experiment pulse sequence (left) and spectral shape (right) (Marasinghe, Buffy et al. 2005), reorientation in chemical shift tensor takes place during mixing time ( $t_m$ ).....	51
Figure 3-1: Schematic representation of arachidonic acid cascade; (Hieke, Greiner et al. 2011) .....	56
Figure 3-2: Structures and nomenclature of pirinixic acid ( <b>1</b> ), pirinixic acid derivatives ( <b>2</b> , <b>3</b> ) and POPC (bottom) .....	57
Figure 3-3: 1-dimensional $^1\text{H}$ -MAS spectra of POPC-d31 (bottom), POPC-d31- <b>2</b> mixture (middle) and POPC-d31- <b>3</b> mixture (top) at 300 K. The aromatic region is zoomed in to see resonances of <b>2</b> and <b>3</b> .....	65
Figure 3-4: $^1\text{H}$ chemical shift differences of pure POPC-d31, POPC-d31- <b>2</b> mixture and POPC-d31- <b>3</b> mixture at 300 K, x-axis shows lipid atoms along the bilayer.....	66
Figure 3-5: $^1\text{H}$ -MAS NOESY spectra of POPC-d31- <b>2</b> and POPC-d31- <b>3</b> mixtures at 50 ms mixing time at 300 K, cross peaks of <b>2</b> and <b>3</b> with POPC head group and lipid tail were depicted in the boxes.....	67
Figure 3-6: $^1\text{H}$ -MAS NOESY spectra of POPC-d31-pirinixic acid derivatives mixtures at 200 ms mixing time at 300 K, crosspeaks of <b>2</b> and <b>3</b> with POPC head group and lipid tail were depicted in the boxes.....	68
Figure 3-7: $^1\text{H}$ -MAS NOESY spectra of POPC-d31-pirinixic acid derivatives mixtures at 400 ms mixing time at 300 K, crosspeaks of <b>2</b> and <b>3</b> with POPC head group and lipid tail were depicted in the boxes.....	69
Figure 3-8: Buildup curves of $^1\text{H}$ -MAS NOESY peak volumes of the mixture of POPC-d31 with compound <b>2</b> at 300 K; mixing times of 5-800 ms were used, yellow region shows crosspeak between <b>2</b> and POPC buildup curves.....	70
Figure 3-9: Buildup curves of $^1\text{H}$ -MAS NOESY peak volumes of the mixture of POPC-d31 with compound <b>3</b> at 300 K; mixing times of 5-800 ms were used, yellow region shows crosspeak between <b>3</b> and POPC buildup curves.....	71
Figure 3-10: Distribution profiles of compound <b>2</b> inside POPC-d31 bilayer from $^1\text{H}$ -MAS	

NOESY of the mixture of POPC-d31 with compound <b>2</b> at 300 K: in the figure legend, substrate protons at pyridine and quinoline rings were shown, 2 and 4 cannot be assigned, 3 and 5 are overlapped and other protons are well-resolved and assigned. ....	72
Figure 3-11: Distribution profiles of compound <b>3</b> inside POPC-d31 bilayer from <sup>1</sup> H-MAS NOESY of the mixture of POPC-d31 with compound <b>3</b> at 300: in the figure legend, substrate protons at pyridine and quinoline rings were shown, 2 and 4 cannot be assigned, 3 and 5 are overlapped and other protons are well-resolved and assigned. ....	73
Figure 3-12: Distribution probabilities of H-3,5 of compound <b>2</b> (top) and <b>3</b> (bottom) along the bilayer calculated by <sup>1</sup> H-MAS NOESY cross-relaxation rates at 300 K, at the top of the figure, distribution probabilities of <b>2</b> and <b>3</b> is represented. ....	74
Figure 3-13: RFDR and NOESY spectra of POPC-d31 - <b>2</b> mixture for 125ms mixing time for both spectra at 300 K, inside the rectangulars, crosspeaks of large (CH <sub>2</sub> ) <sub>n</sub> signal is highlighted. ....	76
Figure 3-14: Buildup curves of diagonal-peak intensities for the resonance of (CH <sub>2</sub> ) <sub>n</sub> and the crosspeak intensities with other lipid resonances from RFDR up to 125 ms (top), NOESY up to 125 ms (middle) and NOESY up to 800 ms (bottom) of POPC-d31 – <b>2</b> mixture at 300 K. ....	77
Figure 3-15: Distribution profiles of compound <b>2</b> inside POPC-d31 bilayer from <sup>1</sup> H-MAS RFDR of the mixture of POPC-d31 with compound <b>2</b> at 300 K: in the figure legend, substrate protons at pyridine and quinoline rings were shown, 2 and 4 cannot be assigned, 3 and 5 are overlapped and other protons are well-resolved and assigned. ....	79
Figure 3-16: Distribution profiles of compound <b>3</b> inside POPC-d31 bilayer from <sup>1</sup> H-MAS RFDR of the mixture of POPC-d31 with compound <b>3</b> at 300 K: in the figure legend, substrate protons at pyridine and quinoline rings were shown, 2 and 4 cannot be assigned, 3 and 5 are overlapped and other protons are well-resolved and assigned. ....	80
Figure 3-17: Starting and final structures of POPC- compound <b>2</b> simulation boxes for 4 different conformations of <b>2</b> with respect to bilayer. ....	84
Figure 3-18: Starting and final structures of POPC-compound <b>3</b> simulation boxes for 4 different conformations of <b>3</b> with respect to bilayer. ....	85
Figure 3-19: Position distributions (Å) on z-direction of carbon atoms (names of atoms were labeled in the figure) of compound <b>2</b> and <b>3</b> with respect to bilayer center of mass (labeled as COM in the figure) for 4 different conformation of the molecules. ....	86
Figure 3-20: Normalized inverse distance on z-direction of simulation box between lipid atoms and carbon atom at position 3 of compound <b>2</b> (top) and <b>3</b> (bottom): calculations were done for the conformation-1, at the top of the figure, locations of <b>2</b> and <b>3</b> is represented. ....	88
Figure 3-21: Snapshots of the trajectory that show compound <b>2</b> partitioning inside POPC bilayer, partition occurs within 10 ns. ....	89
Figure 3-22: Snapshots of the trajectory that show compound <b>3</b> partitioning inside POPC bilayer, partition occurs within 10 ns. ....	90
Figure 4-1: Structure and nomenclature of DPPC and drugs used in this study. ....	93

Figure 4-2: $^1\text{H}$ NMR spectra of DPPC and mixtures of DPPC with ibuprofen (DPPC-IBU), diclofenac (DPPC-DICLO) and piroxicam (DPPC-PIR) at 320 K with 12 kHz spin rate and 16 scan number. ....	98
Figure 4-3: $^1\text{H}$ MAS NOESY spectra of DPPC; spectrum were recorded at 320 K with 12 kHz spin rate and 16 scan with 300 ms mixing time. ....	99
Figure 4-4: $^1\text{H}$ MAS NOESY spectra of Piroxicam (PIR), Diclofenac (DICLO) and Ibuprofen (IBU), DPPC-Piroxicam (PIR-DPPC) spectra were chosen to show the lipid region; spectra were recorded at 320 K with 12 kHz spin rate and 16 scan with 200 ms mixing time. ....	100
Figure 4-5: $^1\text{H}$ MAS NOESY spectra of Piroxicam (PIR), Diclofenac (DICLO) and Ibuprofen (IBU), DPPC-Piroxicam (PIR-DPPC) spectra were chosen to show the lipid region; spectra were recorded at 320 K with 12 kHz spin rate and 16 scan with 400 ms mixing time. ....	101
Figure 4-6: $^1\text{H}$ MAS NOESY spectra of Piroxicam (PIR), Diclofenac (DICLO) and Ibuprofen (IBU), DPPC-Piroxicam (PIR-DPPC) spectra were chosen to show the lipid region; spectra were recorded at 320 K with 12 kHz spin rate and 16 number with 800 ms mixing time. ....	102
Figure 4-7: Distribution probabilities of diclofenac (5-H) and ibuprofen (4-H) along DPPC bilayer derived from $^1\text{H}$ -MAS NOESY crosspeak intensities: at 320 K and 400 ms mixing time. ....	103
Figure 4-8: Simulated (red curve) and experimental (blue curve) $^{31}\text{P}$ static NMR spectra of DPPC-Piroxicam (A), DPPC-Diclofenac (B), DPPC-Ibuprofen (C) and pure DPPC (D), spectra were recorded at 315 K with 512 scan number. ....	105
Figure 5-1: General structures of ceramides. ....	108
Figure 5-2: Structures of DMPC and C16-Ceramide; atoms that were chosen for Delaunay triangulation-Voronoi tessellation were depicted inside blue circles. ....	114
Figure 5-3: The representation of periodicity of Voronoi diagram of a bilayer projection; at the center, xy plane of the original simulation box (highlighted as pink) locates and it is extended from each side to obtain periodicity for Voronoi tessellation. ...	116
Figure 5-4: Spectrum for optimization of $^{13}\text{C}$ -rf field for FSLG-CP conditions: $\omega_{1,C}^+$ and $\omega_{1,C}^-$ are $^{13}\text{C}$ rf-fields matched with $^1\text{H}$ efficient rf-field at spinning side bands +1 and -1, respectively; $\omega_r$ is spinning speed (explained in methods, Chapter 2). ....	119
Figure 5-5: Snapshots from pure DMPC (red) and DMPC-Ceramide mixture (blue). ...	121
Figure 5-6: Area per lipid in DMPC bilayers: pure DMPC (top) and DMPC-C16-Cer mixture (bottom). ....	123
Figure 5-7: Water and system mass density profiles of pure DMPC and DMPC-C16-Cer mixture. ....	124
Figure 5-8: Order parameters of $\text{SN}_1$ and $\text{SN}_2$ (top) chains of DMPC for pure DMPC and DMPC-C16-Cer mixture and acyl and sphingosine (bottom) chains of ceramide for DMPC-C16-Cer mixture. ....	126
Figure 5-9: Number of H-bond that C16-Cer forms with DMPC, water, and C16-Cer itself. ....	127
Figure 5-10: Numbers of hydrogen bonds between ceramide and DMPC: atoms denoted as D stand for H-bond donors, atoms denoted as A stand for H-bond acceptors. ...	129
Figure 5-11: Radial distribution functions for water oxygen with carbonyl carbon of DMPC $\text{SN}_2$ chain for DMPC and DMPC-C16-Cer mixture (top) and with carbonyl	

carbon of ceramide acyl chain for DMPC-C16-Cer mixture (bottom).....	131
Figure 5-12: Electrostatic Potential of DMPC(top) for DMPC and DMPC-C16-Cer; Charge Distribution of DMPC, Water and the System for DMPC bilayer (middle) and DMPC, Ceramide, Water and the System for DMPC-C16-Cer Mixture (bottom). .....	133
Figure 5-13: Histograms of P-N vectors with Z axis of the simulation box for pure DMPC and DMPC-C16-Cer mixture: bulk DMPC (upperleft) and DMPC with close vicinity to random lipids (lowerleft) for DMPC bilayer; bulk DMPC (upperright) and DMPC with close vicinity to ceramides (lowerright) for DMPC-C16-Cer mixture. ....	134
Figure 5-14: $^{31}\text{P}$ static NMR spectra of mixture of DMPCd67- C16-Cer and DMPCd67 at 310 K: isotropic chemical shift ( $\delta_{\text{iso}}$ ) in ppm and chemical shift anisotropy (CSA) in ppm were calculated by lineshape analyses. ....	136
Figure 5-15: Structures and assignments of DMPC and C16-Ceramide.....	137
Figure 5-16: Temperature dependent $^1\text{H}$ NMR spectra of DMPC (left) and mixture of DMPC-C16-Cer (right). Phase transition temperature of DMPC shifted to higher temperature, from 290 K to 300 K, in the presence of C16-Cer. ....	138
Figure 5-17: Temperature dependent $^1\text{H}$ NMR spectra of mixture of DMPCd67- C16-Cer (top), pure DMPCd67 (middle) and pure C16-Cer (bottom). In the mixture, phase transition temperature of C16-Cer shifted to lower temperature, it follows the phase transition of DMPC. ....	139
Figure 5-18: $^1\text{H}$ MAS NOESY spectrum of DMPCd67 with 200 ms mixing time at 300 K: Glycerol peaks and residual acyl chain peaks are depicted into the rectangles. ....	141
Figure 5-19: $^1\text{H}$ MAS NOESY spectrum of mixture of DMPCd67- C16-Cer with 50 ms mixing time at 300 K; boxes showed crosspeak region of g1, g2, g3 protons of DMPC with 6' and 1'a protons of C16-Cer. ....	142
Figure 5-20: $^1\text{H}$ MAS NOESY spectrum of mixture of DMPCd67- C16-Cer with 200 ms mixing time at 300 K; boxes showed crosspeak region of g1, g2, g3 protons of DMPC with 6' and 1'a protons of C16-Cer. ....	143
Figure 5-21: $^1\text{H}$ MAS NOESY spectrum of mixture of DMPCd67- C16-Cer with 400 ms mixing time at 300 K; boxes showed crosspeak region of g1, g2, g3 protons of DMPC with 6' and 1'a protons of C16-Cer. ....	144
Figure 5-22: Buildup curves of peak volumes of $^1\text{H}$ -MAS NOESY of the mixture of DMPC-d67-C16-Ceramide at 300 K: The yellow region shows buildup curves at crosspeaks between DMPC glycerol backbone protons. ....	145
Figure 5-23: Normalized cross relaxation rates of ceramide nuclei 6' (top) and 1'a (bottom) with C16-Cer and DMPC protons for the mixture of DMPCd67-C16-Cer at 300 K; C16-Cer and DMPC protons are depicted in the figure. ....	146
Figure 5-24: $^1\text{H}$ MAS NOESY spectrum of mixture of DMPCd67- C16-Cer with 200 ms mixing time at 330 K: The arrow depicts, crosspeaks between DMPC g2 peak and C16-Cer double bond (4' and 5') peaks inside the rectangles.....	147
Figure 5-25: $^1\text{H}$ MAS NOESY spectrum of mixture of DMPCd67- C16-Cer with 800 ms mixing time at 330 K: The arrow depicts, crosspeaks between DMPC g2 peak and C16-Cer double bond (4' and 5') peaks inside the rectangles.....	148
Figure 5-26: $^1\text{H}$ MAS NOESY spectrum of mixture of DMPCd67- C16-Cer with 1000 ms mixing time at 330 K: The arrow depicts, crosspeaks between DMPC g2 peak and C16-Cer double bond (4' and 5') peaks inside the rectangles.....	149

Figure 5-27: Normalized cross relaxation rates of ceramide nuclei 4' and 5' with DMPC nuclei at the glycerol backbone for the mixture of DMPCd67-C16-Cer at 330 K.	150
Figure 5-28: Normalized cross relaxation rates of resonance A with C16-Cer and DMPC protons for the mixture of DMPCd67-C16-Cer at 300 K; C16-Cer and DMPC protons are depicted in the figure. ....	152
Figure 5-29: <sup>1</sup> H NMR spectra of pure C16-Cer in H <sub>2</sub> O, mixture of DMPCd67-C16-Cer in H <sub>2</sub> O, pure C16-Cer in D <sub>2</sub> O, mixture of DMPCd67-C16-Cer in D <sub>2</sub> O and pure DMPCd67 in D <sub>2</sub> O: peak C is the exchangeable proton and peak A is seen only in the spectra of DMPC-d67-C16-Cer mixtures. ....	153
Figure 5-30: <sup>14</sup> N NMR spectra of DMPCd67 at 300 K, mixture of DMPCd67- (20 %) C16-Cer at 300K and 350K and mixture of DMPCd67- (30 %) C16-Cer at 300K; isotropic chemical shift ( $\delta_{iso}$ ) in ppm and quadrupolar coupling (CQ) in kHz were calculated by side band analyses. ....	155
Figure 5-31: 1D slices of 2D PISEMA spectra of DMPC for the pure DMPC sample at 300 K (left), 315 K (middle) and 330 K (right). ....	158
Figure 5-32: 1D slices of 2D PISEMA spectra of DMPC for the mixture of DMPC-C16-Cer at 300 K (left), 315 K (middle) and 330 K (right). ....	159
Figure 5-33: 1D slices of 2D PISEMA spectra of C16-Cer for the mixture of DMPCd67-C16-Cer at 300 K (left), 315 K (middle) and 330 K (right); a, b, c, d are C16-Cer peaks with increasing chemical shift. ....	160
Figure 5-34: Order parameter profiles of DMPC ( in pure DMPC and DMPC- C16-Cer mixture) and C16-Cer( in DMPCd67-C16-Cer mixture) at 300 (top), 315 (middle) and 330 K (bottom); order parameters for C16-Cer peaks a, b, c and d were plotted in descending order. ....	161
Figure 5-35 : <sup>31</sup> P-CODEX dephasing curves for DMPC and DMPC-C16-Cer mixture at 300 K (top) and 270 K (bottom). ....	164
Figure 5-36: 2D <sup>31</sup> P exchange spectra of DMPC bilayer: at 300K with $t_m$ equals 5 ms (a) and 400 ms (b), at 270K with $t_m$ equals 5 ms (c) and 400 ms (d). ....	167
Figure 5-37: 2D <sup>31</sup> P exchange spectra of DMPC-C16-Cer mixture: at 300K with $t_m$ equals 5 ms (a) and 400 ms (b), at 270K with $t_m$ equals 5 ms (c) and 400 ms (d). ....	168
Figure 6-1: Structures of bTbk (top) and TOTAPOL (bottom) ....	172
Figure 6-2: <sup>1</sup> H-T <sub>1</sub> values for pure DMPC and DMPC-bTbk mixture (Yeansin Ong, 2011): spectra are recorded by Bruker 600WB Avance II at 300 K by saturation recovery experiment. ....	176
Figure 6-3: Starting and final structures of DMPC-bTbk simulation boxes for 4 different conformation of bTbk. ....	178
Figure 6-4: Center of mass of bTbk (labeled as bTbk COM) with respect to bilayer center of mass (labeled as Bilayer COM in the figure) and two carbon atoms (C1 and C14) of DMPC SN1 chains for 4 different conformations of bTbk. Z-positions are in Å and are scaled with the average position of the center of mass of the bilayer. ....	179
Figure 6-5: Snapshots of the trajectory that shows bTbk partitioning inside DMPC bilayer ....	180
Figure 8-1: 1D spectra of POPC extracted from 2D FSLG-CP spectrum for pure POPC (left), mixture of POPC-C12-Cer (10 % C12-Cer) (middle) and mixture of POPC-C4-Cer (10 % C4-Cer) (right): Spectra were recorded by BRUKER 600 WB Avance II spectrometer at 300 K. ....	185

- Figure 8-2: Order parameters profiles of POPC-d31 from samples of pure POPC and the mixture of POPC with C4-, C12-Ceramides (10 % ceramide concentration for each mixture) calculated from FSLG-CP spectra, which were recorded by BRUKER 600 WB Avance II spectrometer at 300 K. (L1 stands for the peak  $C_{4-7,12-15}$ )..... 186
- Figure 8-3:  $^2\text{H}$  Spectra of samples of pure POPC-d31 (a), mixture of POPC-d31 with C4, C12, C16-Ceramides (b, c, d, respectively; 10 % ceramide concentration for each mixture) and POPC with C16-Ceramide-d31 (e). Spectra were recorded by BRUKER 600 WB Avance II spectrometer at 300 K. .... 187
- Figure 8-4: Temperature dependent  $^2\text{H}$  NMR spectra of samples of pure POPC-d31 (left) and the mixture of POPC-d31 with C16-Ceramide (10 % C16-Ceramide) (right), Spectra were recorded by BRUKER 600 WB Avance II spectrometer. .... 188
- Figure 8-5: Temperature dependent  $^{31}\text{P}$  static spectra of samples of pure POPC-d31 (left), mixture of POPC-d31 with C4, C12-Ceramides (middle, right, respectively, 10 % ceramide concentration for each mixture), Spectra were recorded by BRUKER 400 WB Avance II spectrometer..... 189
- Figure 8-6: Spin-lattice relaxation times for  $^1\text{H}$  of pure POPC-d31, mixture of POPC-d31 with C4, C12, and C16-Ceramides (10 % ceramide concentration for each mixture). Saturation recovery experiment was used to measure relaxation times, spectra were recorded by BRUKER 850 WB Avance II spectrometer at 300 K..... 190
- Figure 8-7: Spin-lattice relaxation times for  $^{13}\text{C}$  of pure POPC-d31, mixture of POPC-d31 with C4, C12, and C16-Ceramides (10 % ceramide concentration for each mixture). Decay experiment was used to measure relaxation times, spectra were recorded by BRUKER 850 WB Avance II spectrometer at 300 K. .... 191
- Figure 8-8: Spin-lattice relaxation times in rotating frame for  $^{13}\text{C}$  of pure POPC-d31, mixture of POPC-d31 with C4, C12, and C16-Ceramides (10 % ceramide concentration for each mixture). Spectra were recorded by BRUKER 850 WB Avance II spectrometer at 300 K. .... 192
- Figure 8-9: Area per lipid of POPC-ceramide systems with analogy force-field (each simulation was performed for 10 ns at 300 K)..... 195
- Figure 8-10: Area per lipid of POPC-ceramide systems with server force-field, (each simulation was performed for 10 ns at 300 K)..... 196
- Figure 8-11: Density profiles of POPC-Ceramide systems in different ceramide concentration with analogy force-fields: lower curves displays water density, higher curves displays system density (each simulation was performed for 10 ns at 300 K). .... 197
- Figure 8-12: Density profiles of POPC-Ceramide systems in different ceramide concentration with server force-fields: lower curves displays water density, higher curves displays system density (each simulation was performed for 10 ns at 300 K). .... 198
- Figure 8-13: Order parameters of  $\text{SN}_1$  and  $\text{SN}_2$  chains of POPC for POPC-ceramide systems with analogy force-fields (each simulation was performed for 10 ns at 300 K). .... 199
- Figure 8-14: Order parameters of  $\text{SN}_1$  and  $\text{SN}_2$  chains of POPC for POPC-ceramide systems with server force-fields (each simulation was performed for 10 ns at 300 K). .... 200
- Figure 8-15: Order parameters of  $\text{SN}_1$  and  $\text{SN}_2$  chains of POPC for 10% of POPC-



ceramide systems from last 90 ns of 180 ns long simulations with server force-fields for ceramides at 300 K.....	202
Figure 8-16: Order parameters of acyl and sphingosine chains of ceramide for POPC-ceramide systems with analogy force-fields (each simulation was performed for 10 ns at 300 K). .....	203
Figure 8-17: Order parameters of acyl and sphingosine chains of ceramide for POPC-ceramide systems with server force-fields (each simulation was performed for 10 ns at 300 K).....	204
Figure 8-18: Number of hydrogen bonds between POPC and ceramides for POPC-ceramide systems with analogy force-fields (each simulation was performed for 10 ns at 300 K). .....	206
Figure 8-19: Radial distribution functions for water oxygen with carbonyl carbon of POPC SN <sub>2</sub> chain (left) and carbonyl carbon of ceramide acyl chain (right) for POPC-ceramide systems with analogy force-fields(each simulation was performed for 10 ns at 300 K).....	207

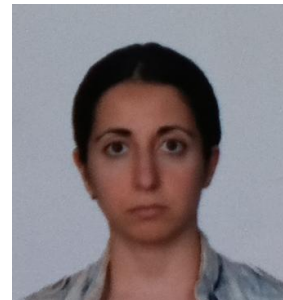
## List of Tables

Table 3-1: Cross relaxation rates of lipid protons with the resonance of $(\text{CH}_2)_n$ by NOESY and RFDR experiments for the POPC- <b>2</b> mixture at 300 K.....	78
Table 3-2: $^1\text{H}$ MAS NMR chemical-shifts of compound <b>2</b> and <b>3</b> ; Crosspeak intensities between pirinixic acid derivatives and POPC for 50 ms mixing time (intensities were extracted by using CARA software); restrained sites are chosen by largest intensities highlighted in red.....	82
Table 3-3: Restraint coordinates at the beginning of simulations and average coordinates of restrained atoms throughout 100ns simulation of each conformation; coordinates were taken only for z-direction in Å unit and scaled with respect to center of mass of the bilayer. ....	87
Table 4-1: Assignment of DPPC and drugs and chemical shift differences of $^1\text{H}$ MAS NMR of DPPC in the presence of drugs; n.a.: not assignable, chemical shifts are given in ppm. ....	96
Table 5-1: Summary of trajectory analysis for DMPC and DMPC-C16-Cer; bilayer area, area per lipid, bilayer width, numbers of hydrogen bonds, 1st maximum of radial distribution function for DMPC-water, electrostatic potentials inside the bilayers, P-N vector orientation with respect to bilayer normal are listed. ....	128
Table 6-1: Average positions on z-direction of C1 and C14 atoms of DMPC and center of mass of bTbk for 4 different starting conformations; positions are in Å and are calculated with respect to the center of mass of bilayer. ....	177
Table 8-1: $^1\text{H}$ -, and $^{13}\text{C}$ - $T_1$ and $^{13}\text{C}$ - $T_{1\rho}$ for three sample, pure POPC and mixtures of POPC-C4-Cer and POPC-C12-Cer (10 % ceramide concentration for each mixture), at different external magnetic fields and temperatures; all the values are in seconds. ....	194
Table 8-2: Bilayer area, area per lipid, bilayer width, 1st maximum of radial distribution function for POPC-water of pure POPC and POPC-Ceramide mixtures in different ceramide concentrations for two different force-fields.....	201
Table 8-3: Number of hydrogen-bonds between ceramide with POPC, water and ceramide itself and between POPC and water for pure POPC and POPC-Ceramide mixtures in different ceramide concentrations for two different force-fields. ....	205

# Curriculum Vitae

## PERSONAL DETAILS

Name: Bercem Dutagaci  
Date of Birth: 1981  
Place of Birth: Diyarbakir-Turkey  
Nationality: Turkey  
Gender: Female



## EDUCATION

Ph.D Johann Wolfgang Goethe University, Institute of Biophysical Chemistry  
Frankfurt am Main, Germany 2013

*Biophysical Studies of Lipid Membranes by Solid-State NMR and Molecular  
Dynamics Simulations*

Supervisor: Prof. Clemens Glaubitz

MSc Bogazici University , The Institute of Science and Engineering,  
Department of Chemistry, Istanbul, Turkey 2008

*The Synthesis and Properties of Weatherable Polymers Derived from  
Hydroxybenzophenones*

Supervisor: Prof. A. Ersin Acar

BSc Bogazici University, Department of Chemistry, Istanbul, Turkey 2006

## WORK EXPERIENCE

Research Assistant, Johann Wolfgang Goethe University, Institute of Biophysical  
Chemistry, Frankfurt am Main, Germany 2008 – 2013

Teaching Assistant, Bogazici University, Department of Chemistry,  
Istanbul, Turkey 2007 – 2008

## **TEACHING EXPERIENCE**

Course supervision in biophysical chemistry for biochemists, Teaching Fourier Transform Infrared Spectroscopy Practical Course – Johann Wolfgang Goethe University, Frankfurt am Main – Germany, 2009-2013

Teaching Assistant in Analytical Chemistry Laboratory – Bogazici University, Istanbul – Turkey

Teaching Assistant in Instrumental Analysis Laboratory – Bogazici University, Istanbul – Turkey

## **PROFESSIONAL TRAINING**

2010 8th NCCR Practical Course in Biomolecular Modelling

January 10 - 15, 2010, Kandersteg, Switzerland

Supervision: Wilfred F. van Gunsteren | ETH, Zurich

2009 CCPN (The Collaborative Computing Project for NMR) Workshop

February 17 - 18, 2009, Frankfurt am Main, Germany

Supervision: Wayne Boucher

## **PUBLICATIONS**

Published:

1. Huesch, J.; Dutagaci, B.; Glaubitz, C.; Geppert, T.; Schneider, G.; Harms, M.; Mueller-Goymann, C. C.; Fink, L.; Schmidt, M. U.; Setzer, C.; Zirkel, J.; Rebmann, H.; Schubert-Zsilavec, M.; Abdel-Tawab, M., Structural properties of so-called NSAID-phospholipid-complexes. *European Journal of Pharmaceutical Sciences* **2011**, *44* (1-2), 103-116.

In preparation:

1. Dutagaci, B; Lopez, J.; Schubert-Zsilavec, M.; Faraldo-Gómez J. D.; Glaubitz C.; (in preparation); Investigation of Interactions between Pirinixic Acid Derivatives and POPC bilayers by Solid-State NMR and Molecular Dynamics Simulations

## **CONFERENCE PRESENTATIONS**

1. Dutagaci, B.; Baldus, J.; Faraldo-Gómez J. D.; Glaubitz, C., Investigation of Influences of Ceramides on Phospholipid Membrane Dynamics by Solid-State NMR and MD Simulations, *EUROMAR 2012*, Poster Presentation.
2. Dutagaci, B.; Baldus, J.; Faraldo-Gómez J. D.; Glaubitz, C., Influences of Ceramides on POPC Membrane Dynamics from ps to ms Timescales: A Solid-State NMR and MD Study, *EUROMAR 2011*, Poster Presentation.
3. Dutagaci, B.; Baldus, J.; Faraldo-Gómez J. D.; Glaubitz, C., Investigation of the Influence of Ceramide on the Dynamics of POPC Membranes via Solid-State NMR and Molecular Dynamics Simulations, *5th BMRZ-CEF Workshop 2011*, Oral Presentation
4. Dutagaci, B.; Faraldo-Gómez J. D.; Glaubitz, C., Investigation of the Influence of Ceramides with Different Chain-Length on POPC Membranes via Molecular Dynamics Simulations, *1st Internal Symposium "Research in Molecular & Cell Biological Sciences"*; Goethe University; Frankfurt am Main **2010**, Poster Presentation.
5. Dutagaci, B.; Acar, A. E., POLY 149-Synthesis and properties of weatherable copolymers. *Abstracts of Papers of the American Chemical Society, ACS National Meeting, New Orleans 2008*, 235, 1, Poster Presentation.

## Acknowledgement

First of all, I would like to express my gratitude to my supervisor Prof. Clemens Glaubitz to give me the opportunity to work in his lab and for his continuous support on my research. He provided a chance to work independently at the same time he was always willing to help me with his guidance.

Besides my supervisor, I also would like to thank Prof. José D. Faraldo-Gómez for his help, support and patience. He has always motivated me during our long and valuable discussions and encouraged me kindly whenever I felt down.

I would like to thank to the members of the PhD thesis committee for their careful and constructive review of the final manuscript of my thesis.

I want to thank Prof. Peter Guntert for his careful reading of the manuscript. Moreover, I am grateful to him for providing computer clusters for my time and space consuming calculations. In addition, I am very thankful to Dr. Teppei Ikeya and Sina Kazemi from Guntert group for their help about the usage of clusters.

I would like to thank Prof. Mona Abdel-Tawab and Dr. Jan Husch for introducing me the project on NSAIDs and kindly donated samples for my measurements. Also, I am very thankful to Prof. Manfred Schubert-Zsilavecz and Martina Hieke for collaborating with the project on pirinixic acid derivatives and providing the samples for NMR measurements.

I also wanted to express my sincere gratitude to Dr. Jakob Lopez for helping me on NMR spectroscopy as well as introducing me the basics of programming for the analysis of experimental and theoretical data. Besides him, I am truly thankful to Dr. Johanna Baldus for her help on NMR spectroscopy. She patiently taught me all the details of the instruments and helped me whenever there was any problem.

For funding, I would like to thank Johann Wolfgang Goethe University-Frankfurt and also Center of Biomolecular Magnetic Resonance (BMRZ) in Frankfurt, for their continuous financial support for my PhD project.

Furthermore, I would like to thank our group secretary Simone Kobyłka for her enormous help and kindness for all these years. I also would like to thank Manfred Strupf for helping me whenever any technical problems occurred in instruments and computers.

I want to express many thanks to current and former members of Glaubitz group; Dr. Karsten Mörs, Dr. Andrea Lakatos, Yean Sin Ong, Sandra Ullrich, Ramona Storch, Dr. Jiafei Mao, Michaela Mehler, Jagdeep Kaur, Jakob Maciejko, Marvin Glaser, Lisa-Marie Rauschendorfer, Dr. Nicole Pflieger, Prof. Jun Yang, Dr. Ute Hellmich, Lenica Reggie, Lena Buchner and Ingrid Weber.

I owe many thanks to my friends especially Luca Fausto Tocchio, Aldo Isidori, Gunnur Gorucu Guler, Isabella Ianni, Johan Jannik Bjerrum-Bohr and Casper Drukier for their friendships and for all the fun times we shared together.

Above all, this thesis could not be written without enormous support of my family. First of all, I am very grateful to my sister Helin for her limitless love and patience. She was supporting me in all aspects and making a huge effort to cheer me up during my hard times. I am also very thankful to my other sister Sevgi for her great sacrifice to take care of our mother when I was abroad for my study. I have always felt lucky having such lovely sisters when I was studying for my PhD.